INL/EXT-06-11749

Evaluation of Alternate Materials for Coated Particle Fuels for the Gas-Cooled Fast Reactor

Laboratory Directed Research and Development Program FY 2006 Final Report

Paul A. Demkowicz
Karen Wright
Jian Gan
David A. Petti
Todd Allen
Jake Blanchard

September 2006

The INL is a U.S. Department of Energy National Laboratory
operated by Battelle Energy Alliance

INL/EXT-06-11749

Evaluation of Alternate Materials for Coated Particle Fuels for the Gas-Cooled Fast Reactor

Laboratory Directed Research and Development Program FY 2006 Final Report

Paul A. Demkowicz[a]
Karen Wright[a]
Jian Gan[a]
David A. Petti[a]
Todd Allen[b]
Jake Blanchard[b]

[a]Idaho National Laboratory
[b]University of Wisconsin

September 2006

Idaho National Laboratory
Idaho Falls, Idaho 83415

Prepared for the
U.S. Department of Energy
Through the INL LDRD Program
Under DOE Idaho Operations Office
Contract DE-AC07-05ID14517

ABSTRACT

Candidate ceramic materials were studied to determine their suitability as Gas-Cooled Fast Reactor particle fuel coatings. The following ceramics examined in this work: TiC, TiN, ZrC, ZrN, AlN, and SiC. The studies focused on (i) chemical reactivity of the ceramics with fission products palladium and rhodium, (ii) the thermomechanical stresses that develop in the fuel coatings from a variety of causes during burnup, and (iii) the radiation resiliency of the materials. The chemical reactivity of TiC, TiN, ZrC, and ZrN with Pd and Rh were all found to be much lower than that of SiC. A number of important chemical behaviors were observed at the ceramic-metal interfaces, including the formation of specific intermetallic phases and a variation in reaction rates for the different ceramics investigated. Based on the data collected in this work, the nitride ceramics (TiN and ZrN) exhibited chemical behavior that is characterized by lower reaction rates with Pd and Rh than with the carbides TiC and ZrC.

The thermomechanical stresses in spherical fuel particle ceramic coatings were modeled using finite element analysis, and included contributions from differential thermal expansion, fission gas pressure, fuel kernel swelling, and thermal creep. In general the tangential stresses in the coatings during full reactor operation are tensile, with ZrC showing the lowest values among TiC, ZrC, and SiC; TiN and ZrN were excluded from the comprehensive calculations due to a lack of available materials data. The work has highlighted the fact that thermal creep plays a critical role in the development of the stress state of the coatings by relaxing many of the stresses at high temperatures. To perform ion irradiations of sample materials, an irradiation beamline and high-temperature sample irradiation stage was constructed at the University of Wisconsin's 1.7MV Tandem Accelerator Facility. This system is now capable of irradiating of materials to high dose while controlling sample temperature up to 800ºC.

EXECUTIVE SUMMARY

Introduction

Several fuel forms are currently being considered for the Gas Fast Reactor (GFR), including coated particle fuel embedded in an inert matrix. The development of this fuel form would build on existing experience with high temperature gas-cooled reactor (HTGR) coated particle fuel, but would differ in several key aspects, including the elimination of pyrolytic carbon as a coating material and an increase in the volume ratio of the fuel kernel to satisfy GFR fissile loading requirements. Because of the severe in-core environments of the GFR (including high temperatures and high neutron fluences) the requirements for fuel materials are demanding. Based on materials property surveys, several ceramic materials have been identified as potential particle coating materials; these are TiC, TiN, ZrC, ZrN, and SiC.

This report presents the results of a cooperative investigation by the INL and the University of Wisconsin into the suitability of these materials for GFR fuel particle coatings. The research has concentrated on three areas:

1. An investigation of the chemical reactivity of the coating materials with certain key fission products which can potentially degrade the coatings and cause particle failures. Palladium (Pd) and rhodium (Rh) were used in this study, and a variety of experiments were used to assess the chemical compatibility of with the candidate ceramics at temperatures as high as 1600ºC. These include bulk diffusion couples and vapor phase interactions.

2. Computational modeling of the thermomechanical stresses that can develop in fuel particle coatings due to a variety of diverse processes during particle fabrication and operation in-reactor. The sources of stress that were included in the analysis are fuel kernel swelling, differential thermal expansion of the kernel and coatings, pressure buildup from fission gas release from the kernel, and thermal creep of the coatings. Uranium nitride and uranium carbide were used as reference fuel kernels.

3. A study of the irradiation properties of the candidate materials using high temperature ion irradiation.This work included design and construction of a unique materials irradiation beamline and sample stage, with independent temperature control of the sample materials during irradiation.

Results Summary

The chemical compatibility experiments showed that all of the Group IV carbides and nitrides (TiC, TiN, ZrC, ZrN) were significantly more resistant to chemical attack by Pd and Rh than SiC, which is the coating material currently used in thermal spectrum reactor particle fuel (i.e. TRISO fuel). The specific chemistry of the interactions was examined in detail, including a study of the intermetallic compounds formed at the diffusion couple interfaces. The nature of the chemical reactions with Pd was fundamentally different for the carbides and nitrides. Some intergranular attack was observed, particularly at higher temperatures. Of the Group IV carbides and nitrides, the TiC sample exhibited the most extensive grain boundary attack by both Pd and Rh. The results show that the nitrides appear to exhibit a superior resistance to corrosion by Pd and Rh, with TiN giving the best performance.

Calculations of the thermomechanical stresses in the coating layers showed that the use of uranium nitride kernels generally gives lower coating stresses than uranium carbide. The kernel-coating combination that gives the lowest pre-irradiation coating stresses (i.e. stresses due to the fabrication process) is UN-TiN, due in part to the good match of thermal expansion coefficients for these materials. Fuel operation in-reactor adds kernel swelling, fission gas pressure, and creep processes to the picture. The results of this work show that creep processes are extremely important with regard to the stresses that can develop in the coatings, as creep during irradiation can have the effect of relaxing stresses that develop from other causes. Given the importance of creep in stresses development, the work was somewhat hampered by a lack of thermal creep data in the literature for TiN and ZrN, and a complete lack of irradiation creep data for any of the Group IV carbides and nitrides. Therefore, a complete treatment for all of the materials could not be completed.

Comprehensive analysis of stress development during reactor operation for particles coated with TiC, ZrC, or SiC—which includes the contribution of all the processes investigated in this study—shows that the tangential stresses in the coatings are tensile, and that a UN-ZrC particle has the lowest stresses. Note, however, that TiN and ZrN were not considered in this analysis due to lack of available data. Because coating fracture and fission product release from the particle is the primary concern, a fracture analysis was performed to compare the performance of TiC and SiC coatings. This demonstrated that, for a given pressure in the fuel particle, a TiC coating could withstand a larger flaw (i.e. elliptical crack) before critical failure.

The materials irradiation beamline and sample stage was constructed at the University of Wisconsin (UW) 1.7 MV Tandem Accelerator Facility. The system is based around a Pelletron ion accelerator and a SNICS (Source of Negative Ions by Cesium Sputtering) ion source, which allows the generation of ions of virtually any element. The sample stage was designed to allow ion irradiation of materials while independently controlling the sample temperature with heaters built into the stage. Sample temperature is monitored using an infrared camera and thermocouples embedded in the stage. The ion beam is rastered over the sample stage area by controlling the electric current to a tantalum aperture, and the beam current at the sample stage can also be monitored. Safety considerations

also required extensive shielding to be constructed around the beamline and sample stage to protect personnel from gamma-rays, x-rays, and neutrons. The end product is a system that can irradiate sample materials with ions (protons can be accelerated up to 3.4 MeV) while controlling the temperature of the samples in a range up to ~800ºC, with precise monitoring of the beam current (and hence sample ion dose).

Calculations were also performed as part of this work to model the dynamics of ion collisions in the samples and determine the irradiation depth and displacements per atom (dpa) rates for each material. A series of test irradiations has been performed on the system, including a 3 dpa run. This work will be continued at UW in FY 2007 under follow-on funding.

The results from this project have demonstrated that the Group IV carbides and nitrides are superior to SiC as GFR fuel particle coating materials in several respects, including chemical reaction with platinum-metal fission products and thermomechanical stress development in the coatings during operation. Distinctions between the specific ceramics are more difficult to draw based on the available data, but the nitrides appear to have a slight edge over the carbides based on thermomechanical stress development in the particles and chemical reactivity with platinum-group metal fission products.

CONTENTS

FIGURES

TABLES

ACRONYMS

AES	Auger electron spectroscopy
AFM	atomic force microscopy
ASTM	American Society for Testing and Materials
BF	bright field
BISO	Bi-ISOtopic coated particles
CBD	convergent beam diffraction
CTE	coefficient of thermal expansion
CVD	chemical vapor deposition
DP	diffraction pattern
dpa	displacements per atom
EBSP	electron back-scatter patterns
EDS	energy dispersive x-ray spectroscopy
EPMA	electron probe microanalyzer
ERD	elastic recoil detection
FCC	face centered cubic
FIB	focused ion beam
GFR	Gas Fast Reactor
GIXRD	grazing incident x-ray diffractometry
HIP	hot isostatic press
HTGR	High Temperature Gas-Cooled Reactor
HOLZ	High-order Laue zone
LDRD	laboratory-directed research and development
IPyC	inner pyrolytic carbon
RMS	root mean square
SEM	scanning electron microscopy

SRIM	stopping and the range of ions in matter
TEM	transmission electron microscope
TRIM	transport of ions in matter
TRISO	TRi-ISOtopic coated particles
UW	University of Wisconsin
VHTR	Very High Temperature Reactor
XRD	x-ray diffraction

EVALUATION OF ALTERNATE MATERIALS FOR COATED PARTICLE FUELS FOR THE GAS-COOLED FAST REACTOR

1. INTRODUCTION

1.1 Background

Two gas-cooled reactors are included in the Generation IV reactor program: the Very High Temperature Reactor (VHTR) and the Gas-Cooled Fast Reactor (GFR). These designs have in common a gaseous primary coolant and a high-temperature core, capable of experiencing fuel temperatures in excess of 1000ºC during normal operation and up to 1600ºC during uncontrolled accident scenarios (Meyer, Fielding, and Medvedev 2003, DOE 2002a). Such performance is possible by utilizing an all-ceramic core that consists of materials with melting points well in excess of the expected fuel temperature maximums.

The reference GFR system is a fast-spectrum, helium-cooled reactor that utilizes a direct-cycle helium turbine for electricity generation to take advantage of the high coolant outlet temperatures (~850ºC) (INEEL 2004). The GFR is expected to operate at much higher power densities (in the range of 50-100MW/m^3), have much higher fissile densities, and peak dose rates that can be in excess of 80 dpa (DOE 2002b).

Due to the extreme conditions envisioned in the GFR core, a number of important criteria have been defined for the fuel materials. These include considerations of melting points, neutronic properties, stability under high-dose irradiation, and mechanical and thermal properties. Specifically, the following properties should apply to the candidate fuel materials:

- High melting point
- Good radiation behavior, including low radiation induced swelling (preferably < 2% over the service life) and minimal degradation of mechanical or thermal properties during irradiation
- Sufficiently high fracture toughness
- Sufficiently high thermal conductivity
- Favorable neutronic properties for the fast spectrum core.

Table 1.1 shows some of the minimum requirements for the specific properties for GFR fuel materials.

Table 1.1. Reference requirements for GFR fuel material properties (Fielding 2004).

Requirement	Reference Value
Melting/decomposition temperature	> 2000°C
Radiation induced swelling	< 2% over service life
Fracture toughness	> 12 MPa $m^{1/2}$
Thermal conductivity	> 10 W/mK
Neutronic properties	Materials allow low core heavy metal inventory and maintain good safety parameters

Based on the requirements in Table 1.1, most metals and alloys are excluded due to insufficient melting point and poor high temperature mechanical properties. Refractory metals such as tungsten, tantalum, molybdenum, niobium, and rhenium and not practical from the standpoint of neutronic penalties associated with high absorption cross-sections. Oxide ceramics tend to be inadequate based on: (1) low thermal conductivities and poor thermal shock resistance, (2) insufficient melting temperatures, or (3) poor irradiation behavior.

By comparison, carbide and nitride ceramics possess many of the required properties that make them suitable for GFR fuel. A number of these ceramic materials are disqualified for neutronic reasons, but a handful appear to be promising potential candidates. These include the carbides TiC, ZrC, and SiC, and the nitrides TiN, ZrN, and AlN (Fielding 2004).

The current GFR fuel designs are based on dispersion fuels, consisting of either rods/fibers or spherical particles embedded in an inert matrix, or solid solution fuel clad in a refractory ceramic such as SiC (DOE2005). The reference fissile phases are UN and UC. The particle fuel option would consist of spherical fuel kernels with multiple ceramic coating layers.

Most coated particle fuel experience historically has been in support of high temperature thermal spectrum gas cooled reactors (HTGRs). The current state-of-the-art fuel form is the TRI-ISOtopic coated particle (TRISO), which consists of a spherical fuel kernel coated with several layers as discussed in EDF-4380, “AGR-1 Fuel Product Specification and Characterization Guide.”

1. A porous pyrolytic carbon “buffer” layer. This layer acts as a plenum for fission gases and a buffer zone to absorb fission recoil atoms.

2. A dense inner pyrolytic carbon (IPyC), which acts as a fission product barrier and a seal coat for the chemical vapor deposition of the following layer.

3. A dense silicon carbide layer, which acts as the primary “pressure vessel” and diffusion barrier to contain the pressure build-up in the particle due to the production of fission gases and the formation of CO(g). This is the primary layer preventing the release of fission products from the particle.

4. An outer dense pyrolytic carbon (OPyC).

The primary purpose of the coating layers is to retain fission products during normal operation and during core heat-up accident scenarios, avoiding contamination of the primary coolant circuit.

Previous experiences with TRISO fuel both in-reactor and in post-irradiated high-temperature accident testing has demonstrated good performance for fission product retention (Martin 2002, Petti

et al. 2003). However, several important issues have been identified during irradiation testing and post-irradiation examinations of HTGR fuel elements. These include:

1. Irradiation-induced dimensional changes of the pyrocarbon layers, causing undesirable mechanical stresses in the coating layers and potential particle failure by breaching of the silicon carbide layer.

2. Fission product migration within the kernel and coating layers and potential diffusive transport of certain fission products out of intact coating layers.

3. Corrosive chemical attack on the silicon carbide layer by certain metallic fission products, most notably palladium, which reacts to form intermetallic phases. These phases can potentially degrade the integrity of the SiC layer and cause particle failures.

The application of particle fuel to the GFR will require several important adaptations when compared to thermal spectrum reactor fuel. One is the elimination of large volumes of carbon, which would moderate neutrons and be undesirable for a fast neutron spectrum. Another is the requirement of a large fissile volume fraction for fast reactor fuel. Thus GFR particle fuel would require a much larger kernel-to-coating volume fraction (compared to TRISO fuel) and eliminate the use of pyrolytic carbon as a coating material. A proposed approach would be to create a porous ceramic buffer layer followed by a dense ceramic coating to act as the fission product barrier (Meyer, Fielding, and Medvedev 2003). Proposed coating materials for these advanced particle fuels are the carbide and nitride ceramics (TiN, TiC, ZrN, ZrC, SiC, and AlN) that have been identified as favorable for GFR fuel applications based on mechanical, thermal, neutronic, and irradiation properties.

A limited amount of work has been performed in the area of fast reactor coated particle fuel development. This includes development of TiN particle coatings (Lowden, McLaughlin, and Kelly 2003) and the development of porous and dense SiC coatings (INL 2005). It should also be noted here that work has been performed in Japan and elsewhere to develop ZrC as an alternative to SiC in conventional TRISO fuel (Minato, Ogawa 2003, Reynolds et al. 1976). However, SiC remains the standard particle fuel coating material with a vast amount of performance data available that has not been duplicated with any other material.

1.2 Properties of Carbides and Nitrides

The Group IV transition metal carbide and nitrides TiC, TiN, ZrC, and ZrN have a unique set of properties, including high hardness, high melting points, and good electrical and thermal conductivities. All of these materials are interstitial alloys and have the NaCl FCC crystal structure in which the metal atoms occupy the close-packed FCC lattice sites and the carbon or nitrogen atoms occupy the octahedral interstitial sites. They have a range of stoichiometry, sometimes quite large, with a maximum C or N content of around 50 at.%. Thus substoichiometric compositions (e.g. TiC_{1-x}) are common, with the lattice constant of the material changing with chemical composition (Storms 1967). Substoichiometric compositions generally are due to vacancies on the nonmetal (interstitial) sites, and these vacancies can exhibit long-range order (Toth 1971).

The properties of these cubic carbides and nitrides are dependent on a number of factors, including (1) chemical composition, which includes stoichiometry (metal-to-nonmetal ratio) and impurity (particularly oxygen) concentrations and (2) microstructure, including defect types and concentrations, grain size, and porosity (Toth 1971). Because these can vary over a wide range, the properties also reflect a wide range of values. Table 1.2 gives some nominal values for the properties of the carbides and nitrides of Ti and Zr.

Silicon carbide exists in cubic, hexagonal, and rhombohedral structures. All of these forms involve layers of close-packed Si and C double layers, and variations in the stacking sequence of the layers give rise to a large number of polytypes. Lattice constants are of course specific to the particular polytype. Like the Group IV carbides, the properties of SiC are highly dependent on microstructure and chemical impurities, which in turn depend strongly on fabrication method. The x-ray density depends on polytype and is typically approximately 3.2 g/cm^3 (Harris 1995). SiC is characterized by a high hardness, high Young's modulus, and good thermal conductivity. The ranges for some SiC properties are summarized in Table 1.3. Silicon carbide oxidizes to form an adherent SiO_2 layer that can limit further oxidation, so it tends to be more oxidation resistant than the Group IV carbides and nitrides. Unlike the Group IV carbides and nitrides, SiC is a line compound, with no range of composition (Massalski 1990).

Table 1.2. Properties of the Ti and Zr carbides and nitrides.

Material	Lattice Constant, a_o (nm)	Density (g cm^{-3})	Melting Point (ºC)[a]	Young's Modulus (GPa)	Micro-hardness (GPa)	Thermal Cond.[b] (W m^{-1} K^{-1})	Electrical Resistivity (μΩ cm)
TiC[c]	0.4328	4.93		450	28.9	21	55
TiC[d]	0.4328	4.91	3067		28.4	20.9	
ZrC[c]	0.4700	6.46		350	24.6	21	40
$ZrC_{0.97}$[d]	0.4698	6.59	3420		25.5		
TiN[e]	0.4242	5.39	3320		17	29	25
TiN[d]	0.4240	5.39	2949		19.6	19.2	
ZrN[d]	0.4577	7.3	2982		14.7	20.5	
ZrN[e]	~0.4570	7.32	3250		15	11	21

a. Or decomposition temperature
b. Room temperature values
c. Ettmayer, Lengauer 1994a
d. Toth 1971
e. Ettmayer,Lengauer 1994b.

Table 1.3. Properties of SiC. Values taken from Shackelford and Alexander 2001.

Property	Value
Density (g/cm^3)	~3.2
Melting point	~2700ºC
Hardness (GPa)	28–44
Thermal conductivity (W m^{-1} K^{-1})[a]	20–120
Young's modulus (GPa)	250–450

a. Room temperature values.

The properties of the all of candidate materials investigated in this work have recently been reviewed in the context of their use in GFR fuels (Meyer, Fielding, and Medvedev 2003), including a summary of available literature data on their under neutron and ion irradiation.

1.3 Project Overview and Approach

The general objective of this research is to study carbide and nitride ceramics as coatings for GFR particle fuels. The work is intended to address some of the important technical issues relevant to fuel coatings, and has proceeded in three focus areas: (1) chemical interaction studies; (2) ion irradiation experiments; (3) computational modeling of stresses in particle coatings.

1.3.1 Chemical Interaction Studies

The goal of the chemical interaction studies is to compare the reactivity of the various candidate materials with various fission products. The fission products analyzed in this study have been limited to the platinum-group metals palladium and rhodium. Palladium has been included as the primary element of interest, due to the observed behavior in TRISO particles, in which Pd is found to accumulate at the inner SiC layer boundary and cause corrosion. Rhodium has been included as a fission product with similar chemistry to palladium, although with a lower yield from fast spectrum fissions (Katcoff 1960), and will be used to compare with the behavior of Pd. Although rhodium has a higher melting point than Pd (1966ºC vs. 1554ºC) and generally has a lower mobility in the particle, it has been found at the inner SiC boundary of irradiated particles in some studies (Minato et. al. 2000, Grübmeier, Naoumidis, and Thiele 1977). The primary method of analyzing the reactivity of the materials was using bulk diffusion couples. The reactivity studies are described in detail in Section 3.

1.3.2 Ion Irradiation

The objective of this study is to investigate the effects of irradiation damage on materials properties such as strength, fracture toughness, and swelling, as well as the microstructural response to irradiation. With the exception of silicon carbide, there is a relatively small amount of data available in the literature for the response of the candidate materials to irradiation at high temperatures. Some neutron irradiation studies are currently in progress (Wachs 2003), but proton irradiations can have several advantages over neutron irradiations, including a much reduced cost, much less sample activation, making post-irradiation characterization much less expensive, and greatly reduced irradiation times.

The first objective of this work was to prepare an irradiation beamline and high temperature irradiation stage at the University of Wisconsin's Tandem Accelerator Facility. The sample stage design must allow irradiation of multiple samples to known ion fluxes, while independently controlling sample temperatures in the range of 800ºC, with proper attention to radiation safety. After beamline and stage construction and testing, samples were to be irradiated and then analyzed using a variety of techniques—including TEM and hardness testing—to determine the materials' response to irradiation.

In the course of the project, beamline and stage construction proved to be more technically involved than initially anticipated, with the most numerous problems having to do with obtaining good thermal control of samples during irradiation via the stage heaters. The system was operational in the summer of 2006, and materials irradiations began in late August 2006. Thus the amount of data on irradiation effects available for this report is very limited. This work will continue at UW in FY 2007 under follow-on funding. Ion-irradiation work is described in detail in Section 4.

1.3.3 Particle Thermomechanical Modeling

The coating layers in particle fuel experience mechanical stresses during burn-up in-pile that arise from a number of different causes, such as thermal expansion during heat-up and cool-down, internal pressure from fission gas formation and release from the kernel, thermal creep, irradiation creep, and swelling of the fuel kernel. These stresses should be managed in such a way that the fracture stress of the coating system is not exceeded, which would result in coating failure and fission product release. This task uses finite element modeling to look at the stresses that develop in coated particles during fabrication and burn-up to identify the optimum kernel-coating combinations and geometries. The particle modeling work is presented in Section 5.

1.4 References for Section 1

DOE, 2002a, *A Technology Roadmap for the Generation IV Nuclear Energy Systems*, GIF-002-00, December 2002.

DOE, 2002b, *Generation IV Roadmap: Description of Candidate Gas-Cooled Reactor Systems Report*; Appendix D, GIF-016-00, December 2002.

DOE, 2005, *Generation IV Nuclear Energy Systems Ten-Year Program Plan, Fiscal Year 2005, Appendix 3.0*: 10-Yr Plan for the Gas-Cooled Fast Reactor, March 2005.

EDF-4380, 2006, *AGR-1 Fuel Product Specification and Characterization Guide; Rev. 7*, ATR Plant Engineering, April 2006.

Ettmayer, Peter and Walter Lengauer in R. Bruce King (Ed.), 1994b "Nitrides: Transition Metal Solid State Chemistry," *Encyclopedia of Inorganic Chemistry*, Vol. 5, John Wiley and Sons.

Ettmayer, Peter and Walter Lengauer in R. Bruce King (Ed.), 1994a "Carbides: Transition Metal Solid State Chemistry," *Encyclopedia of Inorganic Chemistry*, Vol. 2, John Wiley and Sons.

Fielding, R., 2004, *Report on Feasibility Assessment of GFR Fuel Concepts*, ANL-AFCI-135, September 2004.

Grübmeier, H., A. Naoumidis, and B.A. Thiele, 1977, "Silicon Carbide Corrosion in High-Temperature Gas-Cooled Reactor Fuel Particle," *Nuclear Technology*, Vol. 35 pp. 413.

Harris, G. L.(Ed.), 1995, *Properties of Silicon Carbide*, Institution of Engineering and Technology.

INEEL, 2004, *Gas-Cooled Fast Reactor (GFR) FY 04 Annual Report*, INEEL/EXT-04-02361, September 2004.

INL, 2005, *Gas-Cooled Fast Reactor FY05 Annual Report*, INL/EXT-05-00799, September, 2005.

Katcoff, Seymour, 1960, "Fission-Product Yields From Neutron-Induced Fission," *Nucleonics*, Vol. 18, pp. 201-210.

Lowden, R.A., J.C. McLaughlin, and J.R. Kelly, "Nitride Ceramic Coatings for Gas-Cooled Fast Reactor Particle Fuel," *Proceedings of GLOBAL 2003, New Orleans, LA, USA, November 16-20, 2003.*

Martin, David G., 2002, "Considerations Pertaining to the Achievement of High Burn-Ups in HTR Fuel," *Nuclear Engineering and Design,* Vol. 213, pp. 241-258.

Massalsk, Thaddeus B., (Ed), 1990, *Binary Alloy Phase Diagrams, 2nd Ed.,* Vol. 1, ASM International.

Meyer, M.K., R.S. Fielding, and P. Medvedev, *Assessment of Inert Matrices for Use in Gas-Cooled Fast Reactors,* Rev. 0, 2003.

Minato, Kazuo, Kazuhiro Sawa, Toshio Koya, Takeshi Tomita, Akiyoshi Ishikawa, Charles A. Baldwin, William Alexander Gabbard, and Charlie M. Malone, 2000, "Fission Product Release Behavior Of Individual Coated Fuel particles For High-Temperature Gas-Cooled Reactors ," *Nuclear Technology*, Vol. 131, pp. 36-47.

Minato, Kazuo and Toru Ogawa, 2003, "Research and Development of ZrC-Coated Particle Fuel," *Proceedings of GLOBAL 2003, New Orleans, LA, USA, November 16-20, 2003*, pp. 1068-1073.

Petti, D.A., J. Buongiorno, J.T. Maki, R.R. Hobbins, G.K. Miller, 2003, "Key Differences in the Fabrication, Irradiation and High Temperature Accident Testing of US And German TRISO-Coated Particle Fuel, and Their Implications on Fuel Performance," *Nuclear Engineering and Design*, Vol. 222, pp. 281-297.

Reynolds, G.H., J.C. Janvier, J.L. Kaae, and J.P. Morlevat, 1976, "Irradiation Behavior of Experimental Fuel Particles Containing Chemically Vapor Deposited Zirconium Carbide Coatings," *Journal of Nuclear Materials,* Vol. 62, pp. 9-16.

Shackelford, James F., and W. Alexander, 2001, *CRC Materials Science and Engineering Handbook, 3rd Edition*, Boca Raton: CRC Press LLC.

Storms, Edmund K., 1967, *The Refractor Carbides*, New York: Academic Press.

Toth, Louis E., 1971. *Transition Metal Carbides and Nitrides*, New York: Academic Press.

Wachs, D. M., 2003, Irradiation of Fuel Materials for Gas-Cooled Fast Reactor Development the Advanced Test Reactor: Final Experiment Description and Design & Data Package for GFR-1, ANL-W Document Control No. W7520-0594-ES-00, 2003.

2. MATERIALS CHARACTERIZATION

The ceramic materials used in this work were acquired from Cercom[a] and were prepared by hot-pressing and machining into rods. Samples for chemical interaction studies were 20mm long x 4.5mm diameter (Figure 2.1). Samples for ion irradiation experiments were 20mm long x 3mm diameter. It has been shown in a parallel investigation at the INL (INL 2005) that the SiC acquired here is hexagonal 6H-SiC (α-SiC). The as-received ceramics were analyzed with a variety of techniques, including scanning electron microscopy (SEM) and transmission electron microscope (TEM) to characterize the microstructures, x-ray diffraction (XRD) to determine the crystalline phases and lattice parameters, chemical analysis to determine the composition of the compounds, and micro-hardness testing to determine fracture toughness.

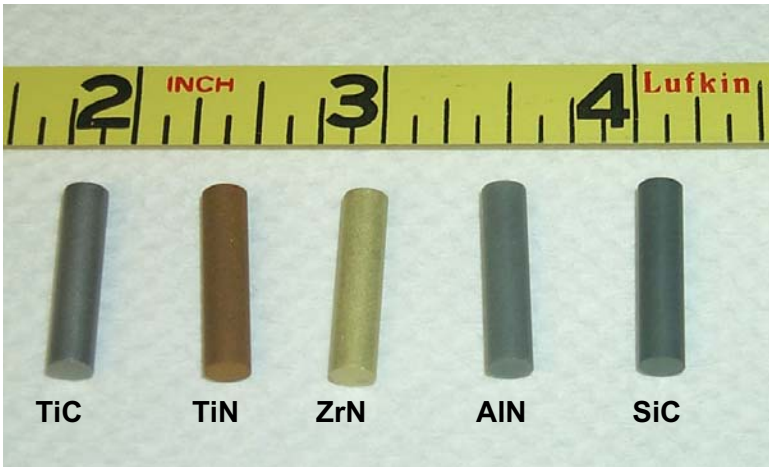

Figure 2.1. Ceramic rods (20mm long x 4.5 mm diameter) used for chemical interaction experiments. Note: ZrC not shown.

2.1 Chemical Analysis

Chemical analysis of the ceramic rods was performed by NSL Analytical[b] to determine metallic element, and carbon, nitrogen, and oxygen content. The results are given in Table 2.1. The stoichiometric ratio, (C or N)/M, where M is the primary metallic constituent, was determined and is shown in Table 2.1.

[a] Cercom, Inc., Vista, CA (www.cercomceramics.com)

[b] NSL Analytical Services, Inc. Cleveland, OHIO (www.nslanalytical.com)

Table 2.1. Chemical composition of ceramic sample materials (all values are in weight percent).

	TiC	TiN	ZrC	ZrN	AlN	SiC
Ti	79.2	78.9	0.19	0.095	<0.001	0.025
Zr	0.027	0.011	84.8	87.6	<0.005	<0.005
Al	0.009	0.022	<0.01	0.09	67.1	1.44
Si	<0.005	0.001	<0.001	0.007	<0.001	62.08
Hf	0.002	<0.005	1.91	0.015	<0.005	<0.005
Fe	0.014	<0.001	<0.01	0.069	0.004	0.65
W	0.29	<0.05	<0.1	0.19	<0.005	<0.05
C	19.4	0.58	NA	0.76	0.059	29.6
N	0.057	14.0	NA	10.8	33.7	0.35
O	0.51	0.46	NA	1.27	0.86	0.58
Other (>0.01%)	Cu: 0.042 Nb: 0.01 Ta: 0.01 Mg: 0.01 Co: 0.019			Ca: 0.011 Cr: 0.034 Mo: 0.021 Sn: 0.011 V: 0.02	Y: 0.3	B: 0.029 Ni: 0.023 Sc: 0.06 V: 0.03
Ratio[a]	0.98	0.61[b]	1.2[c]	0.803	0.967	1.12[d]

a. Ratio of C or N to metal (e.g. C/Ti).
b. Total mass of analytes for TiN was only 94.0%.
c. Ratio for ZrC is based on the wt.% data for metallic elements and assumes all of the remaining composition is carbon (no C,N,O analysis performed).
d. Total mass of analytes for SiC was only 94.9%

2.2 Density

The densities of the ceramic rods were determined by dimension/mass measurements and by immersion. Densities determined by the two methods as well as theoretical densities are given in Table 2.2. The densities of the sample materials were generally very close to theoretical values (>96% TD in all cases).

Table 2.2. Densities of ceramic sample materials.

	Geometric (g/cm^3)	Immersion (g/cm^3)	TD[a]	%TD[b]
TiC	4.91	4.84	4.93	98.2
TiN	5.24	—	5.39	97.2
ZrC	6.55	6.58	6.46	101.9[c]
ZrN	7.03	7.06	7.32	96.4
AlN	3.30	—	3.30	100
SiC	3.21	3.19	3.217	99.2

a. Theoretical density
b. Percent of theoretical density based on immersion density measurements if available; otherwise based on geometric density measurements.
c. Note that the %TD of ZrC may be in excess of 100% due to (a) a range of reported literature values for TD depending on stoichiometry and (b) the presence of almost 2wt% Hf, which substitutes for Zr in the crystal structure and could increase the true FW of the compound.

2.3 Microstructural Analysis

2.3.1 SEM

Samples were mounted in epoxy and polished to a 1 micron finish, and the microstructures were analyzed using SEM. Representative micrographs of the as-received, polished surfaces of the ceramic rods are shown in Figures 2.2–2.7.

The grain sizes of the ceramics were calculated from photomicrographs using the standard method for determining average grain size by the linear intercept procedure (ASTM E112 2004). In most cases, backscattered electron imaging was useful to highlight individual grains. High temperature thermal etching of ceramic surfaces in a vacuum resulted in a slight increase in contrast between individual grains when viewed in backscattered electron mode. Mild oxidation of the TiC surface (400ºC in air for several minutes) was found to enhance the visibility of the grains (Figure 2.2), but this procedure did not produce similar results for any of the other materials. The results of the grain size analysis (average volumetric grain size, per ASTM E112) are given in Table 2.3. Individual grains were not resolved in TiN micrographs and therefore average grain sizes have not been calculated. It can be seen from the micrograph (Figure 2.3), however, that grain sizes typically were between approximately 5–10 μm.

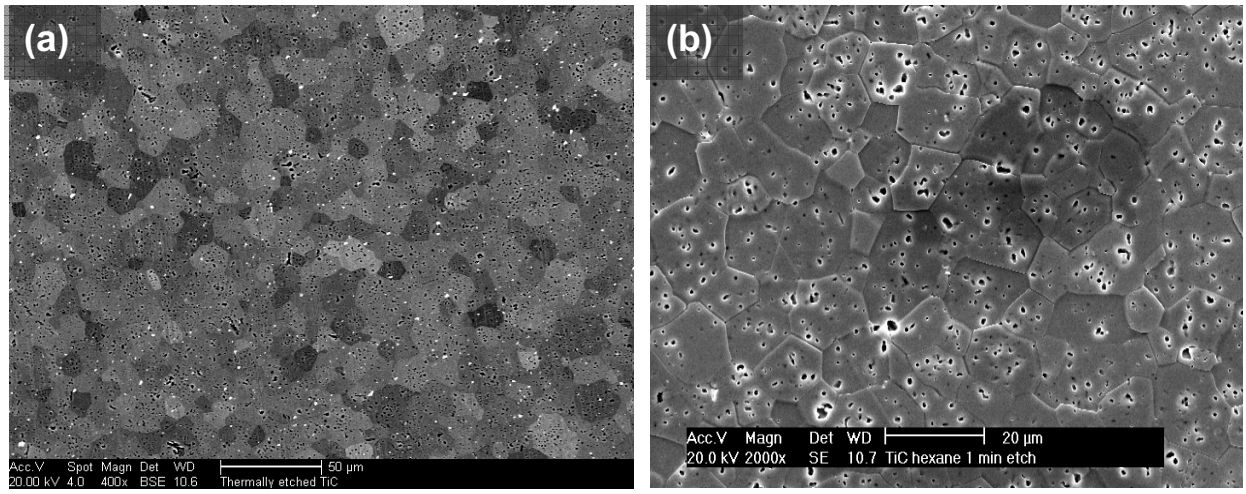

Figure 2.2. (a) Backscattered electron micrograph of polished TiC surface thermally etched at 1400ºC in a vacuum (10^{-5} Torr) for 120 minutes. (b) Secondary electron micrograph of TiC surface thermally etched in air at ~400ºC for approximately 5 minutes.

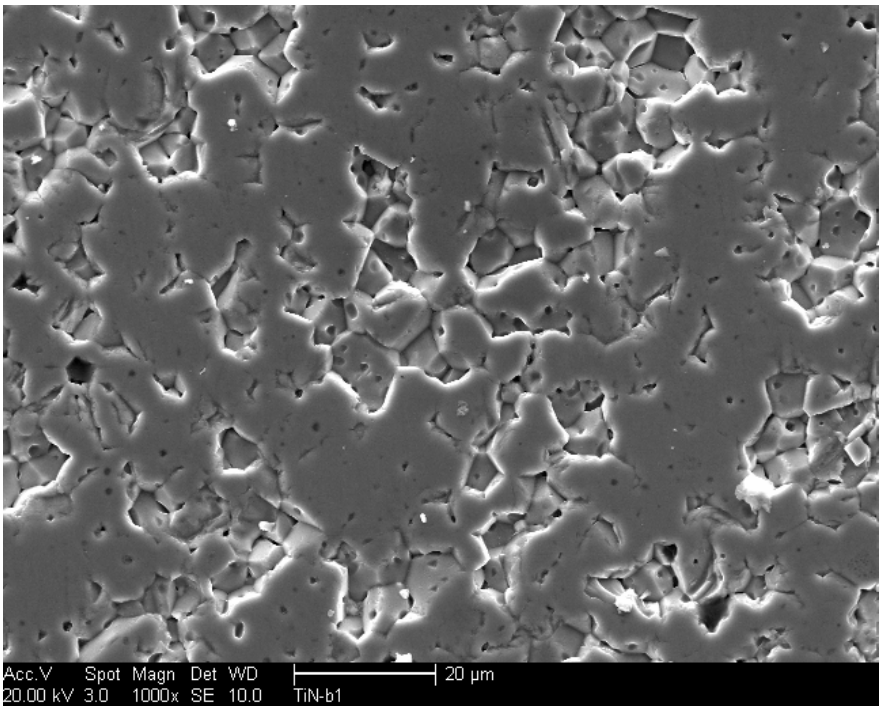

Figure 2.3. Electron micrograph of polished TiN surface. Note: Porosity is due primarily to grain pull-out during polishing.

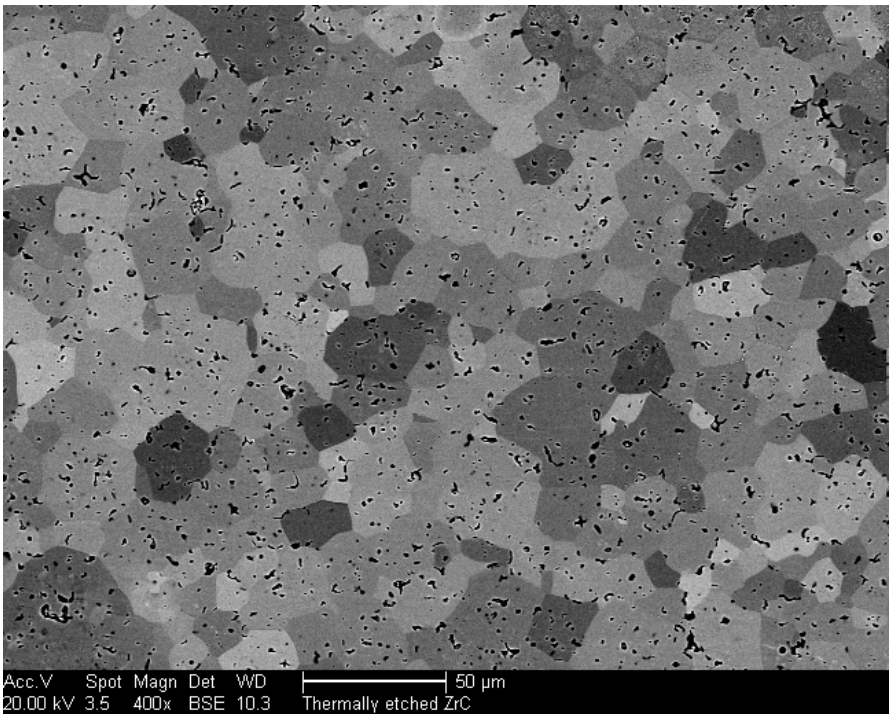

Figure 2.4. Backscattered electron micrograph of polished ZrC surface after thermal etching at 1400ºC in a vacuum (10^{-5} Torr) for 120 minutes.

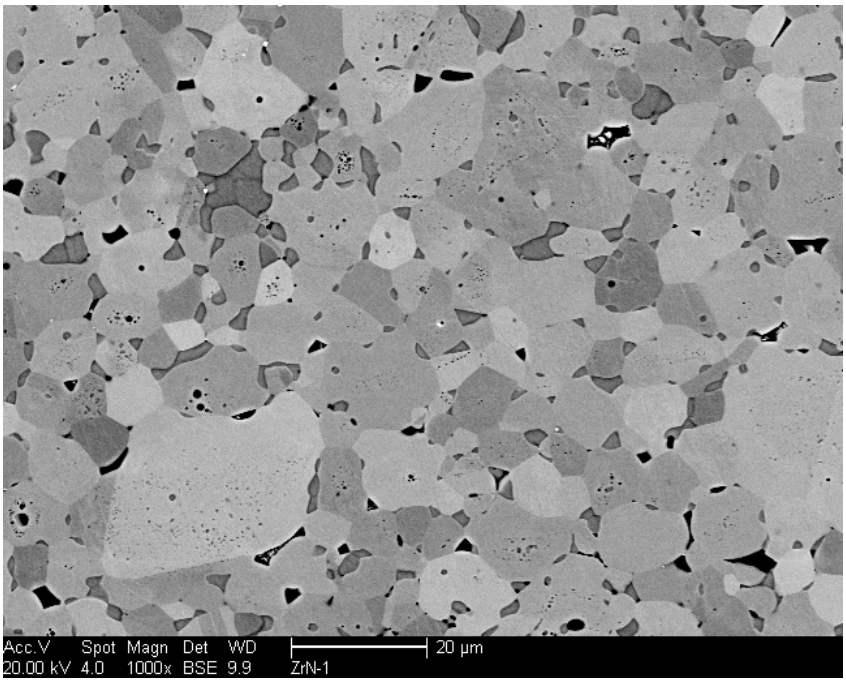

Figure 2.5. Backscattered electron micrograph of polished ZrN surface.

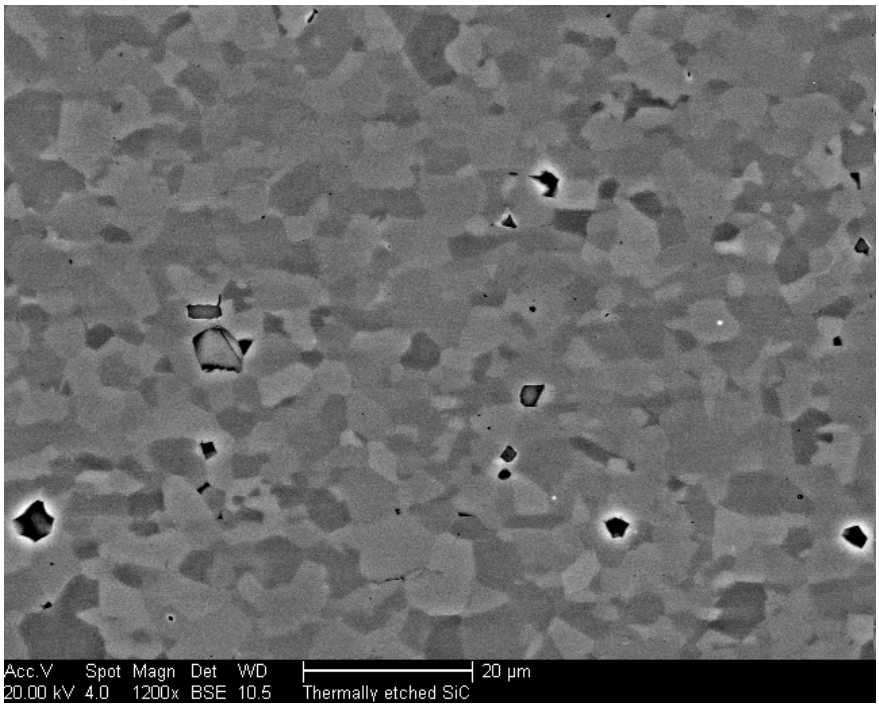

Figure 2.6. Backscattered electron micrograph of polished AlN surface after thermal etching at 1400ºC in a vacuum (10^{-5} Torr) for 120 minutes.

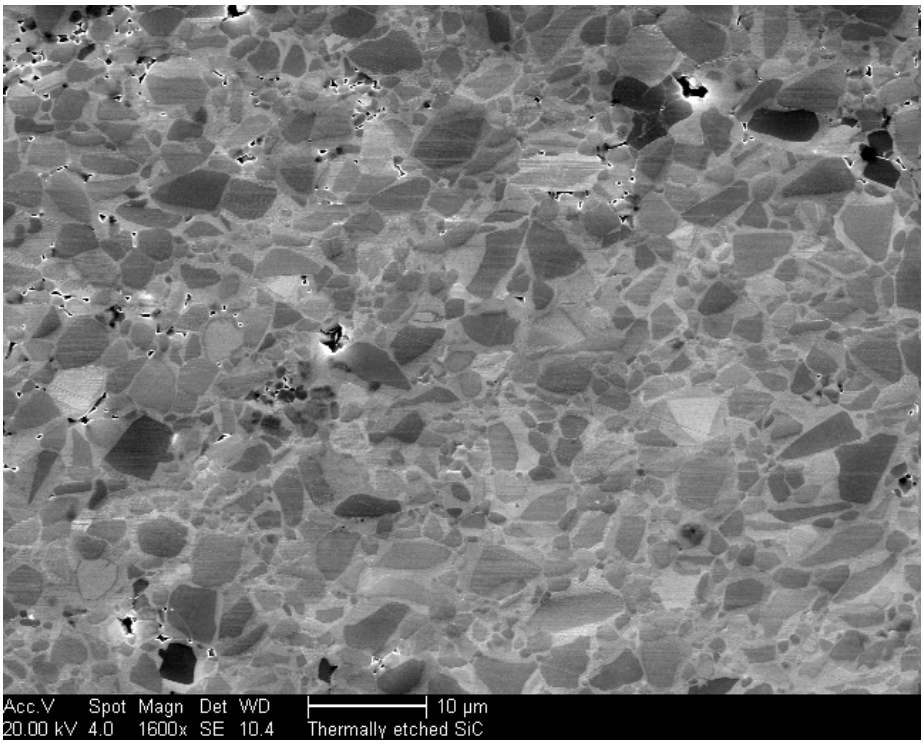

Figure 2.7. Backscattered electron micrograph of polished SiC surface after thermal etching at 1400ºC in a vacuum (~10^{-5} Torr) at for 120 minutes.

Table 2.3. Average grain size of starting ceramics.

Sample	Grain size (µm)
TiC	12.4 (±1.2)[a]
TiN	~5-10
ZrC	24.1 (±1.8)
ZrN	13.3 (±1.4)
AlN	5.5 (±0.3)
SiC	—

a. Error values are 95% confidence intervals.

b. Grain size based on sample thermally etched in air.

2.3.2 TEM

Transmission electron microscopy (TEM) is a direct tool to observe the microstructural evolution of the irradiated materials; a combination of techniques, such bright field (BF), dark field, diffraction and energy dispersive x-ray spectroscopy (EDS) can provide thorough characterization of the material microstructures. TEM was used in this work to characterize the as-received samples prior to irradiation for comparison with irradiated microstructures. The plane-view TEM samples were prepared as wedge specimens; the samples were first manually polished to 1-3° wedges and finally thinned to electron transparent by ion-mill. The TEM was performed on Philips CM200 and JEOL 200CX instruments.

Figure 2.8 shows the plane view of the TiN samples, image (a) is a BF image at zone axis, and it can be found that large thin areas were achieved with wedge polishing method, image (b) is a BF image at 2-beam condition, which shows the edge-on dislocation lines and some loops clearly, the dislocation density varies from grain to grain but they are all very low, image (c) is the diffraction pattern (DP) at zone axis 001, the lattice constant evaluation from the DP is consistent with the XRD result, and image (d) shows the convergent beam diffraction (CBD) of two beam condition, where the Kossel-Mollenstedt fringes can be clearly counted. Based on the CBD (d), the thickness of transparent area was estimated as ~84nm.

The TEM sample of the as-received TiN sample was also prepared as a wedge sample. Compared with ZrN, TiN is much more brittle, which causes difficulty in polishing. To avoid sample cracking at the wedge edge, the wedge was controlled to slightly larger than 3, and the ion-mill time was also increased accordingly. Figure 2.9 shows the BF plane view image (a) and the BF image (b) at 2-beam condition. Many pores were observed at the triple grain boundary, and no clear precipitates were observed. One clear feature of this material is that it is free from defects; no dislocations were found.

A TEM sample of TiC was also prepared and examined. Figure 2.10 shows the BF images of sample at different magnification, the grain boundaries were clearly revealed, and the material is also free from defects, though some spherical voids were generated by ion-mill. Therefore, for the preparation of the irradiated sample, the ion-mill parameters will be adjusted to avoid the ion damage by decreasing the ion mill voltage and current. The EDS in TEM was also performed to verify the elements. Some Cu impurities was detected, as shown in Figure 2.11.

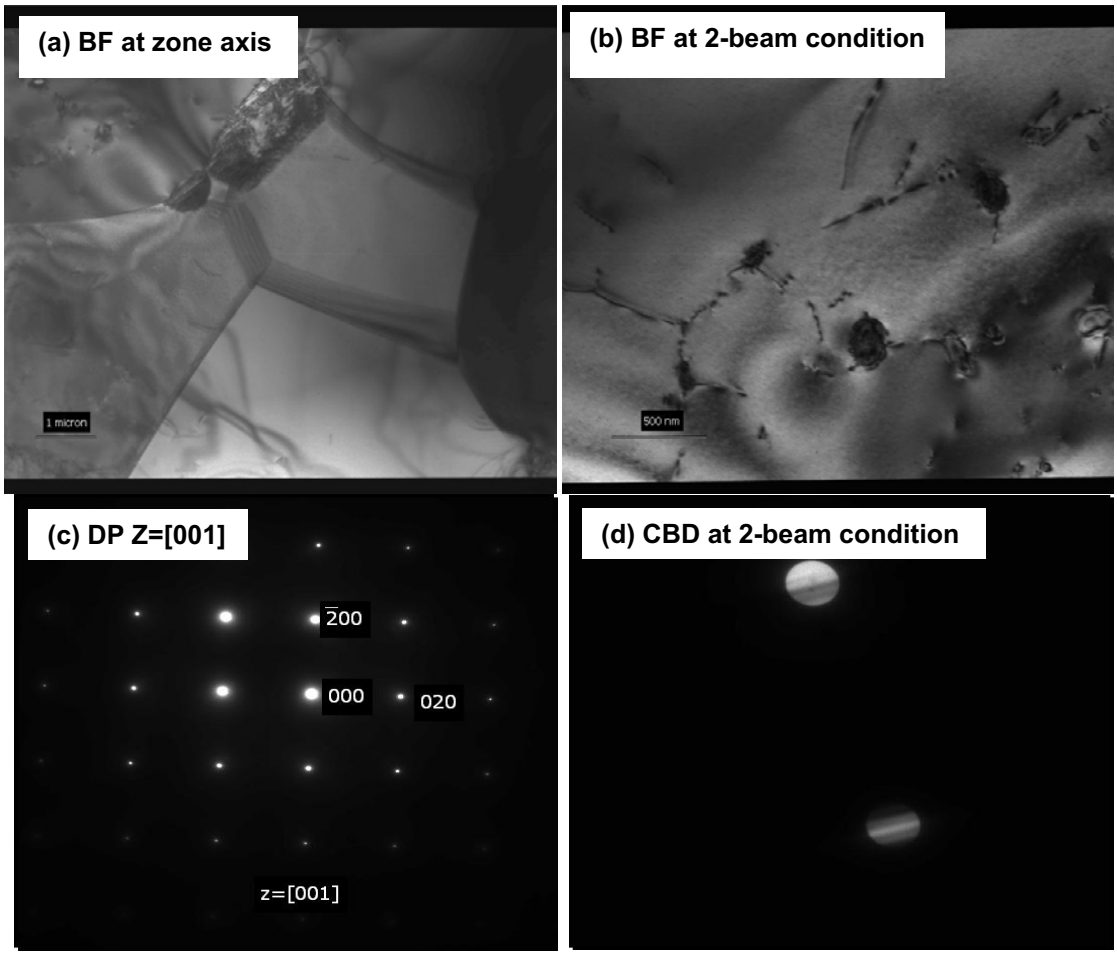

Figure 2.8. TEM images and diffraction of as-received ZrN.

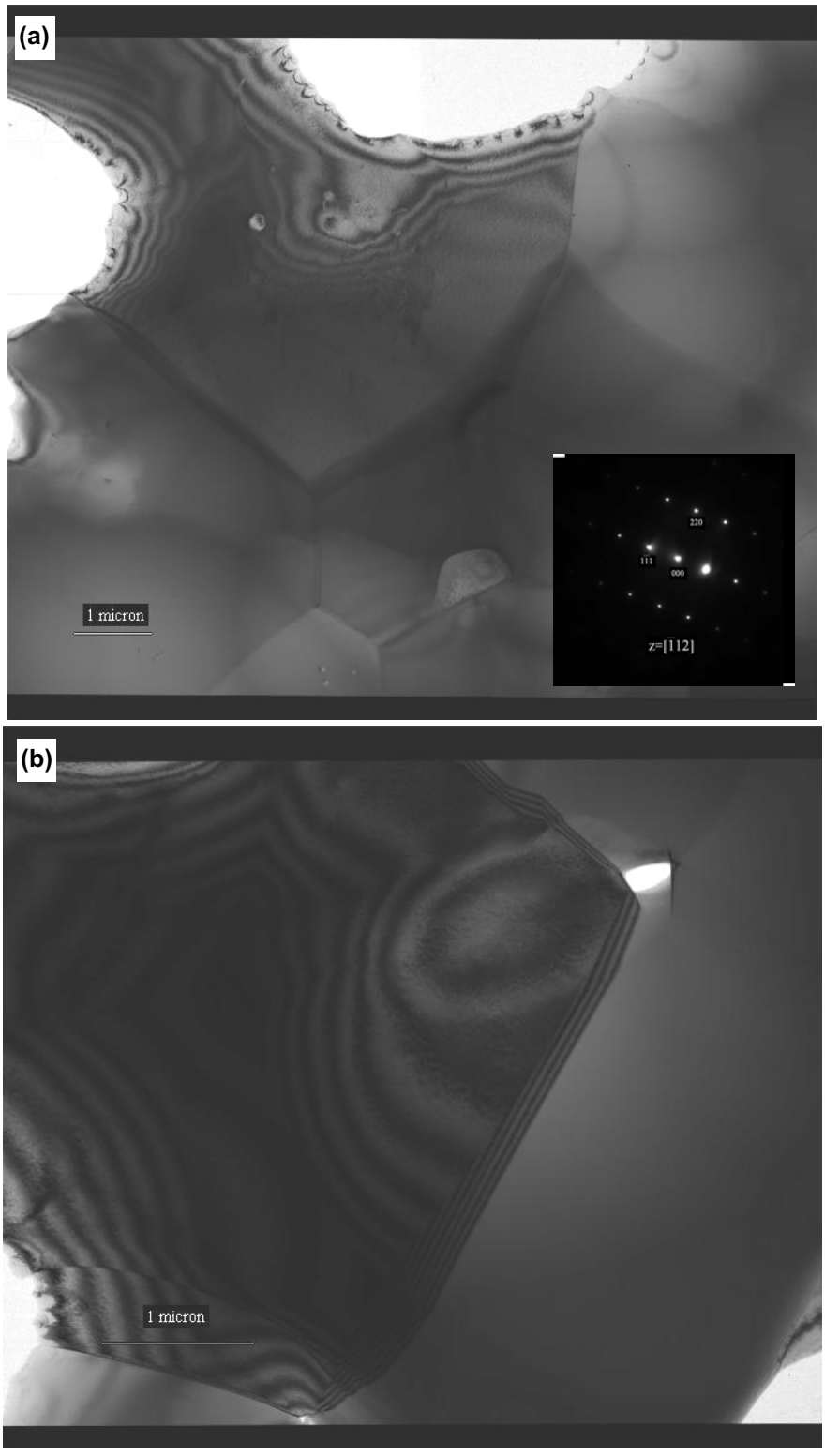

Figure 2.9. BF images of TiN.

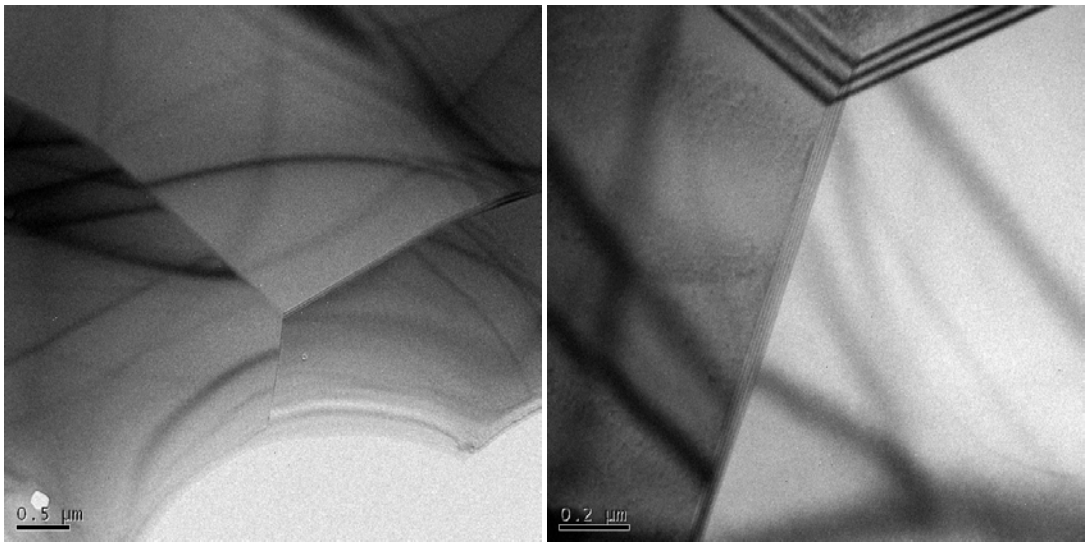

Figure 2.10. BF images of the TiC at different magnifications.

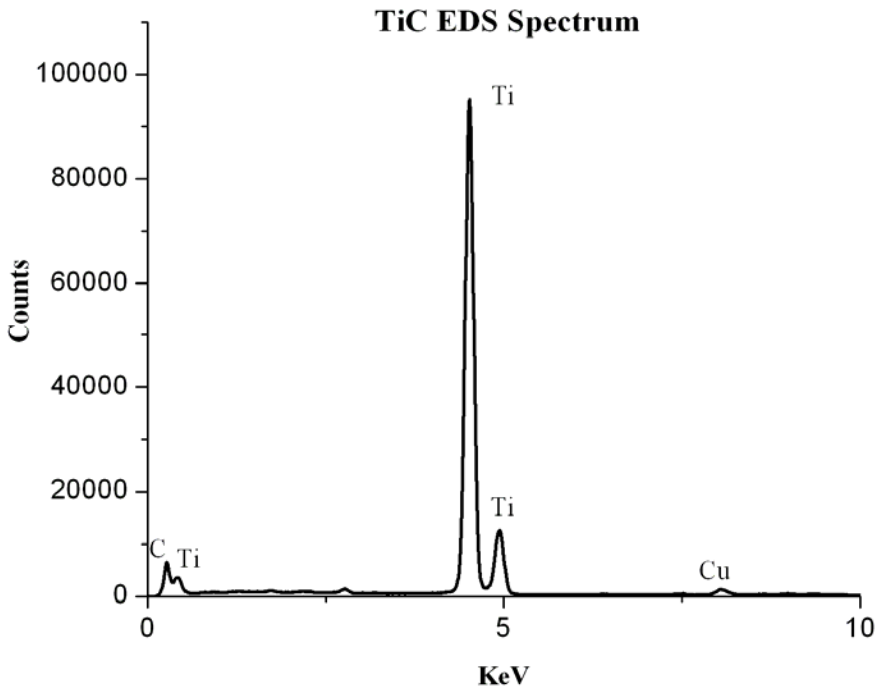

Figure 2.11. EDS spectrum of TiC acquired with TEM.

To profile the proton damage along the irradiation depth in the materials, cross-section TEM samples will be prepared. Currently, two different methods are proposed, one is wedge polishing; another is the focused ion beam (FIB) method. For wedge polishing, the irradiated sample will be cut in two halves and glued together with irradiated surface-to-surface for self-protection purpose, and the standard wedge sample preparation procedure will be followed. For the FIB method, some trials to prepare the cross-section specimen have already been attempted. The FIB lift-out method has some advantages: multiple samples can be prepared from one irradiated disk; precisely controlling position can be achieved. Figure 2.12 shows that two thin TEM samples were milled out from the ZrN disk and ready to be lifted out for final thinning.

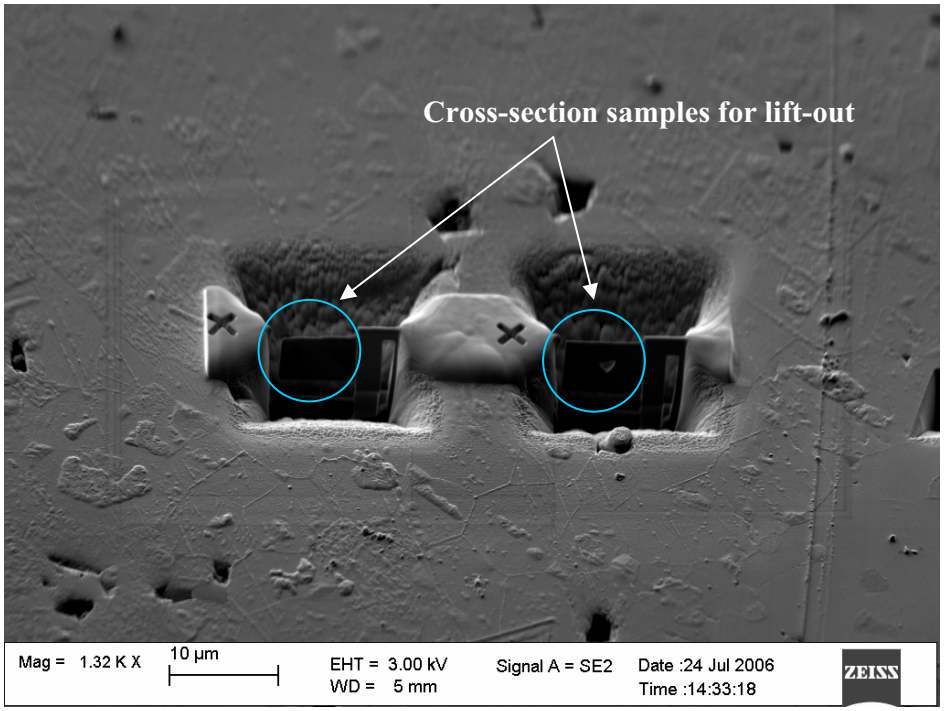

Figure 2.12. Cross-section TEM sample prepared with FIB lift-out method.

Some issues for preparing the irradiated TEM samples are envisioned. The samples damage profile has a depth of ~35 µm according to the stopping and the range of ions in matter (SRIM) calculation and the interesting range for this study is roughly the first 20 µm but the samples oxidize as well. Therefore, the TEM samples should be made between the first 10-20 µm, which requires that a layer of material will need to be removed carefully and precisely. Some trials were performed to precisely remove the 10 µm layer from the surface using tripod 3 µm diamond lapping film, though it is very challenging.

2.4 X-Ray Diffraction

X-ray diffraction (XRD) has also been used to study the microstructure of samples for comparison before irradiation and after irradiation. From the XRD patterns, phases can be identified and the lattice parameters of the material can be calculated according to Bragg's equation. Two different types of XRD, powder diffraction and grazing incident x-ray diffractometry (GIXRD) are being used for this study. For the GIXRD, the very low angles, or grazing incidence angles, produce x-ray reflections from very shallow depths. This very shallow depth of reflection can be changed by changing the incidence angle. GIXRD is used predominantly in thin-film characterization, but can also detect crystallographic changes from ion-modified surface layers of ceramics.

The ceramic samples with fine surface finish were loaded on the STOE x-ray diffractometer. The samples that were analyzed with XRD were the TiC, TiN, and ZrN Cercom samples, and an 85% TD ZrN and a HIP ZrN sample, both obtained from LANL. The SiC and ZrC samples were analyzed and the results were not as expected and more work will be needed. For the Cercom samples, additional runs were completed to verify the results from the STOE. Diffraction angle (2-theta) values of 30–75º were of primary interest, and allow the low valued Miller indices peaks to be identified. The step size was set as 0.040º 2-theta. Figure 2.13 shows an example of an XRD pattern from a ZrN sample obtained by Cercom.

The peaks in the diffraction spectrum can be identified with the STOE data acquisition program, WinXPow, and a peak file showing the peak 2theta value, its intensity, FWHM, and interplanar spacing can be obtained. Based on the expected Miller indices at their respective interplanar spacing value, the lattice parameter for the material can be calculated and averaged over all the peaks. These lattice parameters were compared to literature values and values obtained from TEM analyses at both UW and INL, and are summarized in Table 2.4. It should be noted that the results for the SiC and the ZrC are not included, due to unsatisfactory diffraction patterns. Further work is needed to complete the characterization of these materials.

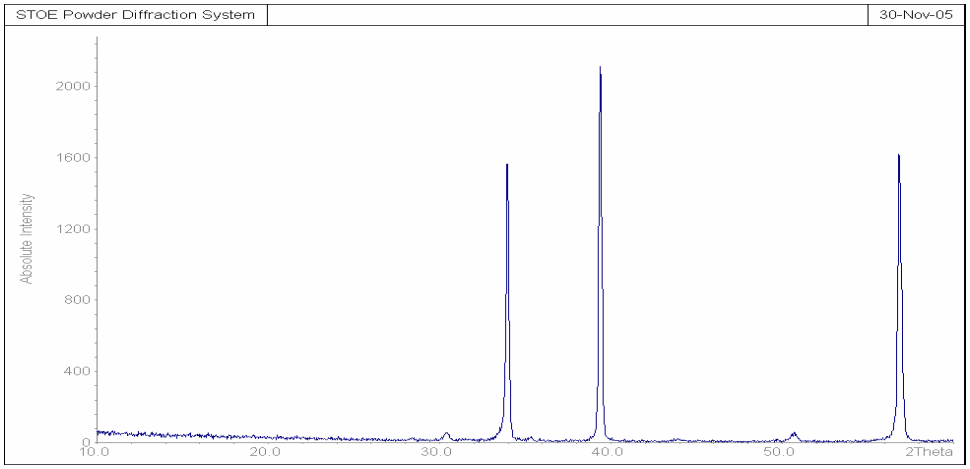

Figure 2.13. X-ray pattern of ZrN from Cercom.

Table 2.4. Lattice parameters of as-received ceramics, determined from XRD and TEM.

Material	Lit. (Å)	TEM (Å)	Diff. from Lit %	XRD (Å)	Diff. from Lit %	INL Values (Å)	Diff. from Lit %
TiC	4.3233	4.336	0.2	4.3	0.03	4.3	0.15
TiN	4.249	4.289	0.9	4.2	0.4	4.2	0.21
ZrN	4.574	4.636	1.3	4.6	0.16	4.6	0.04
ZrN 85%	4.574	TBD	TBD	4.6	0.01	N/A	N/A
HIP ZrN	4.574	TBD	TBD	4.6	0.12	N/A	N/A

The XRD results of as-received materials are very close to the literature values and the minor difference of the peaks will be expected for the irradiated samples. In a typical irradiation, the peaks will broaden or shrink due to presence of the interstitials and vacancies defects. It was observed in the ZrN that the main pattern peaks will split into two or three mini peaks as the samples was irradiated to certain dpa (Egeland 2005). Theoretically, during the irradiation the ZrN lattice can form three different structures with very closely related lattice parameters.

GIXRD will be used for very small incident angles diffraction analysis with very shallow penetration depth, and this technique is useful in determining oxide layers. The GIXRD and powder diffraction results of pre-irradiated samples will be compared with the irradiated samples in the future under separate funding.

2.5 Mechanical Properties

The fracture toughness of the carbides and nitrides is an important property with regard to their use as fuel particle coatings. The hardness of the as-received ceramics was analyzed at UW for comparison with the properties of the ion-irradiated materials. The fracture toughness of the materials was derived from the hardness testing results.

2.5.1 Micro-Hardness

The samples for micro hardness tests were 3 mm diameter discs with approximately 500 μm thickness, as shown in Figure 2.14. The as-received samples were polished to 1 micron finish before micro hardness indention, in accordance with ASTM standards (ASTM E 384-99, ASTM 1327-03, ASTM C 1326-03). The first set of samples were initially polished using a parchment polishing cloth and suspended diamond paste. Better polishing materials were later obtained, and subsequent sample sets were polished to a 1μm finish using a nylon cloth and suspended diamond paste before hardness testing. The Vickers micro-hardness test was conducted using a diamond indenter and applying a controlled force for a controlled amount of time, usually 10 to 15 seconds.

Results of Vickers hardness testing performed on the as-received samples of TiC, ZrC, ZrN, and SiC are shown in Figure 2.15. A set of tests was performed for each of the two sample preparation methods: a parchment polishing cloth and a nylon polishing cloth. The measured hardness values of samples prepared with the parchment cloth were consistently less than the measured hardness values of samples prepared with the nylon polishing cloth. This is a consistent trend across the samples, indicating that the preparation method can affect the measured hardness value.

The measured hardness values were compared to values obtained from the literature. To ensure literature values were comparable to those obtained from the samples used in this study, only hardness values for sintered ceramics obtained using Vickers hardness testing were used in the comparison. The literature hardness values are all larger than the first test (parchment polishing cloth) and smaller than the second test (nylon polishing cloth). This difference may be due to various sample characteristics not accounted for in the literature values, including porosity, grain size, and sample preparation methods. The specific sample preparation is not adequately described in the literature beyond adherence to ASTM standards, so a discussion of techniques used on tested samples is not possible.

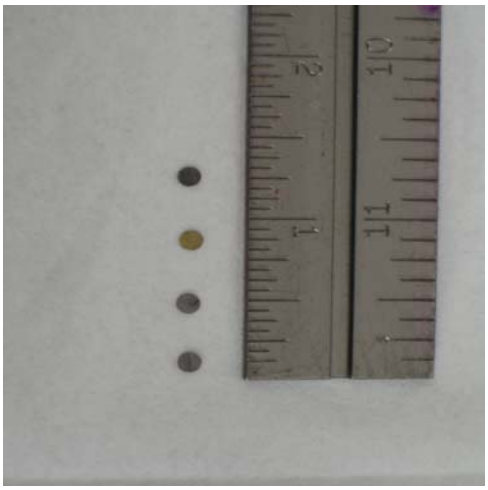

Figure 2.14. Sample disks for micro-hardness tests.

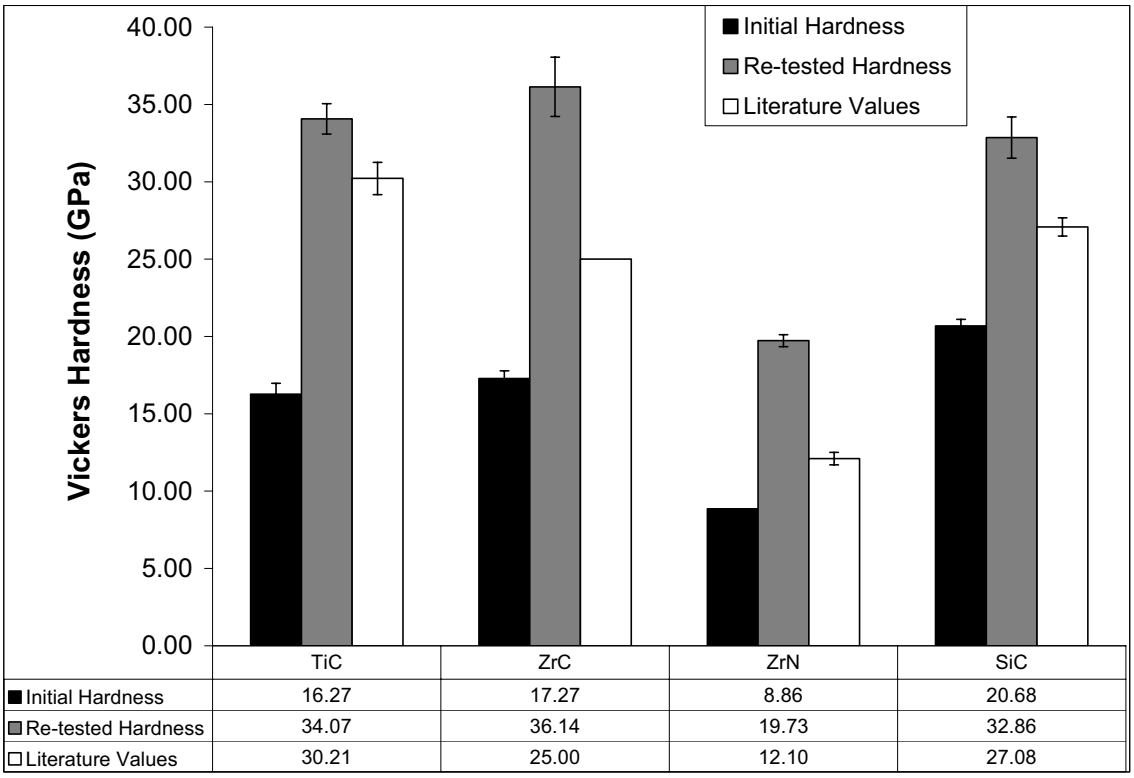

	TiC	ZrC	ZrN	SiC
Initial Hardness	16.27	17.27	8.86	20.68
Re-tested Hardness	34.07	36.14	19.73	32.86
Literature Values	30.21	25.00	12.10	27.08

Figure 2.15. Vickers hardness results compared to average literature values and associated standard error.

2.5.2 Fracture Toughness

Fracture toughness of the material can be estimated by measuring the length of cracks produced by hardness indents. Toughness is a measure of the maximum energy a material can absorb before fracture takes place (Bhat et al. 2005). Fracture toughness is represented by the term K_{IC} and is defined as the critical value of the stress intensity factor at a crack tip necessary to produce catastrophic failure under simple uniaxial loading (Shackelford 2005). The "I" stands for mode one (uniaxial) and the "C" stands for critical. A simple version of the fracture toughness formula is

$$K_{IC} = Y\sigma_f\sqrt{\pi b} \qquad \text{(Eq. 2.1)}$$

where Y is a dimensionless geometry factor, σ_f is the applied stress at failure, and b is the length of a crack in the material. The unit of K_{IC} is $MPa\sqrt{m}$. For small, thin specimens, however, the thickness of the sample plays a much larger role than in large-scale testing, and K_{IC} cannot be accurately determined from conventional tests. Therefore, a methodology has been developed to calculate fracture toughness based on propagation of cracks produced during micro-indentation.

For this measurement, Vickers micro-indentation is specifically considered because it uses a sharp indenter that produces well-defined cracks, and previous work has noted that the fracture toughness values obtained with a Vickers indenter are independent of indenter load (Gong, Wang, and Guan 2002]. Cracks produced via Vickers indention were first recognized as a potential fracture toughness evaluation technique by Palmqvist (1962). Since then, many have improved the initial work relating crack growth from Vickers indentation in brittle materials to fracture toughness. These cracks have been divided into two systems, classic median/radial "half-penny" cracks and "Palmqvist" cracks. The two systems are shown in Figure 2.16 and 2.17.

The primary difference between half-penny and Palmqvist crack systems exists in the sub-surface cracking of the material. In the half-penny system, cracks emanate from the indentation tips laterally and radially. Lateral cracks travel along the surface. Radial cracks protrude from the indention in a starburst within a radius below the surface of the material. In the Palmqvist crack system, cracks only travel laterally. Notice the variables *c*, *l*, and *a* in Figure 2.16 and Figure 2.17. The variable *a* indicates half the length of the diagonal of the indent. The variable *l* indicates the length of a crack from the tip of the indent to its termination in the material. The variable *c* is the sum of *a* and *l*.

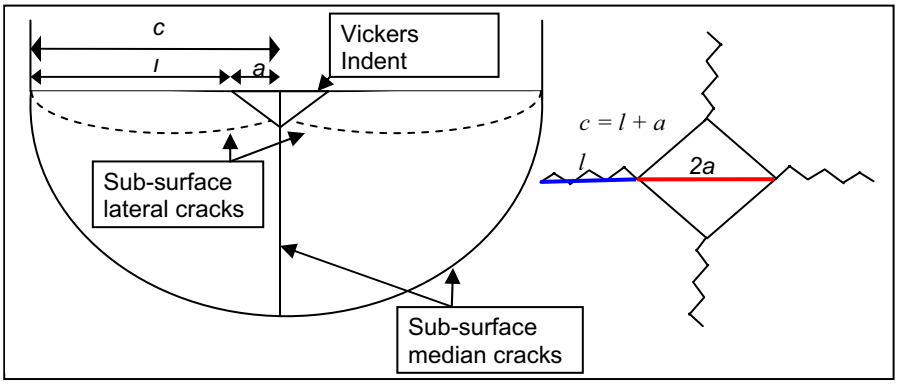

Figure 2.16. Half-penny cracking system.

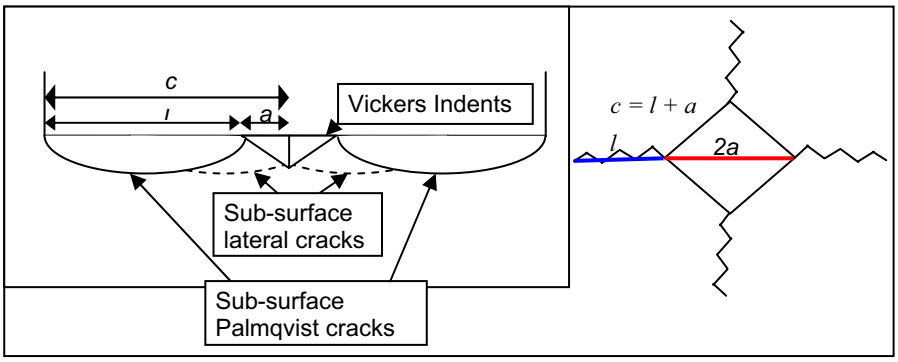

Figure 2.17. Palmqvist cracking system.

Average crack length was determined for each of the as-received samples. An example of an SEM image of a hardness indent and corresponding cracks is demonstrated in Figure 2.18. The cracks follow a zigzag path instead of straight lines. There are two possible methods that can be used to measure the length of the crack. The first is to measure the "crow's flight" distance. The crow's flight distance is the length of the crack from the origin at the tip of the indentation to the termination of the crack without regard to the shape of the crack. The second method is to measure each individual segment of the crack and then add the segments to obtain a length of the total path traveled by the crack.

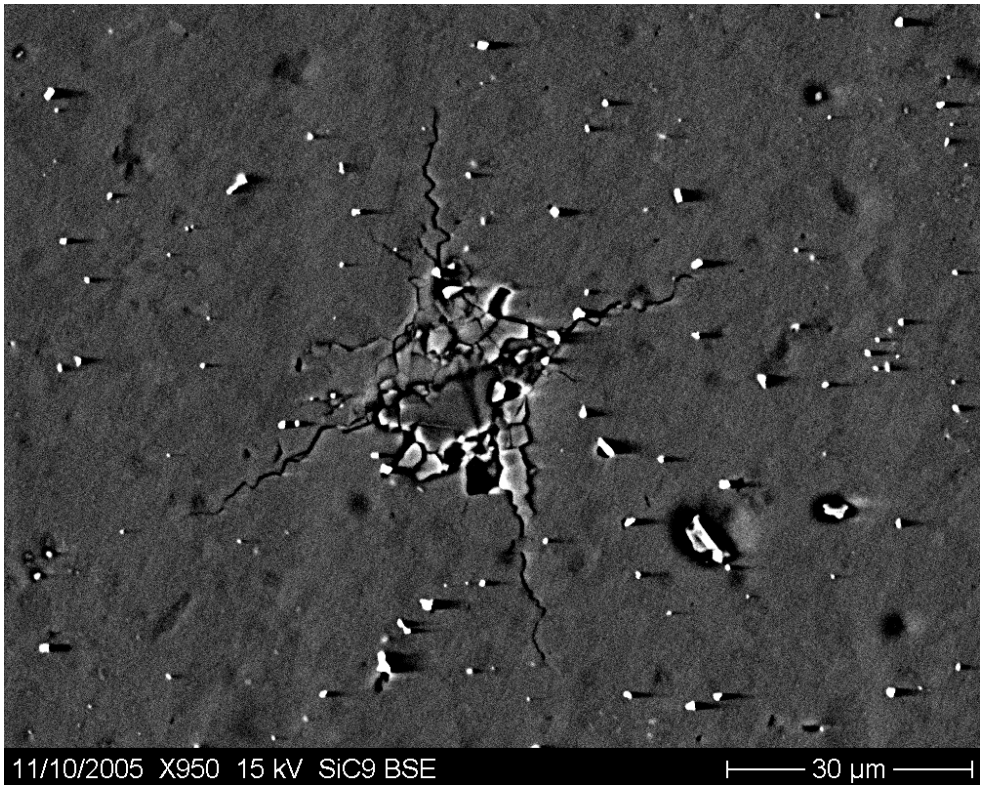

Figure 2.18. Indent of SiC sample.

For most cracks in this study, the added-segment method was used. However, a comparison was made between the added-segment method and the crow's flight method. The results of that comparison are shown in Figure 2.19. The results indicate that the measurement method has little effect on the calculated crack length.

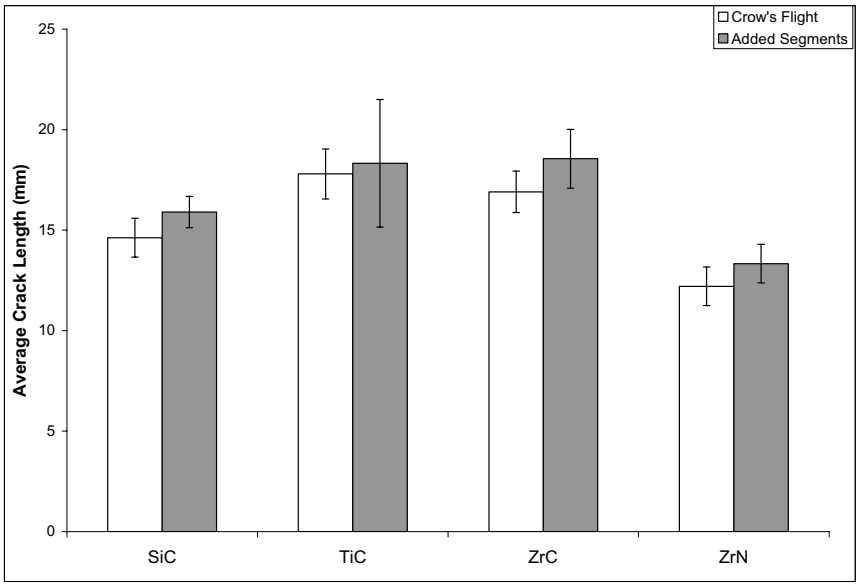

Figure 2.19. Comparisons of crack measurement methods for as-received samples.

The cracks for five acceptable indentations were measured for each sample with the added-segment method and the average was taken to determine an average crack length, and the lengths of the indent diagonals were measured as well. The average crack length values are summarized in Figure 2.20. All the samples were imaged at least 1 day after indention to eliminate the effects of residual stresses in the material which can result in continuous crack growth over time.

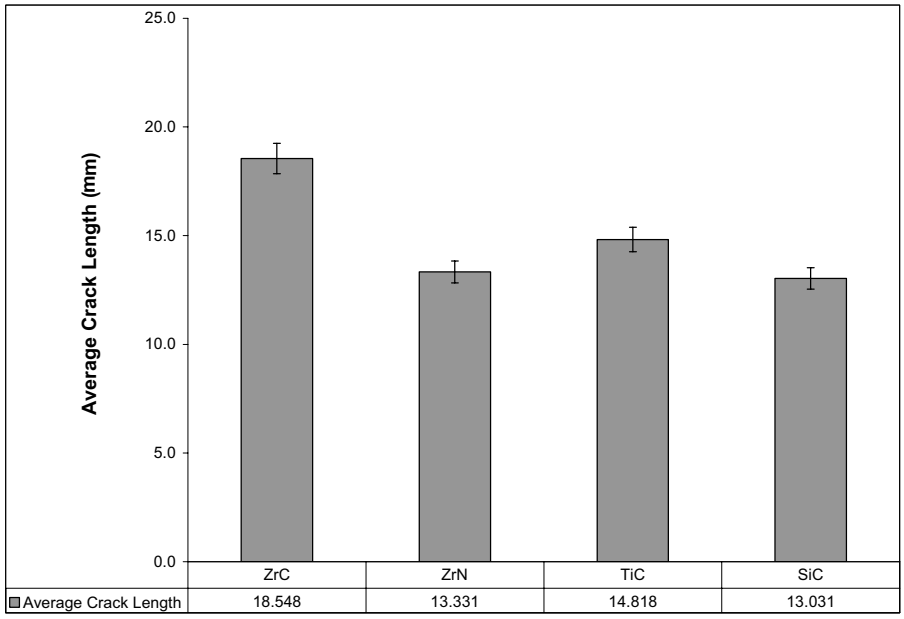

Figure 2.20. Average crack lengths of indentations on as-received samples and associated standard error.

It was observed that cracks preferentially followed the grain boundary and this behavior can have an effect on crack lengths and fracture toughness calculations. In the future, the electron back-scatter patterns (EBSP) should be used to correlate the crack lengths with the associated grain boundary characters.

Crack systems observed for as-received samples of TiC, SiC, and ZrC were half-penny cracks, and for as-received ZrN were Palmqvist cracks. This was determined by an analysis of the *c/a* values for the samples. Based on the criterion established in this study, a *c/a* value greater than or equal to 2 indicates a half-penny crack system, otherwise the crack system in Palmqvist. The results of the *c/a* analysis are listed in Table 2.5 for both the as-received and heat treated samples. It can be found that all the *c/a* values were greater than 2 except for the as-received ZrN. To be consistent in analysis across sample materials, the criterion was relaxed to treat ZrN as a half-penny crack system. Even though this study used 2 as the threshold value between Palmqvist and half-penny cracking, the value is somewhat arbitrary because it is merely based on experimental observation. This threshold value also changes for various materials. Additionally, some literature also shows that for the same material Palmqvist cracking occurs at lower loads while half-penny cracking occurs at higher loads. It was suggested that the range of this transition is 90 to 100 gf. These experiments were all conducted at a load of 1 kgf (1000gf). Therefore, the loads attained during these studies reached ten times the loads suggested for a transition from Palmqvist to half-penny cracking. It is recognized, however, that a detailed crack analysis, utilizing techniques such as accurate polishing, would be required to justify this approach.

Table 2.5. c/a analysis of as-received and heat treated samples.

Material	As-Received	800C HV	1200C HV	1600C HV
TiC	2.30±0.12	2.86±0.34	3.15±0.39	3.15±0.32
SiC	2.15±0.29	2.33±0.84	2.18±0.98	—
ZrC	2.59±0.12	2.13±0.26	3.08±0.24	2.99±0.25
ZrN	1.87±0.11	2.51±0.33	2.46±0.28	2.20±.15

Although a high vacuum (~10^{-5} Torr) was used for heat treatment, some oxidation of the sample surface occurred. This layer was removed from all of the samples before hardness testing and crack length measurement by mechanical polishing. After determining *a, l, c* and the crack system, the relative fracture toughness was calculated according to Eq. 2.2,

$$\frac{K_{IC}}{K_{ICo}} = \frac{c_o^{\frac{3}{2}}}{c^{\frac{3}{2}}} = \frac{\left(a_o + l_a\right)^{\frac{3}{2}}}{\left(a+l\right)^{\frac{3}{2}}}, \qquad \text{(Eq. 2.2)}$$

where the subscript "*o*" denotes the as-received samples. The relative fracture toughness was plotted with respect to hardness for as-received and high vacuum heat treated samples, shown in Figures 2.21–2.24

Figure 2.21 shows that heat treatment of TiC at 800ºC causes substantial softening of the sample, while no significant changes occur at 1200ºC, with slight softening at 1600ºC. The crack lengths for all three experiments increased and were the same within standard error. However, it is important to note that the formation of precipitate phases and impurities in the sintered ceramic could cause localized phase transformation. Since indentation toughness testing is a micro-testing method, it is possible that localized phase transformations interfere with toughness experiments, though localized phase changes could not be detected with SEM/EDS.

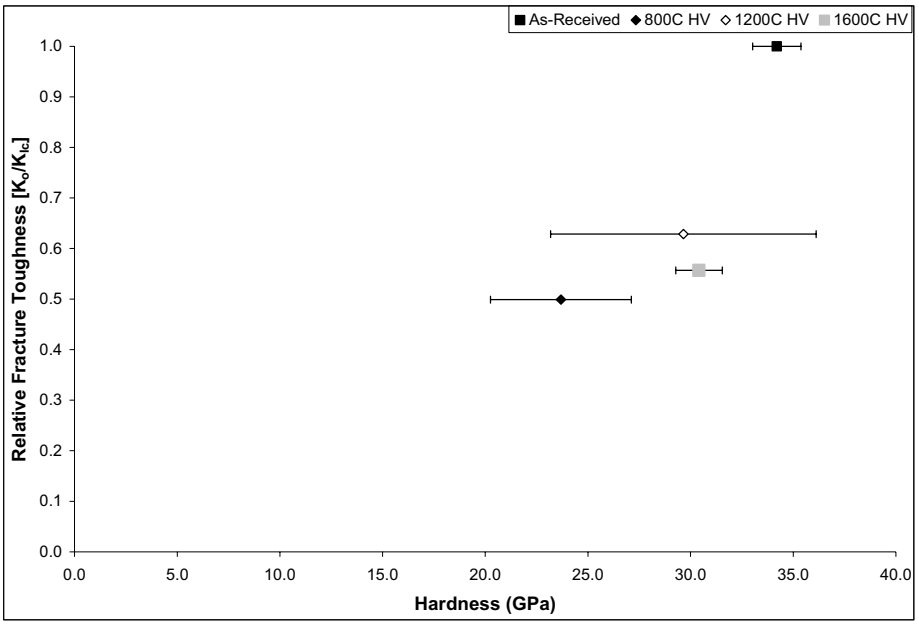

Figure 2.21. Relative fracture toughness versus hardness for heat treated TiC and associated standard error [HV: high vacuum (~10^{-5} Torr)].

For SiC, the sample heat treated at 1600ºC broke during hardness testing even though the thickness criterion in the ASTM standard was followed. Because of this failure, there were not enough data to draw any definite conclusions. Relative fracture toughness versus hardness for SiC is shown in Fig 2.22. There was some softening of the samples after the heat treatments, more so for the 800ºC tests. Relative fracture toughness of the heat treated samples is less than one, indicating a decrease in fracture toughness due to heat treatments. However, it is interesting to note that the relative fracture toughness, though less than one, is the same for both 800 and 1200ºC within standard error. The phase diagram for SiC indicates no phase change is expected under the range of experimental conditions.

Relative fracture toughness versus hardness of ZrC in Figure 2.23 shows values with the lowest hardness and smallest decrease in toughness at 800ºC. The 1200ºC and 1600ºC data points cluster together at larger hardness and a larger decrease in toughness. The results are consistent with the conclusion of material softening and toughness decrease due to heat treatment. The graph indicates that there may be a correlation between toughness, hardness and temperature, since it appears that increasing temperature softens the material and increases crack length. However, there is not currently enough data to develop an empirical correlation between any parameters.

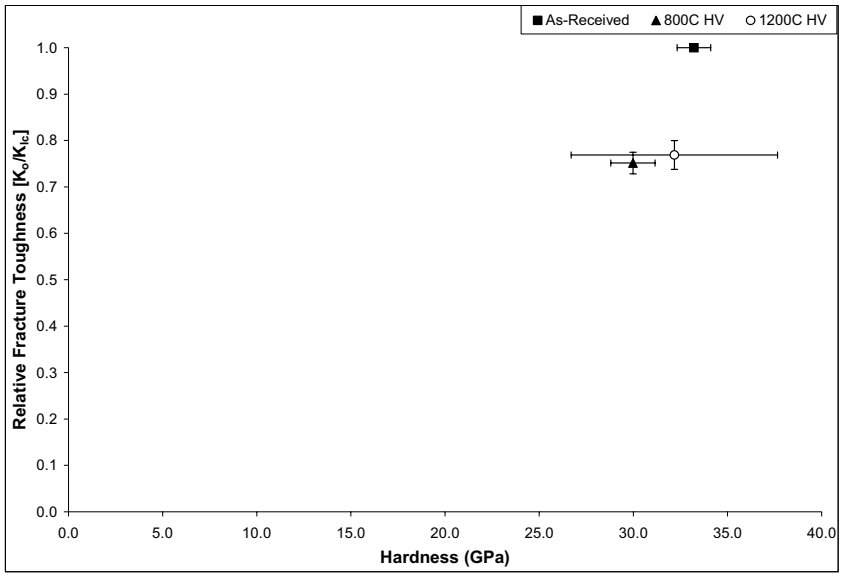

Figure 2.22. Relative fracture toughness versus hardness for SiC and associated standard error [HV: high vacuum (~10^{-5} Torr)].

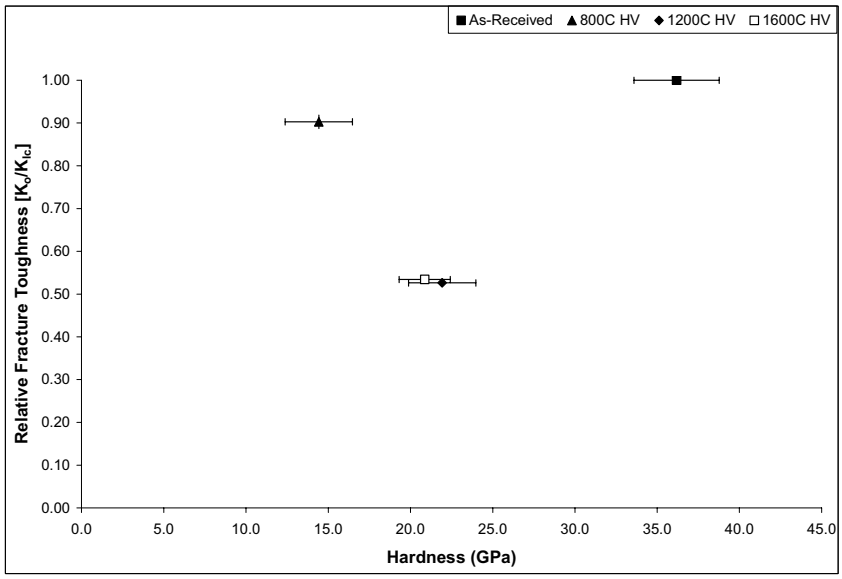

Figure 2.23. Relative fracture toughness versus hardness for ZrC and associated standard error [HV: high vacuum (~10^{-5} Torr)].

Relative fracture toughness versus hardness for ZrN is demonstrated in Figure 2.24. Softening of the materials took place consistently, and the 1200ºC heat treated samples exhibited the least amount of softening, while the 1600ºC heat treated samples displayed the largest amount of softening. This figure also indicates that the fracture toughness decreases after heat treatment. The most significant decrease occurred after the 800ºC heat treatment, and the least significant decrease occurred after the 1200ºC heat treatment. The phase diagram for ZrN does not indicate any phase change is expected at the experiment temperature conditions.

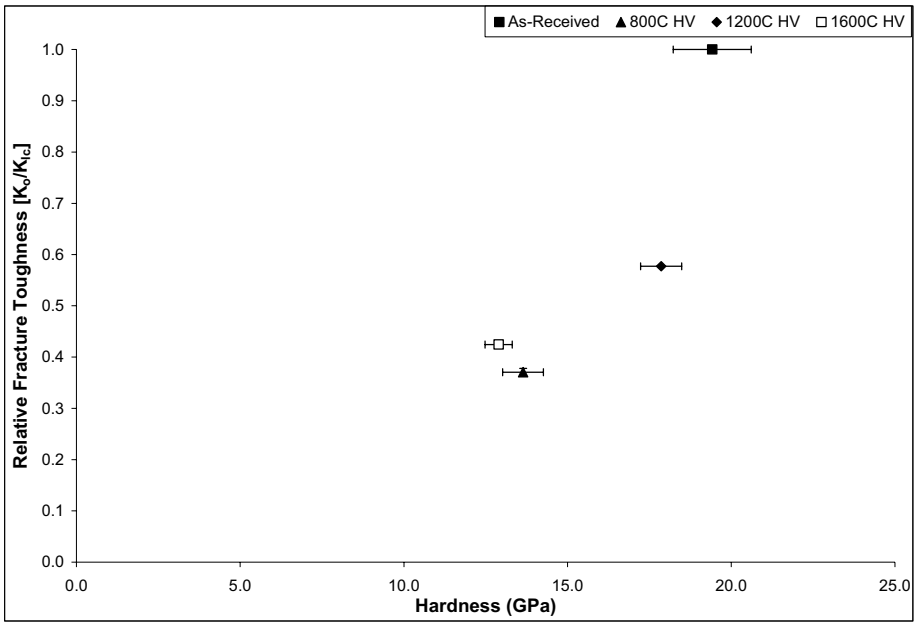

Figure 2.24. Relative fracture toughness versus hardness for ZrN and associated standard error [HV: high vacuum (~10^{-5} Torr)].

2.6 References for Section 2

ASTM E112, 2004, "Standard Test Methods for Determining Average Grain Size," ASTM International.

ASTM E 384-99, 2005, "Standard Test Method for Microindentation Hardness of Materials," ASTM International.

ASTM 1327-03, 2005, "Standard Test Method for Vickers Indentation Hardness of Advanced Ceramics," ASTM International.

ASTM C 1326-03, 2005, "Standard Test Method for Knoop Indentation Hardness of Advanced Ceramics," ASTM International.

Bhat, M., B. Kaur, R. Kumar, K.K. Bamzai, P.N. Kotru, and B.M. Wanklyn, 2005, "Effect of Ion Irradiation on Dielectric and Mechanical Characteristics of $ErFeO_3$ Single Crystals,", *Nuclear Instruments & Methods in Physics Research*, *Section B (Beam Interactions with Materials and Atoms)*, Vol. 234, pp. 494-508.

Egeland, Gerald W., 2005, *Radiation Damage and Fission Product Release in Zirconium Nitride,* PhD thesis: New Mexico Institute of Mining and Technology.

Gong, J., J. Wang, and Z. Guan, 2002, "A Comparison Between Knoop and Vickers Hardness of Silicon Nitride Ceramics," *Mater. Lett.*, Vol. 56, pp. 941-944.

INL/EXT-05-00799, Gas-Cooled Fast Reactor FY 05 Annual Report, September, 2005

Palmqvist, S., 1962, "Energy Causing Cracks at Corners of Vickers Indentations as Measure of Toughness of Hard Metals," *Rissbildungsarbeit bei Vickers-Eindruecken als Mass fuer die Zaehigkeit von Hartmetallen. Archiv fuer das Eisenhuettenwesen*, Vol. 33, pp. 629-634.

Shackelford, J.F., 2005, *Introduction to Materials Science for Engineers*, New Jersey: Prentice Hall.

3. CHEMICAL INTERACTION STUDIES

3.1 Introduction

Chemical interaction of fission products with coating materials can influence coating integrity, as is the case with Pd interaction with SiC observed in irradiated TRISO particles. The introduction of new candidate coating materials requires an analysis of these materials with regard to their chemical compatibility with mobile fission products.

Because of the safety implications, the release of fission products from SiC coated particle fuel has been studied extensively for over 30 years. Many of these investigations have lead to a focus on chemical reactions with the SiC coating or the diffusion of elements through SiC. As a result, fission product interactions with SiC have received considerable attention, including the chemistry of SiC reactions with platinum-group metals, most notably palladium (Suzuki, Takayoshi, and Tetsuji 1977, Tiegs 1982). In addition to the application of SiC as a reactor fuel particle coating, electronic applications of SiC have also spurred research into its interfacial chemistry with Pd and other platinum-group metals (Roy et al. 2002, Chen et al. 1997, Bhanumurthy, Schmid-Fetzer 2001, Rijnders et al. 1997).

By comparison, the chemistry of TiC, TiN, ZrC, and ZrN with platinum group metals has received very little attention in the literature, although interaction of ZrC with Pd in the context of nuclear fuel particles has been the subject of some study (Ogawa, Ikawa 1986).

3.2 Diffusion couples

3.2.1 Experimental methods

Bulk diffusion couples were prepared using ceramic disks and palladium foil. The as-received ceramic rods (20 mm long x 4.5 mm diameter) were sliced into ~1.5 mm thick disks using a low-speed diamond saw. The disks were parallel polished on one side to a 1 micron finish. Palladium foil (0.25 mm thickness) and rhodium foil (99.8%, 0.25 mm thickness) were obtained from Alpha Aesar. The foils were cut into 4.4 mm diameter disks using a modified sheet metal punch and die. The foil disks were then lightly compacted between two tungsten carbide anvils in a pellet die to eliminate any raised surfaces.

Both the ceramic and metal foil disks were ultrasonically cleaned in acetone. Diffusion couples were prepared by sandwiching a metal foil between two polished ceramic disks, or between a polished ceramic disk and a graphite disk used as a non-reactive spacer. A device was designed to enable the diffusion couples to be heated in a tube furnace under an argon gas purge while applying a small normal force to ensure good contact between surfaces (Figure 3.1). The samples were stacked in a graphite holder which was held in place at the end of a ¾" diameter alumina tube. The alumina tube was secured in a Swagelok "tee" fitting with a Teflon ferrule. A force was applied by compression of a calibrated spring, and transmitted to the samples via an alumina rod (see Figure 3.1). A small flow of ultra high purity argon (~100 sccm) was used to purge the device during heating to avoid oxidation of the samples. Gas flow was into the "tee" fitting and out a small laser drilled hole in the end of the ¾" diameter alumina tube. The total force applied using the calibrated spring was 10 lbf (44N) for most experiments. This gave a pressure on the 4.5mm diameter samples of 2.8MPa.

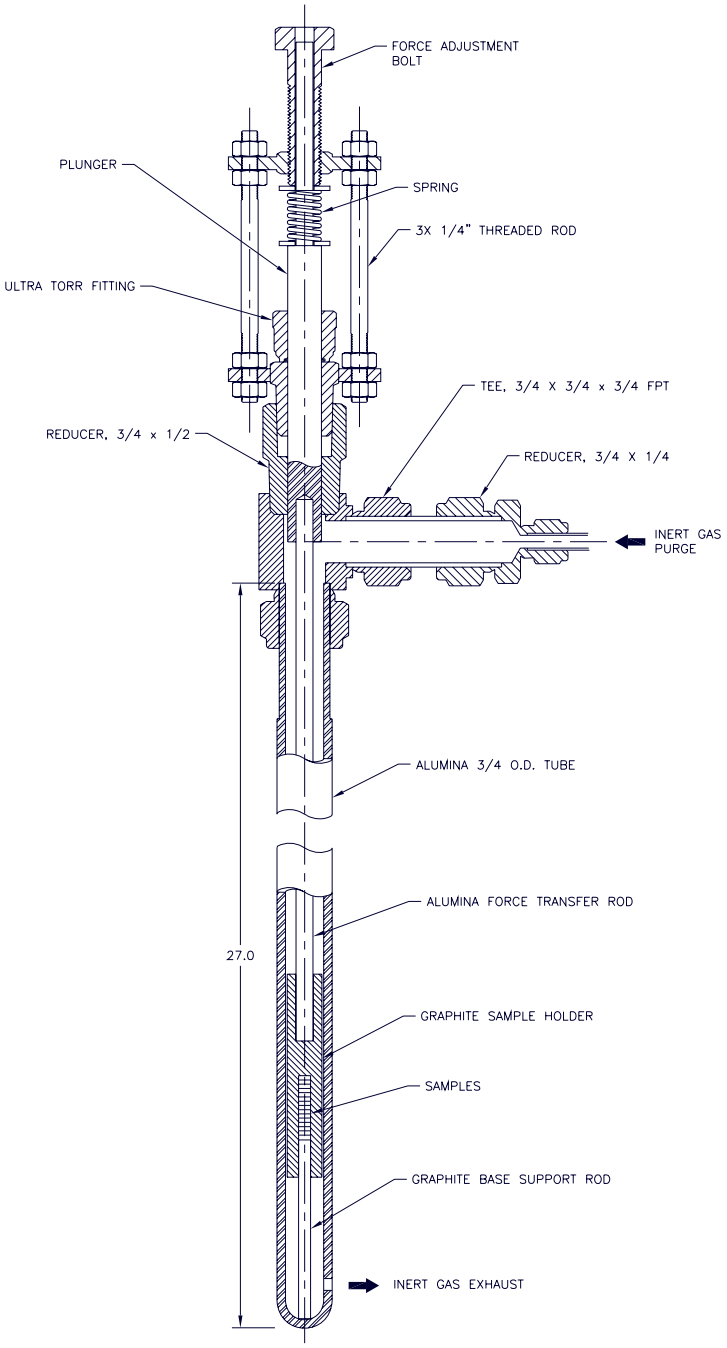

Figure 3.1. Experimental apparatus for diffusion couple annealing.

The sample stack in the compression device was inserted into a tube furnace so that the center of the sample stack was aligned with the center of the furnace hot zone. The furnace was ramped to the target temperature and back down at a rate of ~2.5–3.0ºC/min. The annealing times and temperatures used for the Pd and Rh diffusion couples are given in Tables 3.1 and 3.2. Annealing temperatures for the Rh

samples were higher than the Pd samples due to the higher melting point of Rh and the corresponding intermetallic phases that could form with the ceramics, and an expected lower reactivity compared to Pd at similar temperatures. SiC samples were not annealed at the highest temperatures in each set of conditions due to a much higher reaction rate than the other ceramics which resulted in very large interaction zones at lower temperatures.

Table 3.1. Time and temperature annealing conditions for Pd diffusion couples.

	800ºC	1000ºC	1200ºC	1400ºC
10h	SiC, AlN	TiC, TiN, ZrC, ZrN, AlN, SiC	TiC, TiN, ZrC, ZrN, AlN, SiC	TiC, TiN, ZrC, ZrN
50h	—	TiC, TiN, ZrC, ZrN, AlN, SiC	—	—
250h	—	TiC, TiN, ZrC, ZrN, AlN, SiC	—	—

Table 3.2. List of time and temperature annealing conditions for Rh diffusion couples.

	1200ºC	1400ºC	1600ºC
10h	TiC, TiN, ZrC, ZrN, AlN, SiC	TiC, TiN, ZrC, ZrN, AlN, SiC	TiC, TiN, ZrC, ZrN, AlN
50h	TiC, TiN, ZrC, ZrN, AlN, SiC	—	—
250h	TiC, TiN, ZrC, ZrN, AlN, SiC	—	—

During the course of these experiments, AlN was eliminated from consideration as a fast reactor fuel material in concurrent work due to issues with neutron irradiation performance, as well as the additional consideration of the melting point (~2200ºC), which is only marginally higher than the reference value (Table 1.1). Due to this shift in focus as part of the GFR program, AlN was considered here as a secondary priority material and some of the analyses were not completed on this material in order to focus the efforts on the remaining candidates.

3.2.2 Characterization

3.2.2.1 Sample preparation. Diffusion couples were mounted in epoxy, ground, and polished to a 1 micron finish for cross-section analysis. The metal-ceramic interfaces were analyzed using optical microscopy, scanning electron microscopy, and electron probe microanalysis (microprobe). The polished samples were coated with a thin conducting layer to minimize charging effects during SEM and microprobe analyses. Samples containing nitrogen (i.e. the nitrides) were coated with carbon; samples containing carbon (carbides) were coated with aluminum to avoid interference of a carbon coating during chemical analyses.

3.2.2.2 AFM – Surface roughness. Atomic force microscopy (AFM) was used to measure surface roughness on the polished ceramics. The average values for the ceramic surfaces analyzed were below a root mean square (rms) surface roughness of ~70 nm, with the exception of AlN, which had an average value of ~160 nm.

3.2.2.3 SEM. Secondary and backscattered electron micrographs were obtained with a Phillips ESEM XL 30, with Princeton Gamma Tech Prism EDS. Analysis was typically performed with a 20kV accelerating voltage.

3.2.2.4 Microprobe. Microprobe analyses were performed with a JEOL JXA 8900-R electron probe microanalyzer (EPMA) using an acceleration voltage of 15 kV and current of 2.0×10^{-8} amps. Effective beam spot size was 0.5 μm. Analysis conditions are shown in Table 3.3.

Table 3.3. Crystals used for electron probe microanalysis and detection limits for each analyte.

Element	Al	Zr	Ti	Si	N	C*[a]	C^[b]	Pd	Rh
Crystal	TAP	PET	PET	TAP	LDE1	LDE1	LDE2	PET	PET
Detection Limit, wt.%	0.03	0.04	0.03	0.02	0.4	0.6-1.4	0.06	0.03	0.02

a. C* represents measurement conditions for C in samples with Pd. Detection limit varies depending on what element is bonded to carbon. Light element wavelength position varies with the element it is bonded to, thus the intensity of Pd interference varies, resulting in different detection limits for the different carbon-metal combinations.
b. C^ represents measurement conditions for C in samples with Rh.

Standards consisted of Pd and Rh metal for Pd and Rh couples, respectively. Ceramic standards consisted of the unreacted ceramic within the diffusion couple sample itself, approximately 1 mm away from the reaction interface, where no Pd or Rh was expected in the matrix. This was done because light elements such as N and C are very sensitive to the coating thickness. By using an unreacted part of the coated sample as the standard, it was assured the coating thickness was the same between the standard and the unknown.

For both standard and unknown analyses, the background was measured in two places, before and after the peak. Background was counted for 10 seconds while the peaks were counted for 20 seconds. The only significant interference was that of Pd with C. This was minimized by using the LDE1 crystal; however this raised the detection limit of C because the peak to background ratio is lower with LDE1 than with LDE2, and because there was a small amount of Pd still contributing to C signal. Matrix corrections were accomplished using JEOL ZAF correction software.

Samples were analyzed via automated line scans, in which analysis began in the ceramic, near the reaction zone, then proceeded into the reaction zone, and ended in the unreacted metal. The line was oriented perpendicular to the interface between the ceramic and the metal and was divided into a sufficient number of points such that the center of each analyzed spot was 2 μm apart. In some samples where the reaction zone was particularly large, analyzed spots were 4 μm apart. Data was collected and corrected for matrix effects by JEOL software. In some instances, particular spots did not yield valid analyses (as evidenced by analyte totals deviating significantly from 100%) due to topographical effects.

Every attempt was made to produce cross-section samples with smooth surfaces through careful polishing procedures, but the presence of a certain amount of surface roughness was inevitable, partly due to the very different mechanical properties of the various phases present. Also, porosity that forms as the result of interface reactions adds to the non-planarity of the surface. Since the EPMA method can be sensitive to sample topography, the upshot is that data from areas with rough surfaces or pores is often suspect, with weight percent totals not always amounting to 100.

3.2.2.5 TEM. Transmission electron microscopy was used to analyze a limited number of samples. One TiC-Pd and one TiN-Pd sample were prepared specifically for TEM analysis. These diffusion couples used approximately 2 mm thick disks and consisted of single ceramic/metal/ceramic "sandwiches". Both were annealed at 1200ºC for 10 hours. The annealing procedure was the same as for the standard diffusion couple samples (Section 3.2.1). The annealed diffusion couples were then cut perpendicular to the plane of the interfaces to give thin cross sections, which were then cut with a disk cutter to give 3 mm diameter disks. The disks were mechanically polished to approximately 124 μm thickness and then ground with a dimpler to remove ~55 μm from each side. The disks were finally ion-milled using a precision ion polishing system (7.5 hours, 4 keV ion energy at 7 degree angle) to give electron transparent samples.

3.2.3 Pd Diffusion Couple Results

A representative micrograph of an annealed diffusion couple (TiC/Pd/graphite) polished cross-section is shown in Figure 3.2. In most cases no reaction was observed between the metal foils (Pd or Rh) and the graphite spacers. For the analyses presented here, the focus is on the ceramic-metal interface.

Comparisons of the Pd diffusion couple interfaces at each time-temperature annealing condition are shown in Figures 3.3–3.7. The appearance of the interfaces varies considerably for the different ceramics investigated as did the apparent reactivity with palladium. No direct solubility of palladium in the ceramic phases was observed for any of the samples although palladium could be observed infiltrating the ceramic grain boundaries in a number of cases (see specific descriptions below). The analysis presented here focuses more on the Ti and Zr carbides and nitrides, and less on AlN and SiC.

As can been seen in Figures 3.3(b) and 3.4(e), occasionally the Pd foil cross-section appears much thinner than expected based on the starting thickness and the amount of reaction observed. The result was due to what appeared to be the Pd foil being partially extruded from it's location between the two immobile disks. It is unclear if this occurred due to the elevated temperatures causing extensive creep in the Pd foil, chemical composition changes in the Pd that significantly changed it's mechanical properties, the formation of lower melting point eutectic phases, or some other unidentified cause. It is most likely not simply a temperature-driven effect, as it was not always the highest temperature anneals that resulted in this behavior. The Ti-Pd system, for example, exhibits intermetallic phases with melting points in the 1400ºC range (Massalski 1990). This could account for the thin Pd layer in the TiN-Pd 1400ºC-10h sample [Figure 3.4(e)], but not the TiC-Pd 1000ºC-50h sample [Figure 3.3(b)].

Electron microprobe composition line scan data across the ceramic-metal interfaces are given in Figures 3.8–3.11. Note that this data was not taken in exactly the same location on the samples that is shown in the micrographs (Figures 3.3–3.7). For many samples line scans were taken across the interface at several points, since the extent of reaction was often not uniform over the entire length. For a number of samples it is apparent that no reaction had taken place (i.e. the composition line scans show that there was an abrupt transition from pure ceramic to pure palladium with no intermediate phases or solid solution formation). For other samples reaction products could often be observed in certain regions of the interface but not at others. The reason for this observation was not always clear, but could be due in certain instances to a lack of good contact across the entire ceramic/metal surfaces. For samples in which there were regions of no reaction and isolated areas showing a reaction, scans of the reactive areas are discussed here in great detail. The extent of the reactivity across the entire interface can often be observed in the low magnification micrographs in Figures 3.3–3.7.

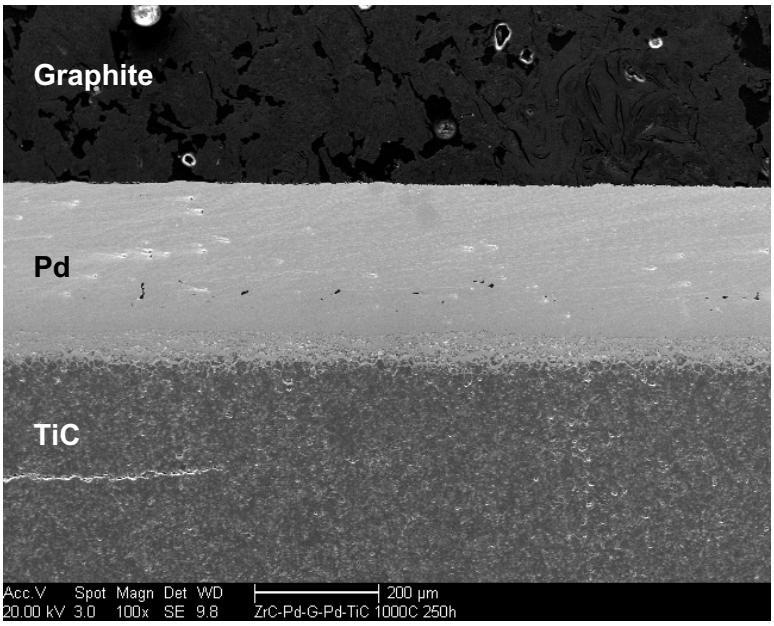

Figure 3.2. Polished cross-section of a TiC-Pd interface annealed at 1000ºC for 250h.

Many line scans exhibited regions with relatively uniform Pd/M (M = Zr, Ti, Si) ratios. These have been labeled on the figures, and are the average of the ratios for each pair of data points over the entire region. Note that the actual values for each pair of data points may still vary from the average in these regions.

It should be noted that there was an interference in x-ray signals from between Pd and C peaks (see discussion in Section 3.2.2, *Characterization*), that resulted in an increased detection limit for carbon. This became an issue in the analysis of diffusion couples containing carbide ceramics (i.e. where carbon was an analyte of interest). The resulting maximum detection limit of 1.5 wt.% (Table 3.3) can correspond to as much as 10 at.%. The carbon contents in these samples of up to ~10 at.% are most likely not accurate and represent an artifact of the Pd-C signal interference rather than actual carbon contents, since carbon solubility in Pd is approximately 2 at.% at 1200ºC and decreases significantly at lower temperatures (Yokoyma, Numakura and Koiwa 1998).

As a general observation, reactions with the carbide samples produced distinctly different interaction zones than the nitrides. The interaction zones for carbide diffusion couples usually exhibited an intermediate heterogeneous microstructure (Figures 3.3, 3.5, 3.7) that suggests the formation of secondary phases. On the other hand, nitride interfaces tended to show abrupt transition from the ceramic to the palladium. In most cases the palladium film at the interface was in fact a solid solution, Pd(M), where M = Zr or Ti. The composition of the secondary metal in the palladium decreases with increasing distance from the interface (see Figure 3.9(a-d) for example).

Key observations and discussions for each specific ceramic are given in the following sections.

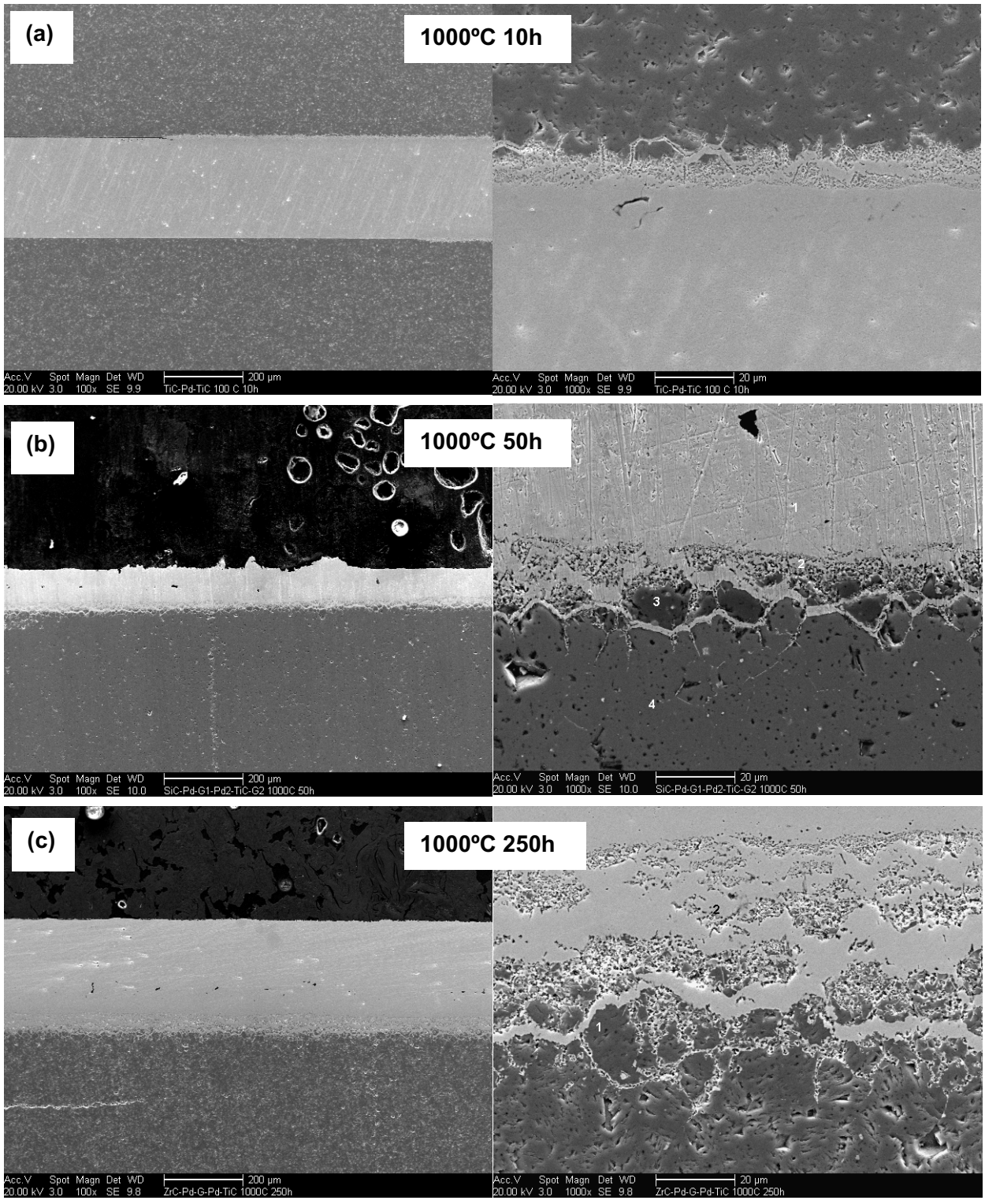
(a)
1000ºC 10h
Acc.V Spot Magn Det WD 200 µm
20.00 kV 3.0 100x SE 9.9 TiC-Pd-TiC 100 C 10h
Acc.V Spot Magn Det WD 20 µm
20.00 kV 3.0 1000x SE 9.9 TiC-Pd-TiC 100 C 10h
(b)
1000ºC 50h
1
2
3
4
Acc.V Spot Magn Det WD 200 µm
20.00 kV 3.0 100x SE 10.0 SiC-Pd-G1-Pd2-TiC-G2 1000C 50h
Acc.V Spot Magn Det WD 20 µm
20.00 kV 3.0 1000x SE 10.0 SiC-Pd-G1-Pd2-TiC-G2 1000C 50h
(c)
1000ºC 250h
1
2
Acc.V Spot Magn Det WD 200 µm
20.00 kV 3.0 100x SE 9.8 ZrC-Pd-G-Pd-TiC 1000C 250h
Acc.V Spot Magn Det WD 20 µm
20.00 kV 3.0 1000x SE 9.8 ZrC-Pd-G-Pd-TiC 1000C 250h

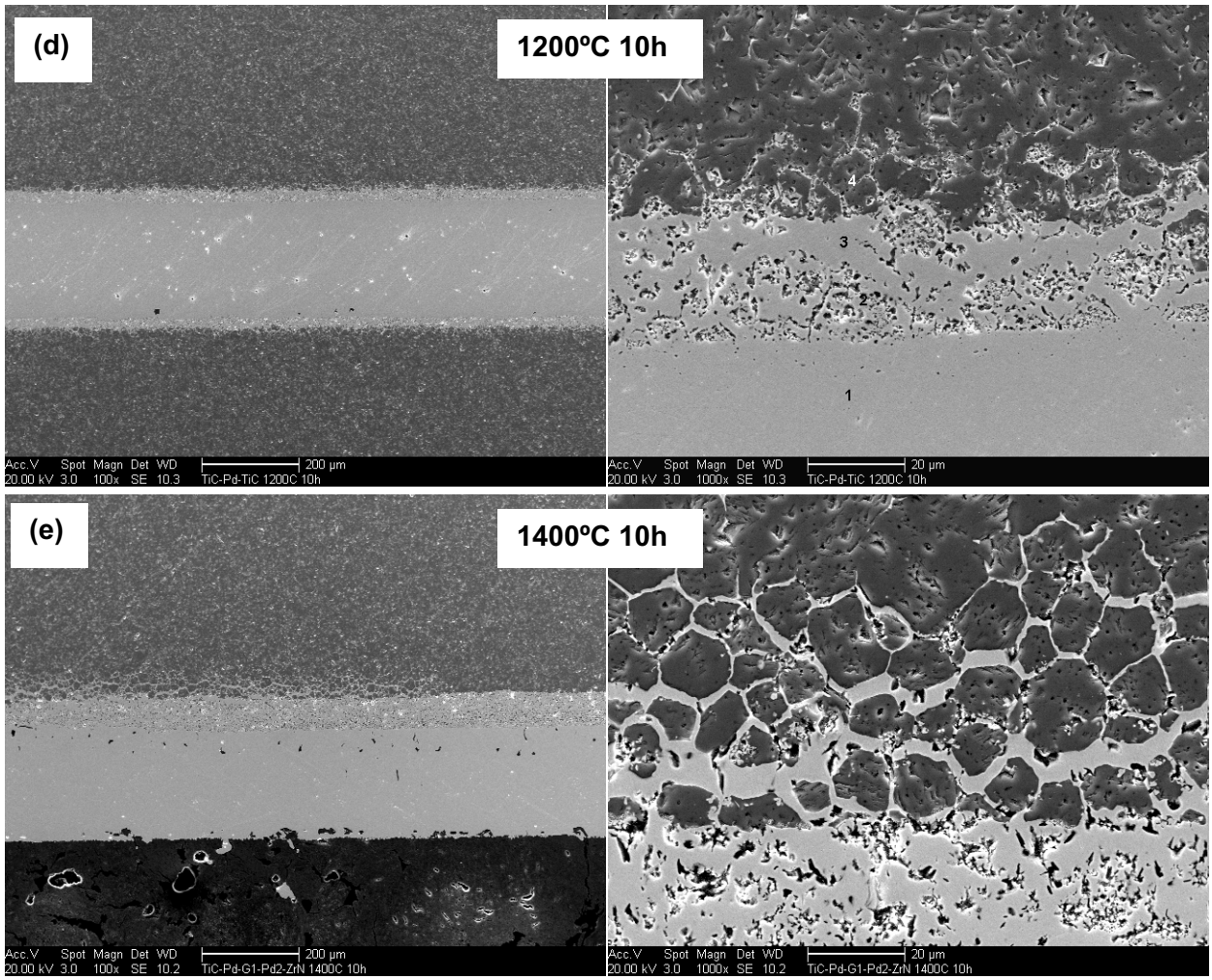

Figure 3.3. Electron micrographs of TiC-Pd interfaces.

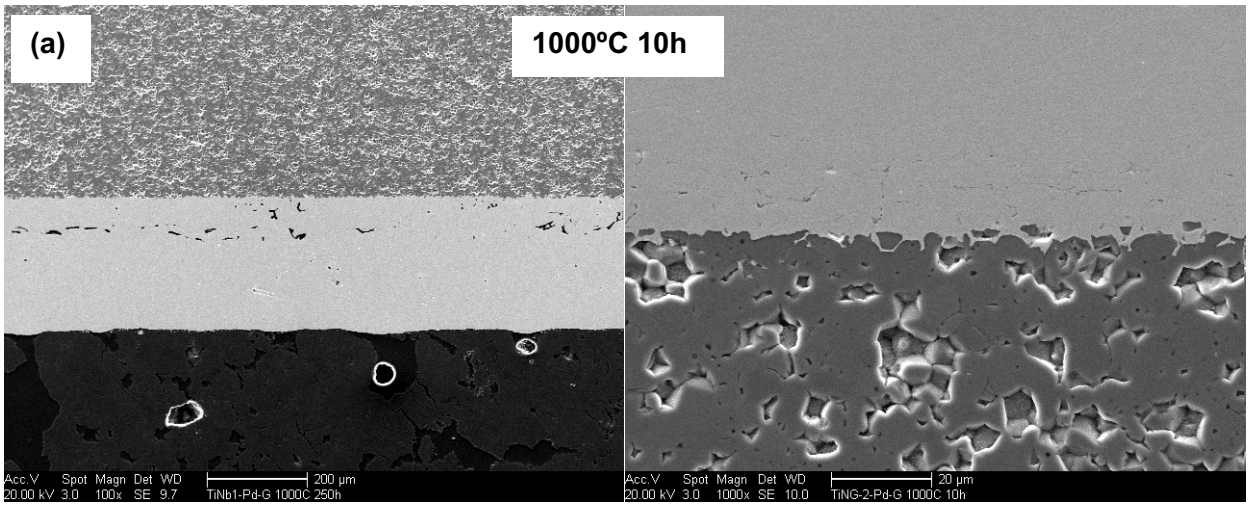
(a)
1000ºC 10h
Acc.V Spot Magn Det WD 200 µm
20.00 kV 3.0 100x SE 9.7 TiNb1-Pd-G 1000C 250h
Acc.V Spot Magn Det WD 20 µm
20.00 kV 3.0 1000x SE 10.0 TiNG-2-Pd-G 1000C 10h

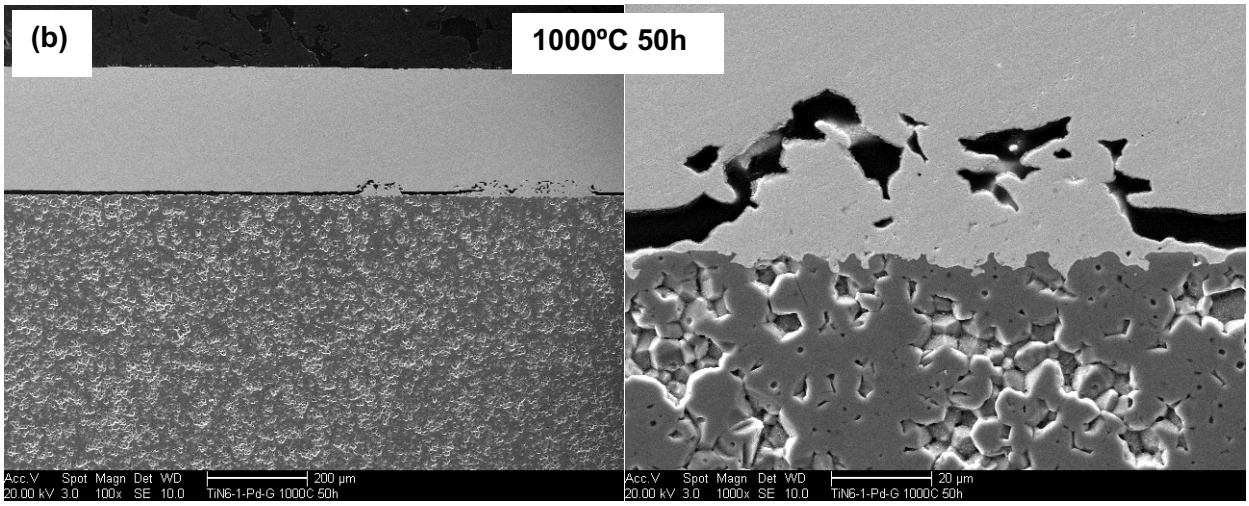
(b)
1000ºC 50h
Acc.V Spot Magn Det WD 200 µm
20.00 kV 3.0 100x SE 10.0 TiN6-1-Pd-G 1000C 50h
Acc.V Spot Magn Det WD 20 µm
20.00 kV 3.0 1000x SE 10.0 TiN6-1-Pd-G 1000C 50h

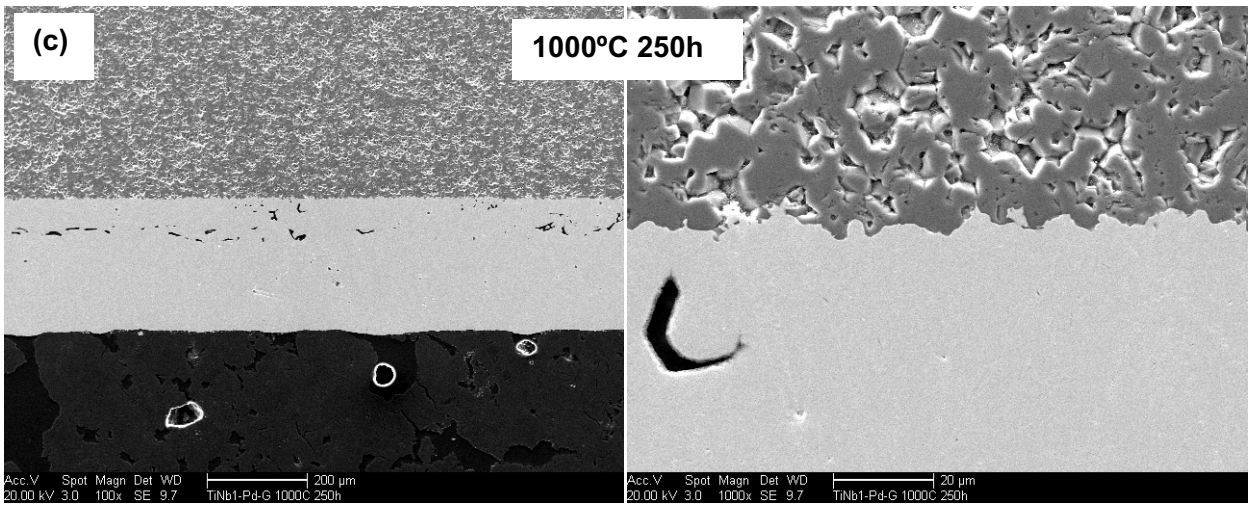
(c)
1000ºC 250h
Acc.V Spot Magn Det WD 200 µm
20.00 kV 3.0 100x SE 9.7 TiNb1-Pd-G 1000C 250h
Acc.V Spot Magn Det WD 20 µm
20.00 kV 3.0 1000x SE 9.7 TiNb1-Pd-G 1000C 250h

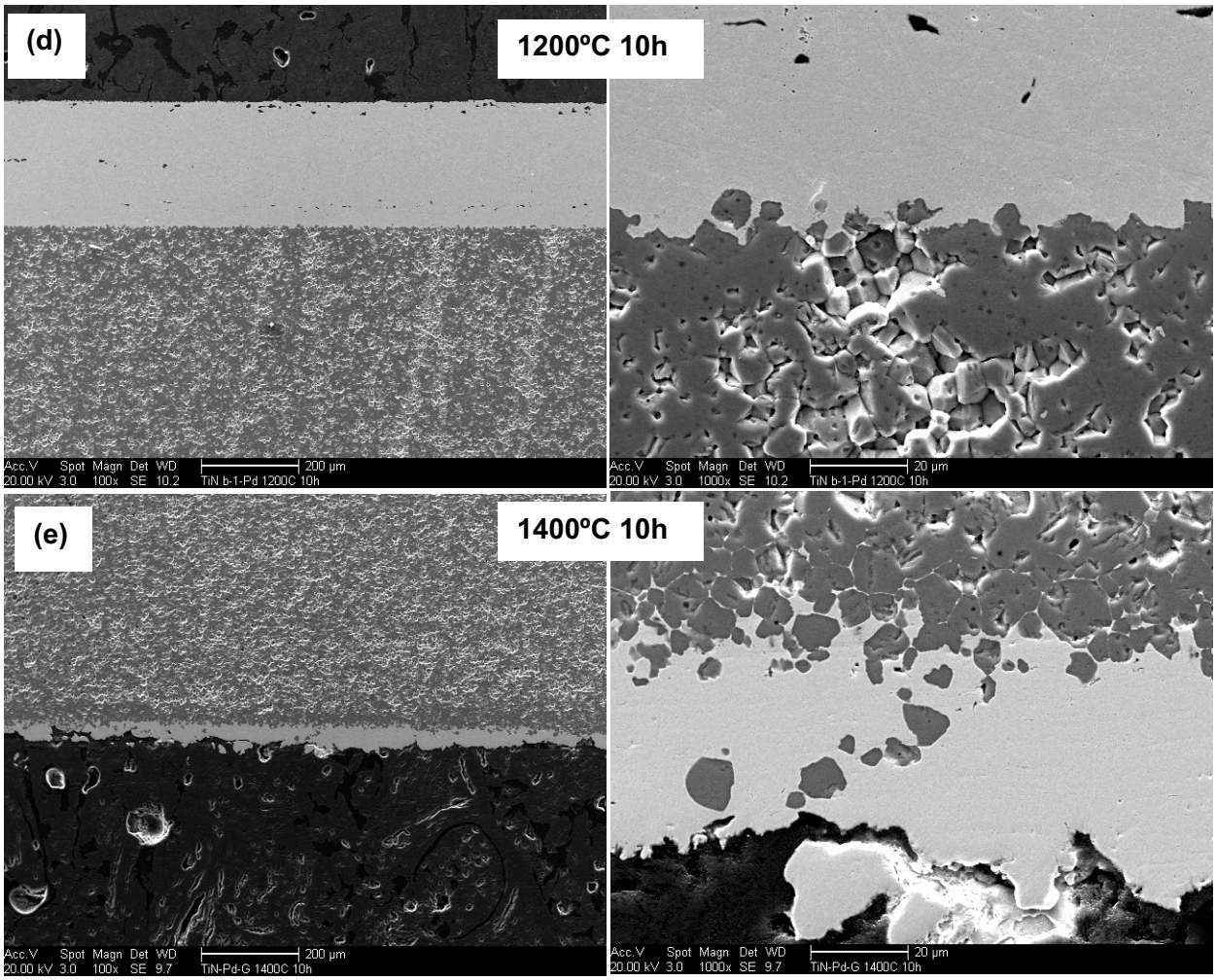

Figure 3.4. Electron micrographs of TiN-Pd interfaces.

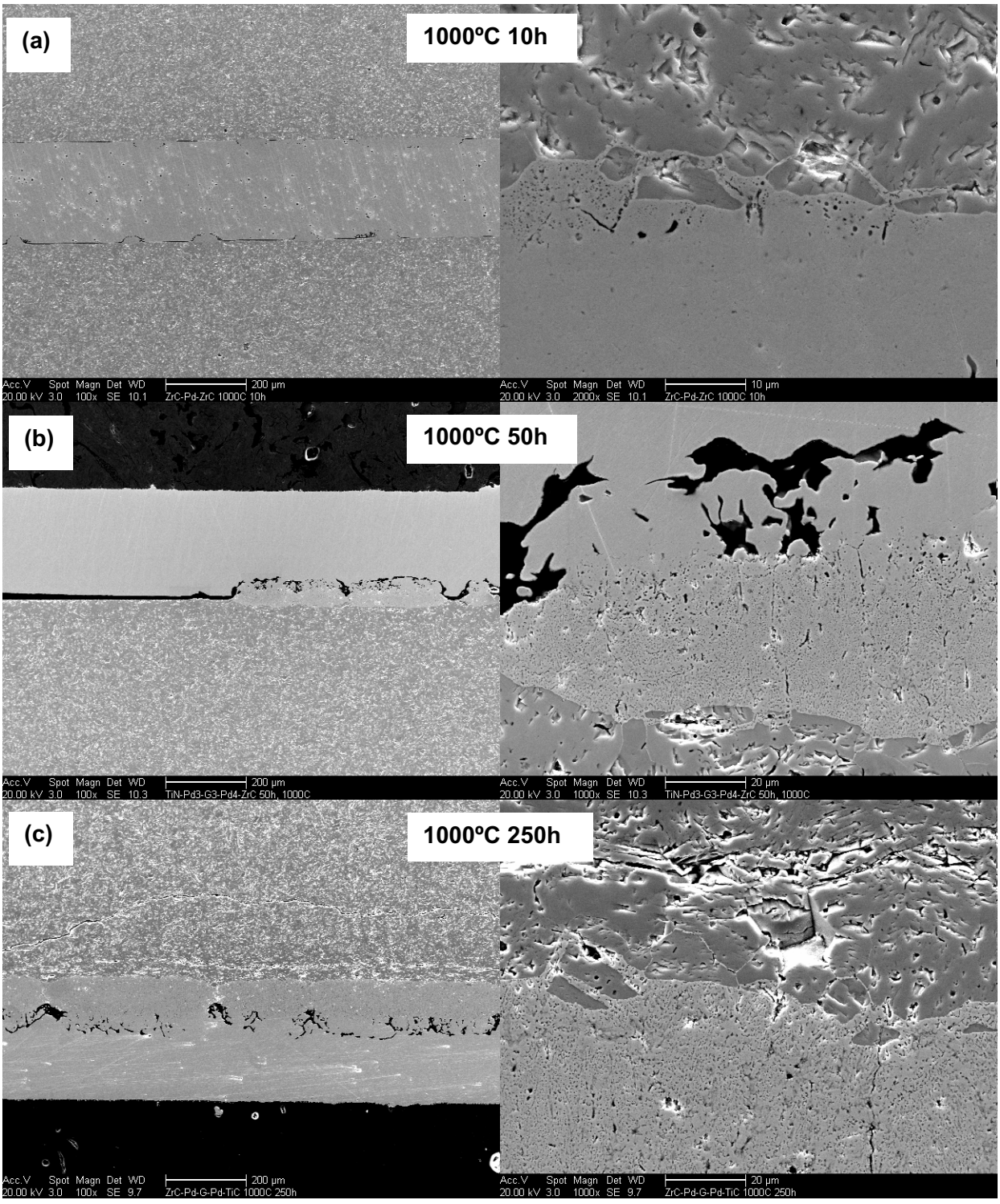
(a)
1000ºC 10h
Acc.V Spot Magn Det WD 200 µm
20.00 kV 3.0 100x SE 10.1 ZrC-Pd-ZrC 1000C 10h
Acc.V Spot Magn Det WD 10 µm
20.00 kV 3.0 2000x SE 10.1 ZrC-Pd-ZrC 1000C 10h
(b)
1000ºC 50h
Acc.V Spot Magn Det WD 200 µm
20.00 kV 3.0 100x SE 10.3 TiN-Pd3-G3-Pd4-ZrC 50h, 1000C
Acc.V Spot Magn Det WD 20 µm
20.00 kV 3.0 1000x SE 10.3 TiN-Pd3-G3-Pd4-ZrC 50h, 1000C
(c)
1000ºC 250h
Acc.V Spot Magn Det WD 200 µm
20.00 kV 3.0 100x SE 9.7 ZrC-Pd-G-Pd-TiC 1000C 250h
Acc.V Spot Magn Det WD 20 µm
20.00 kV 3.0 1000x SE 9.7 ZrC-Pd-G-Pd-TiC 1000C 250h

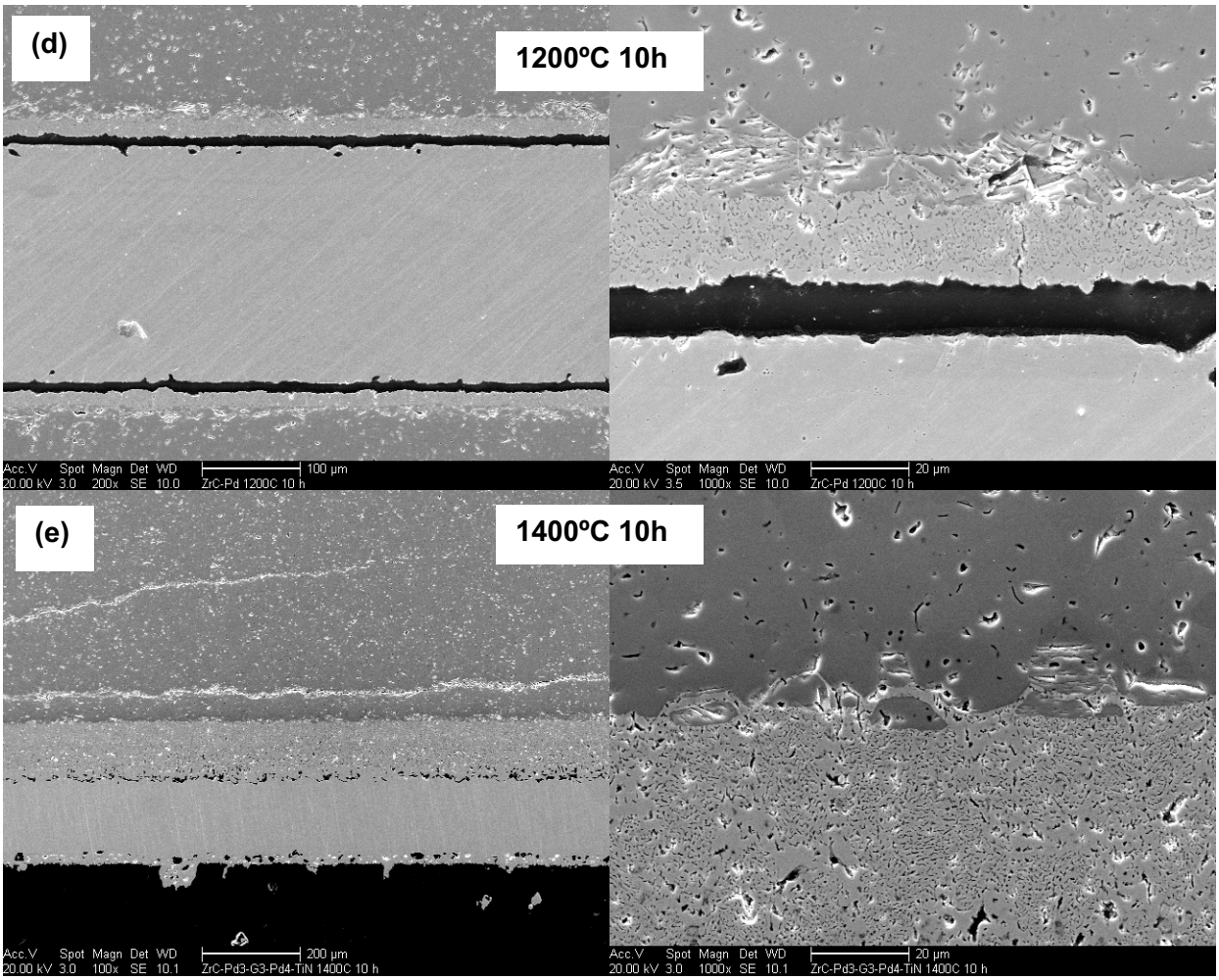

Figure 3.5. Electron micrographs of ZrC-Pd interfaces. (Note the different magnification for the 1000ºC-10h sample).

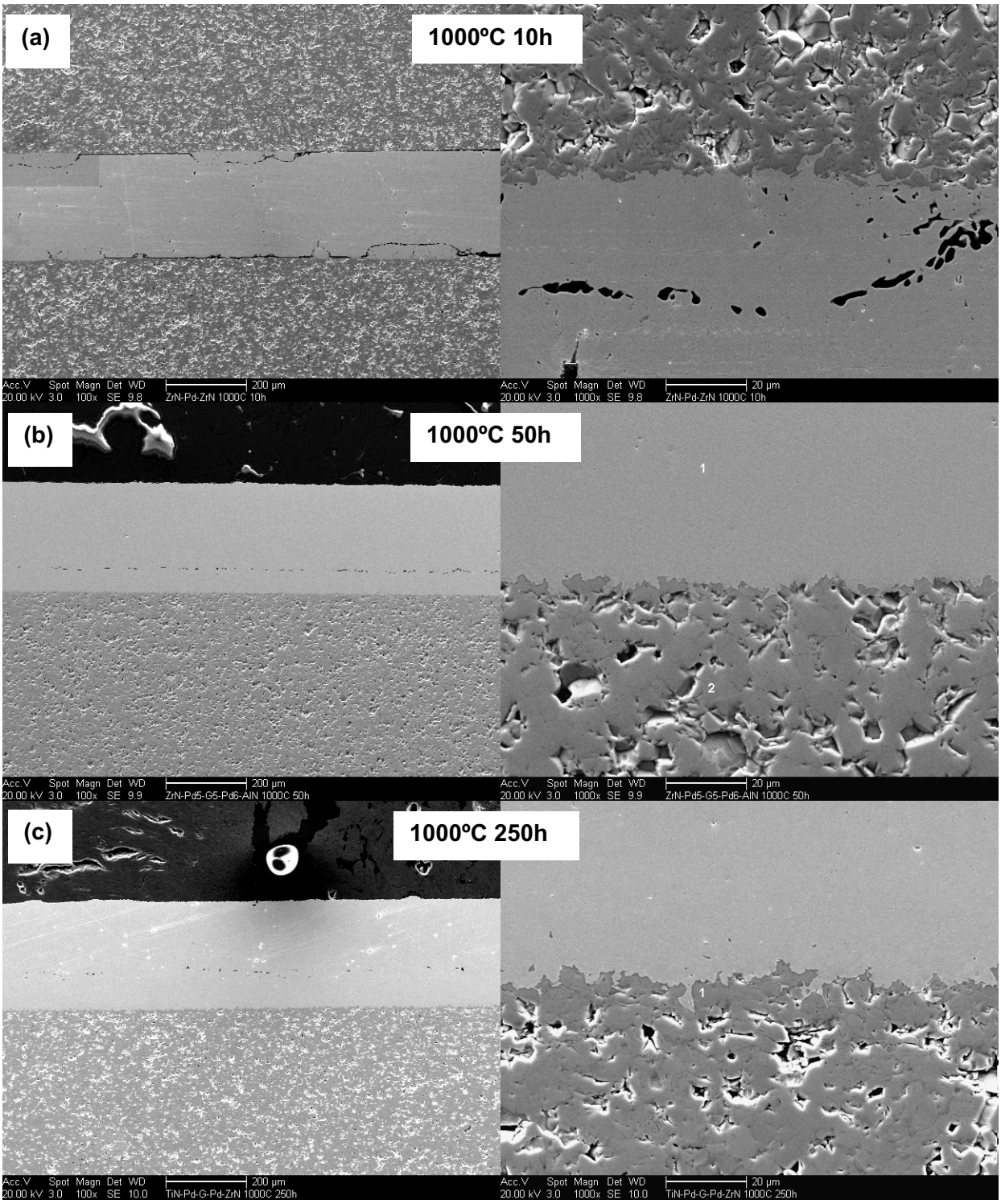
(a)
1000ºC 10h
Acc.V Spot Magn Det WD 200 µm
20.00 kV 3.0 100x SE 9.8 ZrN-Pd-ZrN 1000C 10h
Acc.V Spot Magn Det WD 20 µm
20.00 kV 3.0 1000x SE 9.8 ZrN-Pd-ZrN 1000C 10h
(b)
1000ºC 50h
1
2
Acc.V Spot Magn Det WD 200 µm
20.00 kV 3.0 100x SE 9.9 ZrN-Pd5-G5-Pd6-AlN 1000C 50h
Acc.V Spot Magn Det WD 20 µm
20.00 kV 3.0 1000x SE 9.9 ZrN-Pd5-G5-Pd6-AlN 1000C 50h
(c)
1000ºC 250h
1
Acc.V Spot Magn Det WD 200 µm
20.00 kV 3.0 100x SE 10.0 TiN-Pd-G-Pd-ZrN 1000C 250h
Acc.V Spot Magn Det WD 20 µm
20.00 kV 3.0 1000x SE 10.0 TiN-Pd-G-Pd-ZrN 1000C 250h

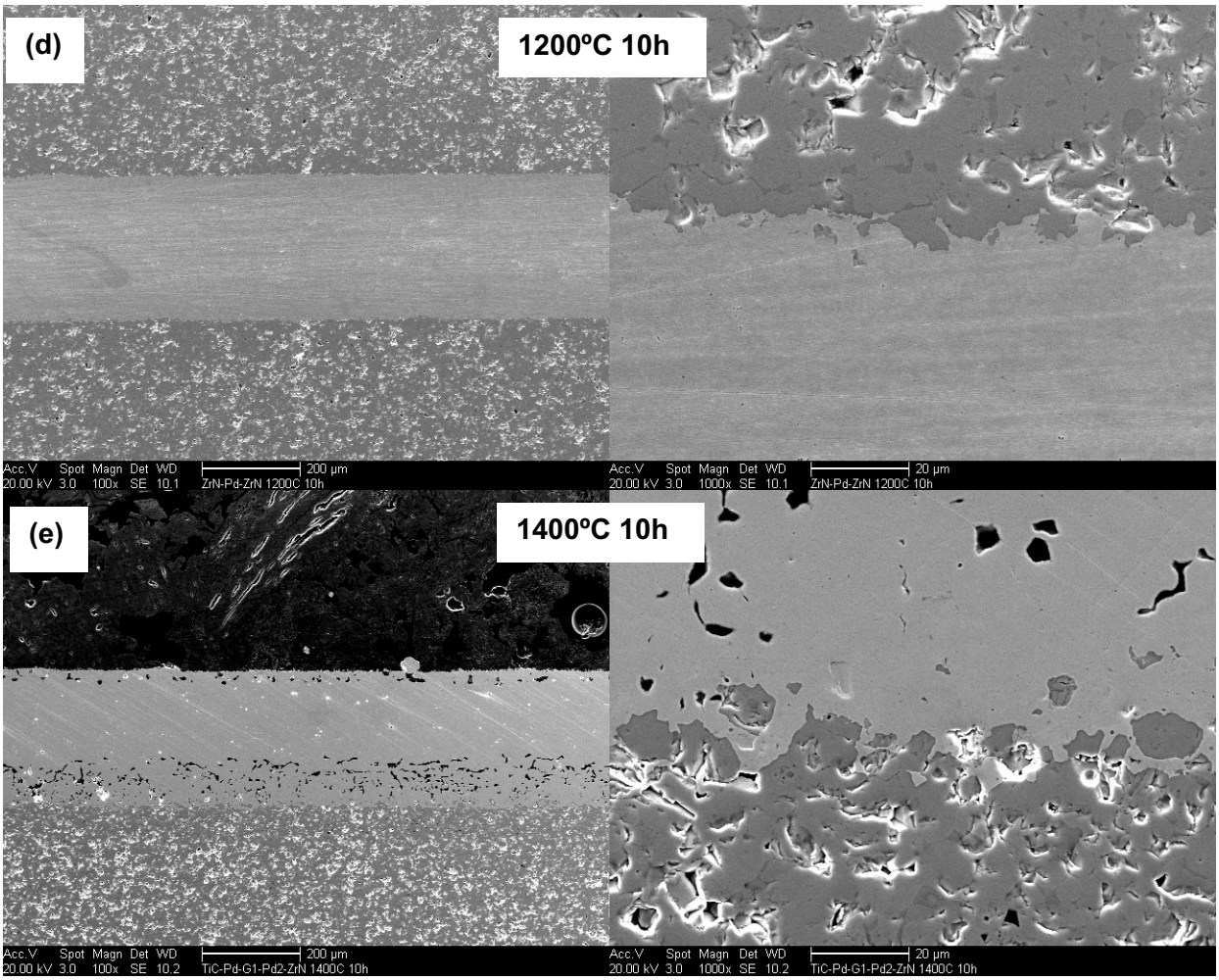

Figure 3.6. Electron micrographs of ZrN-Pd interfaces.

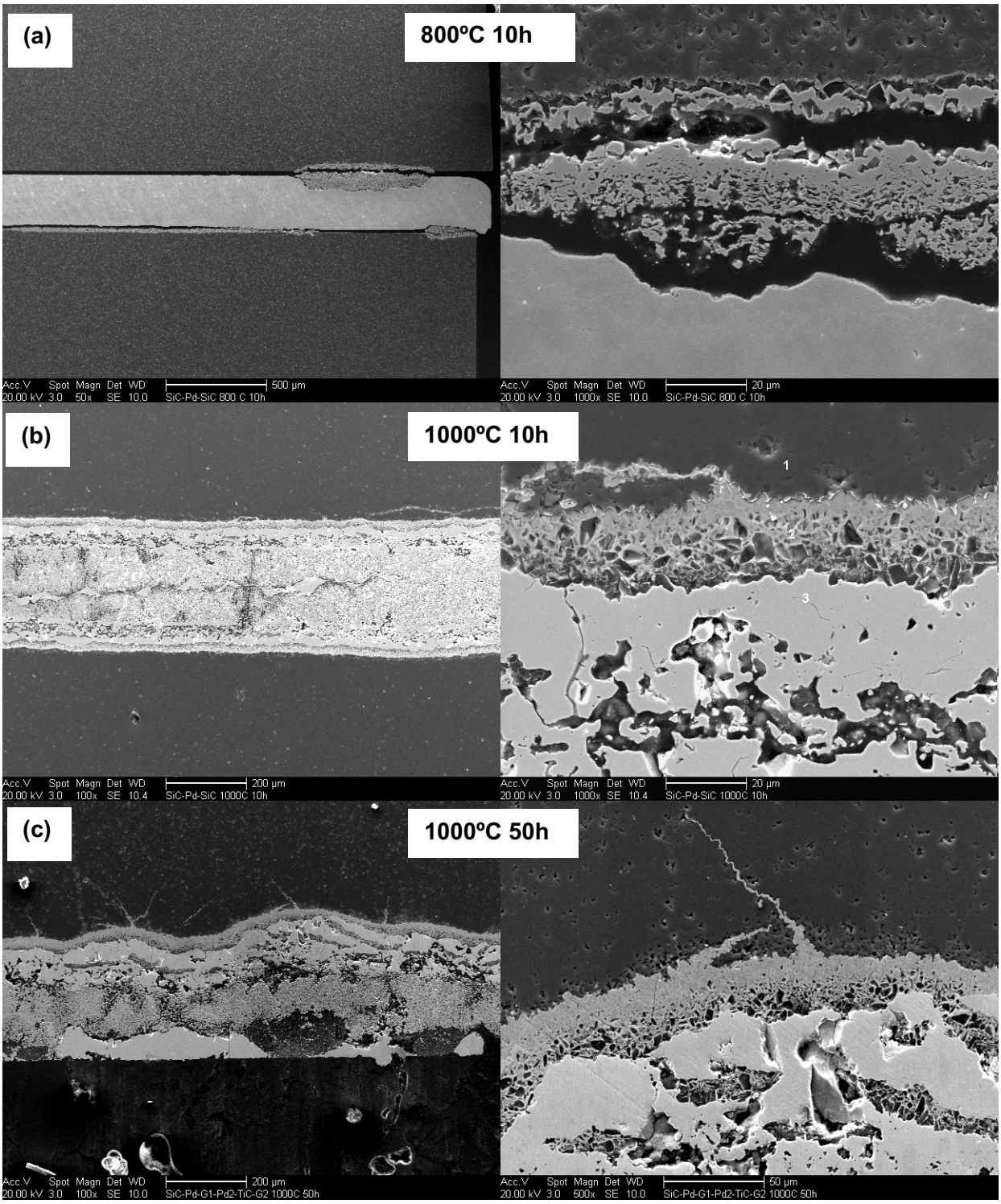
(a)
800ºC 10h
Acc.V Spot Magn Det WD 500 µm
20.00 kV 3.0 50x SE 10.0 SiC-Pd-SiC 800 C 10h
Acc.V Spot Magn Det WD 20 µm
20.00 kV 3.0 1000x SE 10.0 SiC-Pd-SiC 800 C 10h
(b)
1000ºC 10h
1
2
3
Acc.V Spot Magn Det WD 200 µm
20.00 kV 3.0 100x SE 10.4 SiC-Pd-SiC 1000C 10h
Acc.V Spot Magn Det WD 20 µm
20.00 kV 3.0 1000x SE 10.4 SiC-Pd-SiC 1000C 10h
(c)
1000ºC 50h
Acc.V Spot Magn Det WD 200 µm
20.00 kV 3.0 100x SE 10.0 SiC-Pd-G1-Pd2-TiC-G2 1000C 50h
Acc.V Spot Magn Det WD 50 µm
20.00 kV 3.0 500x SE 10.0 SiC-Pd-G1-Pd2-TiC-G2 1000C 50h

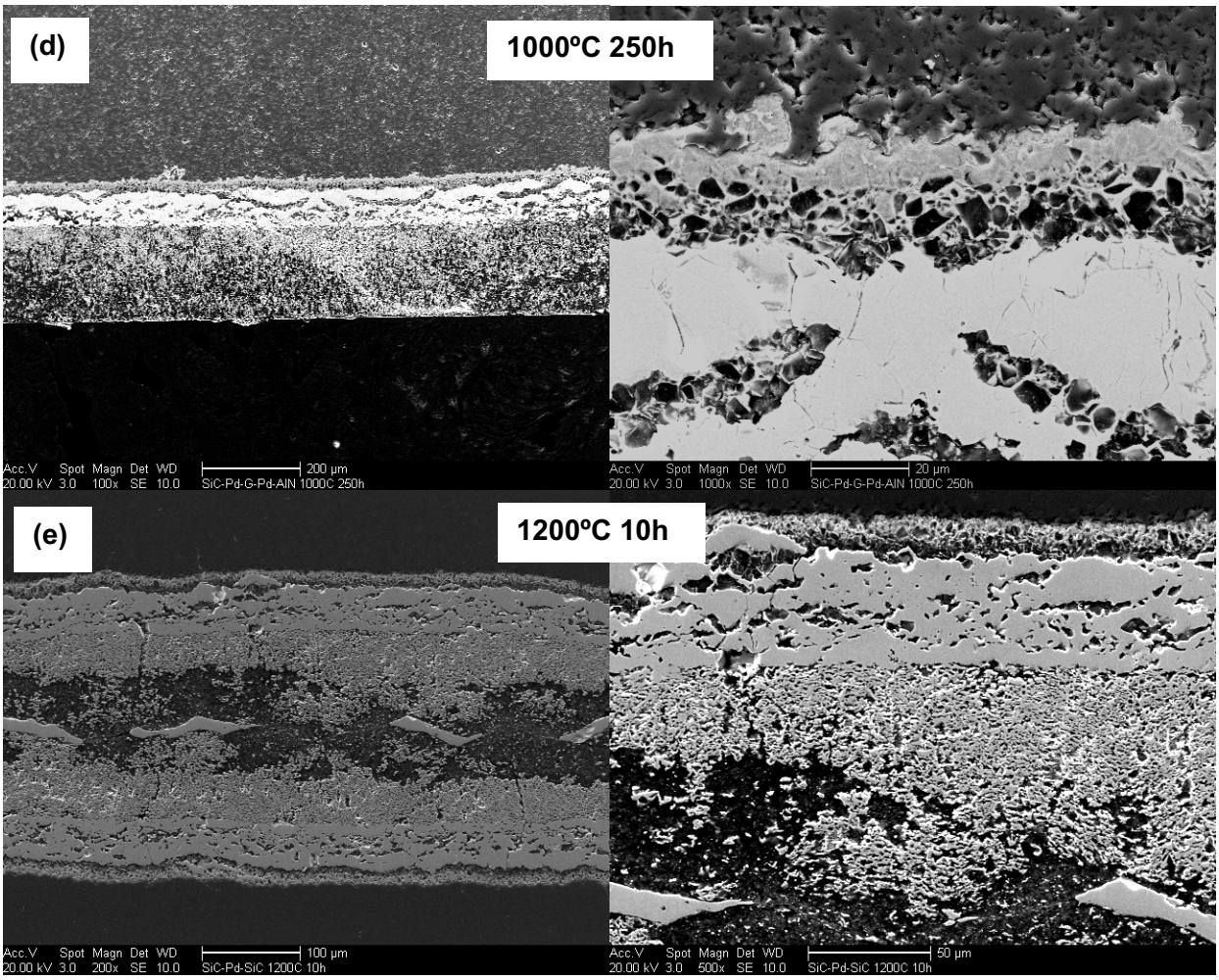

Figure 3.7. Electron micrographs of SiC-Pd interfaces.

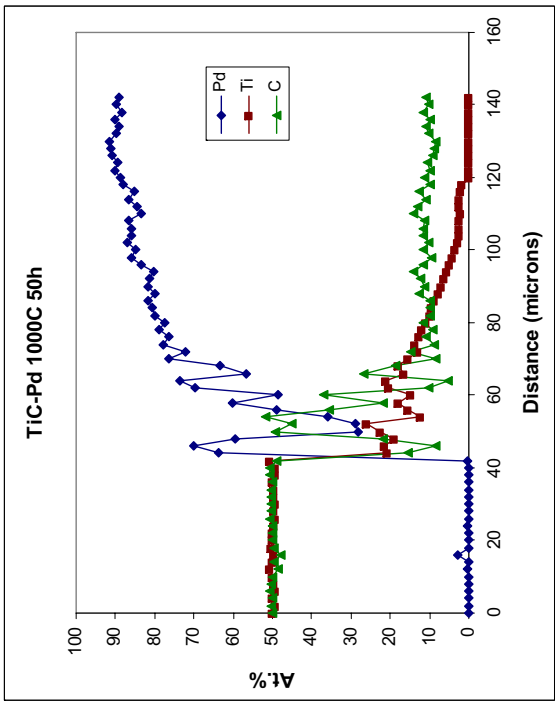
(a)
TiC-Pd 1000C 10h
At.%
Distance (microns)
Pd
Ti
C

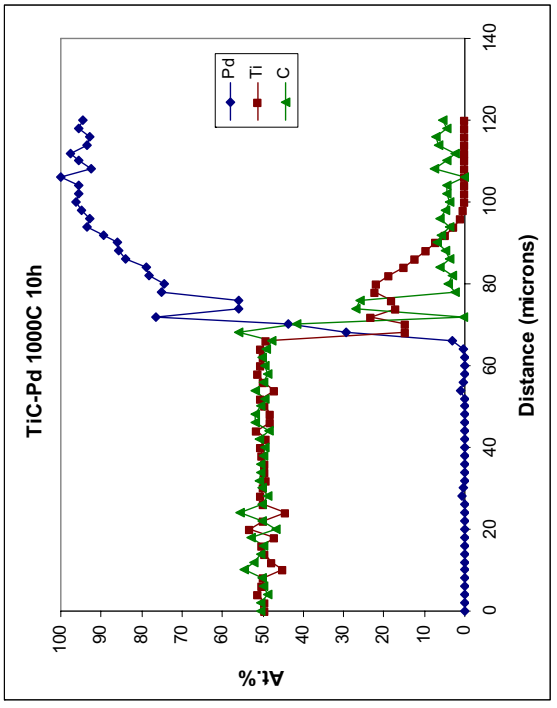
(c)
TiC-Pd 1000C 250h
Pd/Ti 3.3
Pd/Ti 3.4
At.%
Distance (microns)
Pd
Ti
C

(b)
TiC-Pd 1000C 50h
At.%
Distance (microns)
Pd
Ti
C

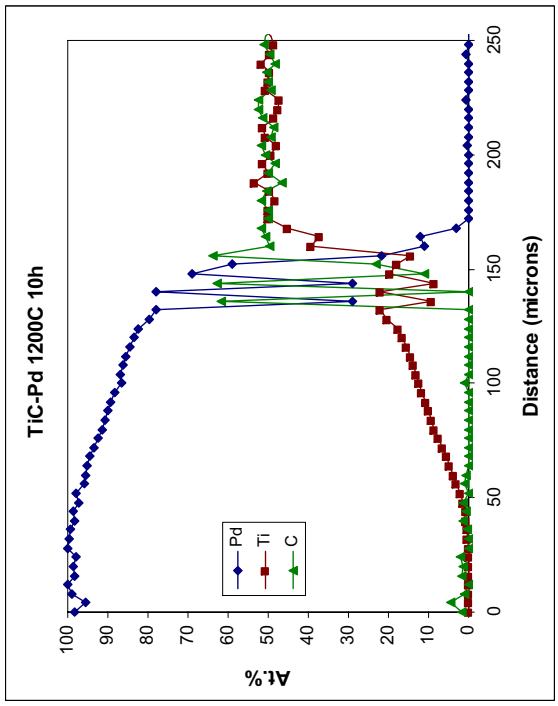
(d)
TiC-Pd 1200C 10h
At.%
Distance (microns)
Pd
Ti
C

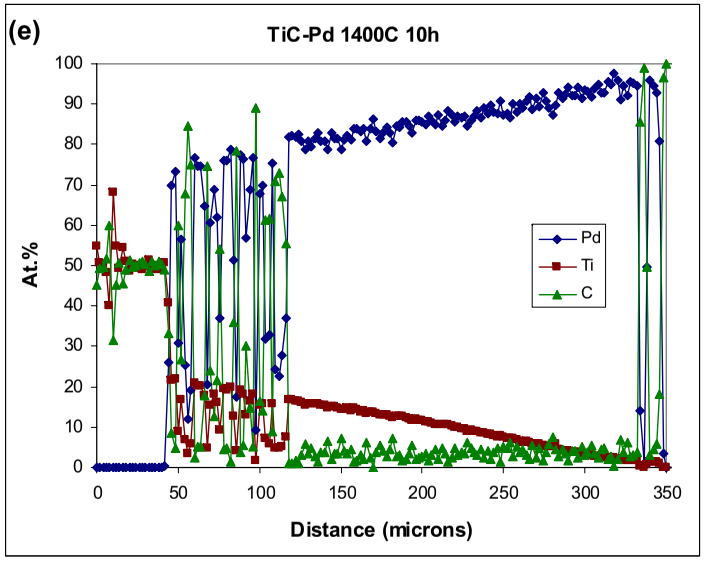

Figure 3.8. EPMA composition line scans of TiC-Pd diffusion couple interfaces.

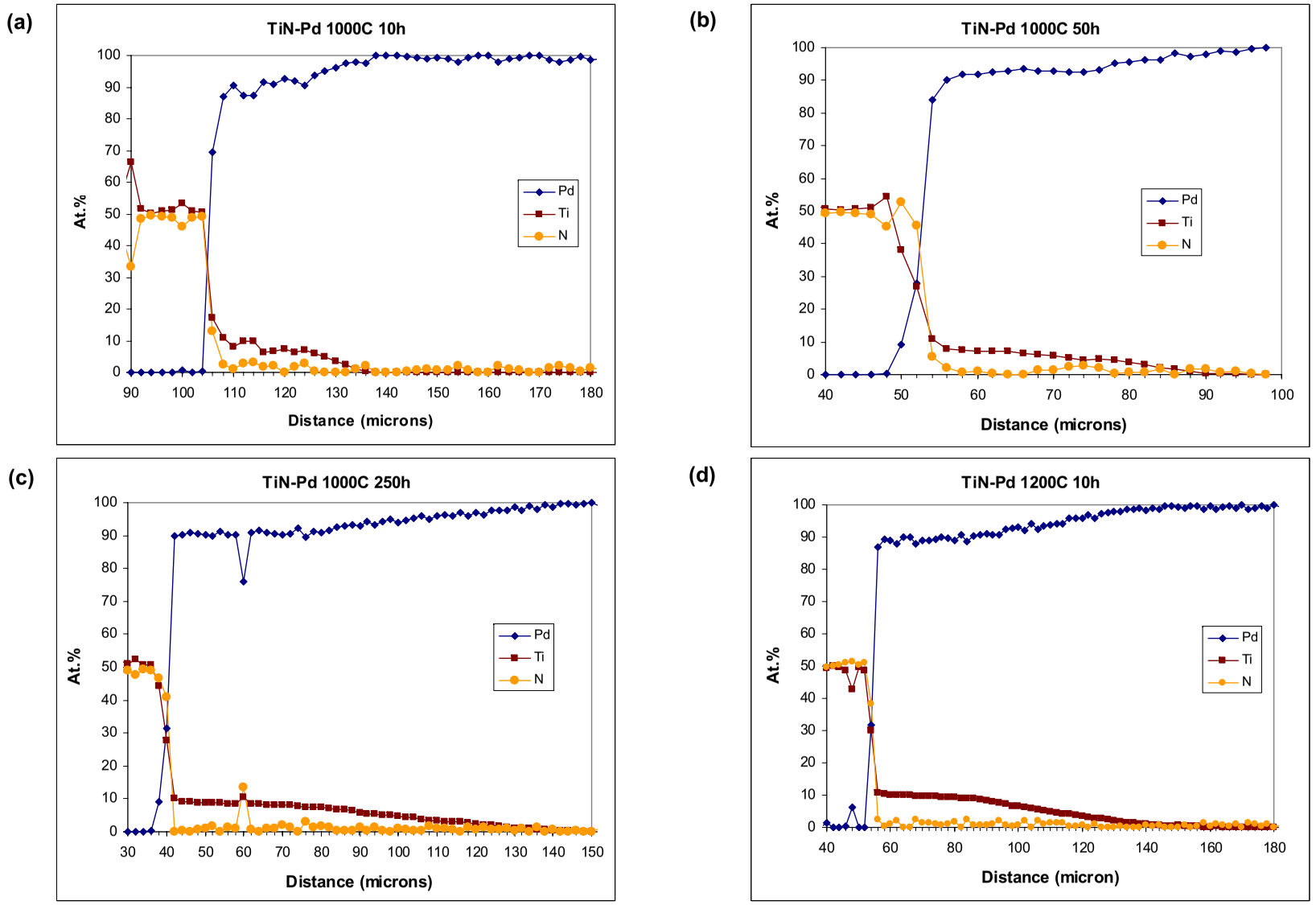

Figure 3.9. EPMA composition line scans of TiN-Pd diffusion couple interfaces.

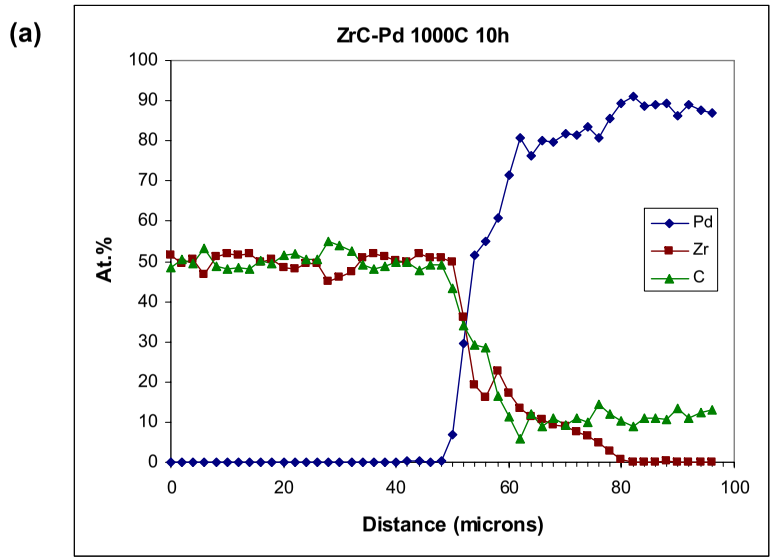
(a)
ZrC-Pd 1000C 10h
At.%
Distance (microns)
Pd
Zr
C

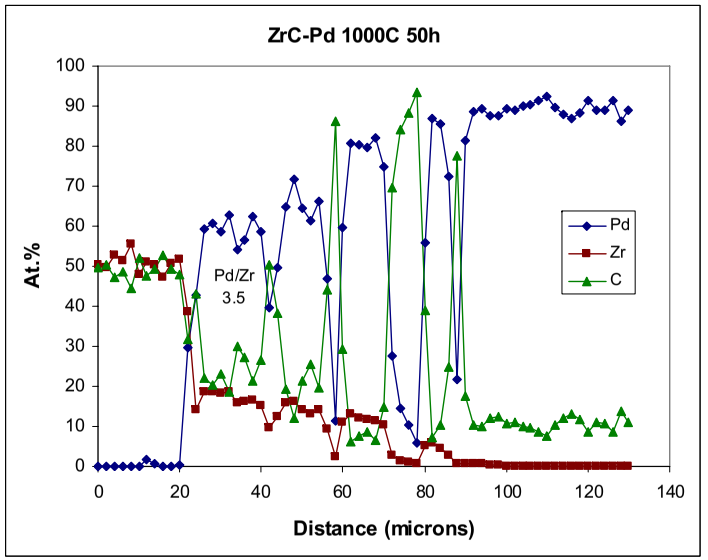
(b)
ZrC-Pd 1000C 50h
At.%
Pd/Zr
3.5
Distance (microns)
Pd
Zr
C

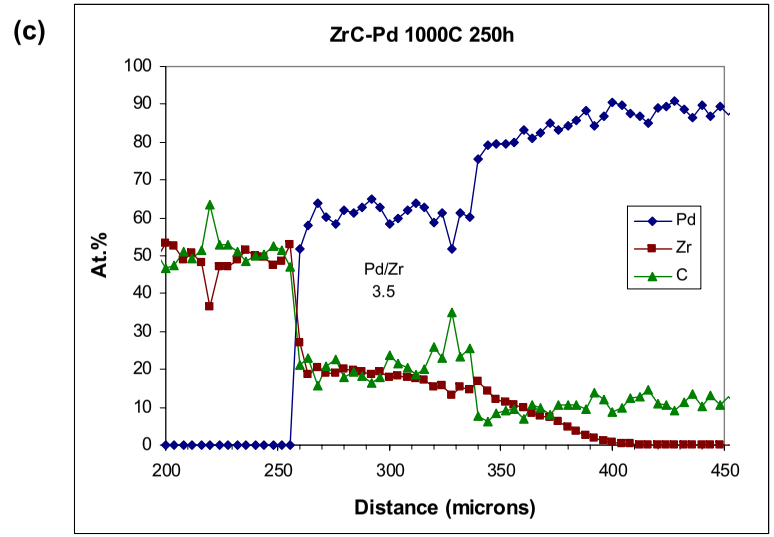
(c)
ZrC-Pd 1000C 250h
At.%
Pd/Zr
3.5
Distance (microns)
Pd
Zr
C

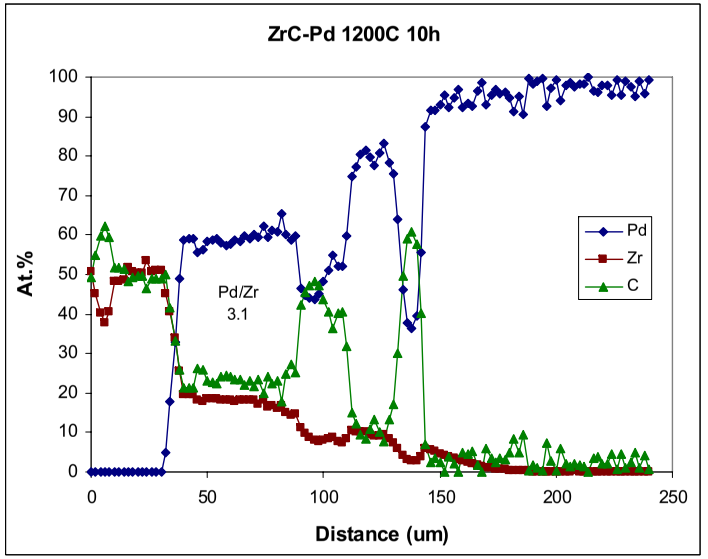
(d)
ZrC-Pd 1200C 10h
At.%
Pd/Zr
3.1
Distance (um)
Pd
Zr
C

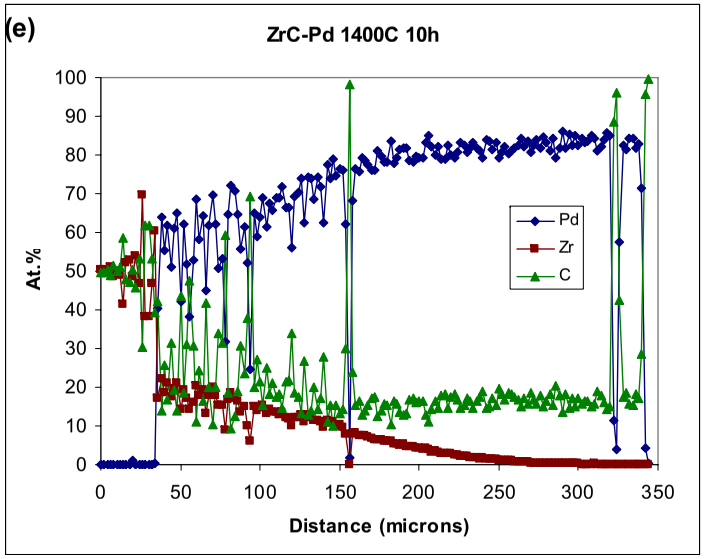

Figure 3.10. EPMA composition line scans of ZrC-Pd diffusion couple interfaces.

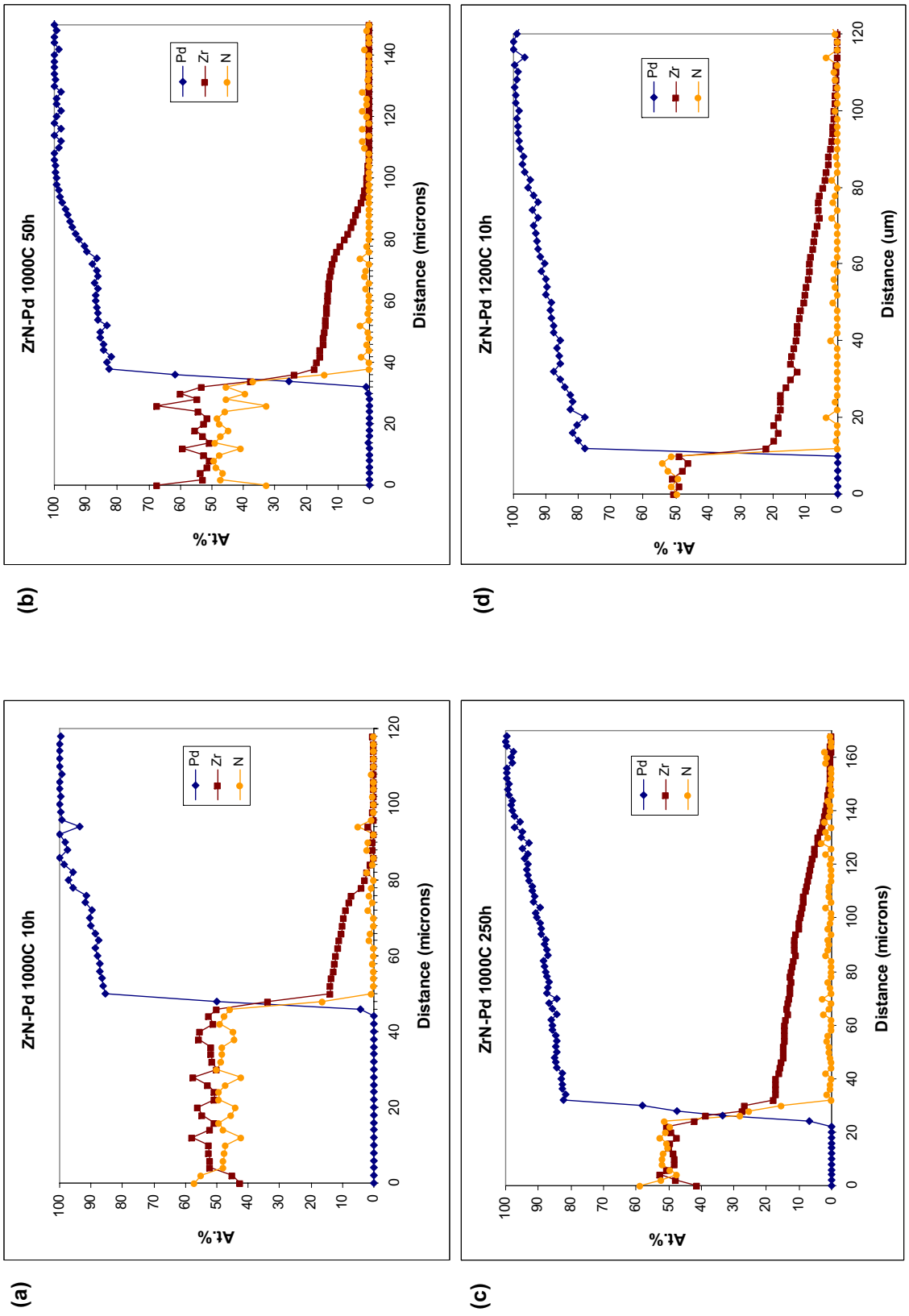

Figure 3.11. EPMA composition line scans of ZrN-Pd diffusion couple interfaces.

3.2.3.1 TiC-Pd. The reaction of palladium with TiC (Figure 3.3) showed the greatest tendency toward infiltration into the grain boundaries. An electron microprobe composition map of a TiC-Pd diffusion couple highlights the movement of Pd into the TiC grain boundaries (Figure 3.12). High magnification images of the heterogeneous reaction zone at the middle of the TiC-Pd interface are shown in Figure 3.13. The backscattered image in particular shows that there are areas of low Z number indicated by darker areas. The most likely explanation for this is free carbon, which would be liberated by the reaction.

$$TiC + xPd = TiPd_x + C, \qquad \text{(Eq. 3.1)}$$

where $TiPd_x$ is an intermetallic phase. The micrographs in Figure 3.13 show that the microstructure in the interaction zone is very fine (features with dimensions at or below 1 μm). From the SEM and EPMA data the TiC-Pd reaction appears to proceed by Pd infiltrating the TiC grain boundaries and reacting with the TiC grains from the outside until they are converted to the reaction products $TiPd_x$ and carbon.

The EPMA composition data (Figure 3.8), in spite of the large amount of variation in the signals due to sample topography and the presence of large intermittent carbon signals, shows that the Pd/Ti ratio in these intermediate regions often falls in the range of 2.7-3.5, which is the approximate composition range for hexagonal $TiPd_3$ (Massalski 1990), suggesting formation of the intermetallic phase.

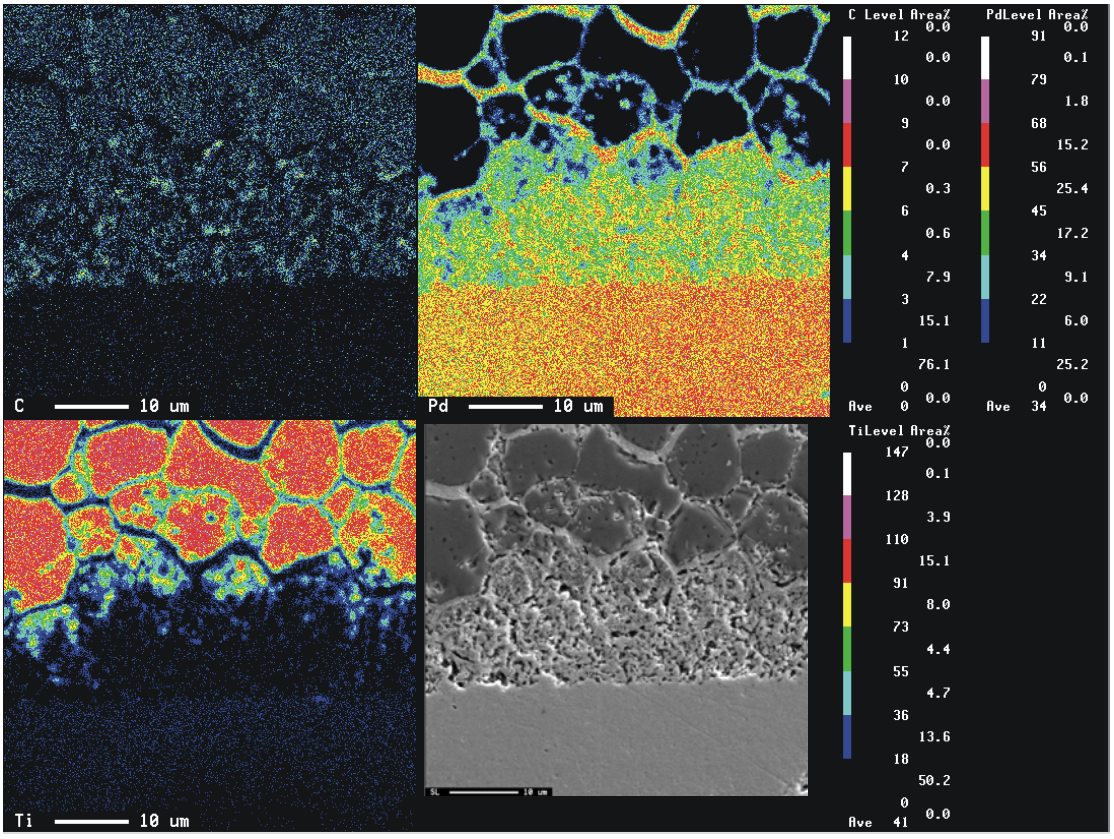

Figure 3.12. EPMA composition maps of a TiC-Pd interface. Sample annealed at 1200ºC for 18h. The secondary electron image is shown at the bottom right.

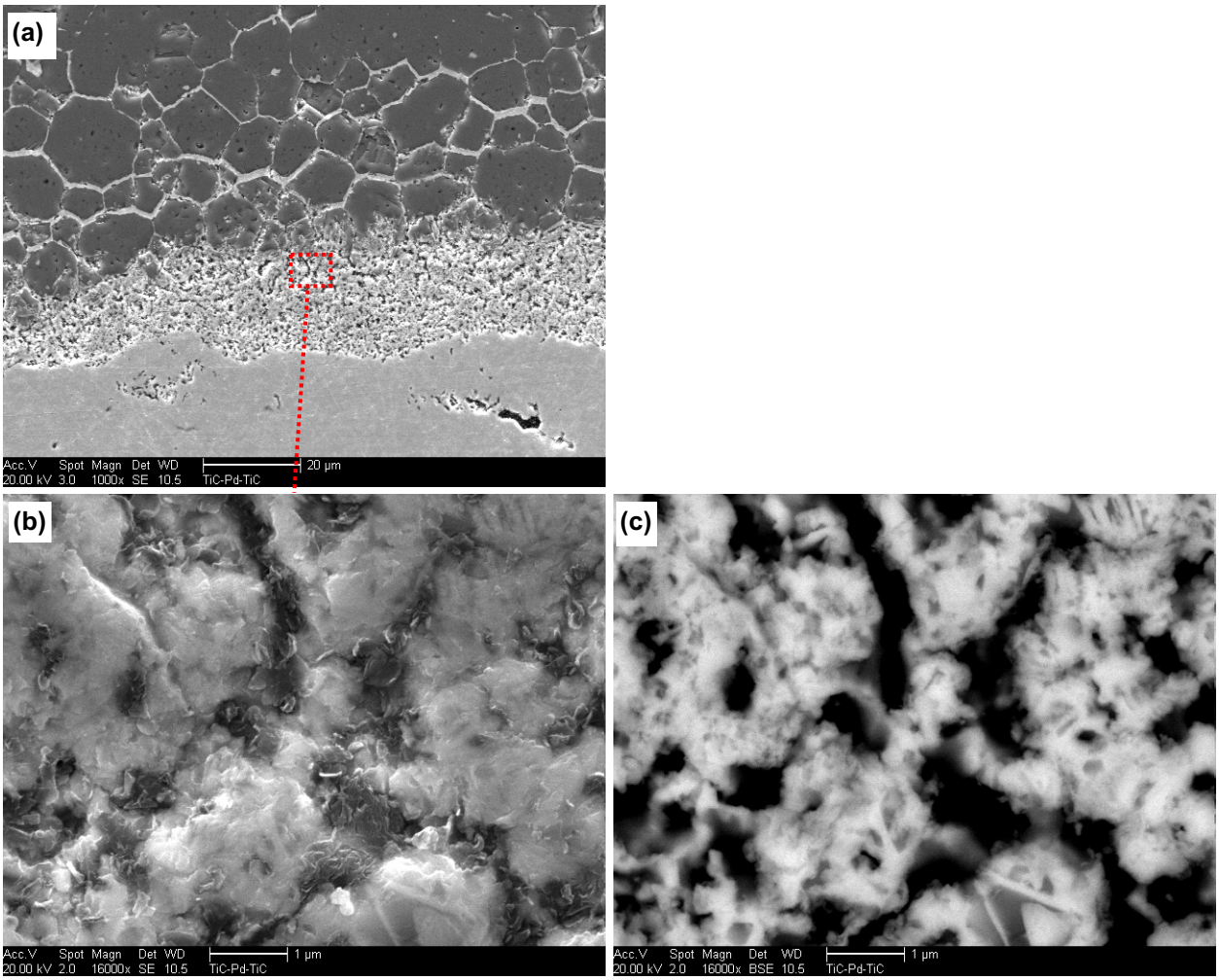

Figure 3.13. High magnification micrograph of the interface between TiC and Pd (annealed 1200ºC for 18h). Micrograph on lower right (c) is a backscattered electron image of region shown in (b).

To examine the TiC-Pd reaction in further detail, TEM samples were prepared as described in Section 3.2.2. The perforated cross-section TEM disk is shown in Figure 3.14, along with the locations of EDS spot analyses that were performed across the diffusion couple. The corresponding values of EDS chemical analyses for the spots shown in Figure 3.14 are given in Table 3.4. Note that only Ti and Pd are included in the analysis (i.e. no carbon is included), so the values effectively give the ratio of Pd to Ti.

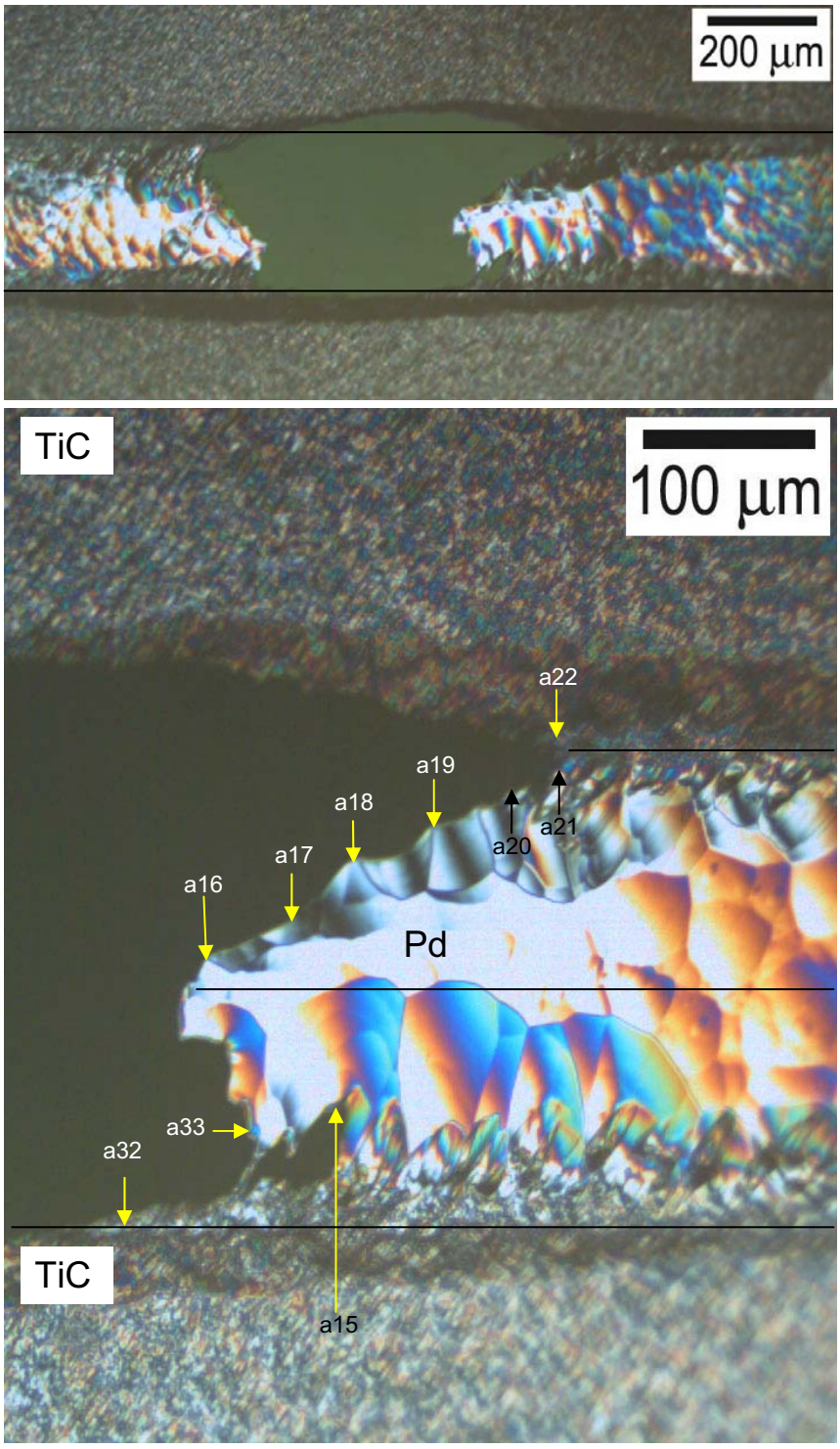

Figure 3.14. Low-resolution optical micrograph of perforated TiC/Pd/TiC cross-section TEM disk (a), and (b) approximate location individual EDS spot analyses listed in Table 3.4.

Table 3.4. TEM EDS spot analysis of TiC-Pd diffusion couple. Locations of spot areas are shown in Figure 3.14.

Area ID	at.% Ti	at.% Pd
a16	7	93
a17	7.6	92.4
a18	12	88
a19	15	85
a20	18.4	81.6
a21	22	78
a22	99.7	0.3
a15	12	88

Detailed microscopic analysis of the interaction zone is shown in Figure 3.15. The analysis revealed the presence of both $TiPd_3$ (determined by EDS composition data and selected area diffraction) and free carbon. The presence of free carbon in this region confirms the general reaction (Eq. 3.1). Note that the carbon regions in the TEM micrographs (Figure 3.15) are similar in dimension to the dark regions in the SEM micrographs [Figure 3.13(b) and (c)].

It should be noted that the $TiPd_3$ phase was an ordered FCC structure ($AuCu_3$ type), instead of the hexagonal ($TiNi_3$) structure. The presence of this phase has been discussed (Massalski 1990). The binary alloy (Ti-Pd) phase diagram (Massalski 1990) indicates that the composition of this FCC $TiPd_3$ phase can contain as much as ~84at.% Pd. The hexagonal $TiPd_3$ phase was not observed in this sample by TEM.

An analysis of the sample microstructure further into the bulk TiC (~5-10 μm from the TiC/Pd interface, showed the presence of $TiPd_3$ forming at the grain boundary triple points with free carbon nearby (Figure 3.16). Again, only the ordered FCC $TiPd_3$ was found, instead of the hexagonal phase. This demonstrates the ability of Pd to diffuse into the TiC grain boundaries, even beyond the extent visible in the scanning electron micrographs (Figure 3.3), and that $TiPd_3$ is formed in an environment with a large excess of TiC.

It is interesting to note that a separate experiment using a different source of TiC revealed the same tendency for intergranular attack of Pd on TiC. In this simple experiment, titanium carbide powder particles were embedded in a matrix of Pd powder and annealed at various times and temperatures. Figure 3.17 shows a TiC particle after reaction with Pd at 800ºC for 10 hours (the Pd powder matrix has completely densified under these conditions). The infiltration of Pd into the TiC grain boundaries of the particle can be clearly seen. The implication is that the grain boundary attack observed for the diffusion couples was not due solely to the properties of the particular hot-pressed TiC ceramic used.

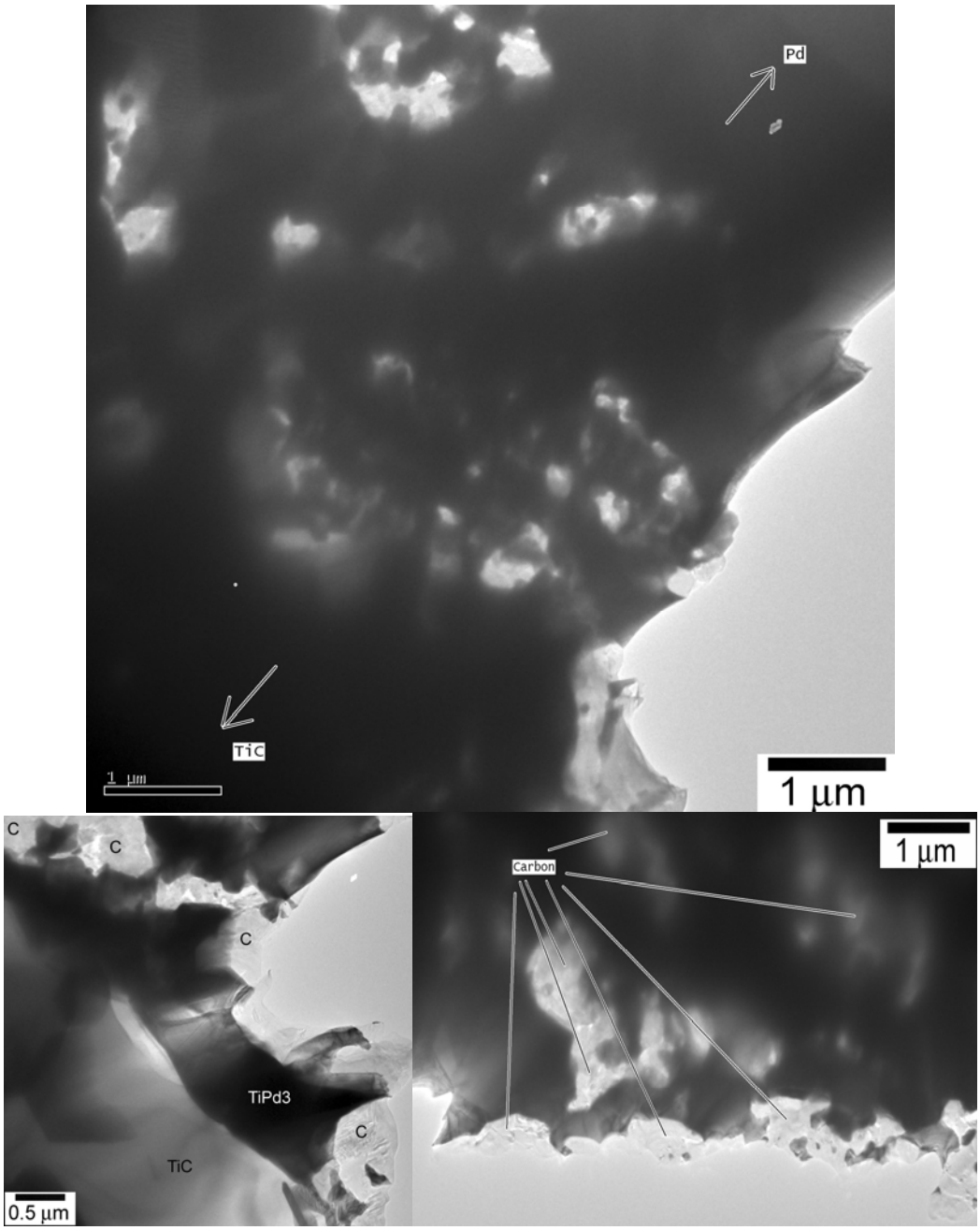

Figure 3.15. TEM micrographs of the TiC-Pd reaction layer. Both free carbon and $TiPd_3$ were identified in this region.

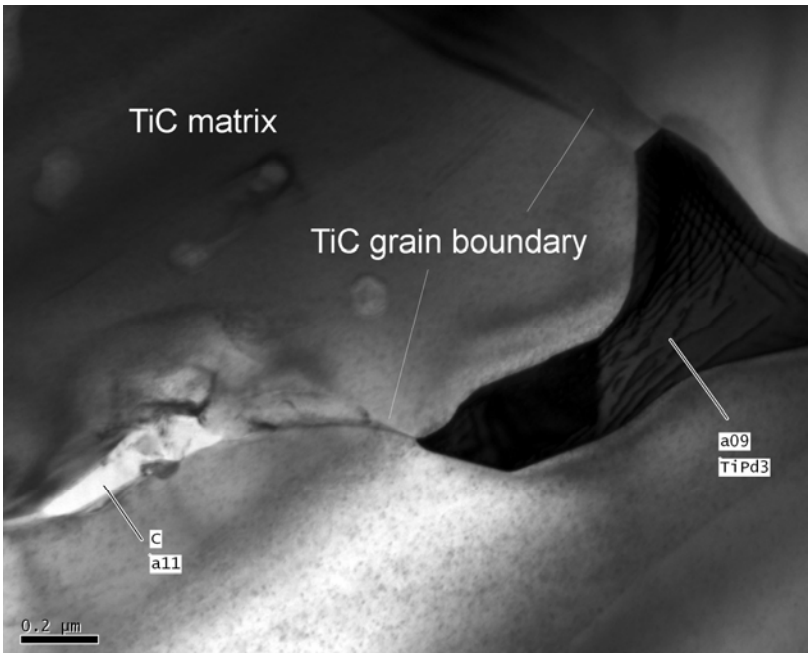

Figure 3.16. TEM micrograph taken in the TiC phase at a distance of approximately 5-10 microns from the TiC-Pd interface $TiPd_3$ and carbon are seen forming at a grain boundary triple point.

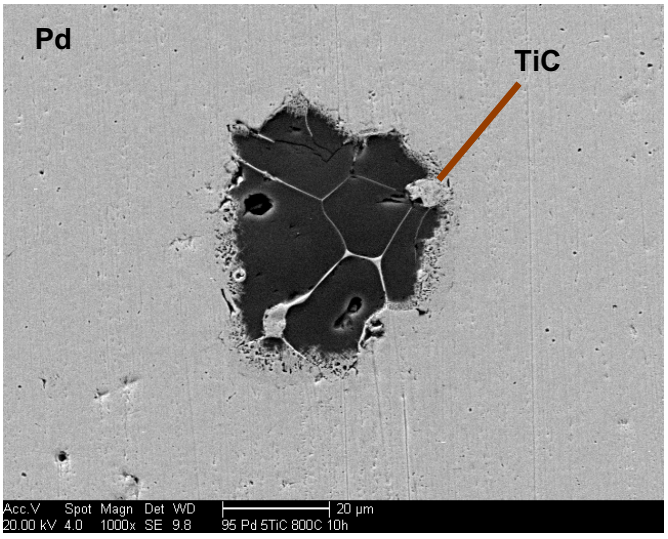

Figure 3.17. TiC particle embedded in Pd matrix and annealed at 800ºC for 10 hours. Note infiltration of Pd into the TiC particle grain boundaries.

3.2.3.2 TiN-Pd. The TiN-Pd interactions (Figure 3.4) did not exhibit the same heterogeneous reaction zone as the TiC samples. Instead, the reacted interface was rather abrupt, transitioning from what appears to be the pure TiN ceramic to the Pd foil. Palladium migration into the TiN grain boundaries was not observed until an annealing temperature of 1400ºC [Figure 3.4(e)]. At this temperature the Pd foil appears to have been partially extruded out from the diffusion couple, as little remains in the sample.

The EPMA line composition data (Figure 3.9) shows that the TiN is unaltered by the reaction, with no Pd observed in the ceramic phase. The Pd film usually contains a significant amount of Ti in solid

solution, in amounts as high as ~11at.% near the TiN-Pd interface, and decreasing with increasing distance from the interface. Unlike the TiC-Pd EPMA data, there was no indication from the compositions in the interaction zone that there was a phase with a composition of $TiPd_3$ or the ordered FCC structure, since the maximum Ti concentration at the boundary appears to be too low.

As with the TiC-Pd diffusion couple, a TEM sample was prepared and analyzed as described in Section 3.2.2 to further examine the formation of phases at the interaction zone. Figure 3.18 shows the perforated interface cross-section with selected spots for EDS analysis. Results of EDS analysis are given in Table 3.5 (carbon not included in the analysis). The TEM EDS results give higher values of Ti content in the Pd(Ti) film versus the EPMA line scan data, and suggest the presence of $TiPd_3$ near the interace. High resolution micrographs of the interface indicate that $TiPd_3$ and $TiPd_4$ crystalline phases are present immediately adjacent to TiN (Figure 3.19). Certain amorphous Ti-Pd phases were also observed near the interface (Ti_2Pd, $TiPd_4$). Upon further examination these were found to in fact be nanocrystalline phases, with diffraction ring patterns from the crystalline portion corresponding to palladium.

High-Order Laue Zone (HOLZ) patterns were measured across the Pd film to observe changes in the Pd(Ti) solid solution lattice parameter with different composition. The results showed no observable lattice parameter change (the method is sensitive to lattice constant changes of 0.2%). This is consistent with the available literature data that indicate only an extremely small change in lattice parameter of Pd when Ti is substituted into the lattice (only a ~0.1% change in lattice constant *a* when Ti content is increased from 0 to 15at.%) (Ellner 2004).

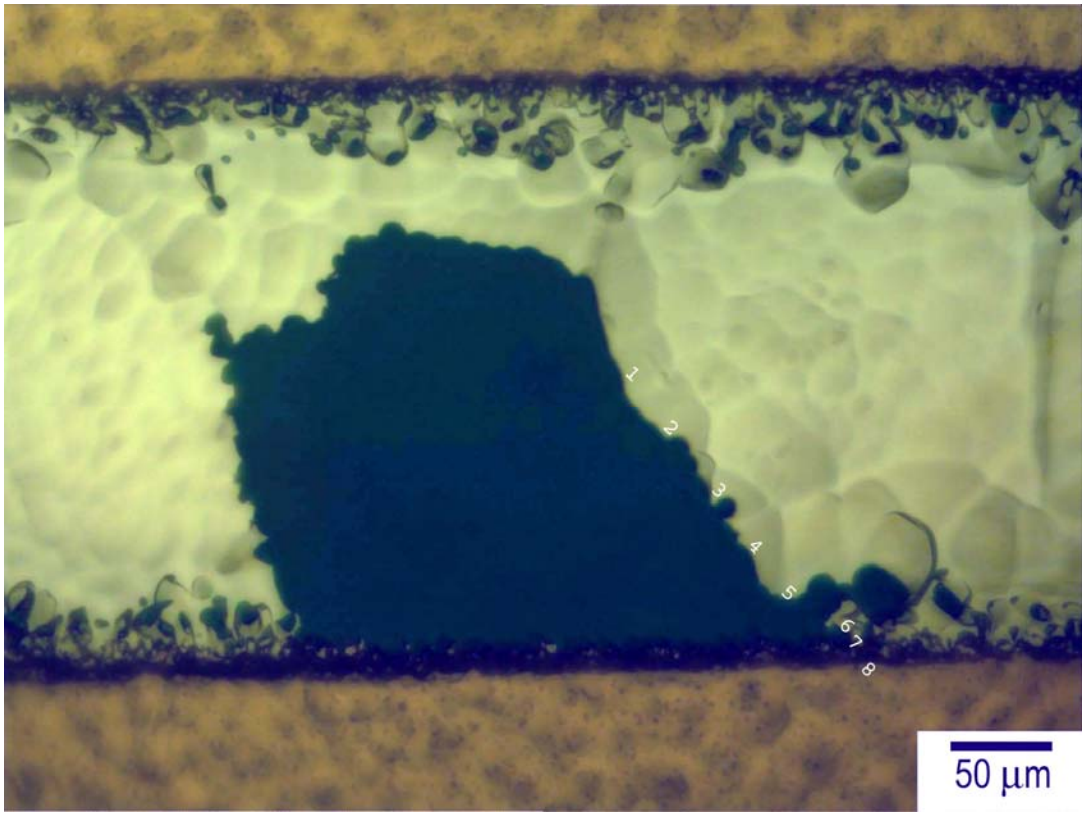

Figure 3.18. TiN-Pd (1200ºC-10h) cross-section prepared for TEM analysis. Locations of EDS spot analyses are shown by numerals.

Table 3.5. Ti and Pd compositions at selected analysis spots on TiN-Pd interface determined by EDS analysis using the TEM. Note that only Ti and Pd are included in the analysis (carbon is not included). Area numbers are shown on Figure 3.18.

Area ID	at.% Ti	at.% Pd
1	7.7	92.3
2	8.5	91.5
3	9.8	90.2
4	13.1	86.9
5	16.8	83.2
6	24.4	75.6
7	73.3	26.7
8	80.1	19.9

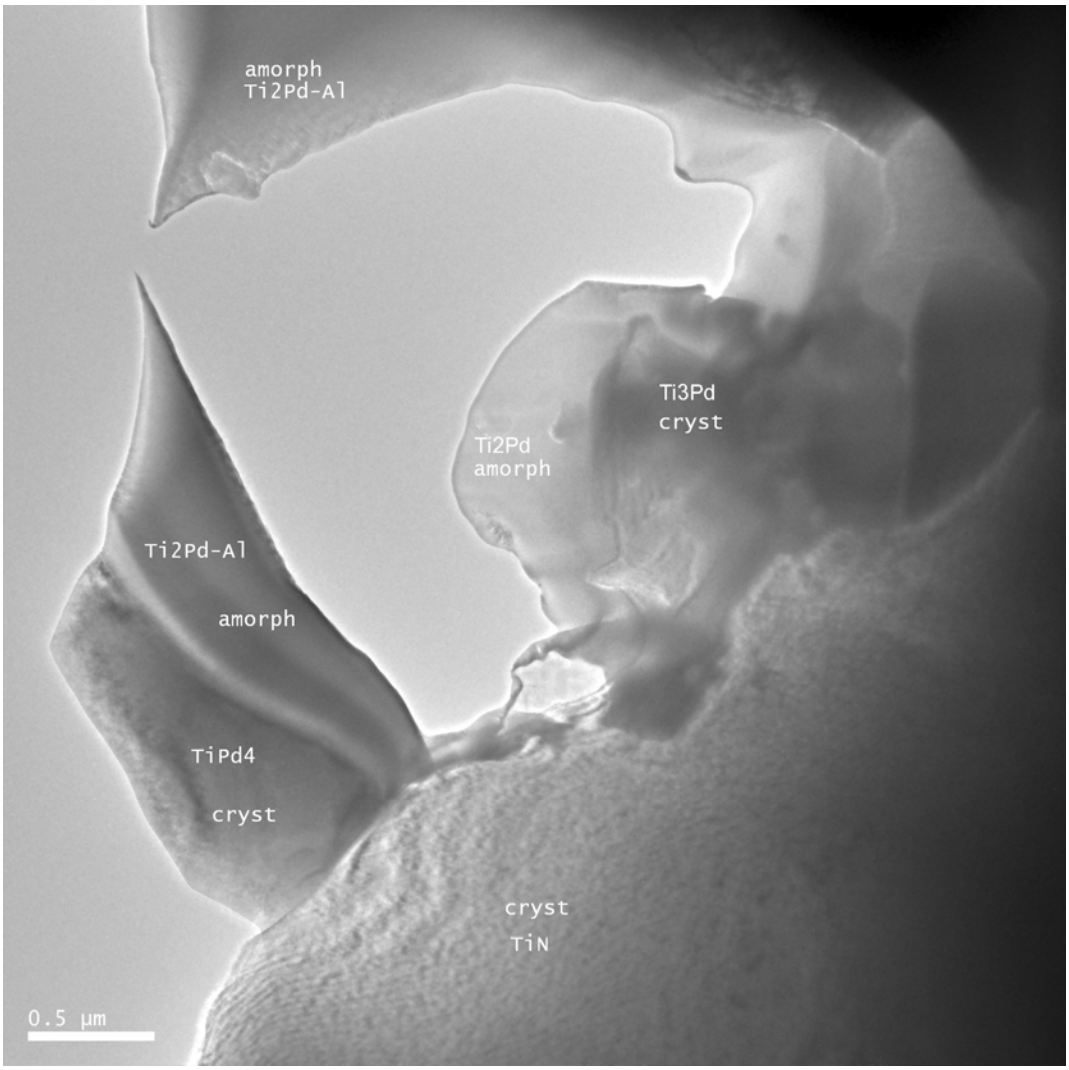

Figure 3.19. High resolution micrographs at the TiN-Pd interface annealed at 1200ºC for 10h.

3.2.3.3 ZrC-Pd. The ZrC-Pd interfaces in general exhibited a similar behavior to the TiC-Pd interfaces; namely, the tendency to form heterogeneous intermediate regions in the interaction zone (Figure 3.5). This could be due to a similar reaction mechanism as the TiC samples (i.e. the formation of free carbon by a reaction similar to that shown in Eq. 3.1).

A peculiar observation that was more or less unique to the ZrC-Pd samples was the formation of localized reaction zones, with the remainder of the interface exhibiting a separation between the ZrC and Pd layers and consequently little or no reaction [Figure 3.5(b)]. The favored explanation for this behavior is that there is a volume expansion in the ZrC-Pd reaction products, either because of larger molar volumes of the phases or from the formation of closed pores. The result is that close initial contact between the ZrC and Pd at a few points across the facing surfaces results in reaction, and the blisters that form tend to push apart the two surfaces due to the volume expansion. This behavior was also observed in the ZrN-Pd 1000ºC-10h sample [Figure 3.6(a)] and the TiN-Pd 1000ºC-50h sample [Figure 3.4(b)]. It is possible that this is related to the fact that a solid solution zirconium in palladium, Pd(Zr), exhibits a volume expansion with increasing Zr content (lattice constant *a* increases ~1.7% with Zr content increase from 0 to 18%) (Ellner 2004). However, this would not explain the observation for the TiN-Pd 1000ºC-50h

Some intergranular attack was observed in the ZrC-Pd samples (see Figure 3.20), although not to the same extent as in the TiC-Pd reactions.

The EPMA composition line scans of several ZrC-Pd samples suggest that the reaction product was the intermetallic phase $ZrPd_3$ (1000ºC-250h and 1200ºC-10h samples; see Figure 3.10).

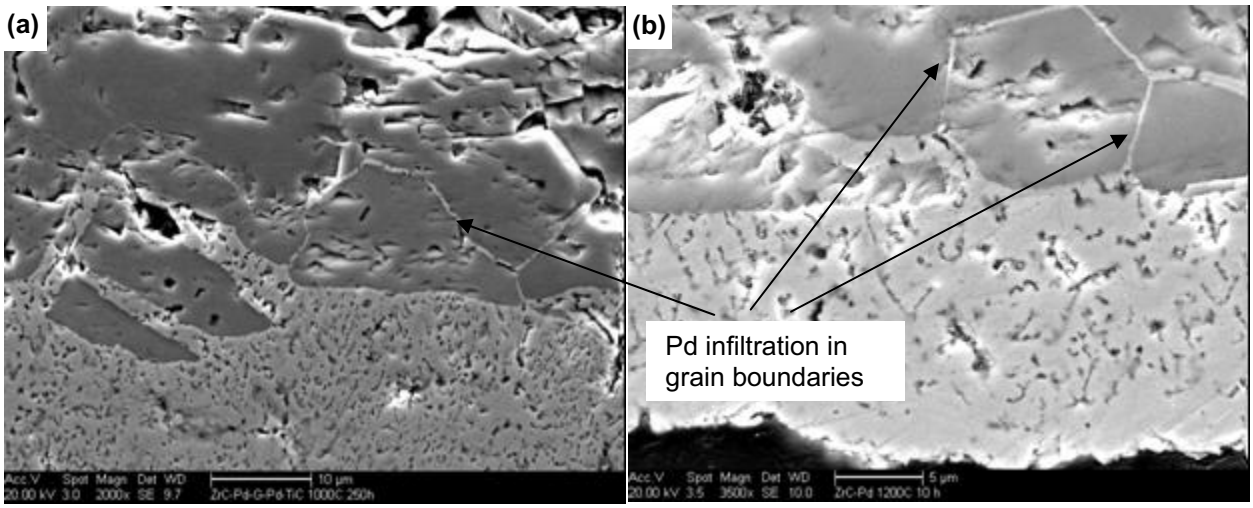

Figure 3.20. Migration palladium into ZrC grain boundaries. ZrC-Pd diffusion couples annealed at (a) 1000ºC for 250h and (b) 1200ºC for 10h.

3.2.3.4 ZrN-Pd. As with the TiN-Pd diffusion couples, the ZrN-Pd interfaces did not have the heterogeneous interface region seen in the TiC-Pd and ZrC-Pd samples, but an abrupt transition from ZrN to Pd(Zr). The EPMA line scan data show that the Pd side of the interface consists of a Pd(Zr) solid solution with Zr contents as high as ~20at.% near the interface. As with the TiN-Pd sample, these data suggest that no intermetallic phases formed at the interface, but that the ZrN phase was consumed by reaction with Pd to form Pd(Zr).

No TEM analysis on ZrN-Pd diffusion interfaces was performed, but it should be noted that unlike the Ti-Pd system, the formation of ordered FCC Pd(Zr) structures have not been observed (Massalski 1990).

3.2.3.5 SiC-Pd. The SiC-Pd diffusion couples exhibited much more extensive reaction with Pd than any of the other ceramics (Figure 3.7). Note that the 1000ºC-10h sample showed reaction through the entire width of the original Pd foil. The large amount of finely mixed phases in the reaction zone and the apparent topography of this region resulted in EPMA line scan data (not shown) that had a large amount of scatter and was difficult to interpret. The microstructural features and separate phase regions were often smaller than the microprobe interaction volume, making definitive measurement of phase compositions difficult.

3.2.4 Rh Diffusion Couples

Micrographs of the Rh diffusion couples at different annealing times and temperatures are given in Figures 3.21–3.25. The Rh diffusion couples followed the general trend of a lower reactivity than that of the Pd couples. These interfaces were taken to higher temperatures and nonetheless often showed thinner reaction layers than with the Pd couples. There was also much less tendency to produce the heterogeneous intermediate phase that was observed in carbide-Pd interface reactions. Instead, the systems showed a greater tendency to form distinct layers that appear to be near-stoichiometric intermetallic phases, based on microprobe composition analysis. EPMA line scan data for the Rh diffusion couples are shown in Figures 3.26–3.30. Key observations and discussions for each specific ceramic are given in the following sections.

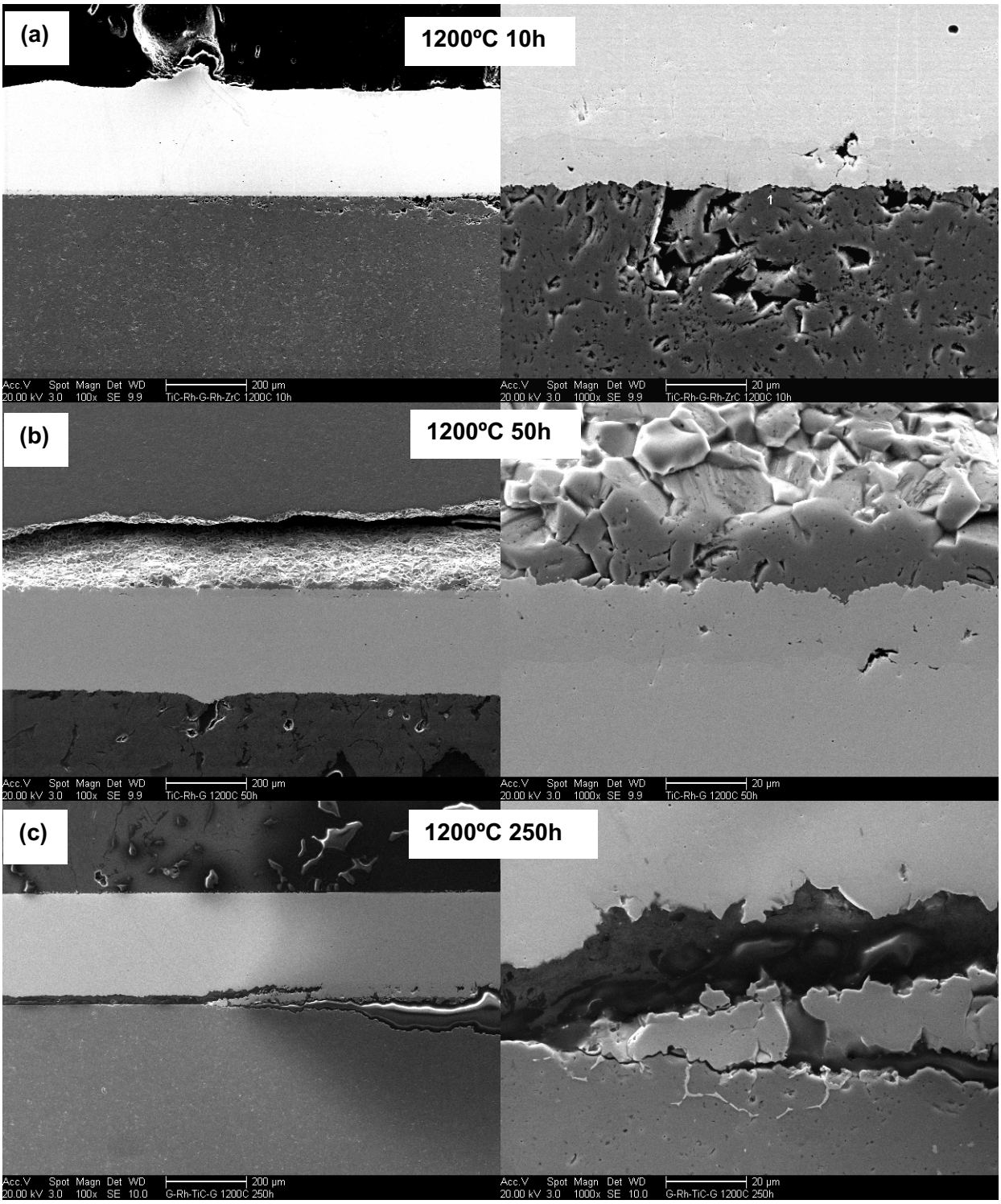
(a)
1200ºC 10h
Acc.V Spot Magn Det WD 200 µm
20.00 kV 3.0 100x SE 9.9 TiC-Rh-G-Rh-ZrC 1200C 10h
Acc.V Spot Magn Det WD 20 µm
20.00 kV 3.0 1000x SE 9.9 TiC-Rh-G-Rh-ZrC 1200C 10h
(b)
1200ºC 50h
Acc.V Spot Magn Det WD 200 µm
20.00 kV 3.0 100x SE 9.9 TiC-Rh-G 1200C 50h
Acc.V Spot Magn Det WD 20 µm
20.00 kV 3.0 1000x SE 9.9 TiC-Rh-G 1200C 50h
(c)
1200ºC 250h
Acc.V Spot Magn Det WD 200 µm
20.00 kV 3.0 100x SE 10.0 G-Rh-TiC-G 1200C 250h
Acc.V Spot Magn Det WD 20 µm
20.00 kV 3.0 1000x SE 10.0 G-Rh-TiC-G 1200C 250h

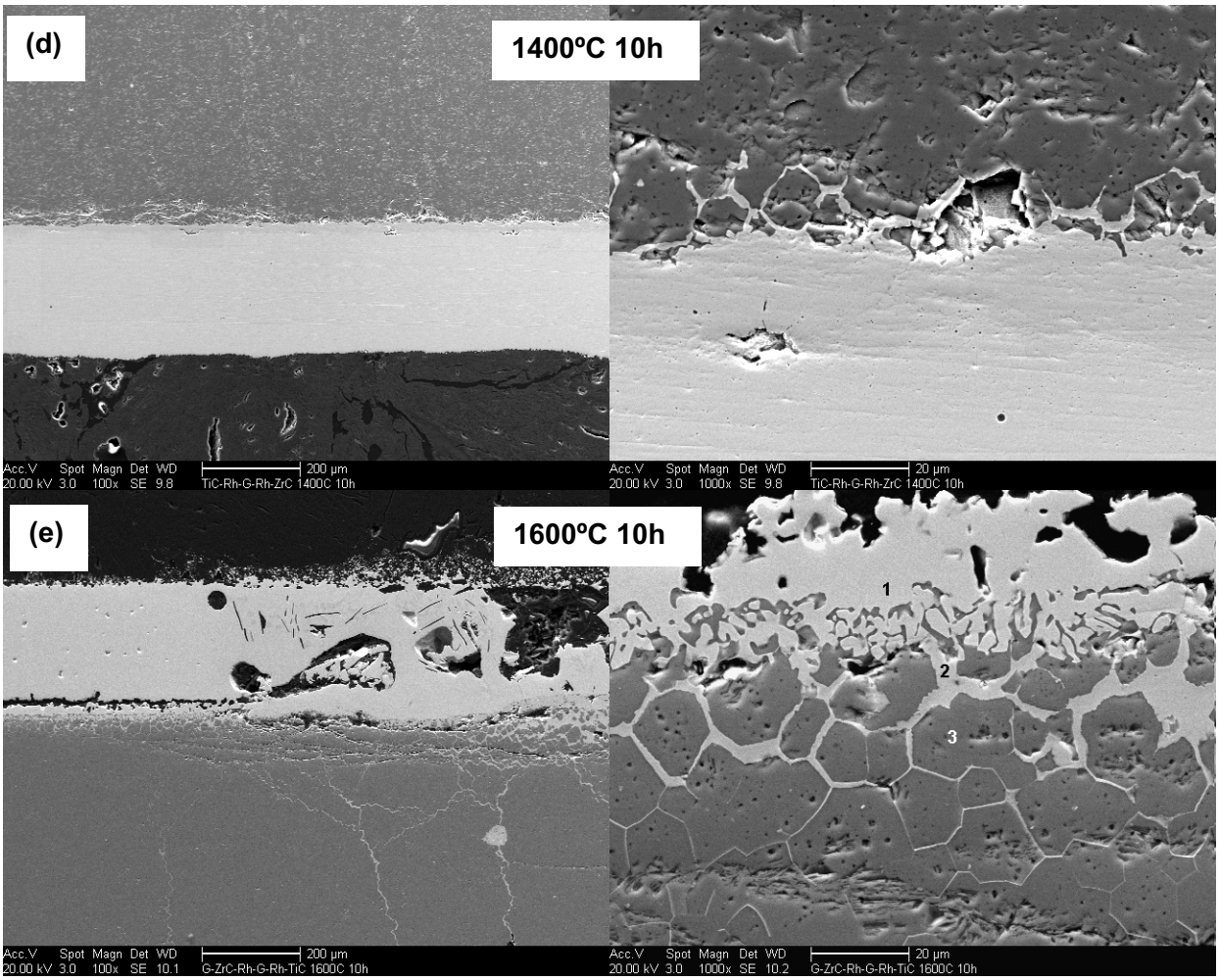

Figure 3.21. Electron micrographs of TiC-Rh interfaces.

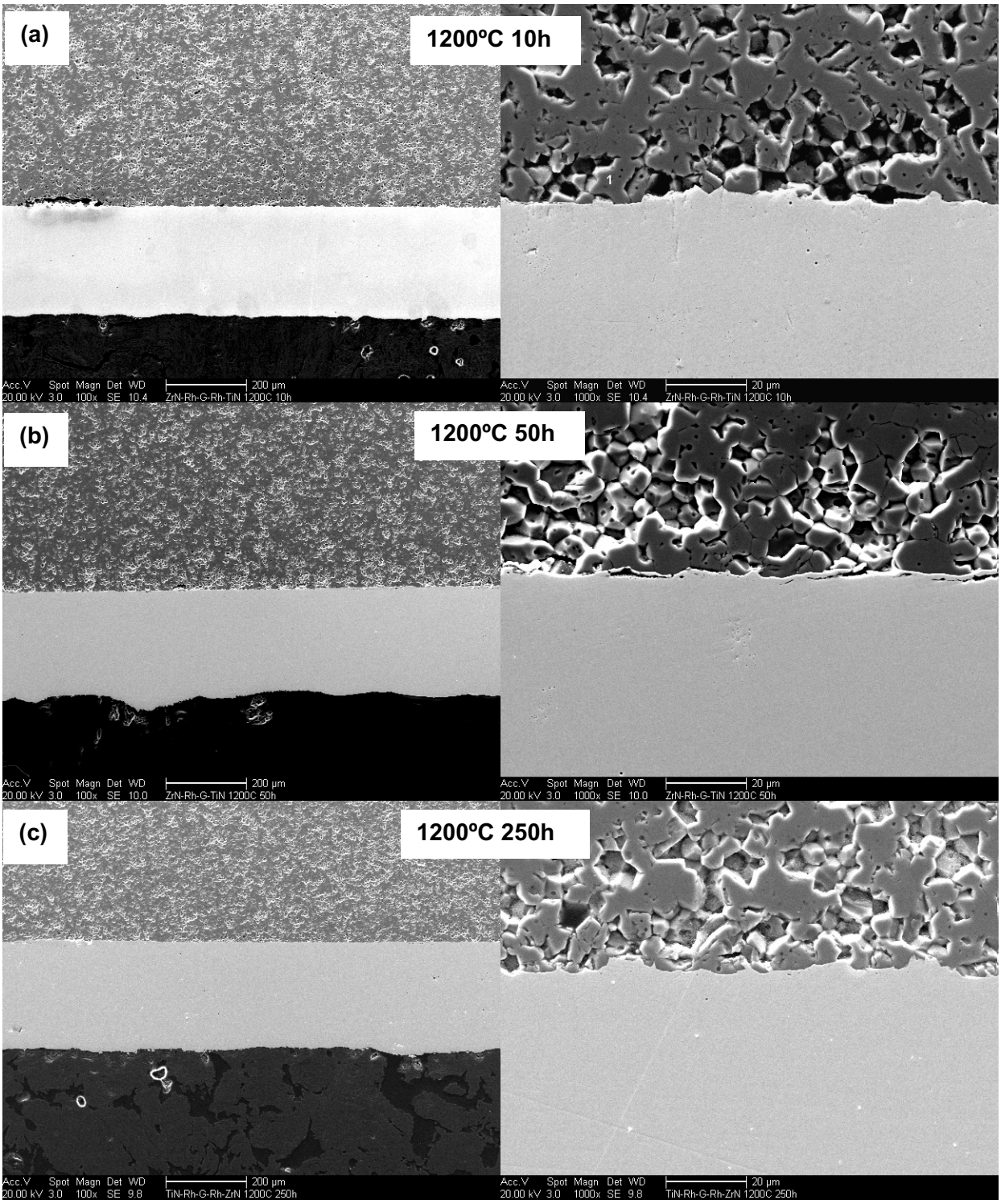
(a)
1200ºC 10h
Acc.V Spot Magn Det WD 200 µm
20.00 kV 3.0 100x SE 10.4 ZrN-Rh-G-Rh-TiN 1200C 10h
Acc.V Spot Magn Det WD 20 µm
20.00 kV 3.0 1000x SE 10.4 ZrN-Rh-G-Rh-TiN 1200C 10h
(b)
1200ºC 50h
Acc.V Spot Magn Det WD 200 µm
20.00 kV 3.0 100x SE 10.0 ZrN-Rh-G-TiN 1200C 50h
Acc.V Spot Magn Det WD 20 µm
20.00 kV 3.0 1000x SE 10.0 ZrN-Rh-G-TiN 1200C 50h
(c)
1200ºC 250h
Acc.V Spot Magn Det WD 200 µm
20.00 kV 3.0 100x SE 9.8 TiN-Rh-G-Rh-ZrN 1200C 250h
Acc.V Spot Magn Det WD 20 µm
20.00 kV 3.0 1000x SE 9.8 TiN-Rh-G-Rh-ZrN 1200C 250h

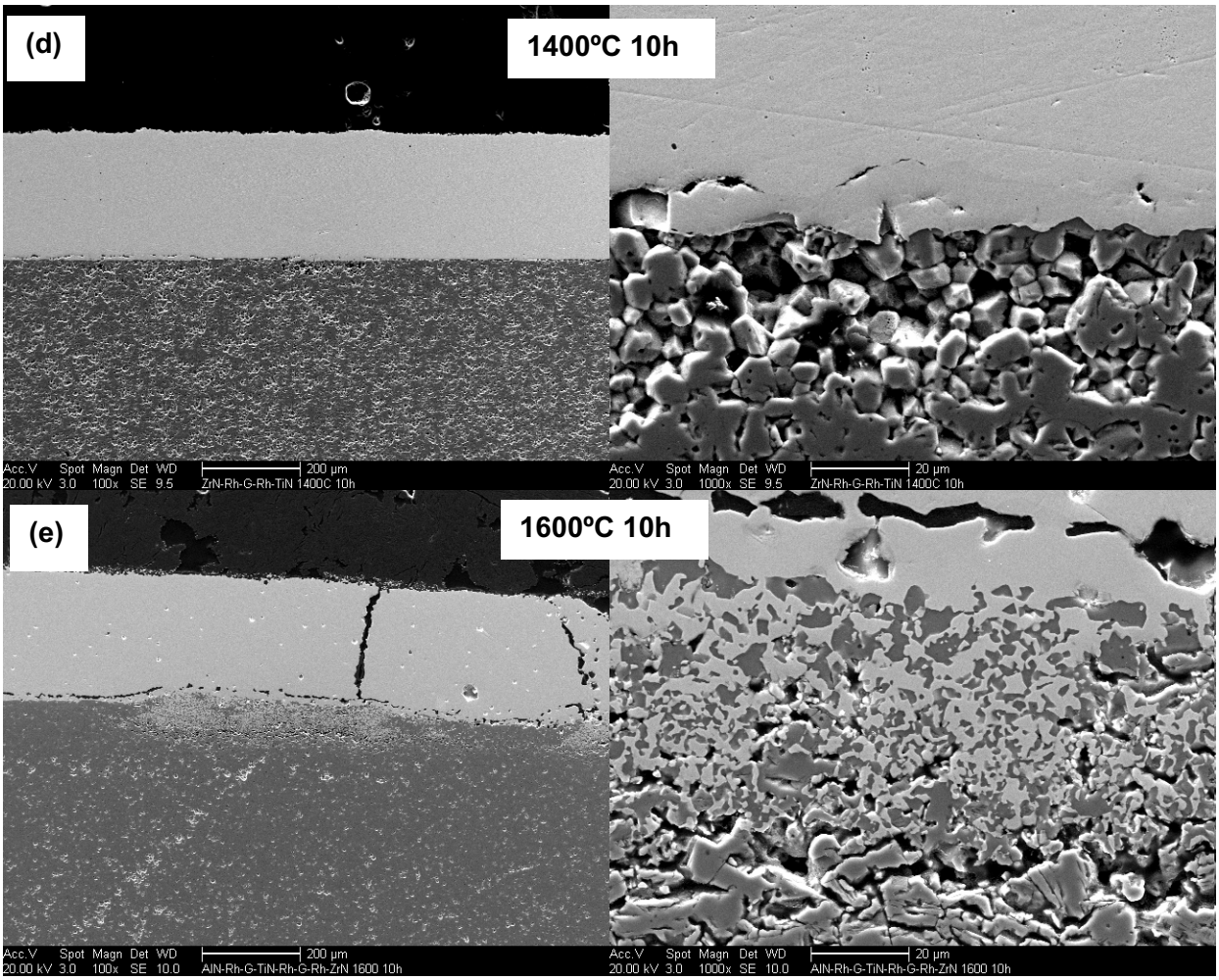

Figure 3.22. Electron micrographs of TiN-Rh interfaces.

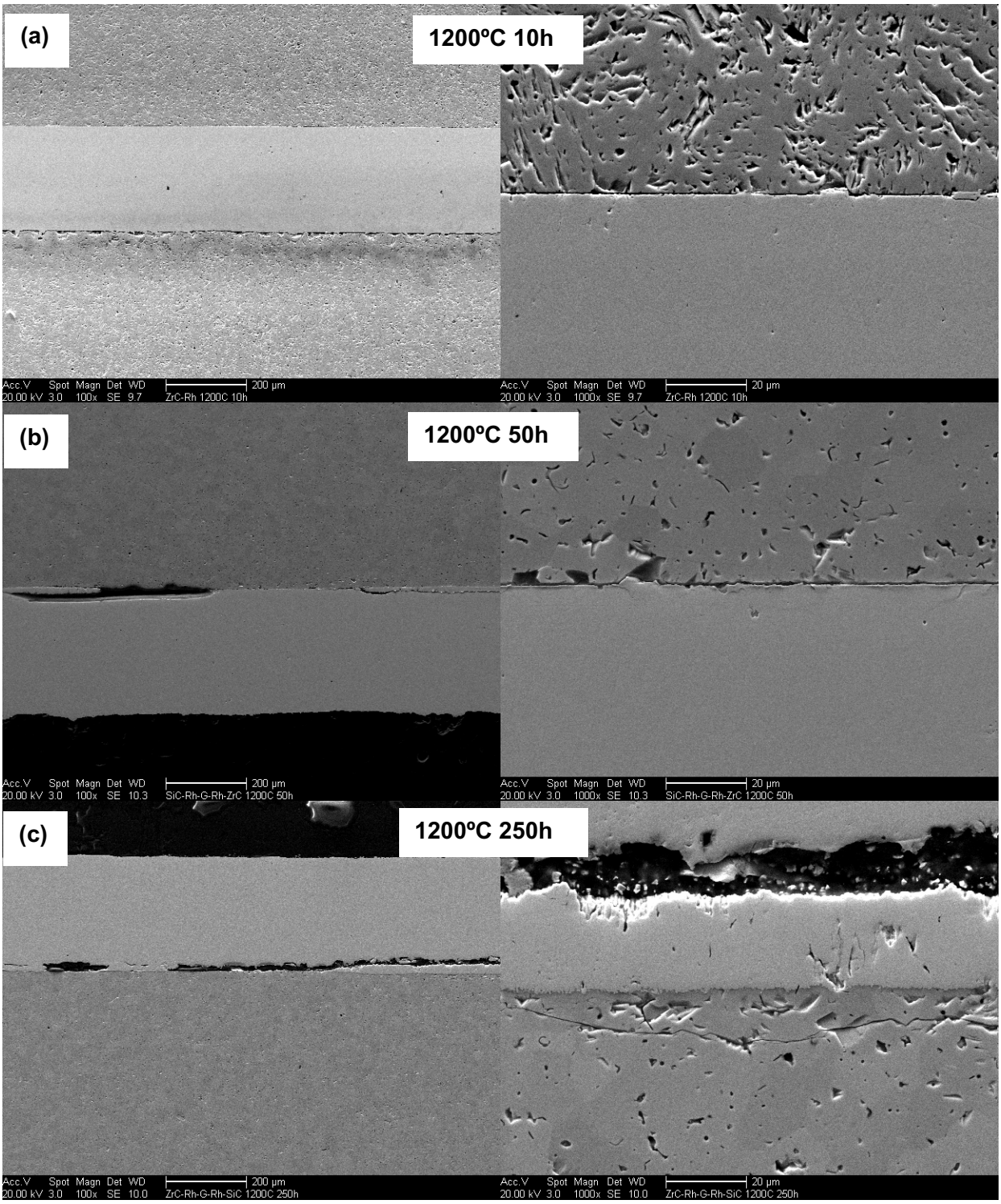
(a)
1200ºC 10h
Acc.V Spot Magn Det WD 200 µm
20.00 kV 3.0 100x SE 9.7 ZrC-Rh 1200C 10h
Acc.V Spot Magn Det WD 20 µm
20.00 kV 3.0 1000x SE 9.7 ZrC-Rh 1200C 10h
(b)
1200ºC 50h
Acc.V Spot Magn Det WD 200 µm
20.00 kV 3.0 100x SE 10.3 SiC-Rh-G-Rh-ZrC 1200C 50h
Acc.V Spot Magn Det WD 20 µm
20.00 kV 3.0 1000x SE 10.3 SiC-Rh-G-Rh-ZrC 1200C 50h
(c)
1200ºC 250h
Acc.V Spot Magn Det WD 200 µm
20.00 kV 3.0 100x SE 10.0 ZrC-Rh-G-Rh-SiC 1200C 250h
Acc.V Spot Magn Det WD 20 µm
20.00 kV 3.0 1000x SE 10.0 ZrC-Rh-G-Rh-SiC 1200C 250h

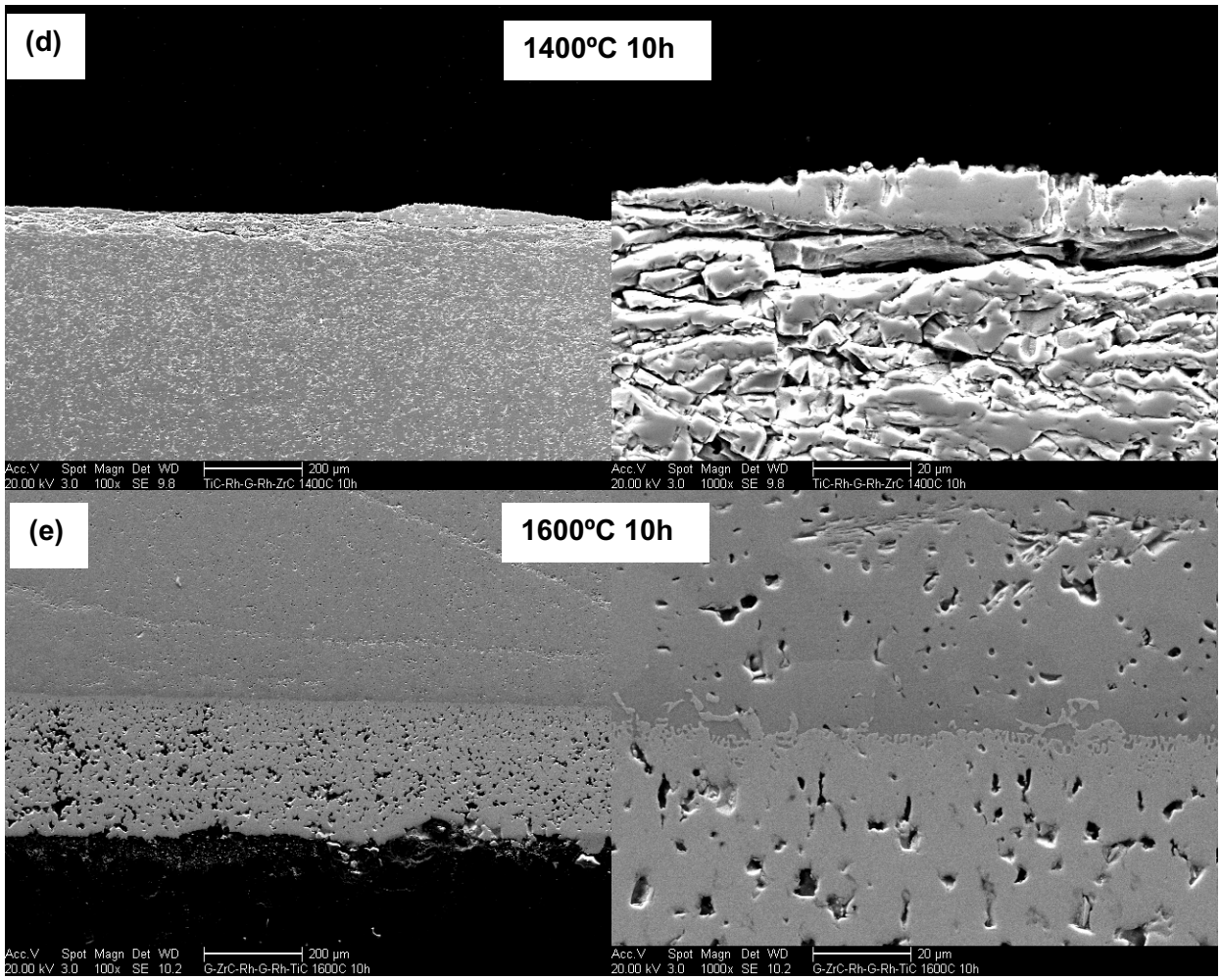

Figure 3.23. Electron micrographs of ZrC-Rh interfaces.

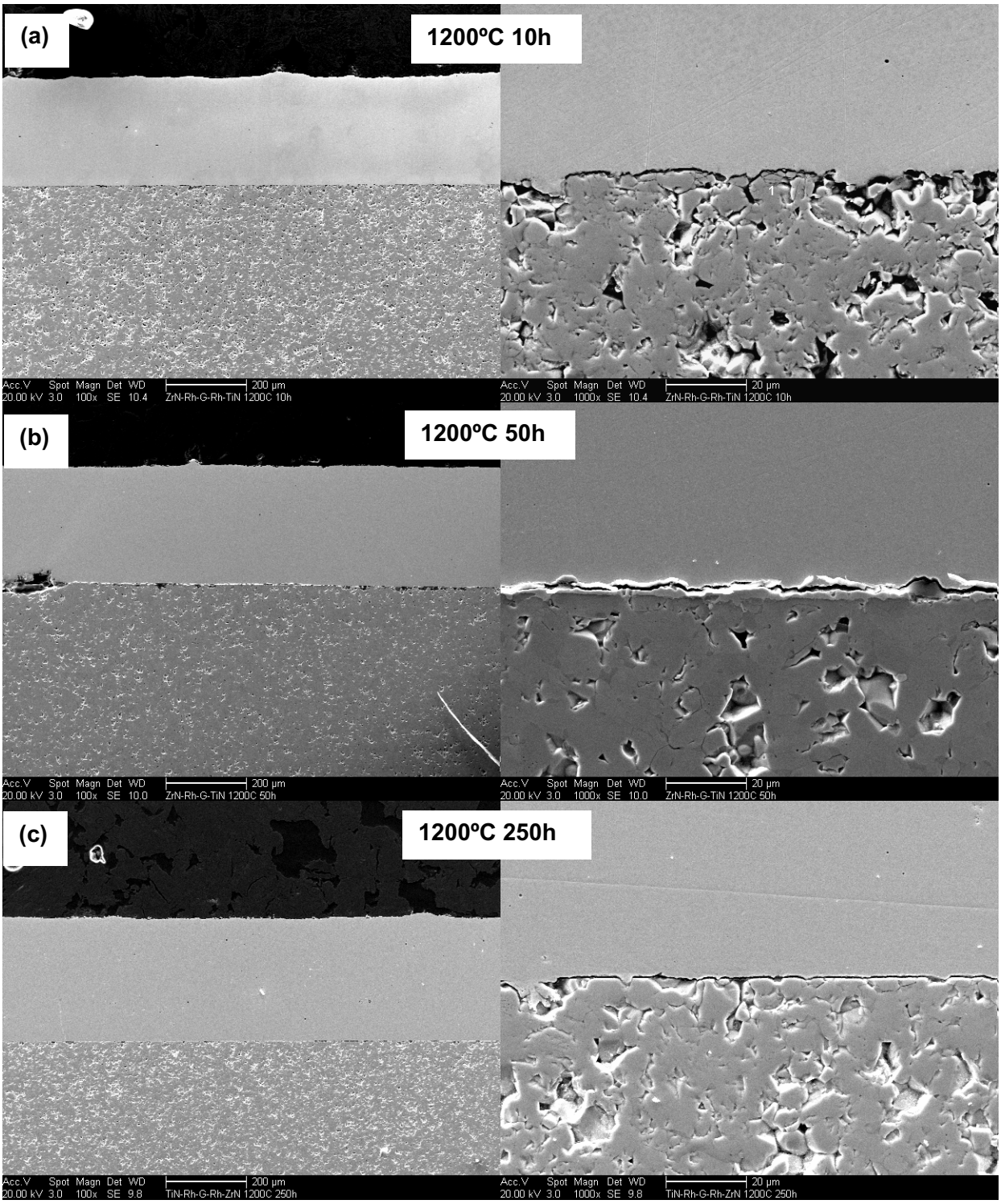
(a)
1200ºC 10h
Acc.V Spot Magn Det WD 200 µm
20.00 kV 3.0 100x SE 10.4 ZrN-Rh-G-Rh-TiN 1200C 10h
Acc.V Spot Magn Det WD 20 µm
20.00 kV 3.0 1000x SE 10.4 ZrN-Rh-G-Rh-TiN 1200C 10h
(b)
1200ºC 50h
Acc.V Spot Magn Det WD 200 µm
20.00 kV 3.0 100x SE 10.0 ZrN-Rh-G-TiN 1200C 50h
Acc.V Spot Magn Det WD 20 µm
20.00 kV 3.0 1000x SE 10.0 ZrN-Rh-G-TiN 1200C 50h
(c)
1200ºC 250h
Acc.V Spot Magn Det WD 200 µm
20.00 kV 3.0 100x SE 9.8 TiN-Rh-G-Rh-ZrN 1200C 250h
Acc.V Spot Magn Det WD 20 µm
20.00 kV 3.0 1000x SE 9.8 TiN-Rh-G-Rh-ZrN 1200C 250h

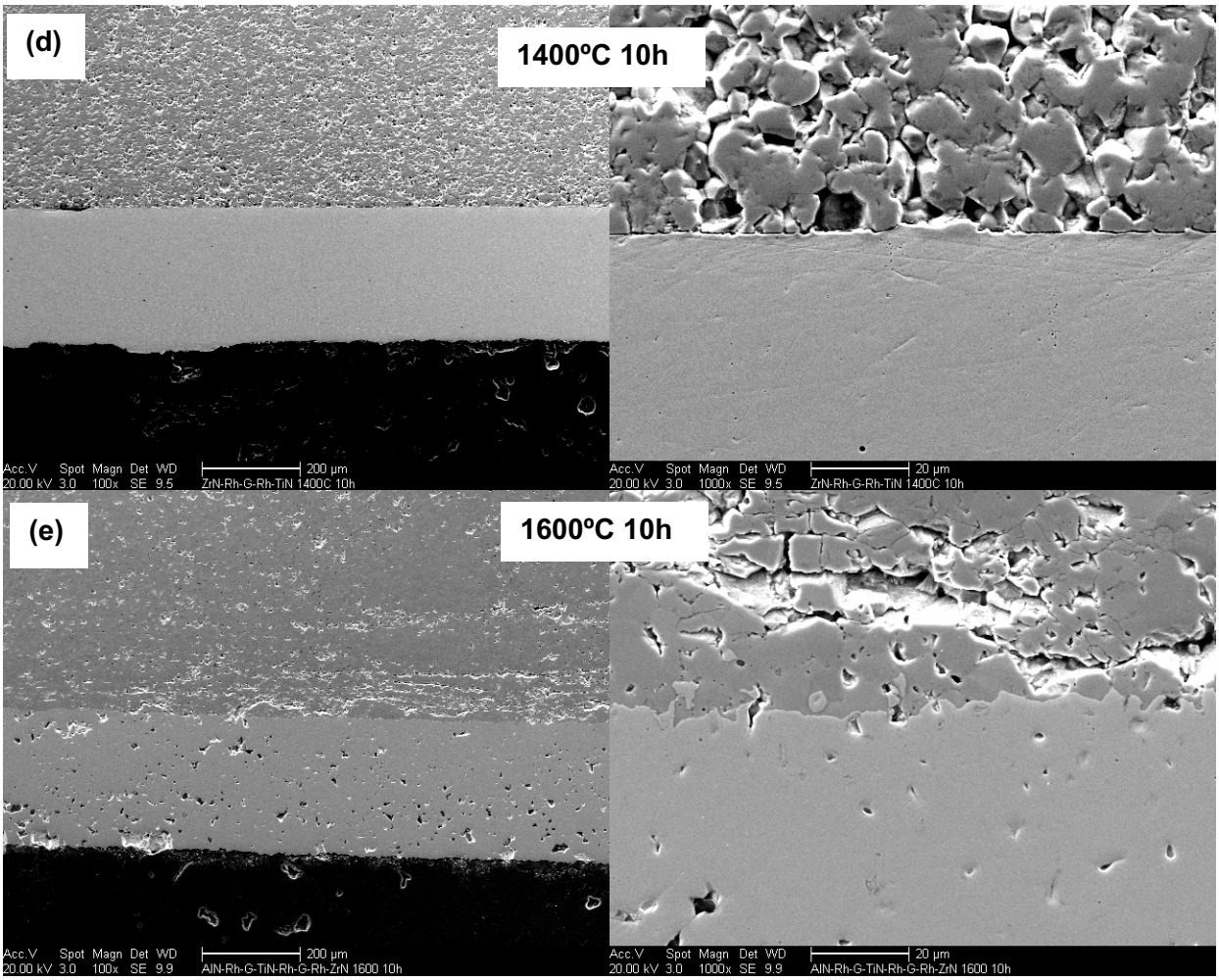

Figure 3.24. Electron micrographs of ZrN-Rh interfaces.

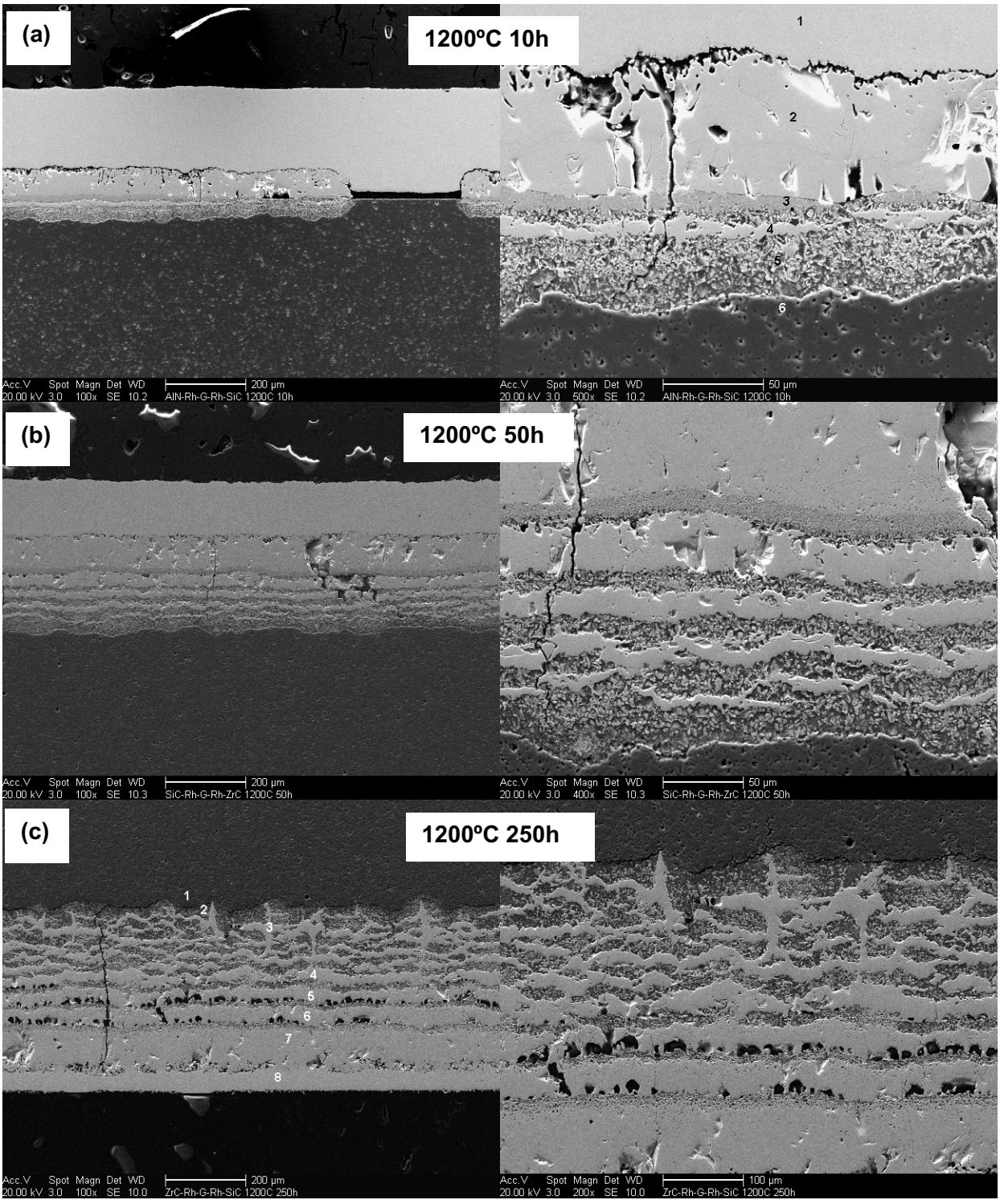
(a)
1200ºC 10h
0
1
2
3
4
5
6
Acc.V Spot Magn Det WD 200 µm
20.00 kV 3.0 100x SE 10.2 AlN-Rh-G-Rh-SiC 1200C 10h
Acc.V Spot Magn Det WD 50 µm
20.00 kV 3.0 500x SE 10.2 AlN-Rh-G-Rh-SiC 1200C 10h
(b)
1200ºC 50h
Acc.V Spot Magn Det WD 200 µm
20.00 kV 3.0 100x SE 10.3 SiC-Rh-G-Rh-ZrC 1200C 50h
Acc.V Spot Magn Det WD 50 µm
20.00 kV 3.0 400x SE 10.3 SiC-Rh-G-Rh-ZrC 1200C 50h
(c)
1200ºC 250h
1
2
3
4
5
6
7
8
Acc.V Spot Magn Det WD 200 µm
20.00 kV 3.0 100x SE 10.0 ZrC-Rh-G-Rh-SiC 1200C 250h
Acc.V Spot Magn Det WD 100 µm
20.00 kV 3.0 200x SE 10.0 ZrC-Rh-G-Rh-SiC 1200C 250h

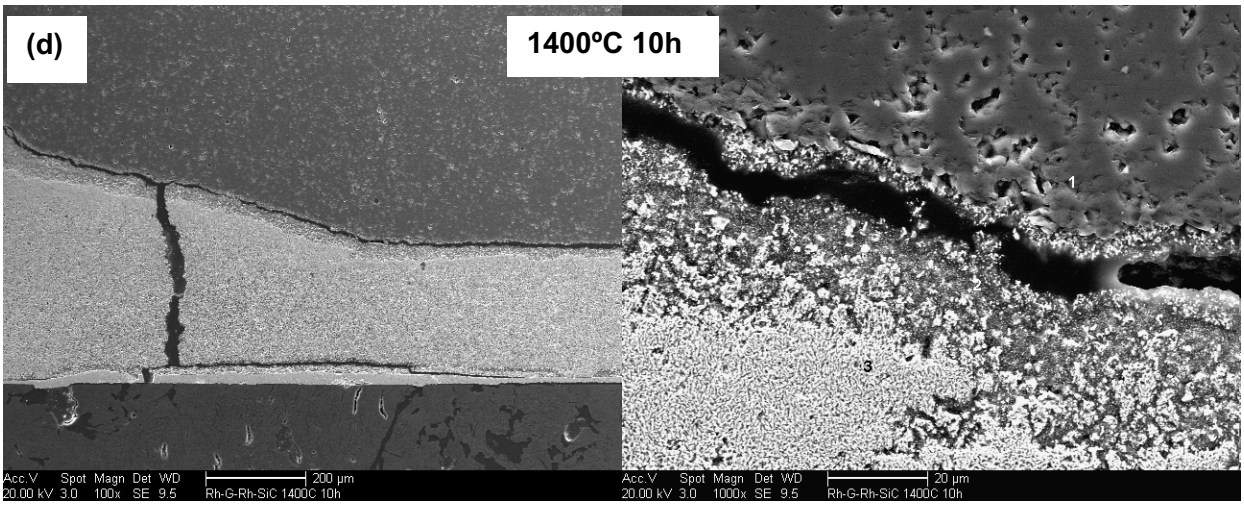

Figure 3.25. Electron micrographs of SiC-Rh interfaces.

(a)

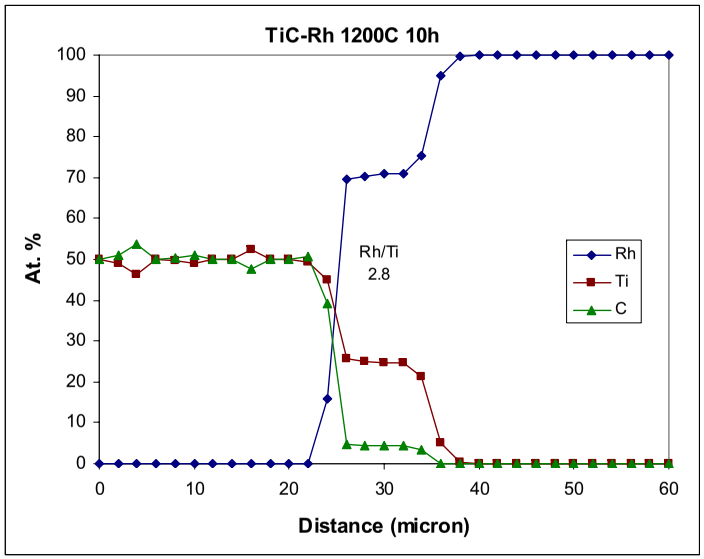
TiC-Rh 1200C 10h
At. %
Distance (micron)
Rh/Ti
2.8
Rh
Ti
C

(b)

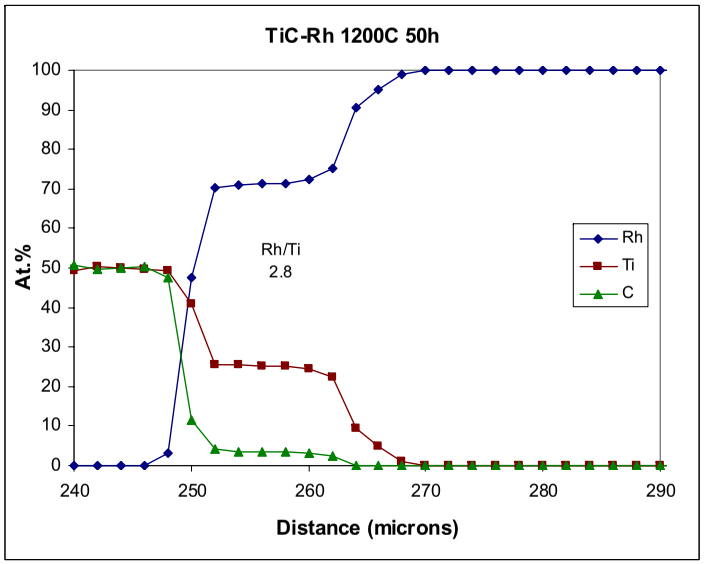
TiC-Rh 1200C 50h
At.%
Distance (microns)
Rh/Ti
2.8
Rh
Ti
C

(c)

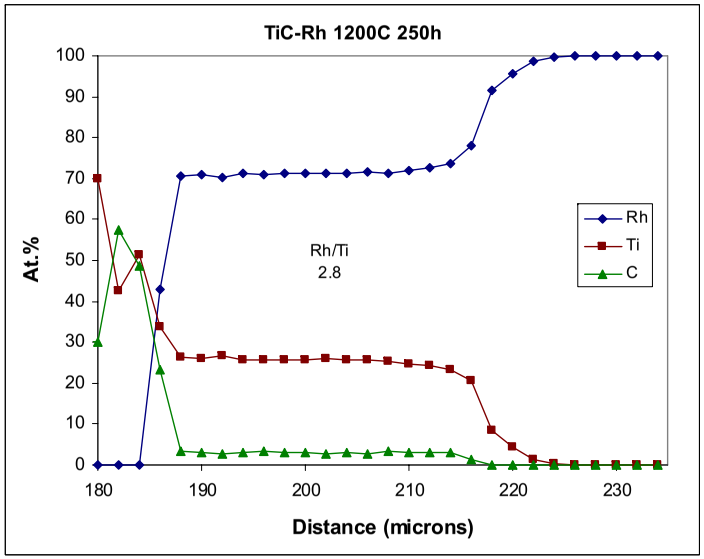
TiC-Rh 1200C 250h
At.%
Distance (microns)
Rh/Ti
2.8
Rh
Ti
C

(d)

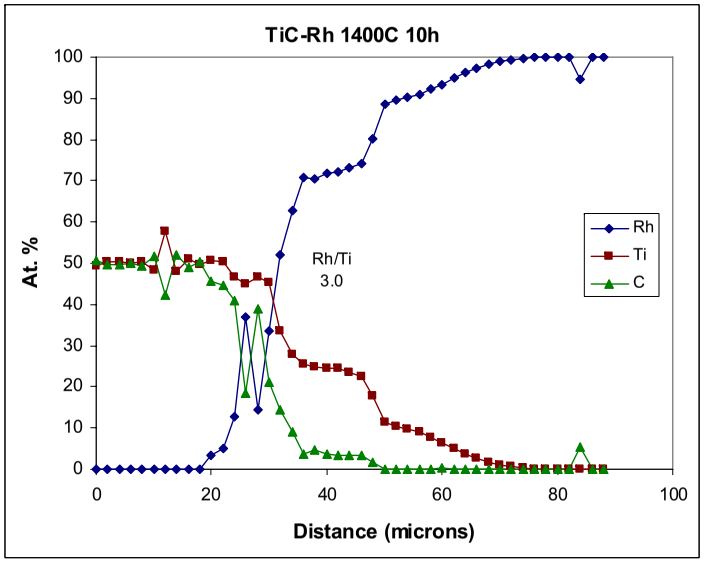
TiC-Rh 1400C 10h
At. %
Distance (microns)
Rh/Ti
3.0
Rh
Ti
C

(e)

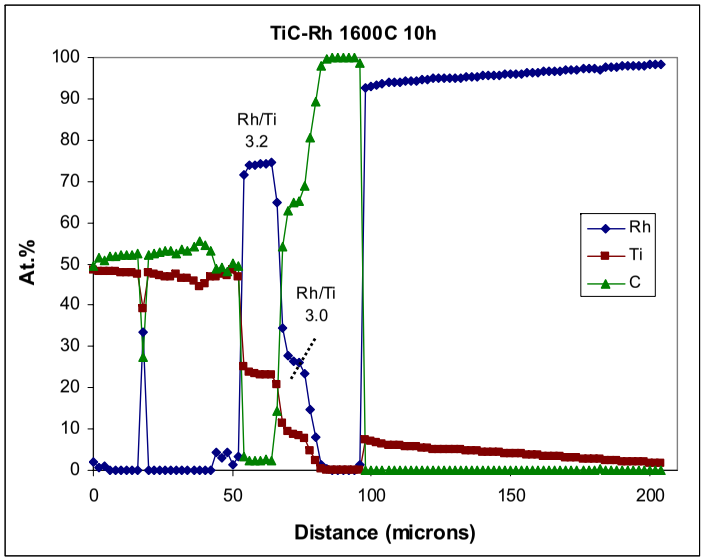

Figure 3.26. EPMA composition line scans of TiC-Rh diffusion couple interfaces.

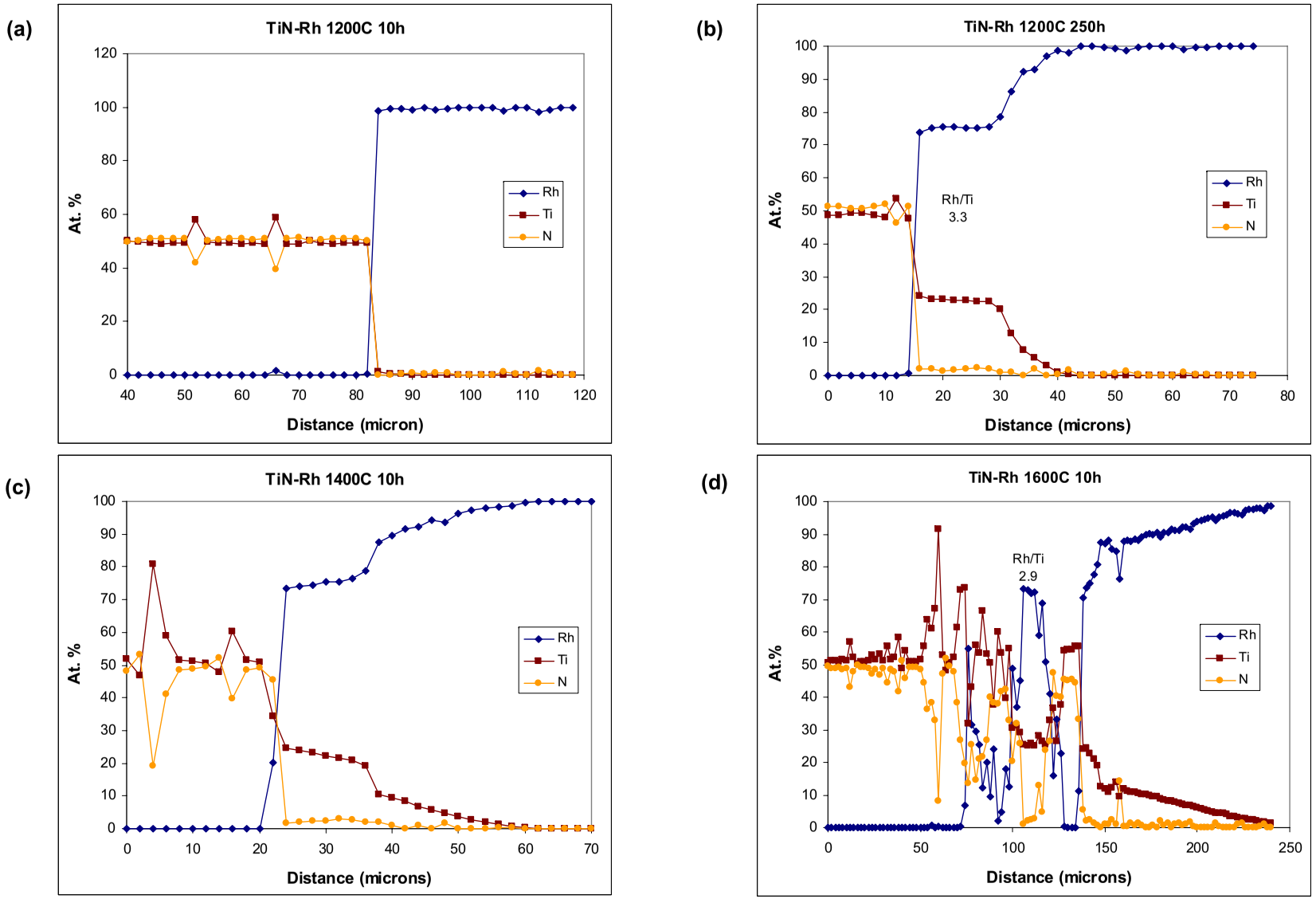

Figure 3.27. EPMA composition line scans of TiN-Rh diffusion couple interfaces.

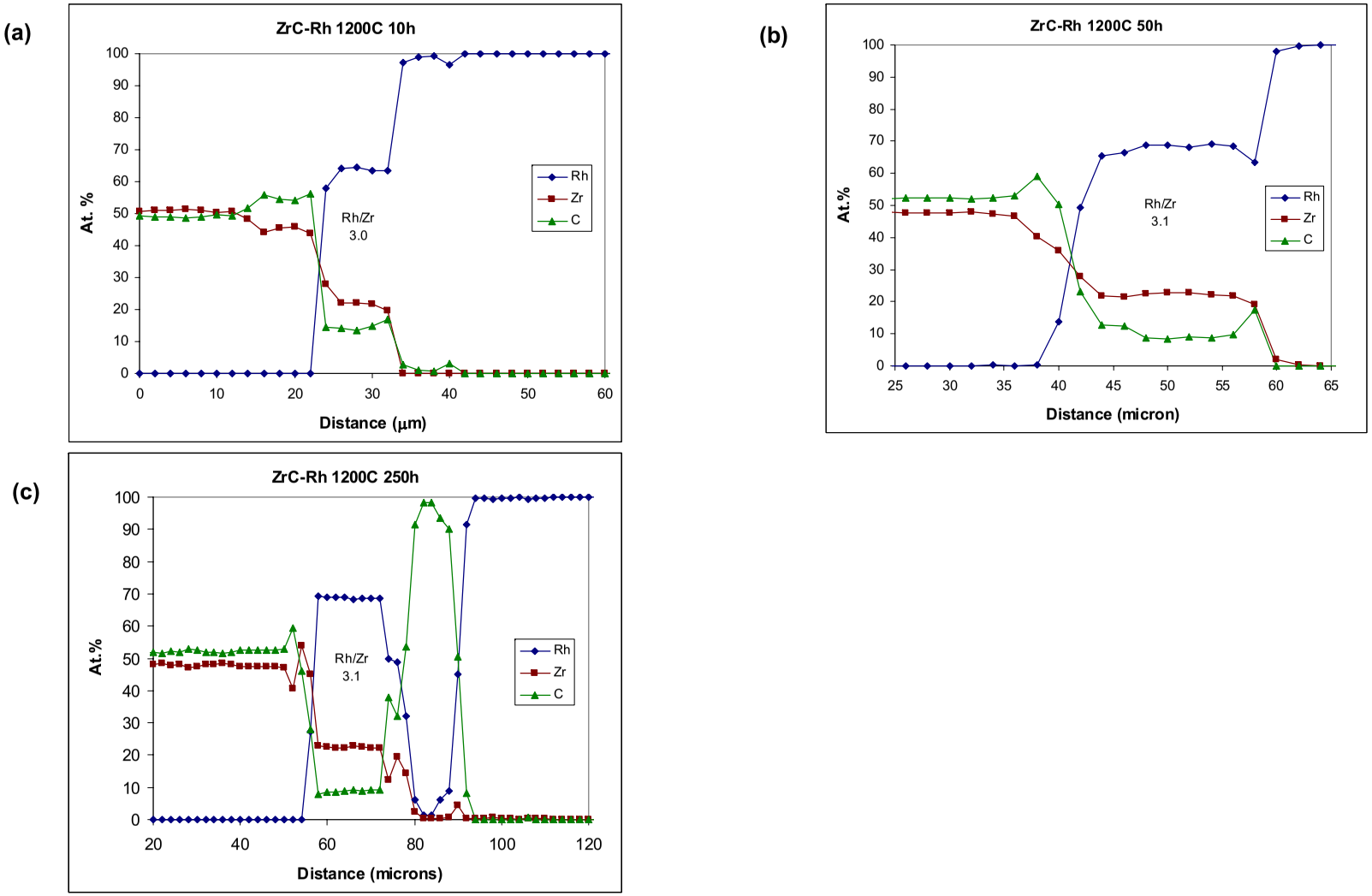

Figure 3.28. EPMA composition line scans of ZrC-Rh diffusion couple interfaces.

(a)

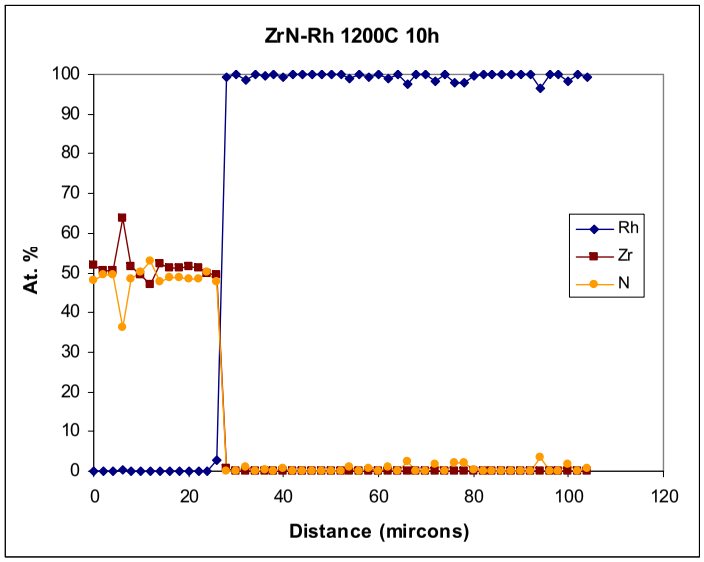
ZrN-Rh 1200C 10h
At. %
Distance (mircons)
Rh
Zr
N

(b)

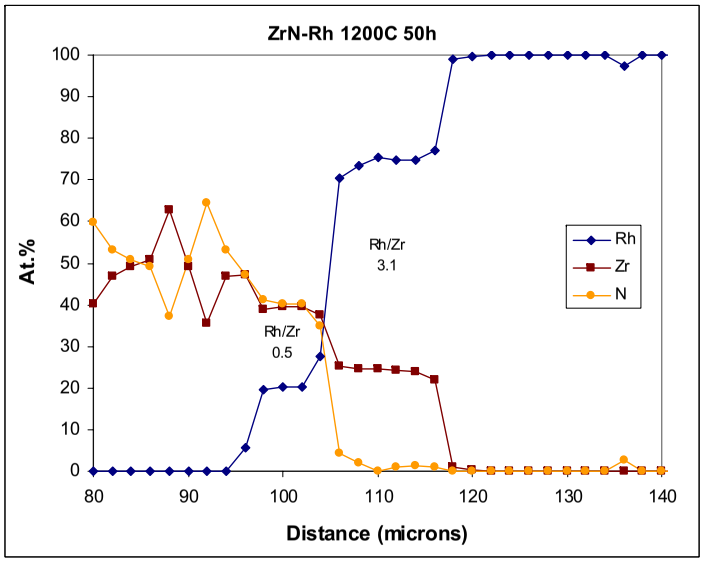
ZrN-Rh 1200C 50h
At.%
Distance (microns)
Rh/Zr
3.1
Rh/Zr
0.5
Rh
Zr
N

(c)

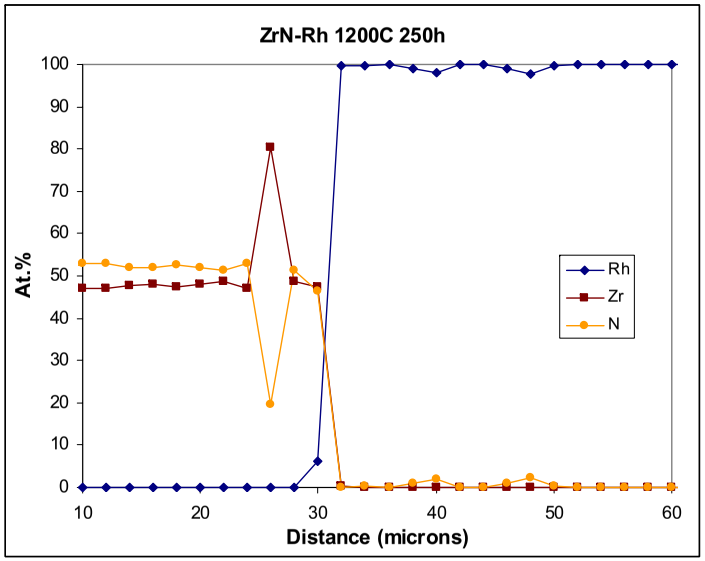
ZrN-Rh 1200C 250h
At.%
Distance (microns)
Rh
Zr
N

(d)

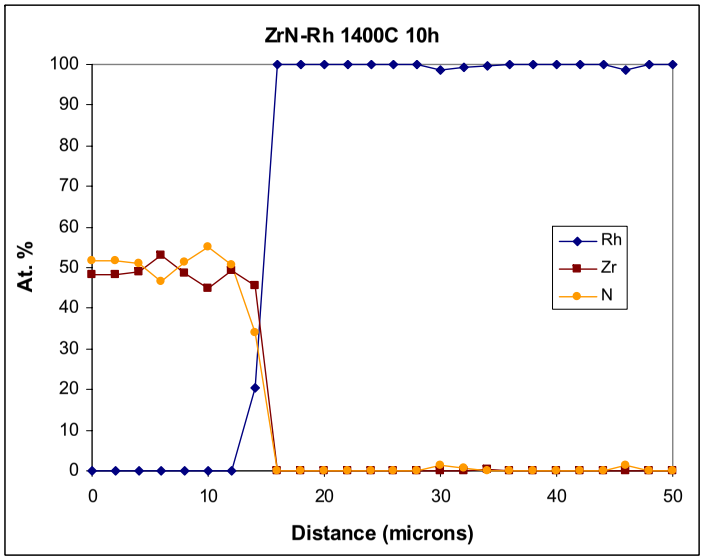
ZrN-Rh 1400C 10h
At. %
Distance (microns)
Rh
Zr
N

(e)

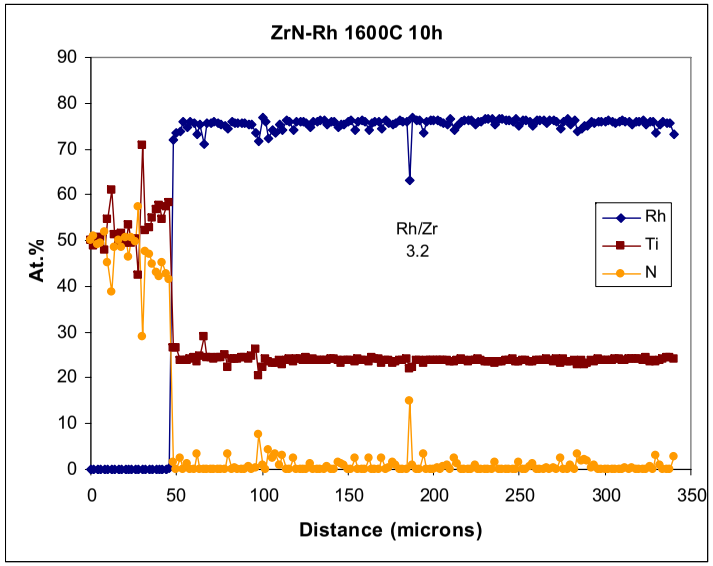

Figure 3.29. EPMA composition line scans of ZrN-Rh diffusion couple interfaces.

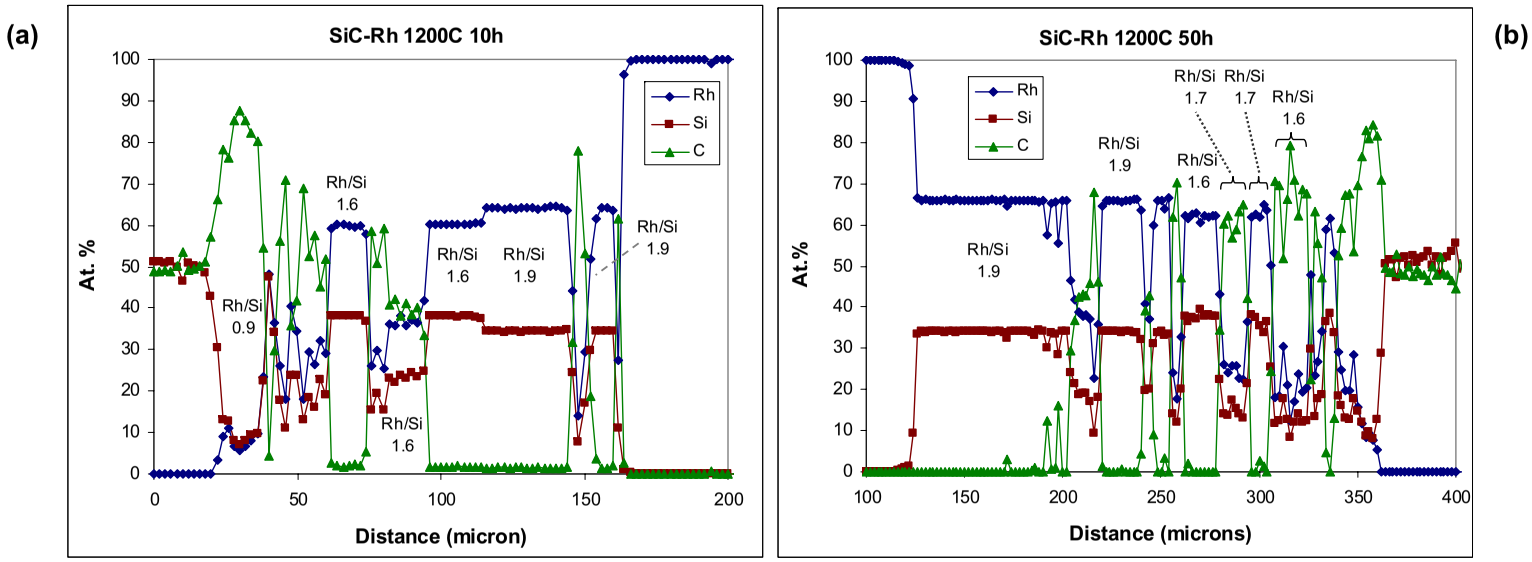

Figure 3.30. EPMA composition line scans of SiC-Rh diffusion couple interfaces.

3.2.4.1 TiC-Rh. All of the TiC-Rh diffusion couples resulted in a layer of an intermetallic phase with average Rh/Ti ratio ranging from 2.8 to 3.2, suggesting the formation of $TiRh_3$. The $TiRh_3$ phase has an FCC, cP4 structure (Villars and Calvert 1991), and has a composition range of approximately 22-27at.% Ti which is relatively independent of temperature (Massalski 1990). This layer is visible in micrographs of the interfaces (Figure 3.31), particularly the backscattered electron image. The EPMA line scan data show that this layer increased in thickness with annealing time and temperature (Figure 3.26). The approximate thickness of the intermetallic layer for these samples (determined from backscattered electron micrographs) is given in Table 3.6. Also note that intergranular migration of the Rh in TiC can be observed for the samples annealed at 1400ºC and 1600ºC (Figure 3.21). This intergranualar attack is pronounced at 1600ºC, and numerous veins of Rh have reached several hundred microns into the TiC.

Table 3.6. Thickness of $TiRh_3$ layer forming at the TiC-Rh interface.

TiC-Rh annealing conditions	$TiRh_3$ layer thickness (μm)
1200ºC-10h	12.3 (±0.4)
1200ºC-50h	19.1 (±0.9)
1200ºC-250h	34.3 (±0.9)
1400ºC-10h	18.8 (±1.4)

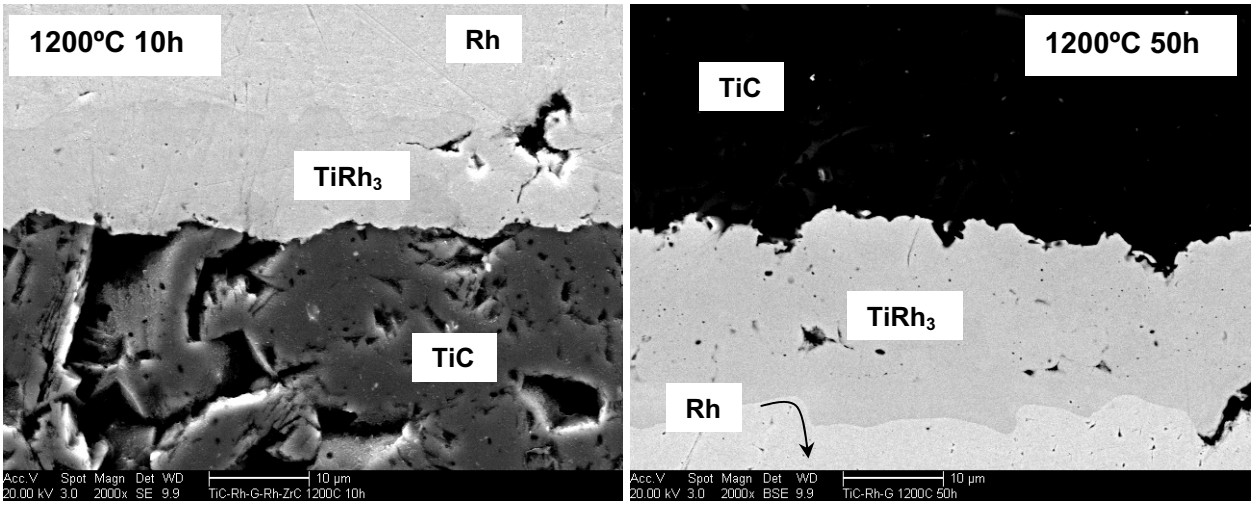

Figure 3.31. Micrographs of TiC-Rh diffusion couple cross-sections. Annealing times and temperatures are given on the images. The presence of a $TiRh_3$ intermediate phase is more easily seen in the backscattered electron image on the right.

Note that significant stresses must have developed in the 1200ºC-50h sample during the heat treatment, as a large wedge of material from the TiC side of the interface spalled away from the polished cross-section [Figure 3.21(b)]. Nonetheless a layer of $TiRh_3$ is still observed at the interface with SEM (Figure 3.31) and EPMA (Figure 3.26).

3.2.4.2 TiN-Rh. The TiN-Rh interface microstructures showed very little evidence of interaction until 1600ºC (Figure 3.22). EPMA line scan data show that interdiffusion was negligible at 1200ºC for 10 and 50 hours, but that a $TiRh_3$ phase appears to have formed at 1200ºC-250h and at higher temperatures. At 1600ºC the reaction appears to have been much more extensive, and $TiRh_3$ can be identified at the interface with EPMA (Figure 3.27).

3.2.4.3 ZrC-Rh. The majority of the observed interfacial areas of the ZrC-Rh samples annealed at 1200ºC showed no evidence of a reaction; however, there were small regions along the length of the interface where a reaction took place. The EPMA line scan data in Figure 3.28 reflect the compositions at these locations for the 1200ºC samples. The composition of the reaction product in these samples indicates that $ZrRh_3$ has formed. An EPMA composition map and secondary electron image of the reaction product is shown in Figure 3.32 for the 1200ºC-10h sample. Beyond the intermetallic phases, there appeared to be very little interdiffusion of Zr into the Rh foil to form a Rh(Zr) solid solution.

The 1400ºC-10h ZrC-Rh sample delaminated during sample preparation, leaving only the ZrC layer intact with a small amount of $ZrRh_3$ intermetallic phase attached (Figure 3.23). Analysis across the interface was limited for this sample. The sample annealed at 1600ºC showed evidence of Al in the Rh foil, which may have been introduced by vapor phase migration of Al-containing species when the different diffusion couples were annealed together at this temperature.

3.2.4.4 ZrN-Rh. The ZrN-Rh diffusion couples heated at different temperatures and times exhibited inconsistent behavior which may suggest that there was not good contact between the ZrN and Rh layers for all samples. EPMA composition data (Figure 3.29) show that the 1200ºC-10h, 1200ºC-250, and 1400ºC-10h samples did not produce any reaction product between the two layers. However, thin intermetallic phases (Zr_2Rh and $ZrRh_3$) were observed at isolated regions along the interface of the 1200ºC-50h sample (Figure 3.29). The reaction was sufficient in the 1600ºC-10h sample to completely consume the Rh foil and produce a uniform $ZrRh_3$ layer.

3.2.4.5 SiC-Rh. As with the Pd diffusion couples, the SiC-Rh interface produced the most extensive reactions. The reactions products were often in a layered structure, as indicated most distinctly in the samples annealed at 1200ºC (Figure 3.25). Three distinct intermetallic compounds were formed by the reaction, as indicated by the EPMA composition data (Figure 3.30). Based on the Si-Rh compositions in these regions, the phases formed were SiRh, Si_3Rh_5, and, probably, $SiRh_2$, although the Rh/Si ratio of this phase ranged from ~1.8 to 2.0. The phases formed in the order SiRh–Si_3Rh_5–$SiRh_2$ from the SiC side to the Rh side of the original interface (see EPMA line scan data in Figure 3.30). Both $SiRh_2$ and Si_3Rh_5 are listed in the literature as line compounds, and SiRh has a very small range of homogeneity (~1at.%) (Massalaski 1990).

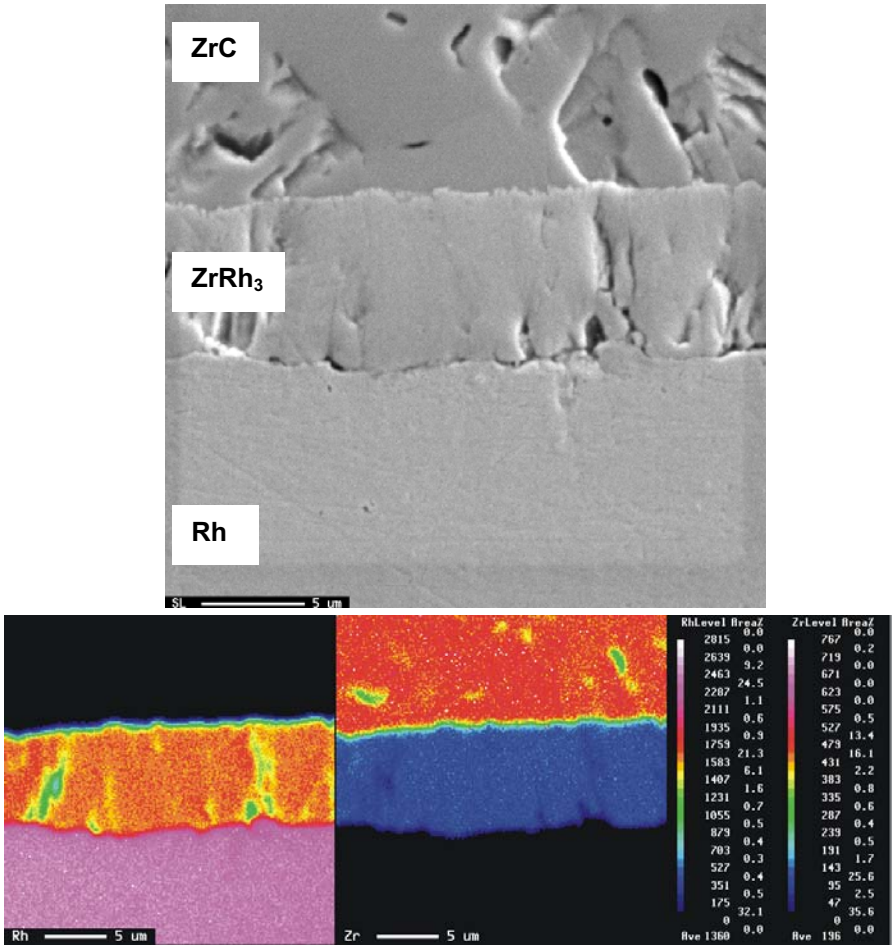

Figure 3.32. EPMA composition maps (bottom) and secondary electron image (top) of ZrC-Rh interface annealed at 1200ºC for 10h.

3.2.5 Reaction Rate Analysis

One means of quantitatively comparing reaction rates among the ceramics is an analysis of the diffusion curves (EPMA composition line scans). However, a number of factors in the current data set complicate the integration of the diffusion curves, making comparisons of reaction rates among the different ceramics difficult.

Analysis of the diffusion curves involves determining the location of the initial ceramic-metal interface and calculating the amount of ceramic that had been consumed during the reaction. Integration of the diffusion curves is performed to determine the line of equal flux; i.e. the plane parallel to the interface in which the total flux of atom A in one direction is equal to the total amount of atom A that has been depleted from the other side (Figure 3.33). This plane is known as the Matano plane, and represents the original interface (Reed-Hill 1992). This analysis assumes a uniform molar volume across the interface.

A number of factors in the current data set complicate this analysis. One is the presence of secondary phases of different molar volume, since that analysis above assumes constant molar volumes of the interacting species. To address this, one must take into account the variation of volumetric density of each element across the interface and adjust accordingly.

A second complication is the presence of porosity along the analyzed volume (or area, in a cross-sectional analysis). This must be quantified and incorporated into the calculations.

A third problem with the analysis of the present data is the presence of free carbon across the interface. It is often unknown for these samples whether the carbon is a reaction product (e.g. as in Eq. 3.1), or whether it is the result of epoxy from the metallographic mounting process that has filled pores in the sample. In the former case, the carbon should be included in the analysis; in the later, the carbon-containing regions should be treated as porosity. Unfortunately it is very difficult to determine the source of the carbon in the case of samples that contain carbide.

Another issue is the interference of the Pd and C signals in the EPMA analysis which will result in additional error in the quantitative chemical analysis of carbide-Pd samples, which further complicates the diffusion analysis.

Finally, the appearance of the diffusion couple cross-sections demonstrates that it was possible to have incomplete contact across the interface during the anneal. This sometimes resulted in a lack of any observed reaction between the two layers, even though a reaction was observed at lower annealing times and/or temperatures.

These factors make a comprehensive quantitative analysis of the diffusion data obtained here questionable, and eliminate many of the diffusion couple cross-sections from a rigorous treatment. Because of these considerations, the analysis was restricted to samples that had relatively continuous interfaces (that is, little or no porosity and therefore no possibility of epoxy filling voids in the reaction zone) and the absence of multiple phases across the reaction zone.

Good candidates for this analysis were the TiN-Pd and ZrN-Pd interfaces. Because integration of the diffusion curves only takes place in the Pd side of the final interface, we deal with only one phase. The change in lattice parameter, *a*, of Pd when Ti is substituted into the FCC lattice is extremely small, only about a 0.1% decrease at 15at.% Ti (Ellner 2004), which can be ignored for the purposes of the present calculations. For Zr in Pd, the change in *a* is more significant, amounting to about a 1.7% increase at 18at.% Zr. However, for the present analysis, this change will be considered negligible compared to other uncertainties in the composition measurements.

The approach to calculate the area under the diffusion curves was graphical integration using the trapezoidal method. Integration was performed on the Pd curves, and calculations were performed to find the point at which the area under the curve to that point is equal to the area above the curve beyond this point; in other words, the initial interface or Matano plane (Figure 3.33). A plot of the diffusion data for ZrN-Pd diffusion couples annealed at 1000ºC at different times, normalized to the location of the initial interface, is shown in Figure 3.34. This figure shows the amount of ZrN that was consumed by the reaction with Pd by comparing the final interface with the initial interface.

Based on the location of the initial and final interface, the thickness of ceramic phase that was reacted can be calculated. This was done for the ZrN-Pd and TiN-Pd diffusion couples, and the interaction depth is plotted against annealing time and temperature in Figure 3.35. Note that the data from the 1400ºC anneals is not included here because the interfaces were sufficient degrading as to make the integration

problematic. The data indicate a consistent trend that shows ZrN to have a higher reaction rate with Pd than TiN.

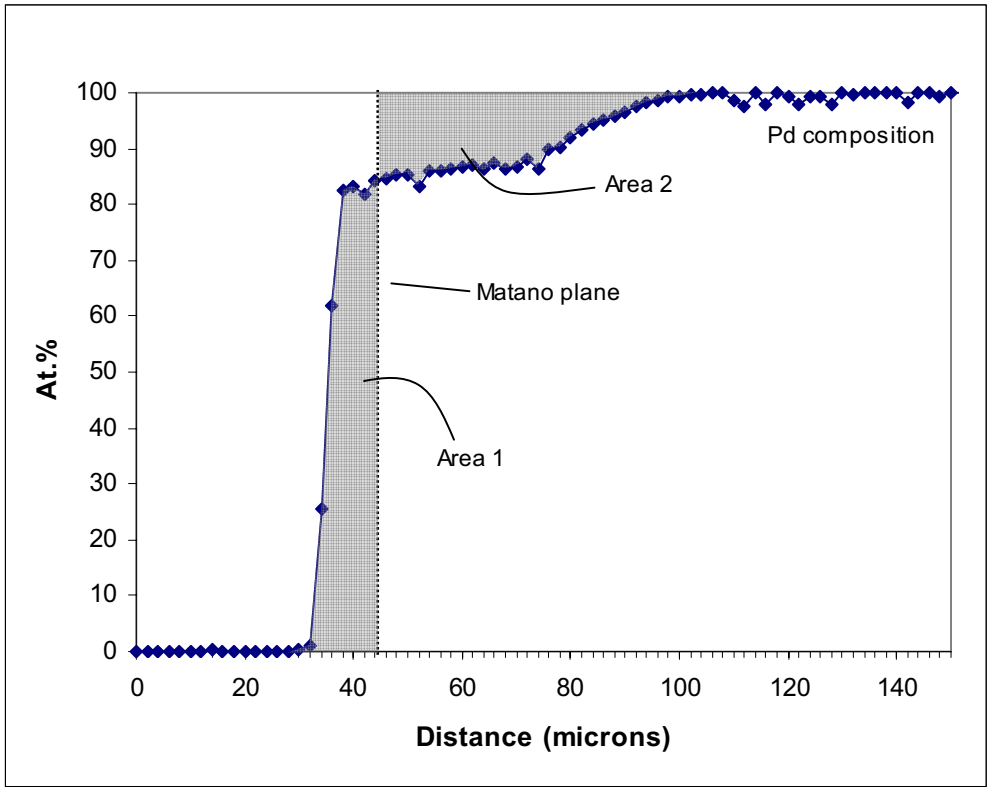

Figure 3.33. Location Matano plane, at which Area 1 is equal to Area 2 (assuming uniform molar volumes).

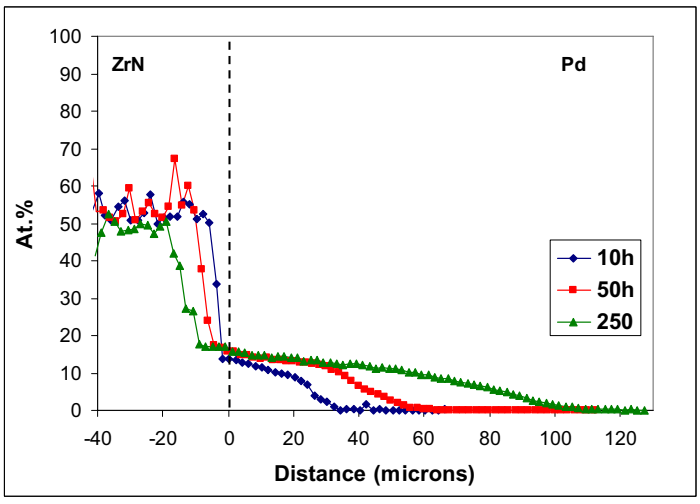

Figure 3.34. Diffusion data (Zr composition lines) for ZrN-Pd diffusion couples annealed for different times at 1000ºC. Data is normalized so that zero distance corresponds to the initial ZrN-Pd interface.

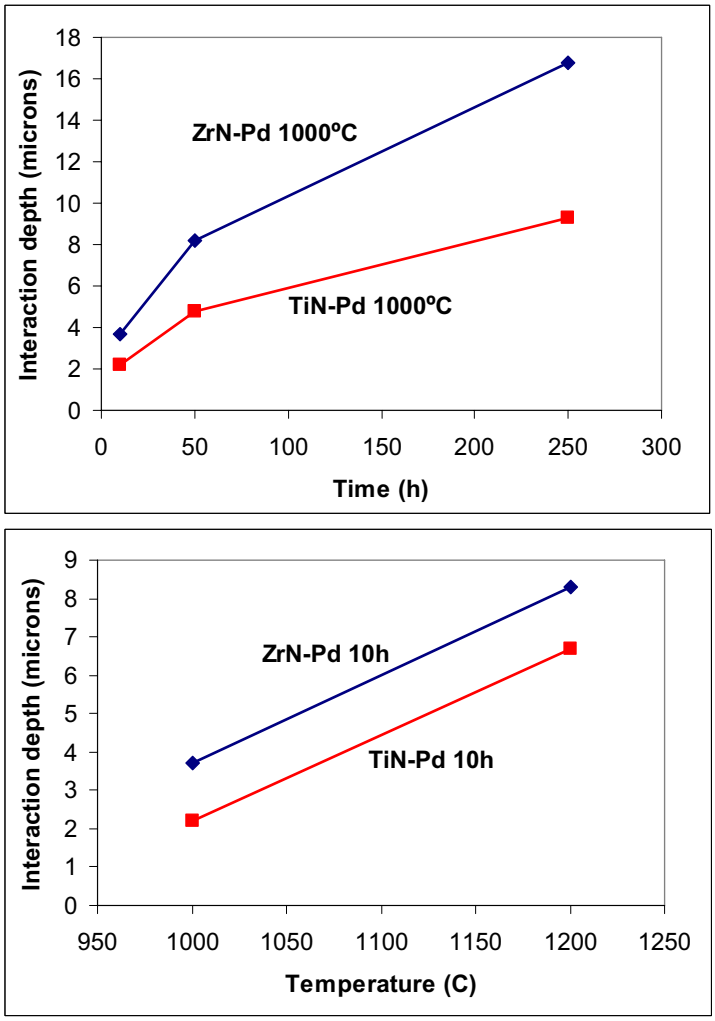

Figure 3.35. Comparison of interaction depth for ZrN-Pd and TiN-Pd diffusion couples as a function of annealing time (top) and temperature (bottom).

If a parabolic reaction rate is assumed for the Pd-ceramic interaction, i.e.

$$d = t^{1/2} K \qquad \text{(Eq. 3.2)}$$

where d is the interaction depth, and t is the reaction time, the reaction rate constant (K) can be calculated. The activation energy of the overall reaction can be obtained from a plot of ln(K) vs. 1/T, based on the Arrhenius relationship

$$K = K_o \exp\left(\frac{-E}{RT}\right), \qquad \text{(Eq. 3.3)}$$

where, K_o is a constant, E is the activation energy, R is the universal gas constant, and T is the temperature (in Kelvin).

Arrhenius plots for the ZrN-Pd and TiN-Pd data are shown in Figure 3.36. The activation energies obtained from the slope of the plots are 63.0 kJ/mol for ZrN-Pd and 86.8 kJ/mol for TiN-Pd.

Additional quantitative analyses of the diffusion data has been limited due to the complications mentioned above.

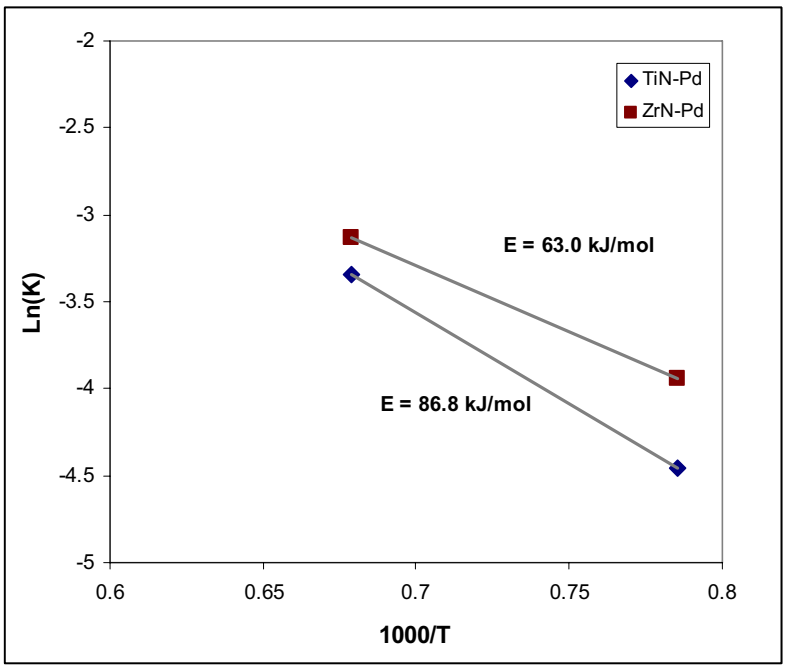

Figure 3.36. Arrhenius plots of ZrN-Pd and TiN-Pd reaction data with the corresponding activation energies.

3.3 Powder Reactions

In order to determine the crystalline phases that were formed by the various interface reactions in the diffusion couples, powder mixtures were annealed and analyzed with powder x-ray diffraction. The starting materials are described in Table 3.7.

Table 3.7. Specifications for powders used in annealing experiments.

Material	Purity	Particle size
Pd	99.9%	-200 mesh
TiC	99.5%	2 μm
TiN	99%	-325 mesh
ZrC	99.5%	-325 mesh
ZrN	99.5%	-325 mesh
AlN	99%	-200 mesh
SiC	99.8%	1 μm

Pellets were formed by blending the powders in a ratio of 1 mole ceramic with 2 moles palladium and the powder mixtures were compacted under a uniaxial pressure of ~150 MPa to give pellets with 6 mm diameter and approximately 2 mm thickness. The pellets were then annealed under a vacuum (~10^{-6} Torr) at several times and temperatures to mirror the conditions of the diffusion couples. After annealing, the pellets were broken apart, ground to a powder, and analyzed using a Bruker D-8 Advance X-ray diffractometer to determine the crystalline phases.

Figure 3.37 shows an example of the results for a ZrC-Pd pellet annealed at 1200ºC for 10 hours. In this case all of the Pd and most of the ZrC have been consumed by the reaction to form $ZrPd_3$. This offers confirmation of the reaction that takes place in the diffusion couples. The reference diffraction pattern for $ZrPd_3$ is from Weissmüller and Ehrhardt (1998).The XRD patterns for each of the ceramic powders mixed with Pd powder and annealed at 1200ºC for 10 hours are shown in Figures 3.38–3.41. The results for each of the powder mixtures are summarized in Table 3.8.

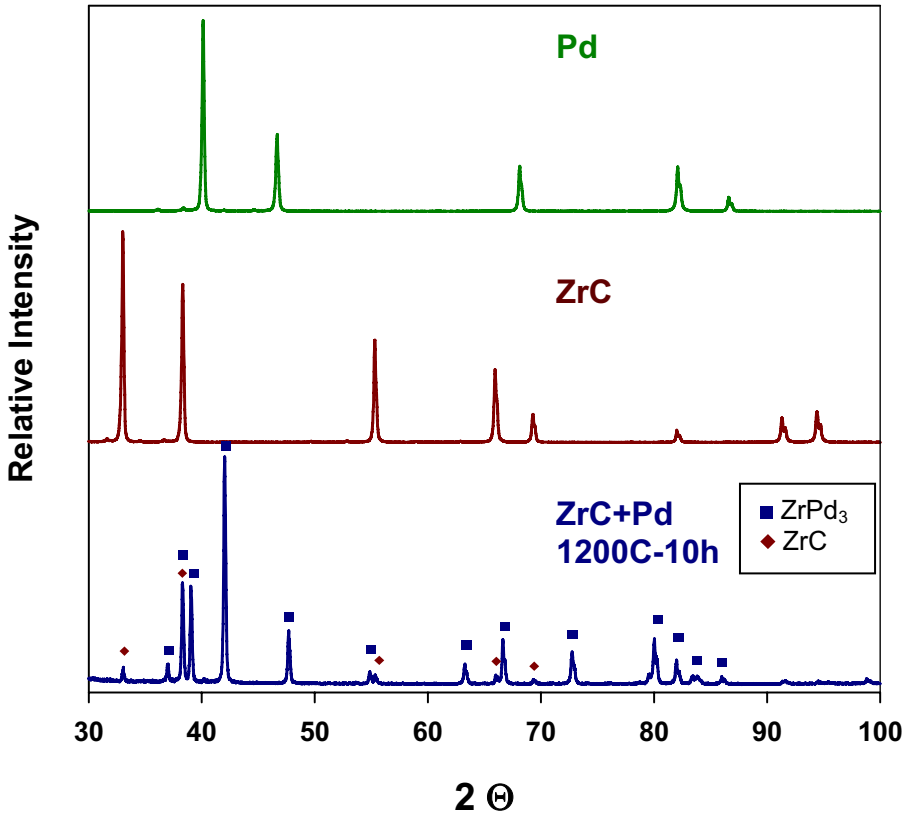

Figure 3.37. X-ray diffraction patterns for starting powder Pd and ZrC and the reaction product after annealing for 1200ºC for 10 hours in a vacuum. Peaks corresponding to either $ZrPd_3$ or ZrC in the annealed mixture are indicated with symbols.

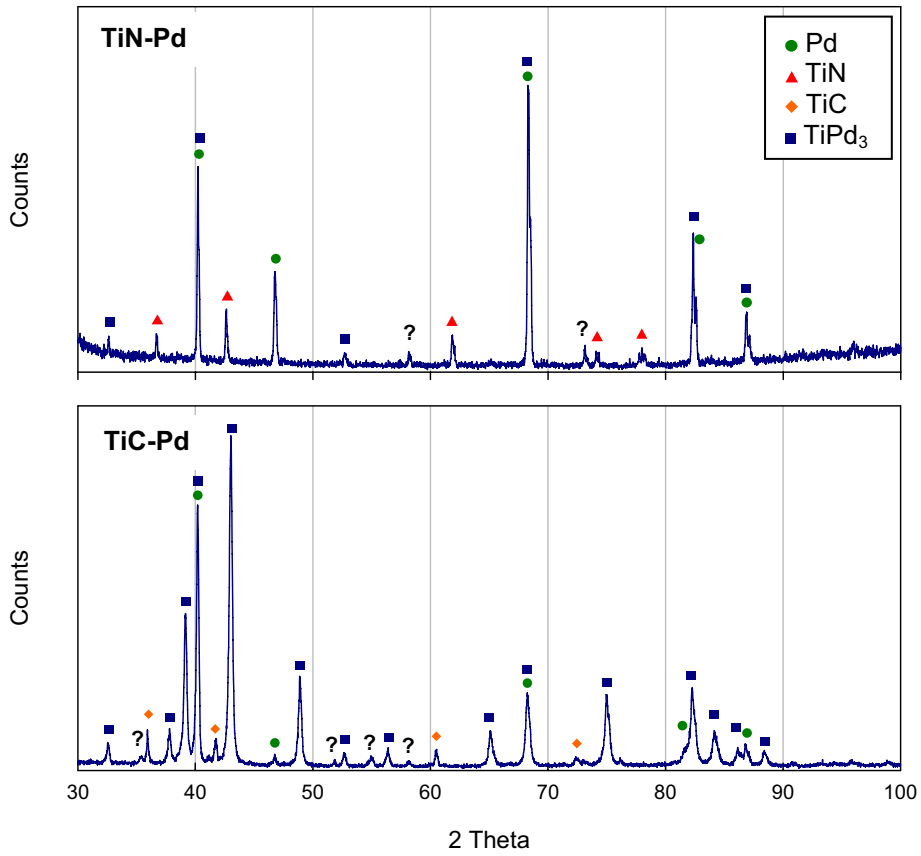

Figure 3.38. Reaction products of TiN-Pd and TiC-Pd powder mixtures annealed at 1200ºC for 10 hours in vacuum. Unidentified peaks are identified with a "?".

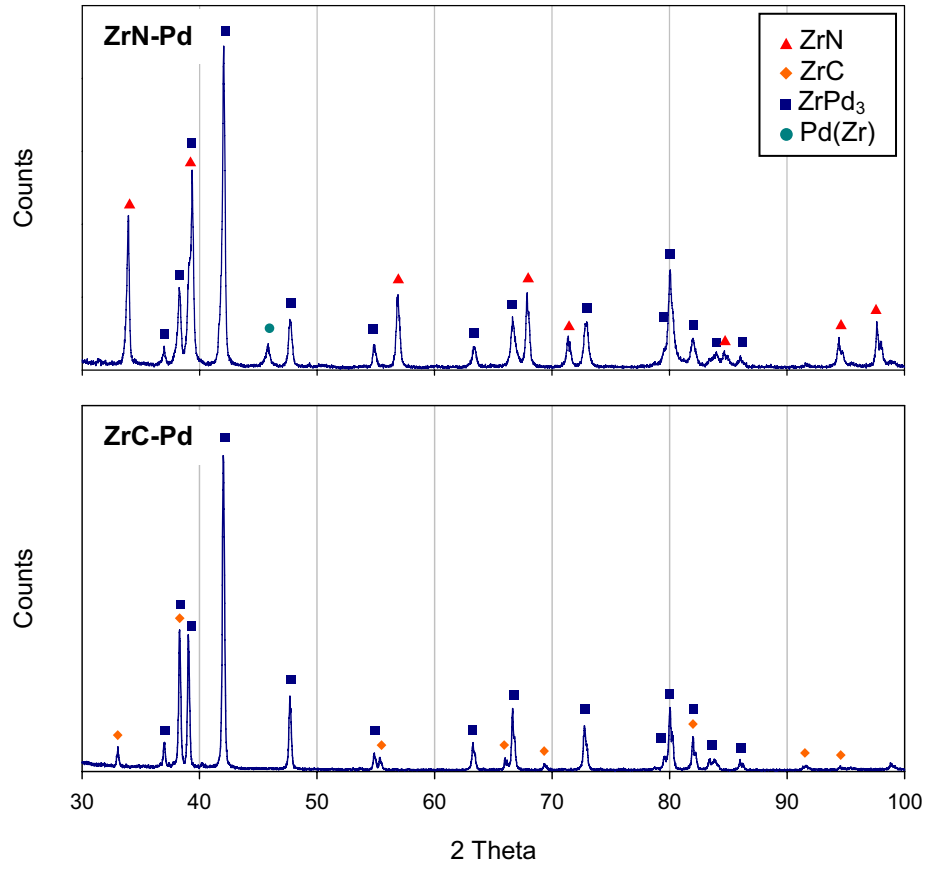

Figure 3.39. Reaction products of ZrN-Pd and ZrC-Pd powder mixtures annealed at 1200ºC for 10 hours in a vacuum.

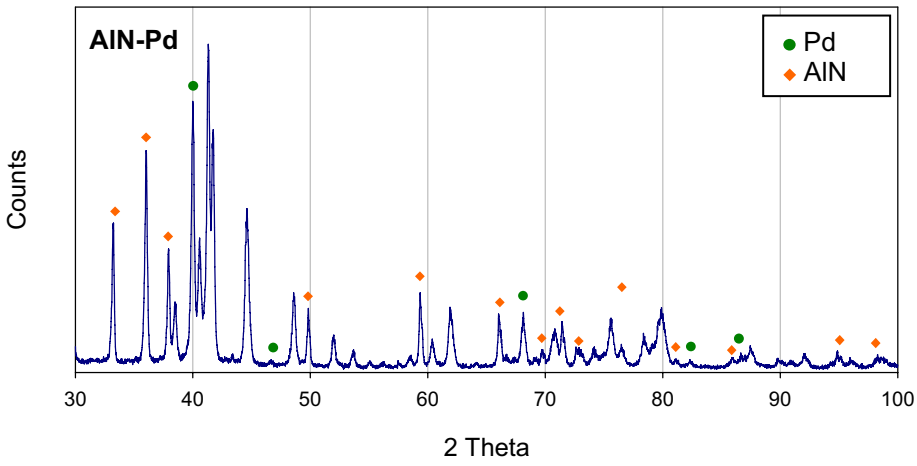

Figure 3.40. Reaction products of AlN-Pd powder mixture annealed at 1200ºC for 10 hours in a vacuum.

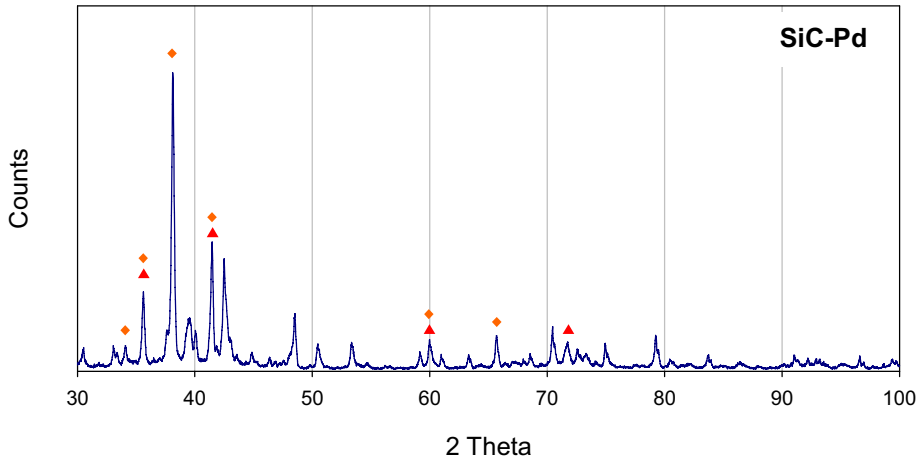

Figure 3.41. Reaction products of SiC-Pd powder mixture annealed at 1200ºC for 10 hours in a vacuum.

Table 3.8. Results of XRD analysis of ceramic-Pd powder mixtures annealed at 1200ºC for 10h.

Reactants	Products[a,b]	
	Major phases	Minor phases
TiC + Pd	$TiPd_3$ (hex)	TiC, unk
TiN + Pd	TiN, Pd	$TiPd_3$ (hex), unk
ZrC + Pd	$ZrPd_3$	ZrC
ZrN + Pd	$ZrPd_3$, ZrN	Pd(Zr)
AlN + Pd	AlN, Pd, unk	
SiC + Pd	SiC, unk	

(a) "unk" denotes unidentified XRD peaks.
(b) "hex" denotes hexagonal phase.

The TiC-Pd reaction resulted in almost complete conversion to $TiPd_3$. Several minor peaks were present that were not identified. The TiN-Pd sample exhibited a much smaller amount of $TiPd_3$ formation (compared to TiC-Pd sample), with significant amounts of Pd and TiN remaining. Unidentified peaks were also present in the XRD pattern for the TiN-Pd sample, but these were different from those observed in the TiC-Pd pattern. It should be noted that in both cases the $TiPd_3$ that formed was the hexagonal phase, not the ordered FCC phase that was observed exclusively in the TEM results of the diffusion couples.

Neither the ZrC-Pd nor ZrN-Pd patterns (Figure 3.39) showed any Pd remaining in the mixture. The main phases are $ZrPd_3$ and either ZrC or ZrN. This is explained by the starting ratio of metal to ceramic, which was 2:1. The formation of $ZrPd_3$ did not allow for complete reaction of the ceramic phase as there was not enough palladium present. It is interesting to note that a single small peak at 2θ ~45.9º is present in the ZrN-Pd mixture. This peak is assigned by Weissmüller and Ehrhardt (1998) to the [002] reflection of the solid solution Pd(Zr), which forms prior to precipitation of the intermetallic phase $ZrPd_3$.

A detailed analysis of the AlN-Pd and SiC-Pd patterns was not completed. Automatated indexing of the patterns left many peaks unidentified. The task is complicated by the fact that many Al-Pd and Si-

Pd phases are possible, often with complex crystal structures (orthorhombic, rhombohedral), as well as many polymorphs of SiC that complicate the analysis.

The results of these experiments show that the $ZrPd_3$ and $TiPd_3$ hexagonal crystalline phases appear to be formed at equilibrium in the respective systems. The observation of incomplete reaction of TiN compared to essentially complete reaction of ZrN (evidenced by the complete consumption of the Pd in the sample) is consistent with the analysis in the previous section that demonstrated a higher reactivity of ZrN vs. TiN (i.e. Figures 3.35 and 3.36). The nominal particle sizes of the TiN and ZrN powders was the same (-325 mesh); however, it should be noted that the particle size distribution or specific surface area of the powders, which would have an impact on the extent of reaction between the ceramic and Pd in a given time, was not measured.

3.4 Results Summary

Qualitatively, all of the ceramics exhibited much less reactivity to Pd and Rh compared to SiC. Intermetallic phases with 3:1 Rh: M (M = Ti, Zr) stoichiometry were formed in most of the TiC, TiN, ZrC, and ZrN diffusion couples, and 3:1 compounds were also formed in the TiC-Pd and ZrC-Pd diffusion couples. By contrast, the TiN and ZrN interfaces did not appear to produce significant regions of $TiPd_3$ or $ZrPd_3$, although high resolution TEM examination of the TiC-Pd sample shows that FCC $TiPd_3$ was formed very close to the interface. The reason for this behavior in the nitride-Pd reactions is not immediately clear.

The reaction zone in carbide-Pd diffusion couples consistently showed a heterogenous region, that apparently consisted of areas of free carbon liberated by the TiC or ZrC reaction with Pd according to Eq. 3.1. It is possible that this reaction facilitated the formation of the intermetallic phases ($TiPd_3$ and $ZrPd_3$), explaining why the nitride-Pd interfaces did not have the intermetallics, however the exact mechanism is unknown. It is also unclear why SEM micrographs of the carbide-Rh diffusion couples did not appear to demonstrate similar behavior in the reaction zone (i.e. formation of heterogeneous regions with free carbon). The ternary phase diagrams for the Rh-C-M and Pd-C-M (M = Ti, Zr) systems (Villars 1995) show that both $TiRh_3$ and $ZrRh_3$ has appreciable carbon solubility (up to ~10at.%) at elevated temperatures, while $TiPd_3$ and $ZrPd_3$ do not have any carbon solubility. This would account for some of the carbon from TiC and ZrC in the Rh systems, but not all (i.e. the C/Ti ratio in $(Ti_{0.25}Rh_{0.75})_{0.9}C_{0.1}$ is not 1:1 as in TiC).

It is assumed that nitrogen liberated from the reaction of nitrides with Pd or Rh to form intermetallic phases is able to diffuse rapidly away from the reaction zone. No appreciable concentrations of nitrogen were found in the diffusion couples outside of the original nitride phase. Pores are sometimes observed near the nitride interfaces, but these seem to appear too inconsistently to be due to accumulation of $N_2(g)$.

Intergranular diffusion of Pd and Rh into the samples was observed in certain instances, and increased at higher temperatures. The TiC sample appeared to be particularly susceptible to intergranular diffusion.

A direct comparison of reactivity rates between ZrN-Pd and TiN-Pd interactions demonstrated that TiN is consumed more slowly by Pd than ZrN, which has favorable implications for fuel coatings. A quantitative reaction rate comparison for other materials was more difficult due to the nature of the multicomponent-multiphase reaction zones.

The results to date tend to favor the nitride ceramics, and in particular TiN, as a particle fuel coating with respect to chemical reactivity with platinum-group metal fission products, although it should be noted that all of the Group IV carbides and nitrides studied here showed much less corrosion by Pd and Rh than SiC.

3.5 Future Work: Cs Vapor Experiments

3.5.1 Background

During the operation of TRISO particles in HTGRs, a variety of fission products migrate in the kernels and coating layers and at sufficiently high temperatures can escape from the particles in spite of the coatings remaining intact. Cesium a volatile fission product in that it has a very low melting point (T_m = 28.4ºC) and can migrate readily in the particle via vapor phase transport. The reactivity of Cs with the other elements in the particle is complicated, and often dependent on the chemistry of the particular fuel particle. Cesium is often a fission product of concern in these systems, particularly during accident scenarios where the particles may reach temperatures as high as 1600ºC. While Cs release from irradiated particles has been studied extensively, the fundamental chemistry of the interactions of Cs with the SiC coating layer of TRISO particles, and the mechanisms of Cs migration through this layer, is not well understood.

The Advanced Gas Reactor (AGR) Fuel Development and Qualification Program is currently developing and irradiation testing state-of-the-art coated particle fuel for use in the Very High Temperature Reactor (Petti et al. 2005). The issue of Cs behavior in irradiated particles has been identified as a concern, and better data on Cs reactivity, solubility, and diffusion behavior in SiC is needed to support fuel particle modeling activities.

3.5.2 Experimental plan and apparatus

Initial workscope for this laboratory-directed research and development (LDRD) included a study of fission product Cs interactions with the candidate materials. Because of the very different properties of cesium, including a very low melting point, the experimental approach is significantly different than for the platinum-group metals. Budget reductions in years 2 and 3 resulted in a reduction in workscope for the project, and Cs studies were not pursued. However, an apparatus has been designed for reacting sample materials with Cs vapor at temperatures as high as 2000ºC. The experiment is based on that of Coen and Quataert (1972) and is designed to provide a specific vapor pressure of cesium by controlling the temperature of a Cs reservoir that is attached to the sample chamber (Figure 42).

The sample chamber consists of a 0.75” tantalum tube with a small section of 0.25” tantalum tube welded to the bottom. The 0.25” tube acts as the Cs reservoir, and is placed inside a machined recess in a solid copper block. The copper block is heated to as high as 550ºC using a high temperature tape heater, and the temperature of the Cs reservoir is monitored by a thermocouple embedded in the copper block. The sample is placed in a holder suspended from the top of the 0.75” tube by a second 0.375” tube welded to a top plate. The inside of the 0.375” tube is open at the top, and acts as a well at which the temperature near the sample can be read using an optical thermometer. After a sample is placed on the holder, the entire sample chamber, consisting of all three tantalum tubes, is electron-beam welded closed in a vacuum.

The sample is heated inductively to temperatures as high as 2000ºC. A quartz tube is placed over the outer tantalum tube and the space inside is filled with flowing argon to prevent oxidation of the tantalum. The argon is preheated prior to being injected into the quartz tube so that no cold spots are created between the Cs reservoir and the sample. Thermal calculations were performed to verify that the Cs reservoir is the coolest part of the system.

Parts have been acquired to fabricate this experimental apparatus. The AGR program has allocated follow-on funding to pursue the Cs interaction experiments in FY 2007. It is expected that these will initially be performed only on several different types of SiC, as this has the greatest immediate relevance to the current coated particle fuel development activities. Future experiments may expand the work to include alternative particle coating material candidates studied in this LDRD project (for example, ZrC).

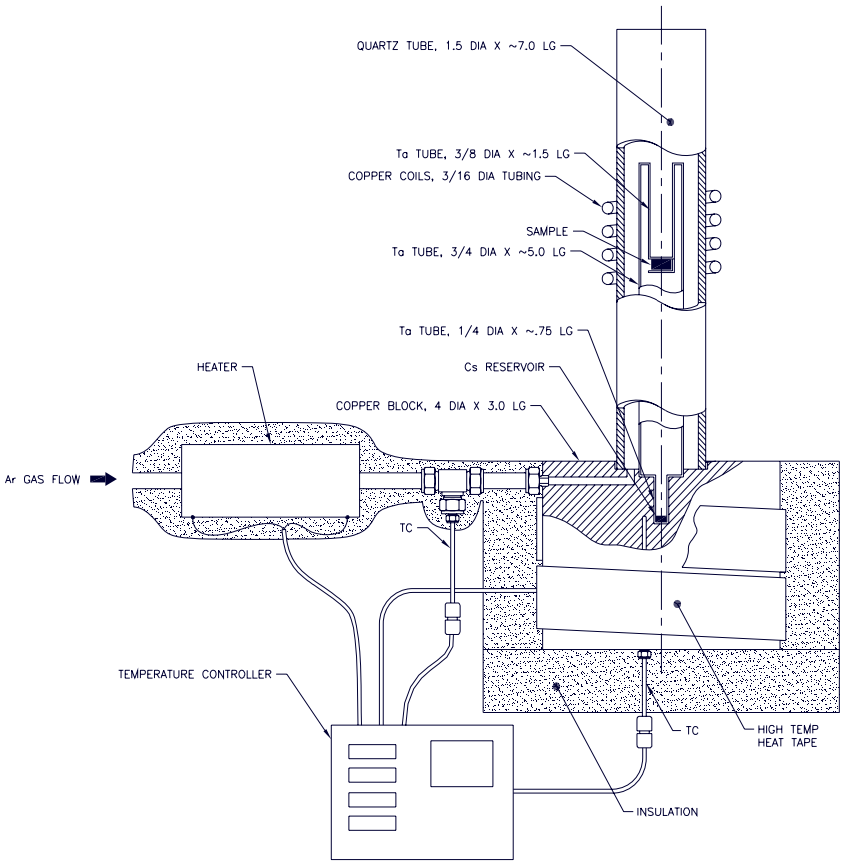

Figure 3.42. Experimental apparatus for exposing SiC samples to Cs vapor.

3.6 Acknowledgments

The authors would like to acknowledge the contribution of Tammy Trowbridge at the INL for the SEM and AFM analyses.

3.7 References for Section 3

Bhanumurthy, K. and R. Schmid-Fetzer, 2001, "Interface Reactions Between Silicon Carbide and Metals (Ni, Cr, Pd, Zr)," *Composites: Part A,* Vol. 32, pp. 569-574.

Chen, Liang-Yu, Gary W. Hunter, Philip G. Neudeck, Gaurav Bansal, Jeremy B. Petit, and Dak Knight, 1997, "Comparison of Interfacial and Electronic Properties of Annealed Pd/SiC And Pd/SiO_2/SiC Schottky Diode Sensors," *Journal of Vacuum Science and Technology A,* Vol. 15, pp. 1228-1234.

Coen, V., H. Hausner, and D. Quataert, 1972-1973, "Cesium Migration in Silicon Carbide," *Journal of Nuclear Materials*, Vol. 45, pp. 96-104.

Ellner, M., 2004, "Bond Energy in Palladium and Platinum-Rich Alloys with the A^4 Transition Metals," *Journal of Alloys and Compounds*, Vol. 366, pp. 222-227.

Massalski, Thaddeus B., (Ed), 1990, *Binary Alloy Phase Diagrams, 2nd Ed., Vol. 3,* ASM International.

Ogawa, T., and K. Ikawa, 1986, "Reactions of Pd with SiC and ZrC," *High Temperature Science,* Vol. 22, pp. 179-193.

Petti, David, Richard Hobbins, James Kendall, and John Saurwein, 2005, "*Technical Program Plan for the Advanced Gas Reactor Fuel Development and Qualification Program*," INL/EXT-05-00465, Rev. 1 August 2005.

Reed-Hill, Robert E., and Reza Abbaschian, 1992, *Physical Metallurgy Principles, 3rd Ed.,* PWS-Kent Publishing

Rijnders, M. R., A. A. Kodentsov, J. A. van Beek, J. van den Akker, and F. J. J. van Loo, 1997, "Pattern Formation in Pt-SiC Diffusion Couples," *Solid State Ionics*, Vol. 95, pp. 51-59

Roy, S., S. Basu, C. Jacob, and A. K. Tyagi, 2002, "SIMS and RBS Study of Thermally Annealed Pd/β-SiC Interfaces," *Applied Surface Science,* 202, pp. 73-79.

Suzuki, Hiroshige, Takayoshi Iseki, and Tetsuji Imanaka, 1977, "Reactions Between SiC and Pd or CeO_2 at High Temperatures," *Journal of Nuclear Science and Technology*, Vol. 14, pp. 438-442.

Tiegs, T.N., 1982, "Fission Product Pd-SiC Interaction in Irradiated Coated-Particle Fuels," *Nuclear Technology*, Vol. 57, pp. 389-398.

Villars, Pierre, Alan Prince, and H. Okamoto (Eds.), 1995, *Handbook of Ternary Alloy Phase Diagrams*, ASM International.

Villars, P., and L. D. Calvert (Eds.), 1991, *Pearson's Handbook of Crystallographic Data for Intermetallic Phases, 2nd Edition,* ASM International.

Weissmüller, Jorg, and Hendrik Ehrhardt, 1998, "Segregation-Induced Instability of Nanocrystalline Line Compounds," Physical Review Letters, Vol. 81 pp. 1114-1117.

Yokoyam, H., H. Numakura, and M. Koiwa, 1998, "The Solubility and Diffusion of Carbon in Palladium," *Acta Mater.*, Vo. 46, pp. 2823-2830

4. ION IRRADIATION

4.1 Background

Little data on the response to radiation damage at high temperatures currently exists for the candidate carbide and nitride materials investigated in this study. Although these candidate ceramic matrix materials for new fuel types are currently being irradiated in the Advanced Test Reactor and are slated for irradiation in the French LMFBR Demonstration Plant (PHENIX) fast test reactor, the limited neutron exposure and limited available irradiation temperatures that will come available will be insufficient to fully understand the microstructural stability under radiation. The primary irradiation effects occurring in ceramics under radiation are swelling, decrease in thermal conductivity, and changes in mechanical properties (Ossi 2001, Yano 1994, Hurley and Bunch 1980).

Dimensional changes in ceramics under radiation can be caused by several mechanisms such as amorphization, lattice strain, void swelling, and other mechanisms. Swelling at low temperature is due to amorphization and lattice strain. As temperature is increased, in the lattice strain regime, the number of surviving defects is reduced due to temperature-enhanced diffusion and recombination of point defects that reduces the driving force for lattice strain. At very high temperature, swelling can occur due to the formation and growth of voids. In the intermediate temperature range between lattice strain and void swelling, the dimensional changes due to swelling may be acceptable. The exact temperature at which the lattice strain and void swelling are the dominant mechanism is dependent on the specific ceramic. For ceramics with a hexagonal crystal structure, such as SiC, anisotropic swelling may occur. Swelling due to lattice strain typically saturates after a few dpa where void swelling may increase with increasing dose.

The thermal conductivity of all ceramics degrades with neutron irradiation and tends to saturate at a very low dose (a few dpa). The cause of this degradation in thermal conductivity is phonon-scattering by irradiation-induced defects (primarily vacancies and small vacancy clusters). Although the non-irradiated thermal conductivity is dependent on the sample material and processing route, the thermal conductivity following radiation is a function of the radiation parameters that drive the final microstructures. The unirradiated thermal conductivity is not a good metric for selecting materials with the highest irradiated thermal conductivity. Thermal conductivity typically saturates after less than 1 dpa.

With the exception of graphite and very limited information on alumina, magnesium aluminate spinel, and silicon carbide, there is very little information on the effect of irradiation on the strength, elastic modulus, or fracture toughness of ceramics, especially at higher temperature. The change in fracture toughness as a function of radiation is a critical data need for advanced fuel forms.

Proton irradiation is the primary tool for carrying out irradiation studies. Although, like any ion irradiation technique, proton irradiation cannot provide an irradiated volume sufficient to perform bulk mechanical testing, it is a fast and economical technique for studying the effect of radiation on microstructures. Since all bulk property changes are linked to microstructural changes, analysis of samples following proton radiation provides key information on radiation stability. Proton irradiation has several significant advantages over neutron irradiation in studying structural materials degradation (Bringas et al. 2005): (a) it is significantly less expensive than neutron irradiation; (b) the irradiation time is substantially shorter; and (c) sample activation is negligible so that extensive characterization is more straightforward. Figure 4.1 is example of the utility of proton irradiation and shows that the trends in swelling for steels irradiated with neutrons, protons, and heavy ions all follow the same experimental trends.

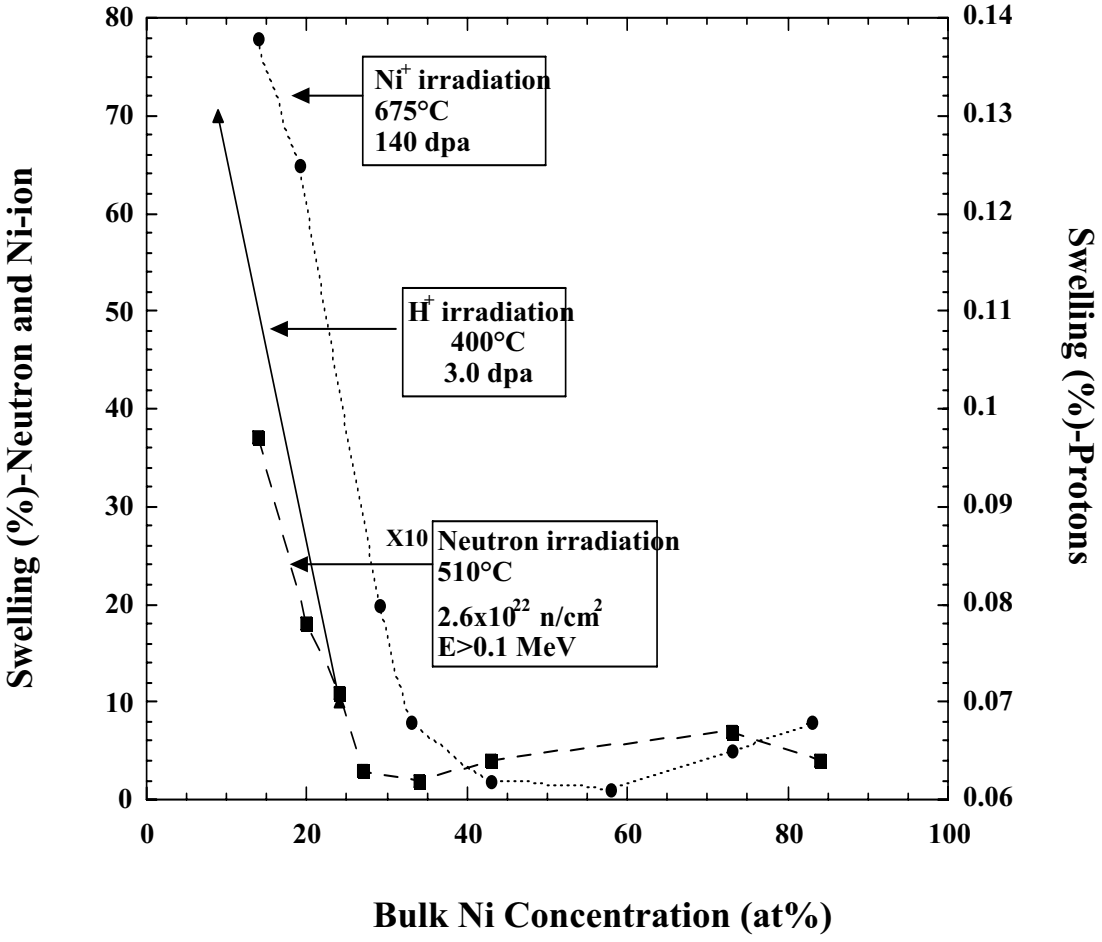

Figure 4.1. Swelling as a function of bulk nickel content. The trends are the same regardless of irradiating particle.

However, there are some limitations of proton irradiation that must be recognized during analysis, besides the inability to perform bulk mechanical tests on irradiated material. Since only a few MeV are required to surmount the Coulomb barrier for light ions, there is a minor amount of sample activation that increases with proton energy. The final energy chosen for the irradiation is based on the balance between irradiation depth and sample activation. Additionally, depending on the particular ceramic, the basic radiation induced primary damage may be influenced by radiolysis (electronic excitations generated by interaction with ionizing radiation).

Due to the relatively low neutron fluxes present in fast test reactors as compared to proton beams from ion accelerators, the displacement rates from neutron irradiations are considerably lower. It is important here to point out this fundamental difference and discuss how proton irradiation experiments can be modified to adequately compare to neutron experiments. Based on Mansur's development (Mansur 1994), a rough estimate of radiation induced changes in microstructures can be made by defining a variable, N_s, as the number of point defects absorbed at sinks and holding this value constant. For a given total dose, the proton and neutron irradiation temperatures must have the following relation for the difference in neutron to proton dose rates to have no effect on N_s:

$$T_2 - T_1 = \frac{\left(kT_1^2 / E_v^m\right)\ln\left(K_2/K_1\right)}{1-\left(kT_1/E_v^m\right)\ln\left(K_2/K_1\right)} \qquad \text{(Eq. 4.1)}$$

In Eq. 4.1 T is temperature, k is Boltzmann's constant, E_v^m is the vacancy migration energy, and K is the displacement rate (Mansur 1994). With values for the migration energy, proton irradiations can be conducted such that the resulting microstructure will be very similar to those experiments using neutrons to similar doses.

4.2 Experiment, Results and Discussion

4.2.1 Experimental Setup

4.2.1.1 Beamline Design and Construction. A beamline and sample stage for performing materials irradiations have been constructed at the UW Tandem Accelerator Facility and High Temperature Radiation Stage. This accelerator is a 1.7 MV machine capable of accelerating protons up to 3.4 MeV. Samples are irradiated in the form of 3 mm diameter disks coupled to a metallic stage through a graphite foil which can provide enough compliance to ensure samples of slightly varying thickness are in sufficient contact with the stage for adequate temperature control. Fifteen different samples can be irradiated simultaneously and temperature is monitored and controlled through beam heating and a stage temperature controller. The rastered irradiation beam is centered on the target via an aperture system with total beam current measured to provide a measure of radiation dose.

The primary goal of the experimental system is to produce radiation damage similar to that occurring in a gas-cooled fast reactor core. The radiation is produced by a linear accelerator, a National Electrostatics Corporation (NEC) 5SDH-4. The major increase in particle energy is due to an electrostatic field produced by the Pelletron® accelerator (Davis 2001), which operates similarly to a Van de Graff machine in which charge is accumulated on an insulated terminal thereby creating an electric field. Ions are produced from the Source of Negative Ions by Cesium Sputtering (SNICS), shown schematically in Figure 4.2. Cesium is heated and vaporized into the source chamber, whereupon it is ionized by an energized filament coil while some condenses on the cool cathode surface. The ionized cesium is accelerated toward the cathode by an applied potential, and the cathode material is sputtered. As neutral and positively charged sputtered atoms pass through the condensed cesium layer, they pick up electrons and become negatively charged. The SNICS allows an ion beam of virtually any element to be produced as long as a cathode can be made containing the element.

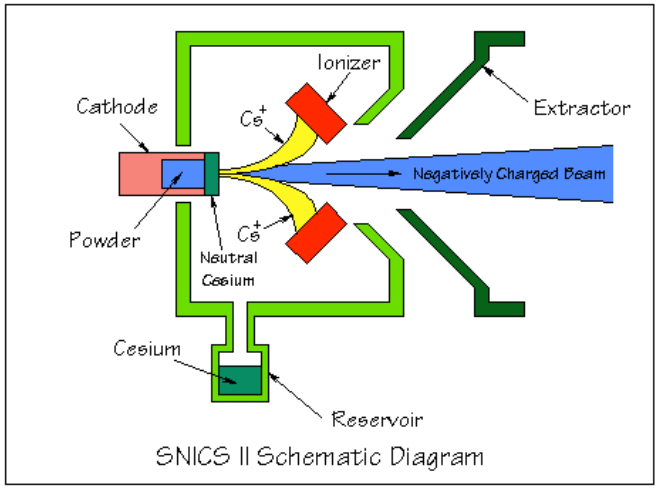

Figure 4.2. Schematic diagram of SNICS (Univeristy of Notre Dame 2006).

4.2.2 Stage Design and Construction

The experimental stage needs to incorporate heating and cooling capabilities and a reliable method for positioning and securing samples while minimizing interference with monitoring equipment and the ion beam. A cartridge heater was the best choice based on reliability and ease of implementation. The bore used to house the heater was machined to a high tolerance to provide good heat transfer. The heater size and power capabilities were decided upon after considering radiative and conductive heat transfer losses within the chamber. In addition to the heater bore in the back end of the stage two cooling circuits were also machined to provide an extra measure of control.

The stage consists of a flange welded to a steel cylinder, a sample holding plate, and a face plate, as shown in Figure 4.3. The samples, *Ø*3mm x *T*0.30mm disks, are placed in wells milled into the sample plate which is then attached to the stage and precisely positioned using dowel pins. By making the sample holding mechanism independent of the flange, modifications to the system are easily implemented. A facing plate is then placed over the sample holding plate to secure the samples. Slots in the facing plate eliminate interfering reflection to the camera and expose a great amount of the sample to the beam. The sample holding plate and facing plate also work to secure three thermocouples.

The experimental temperature is achieved by heating the chamber via a Gaumer GB301X-500-CB cartridge heater to a temperature below that which will be reached when the beam is introduced. The relation between beam power and the sample temperatures has been studied to determine the ultimate sample temperature before exposure, shown in Figure 4.4. To sufficiently thermally couple the beam, the samples, and the stage, Grafoil GT-B 0.127mm thick flexible graphite is placed between the samples and sample plate. Due to the Grafoil's compressibility, an important advantage over many other candidates, adequate pressure is achieved between interfaces to allow ample heat transfer. Moreover, due to the Grafoil's compressibility variations in sample thickness can be accommodated. Three K type thermocouples and a Mikron 7302 infrared camera are used to monitor the sample temperatures. The thermocouples are fastened to the sample plate, and their readings are used to calibrate the local sample emissivities via the camera prior to beam exposure. To better facilitate the acquisition of the infrared signals the stock sapphire viewport window was replaced with a custom built zinc selenide window. The ZnSe allows 90% transmission between 8 and 14 micron wavelengths which corresponds to the temperatures at which the experiment is conducted. During an irradiation the camera can be used to monitor differences in sample temperatures caused by beam irregularities.

The beam is rastered as it approaches the stage to achieve an even distribution of current over the sample area. To ensure the beam maintains a centered position throughout the length of an irradiation the current from four electrically isolated aperture plates is monitored. To achieve this isolation, tantalum plates are fastened to an alumina base which is then aligned and secured with the chamber via a collar and set screws, as shown in Figure 4.5. The beam is considered centered on the stage when opposing plates (top-bottom and right-left) read similar currents. The aperture also defines the area of the irradiation which is used in calculating the flux and irradiated doses of the samples. Current readings from the individual aperture plates as well as the from the stage are lead out of the chamber and terminated at separate picoammeters, each of which gives a proportional output that is recorded and monitored via a National Instruments DAQ. Monitoring of the stage current would be impossible if not for ceramic breaks which isolate the chamber from ground.

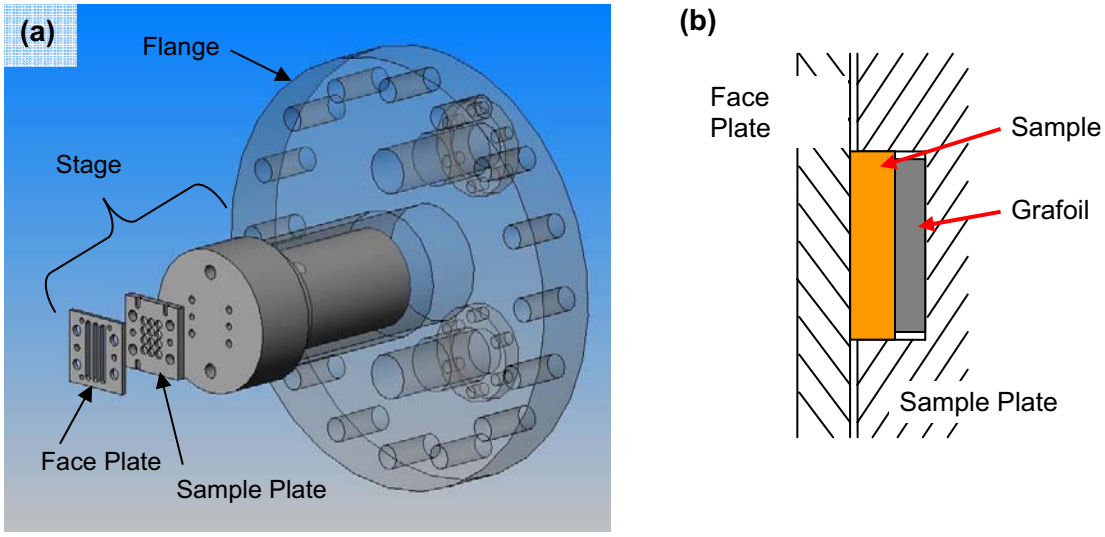

Figure 4.3. (a) Stage design. (b) Schematic of sample securing components.

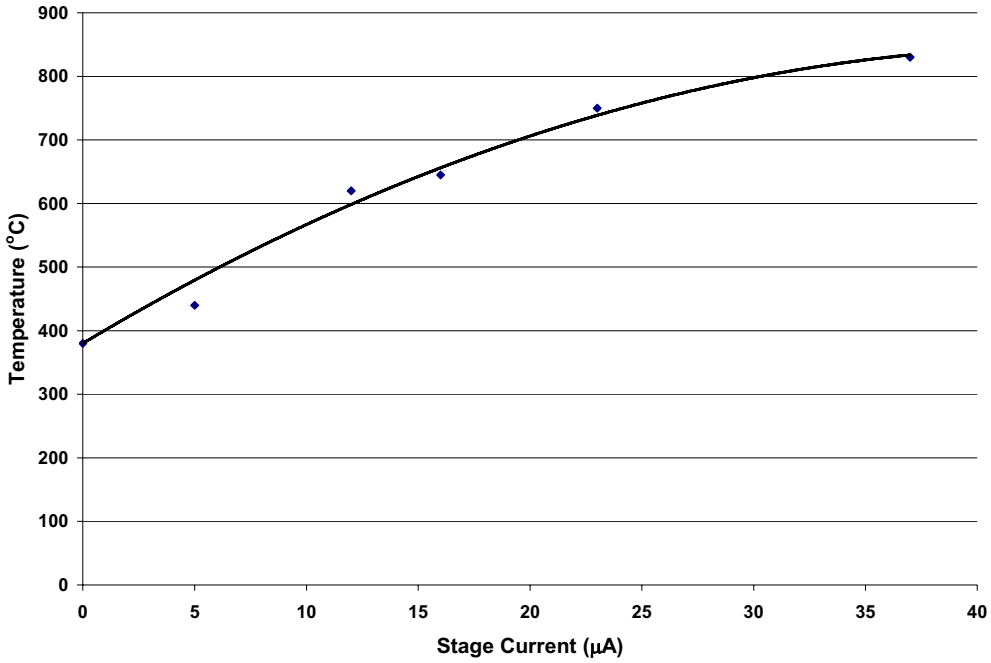

Figure 4.4. Temperature increase of stage due to beam exposure.

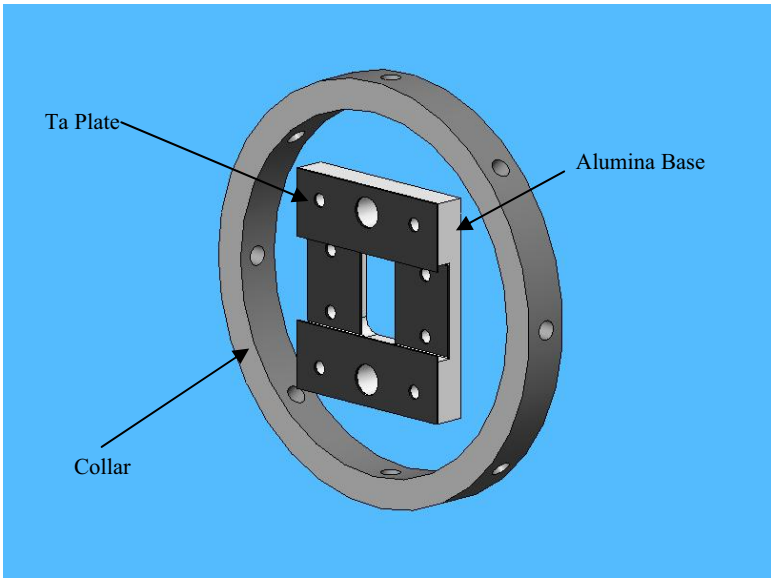

Figure 4.5. Aperture (set screws are not shown).

4.2.3 Beamline Shielding

High radiation fields, up to 150mRem/hr at the source, are produced by our experiment when the accelerated ion beam collides with the sample stage. Further investigation showed that radiation was present at the two Faraday cups after the accelerator as well, which are used to focus and steer the beam down to the stage. Radiation was only produced when the beam was being focused on the cups and decreased to almost zero after the beam was removed. Shielding was constructed for these three points, i.e. the stage and both cups. After the shielding was constructed, the current was adjusted until the radiation levels were under 2 mRem/hr at the shielding and a beam current of ~40μA was achieved.

The three main sources of radiation are gamma rays, x-rays, and neutrons. The gamma rays and x-rays are stopped by high "Z" materials, which have larger absorption cross section. Lead is common gamma ray shielding. The neutrons are slowed down by low "Z" materials. To slow the neutrons, polyethylene was selected as the primary stopper. To save the cost for the shielding materials, standard concrete blocks and boronated blocks were used and they function well. The boronated blocks have implanted boron which can absorb the neutrons. The concrete blocks contain high and low "Z" materials in its composition, functioning as shielding for both main types of radiation. A steel frame was constructed to support concrete blocks and prevent their moving. One inch thick sheets of polyethylene were added to the outside of the concrete blocks for additional neutron shielding. At Farady cups, 1/8" thick lead shielding was wrapped and tied with cables. This configuration gave radiation levels under the 2 mRem/hr as expected. Shielding was only constructed on the side facing the control console. During beam operation, the backside is blocked off and the radiation levels are under 5mRem/hr.

The stage is the major source of radiation during the experiment, with levels reading up to 150mR/hr. It was the primary focus of the shielding design. Gamma levels are fairly low and the concrete blocks offer enough shielding. Due to the complexity of the stage, wrapping the stage with lead was not a feasible option. The stage was entombed with shielding on every side except for the bottom. The concrete floor provided adequate shielding for the experiment in that direction. All sides were shielded due to the backscatter of the radiation being above acceptable levels. Another requirement of the shielding is that two sides needed to be removable so that there is access to the stage. Shielding was designed so that there is fixed shielding upstream and downstream of the beam direction. The sides of the stage were the removable sides. Concrete blocks were the main source of shielding for the stage, while the top is shielded by 2" thick polyethylene, to lower the neutron levels.

Safety was checked after the shielding was in place and secured. A beam of 40uA at 2.671 MeV was focused onto the stage and safety conducted a radiation survey. It was determined that the shielding was adequate for the operating conditions.

4.3 Irradiations

4.3.1 SRIM Calculations

Stopping and the range of ions in matter (SRIM) calculations and subsequent analysis were performed to determine the damage depth in TiC, TiN, ZrC, ZrN, and SiC under proton irradiation at 2.6MeV, and the corresponding parameters are listed in Table 4.1 for the full damage cascade mode calculation, the ion was H^+, and incident angle was set to 0^o.

Depth profiles were calculated with two methods. For the K-P Model calculations, the range tables were calculated using transport of ions in satter (TRIM) Quick Range Tables which gave a maximum depth profile. The damage curves from the SRIM Full Damage Cascade Mode calculation were used to determine the appropriate depths for the damage that is most desirable. Figures 4.6–4.10 show the collision events vs. depth graphs for five different materials.

The depth of greatest interest is the relatively flat region before the peak. This region is where dpa is calculated. The damage rates were taken from the Full Damage Cascade calculation. Table 4.2 lists the minimum and maximum values of the depth of the flat region. This is also the range in which samples will be made for examination in the TEM.

Table 4.1. Assumed TRIM parameters for full damage cascade model calculations.

	TiC	TiN	ZrC	ZrN	SiC
Layers	Ti, C	Ti, N	Zr, C	Zr, N	Si, C
Mat. Den. (g/cm^3)	4.93	5.4	6.56	7.32	3.18
Sample width (μm)	500	500	500	500	500
Total number of ions	50,000	50,000	50,000	50,000	50,000
Displacement Energies	Ti: 25 eV	Ti: 25 eV	Zr: 25 eV	Zr: 25 eV	Si: 35 eV
	C: 28 eV	N: 28 eV	C: 28 eV	N: 28 eV	C: 21 eV

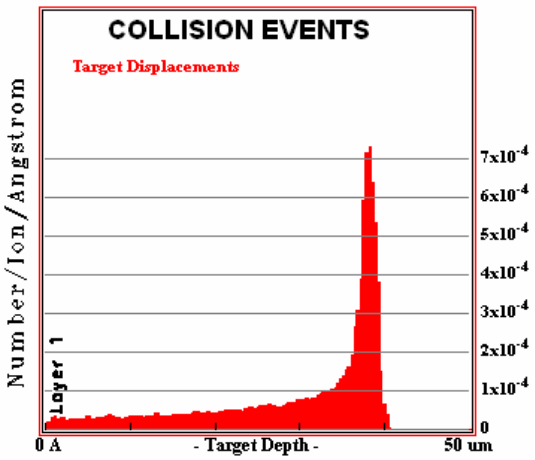

Figure 4.6. Collision events vs. depth for TiC.

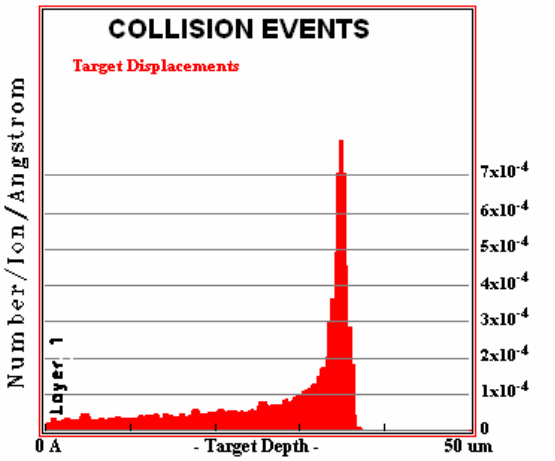

Figure 4.7. Collision events vs. depth for TiN.

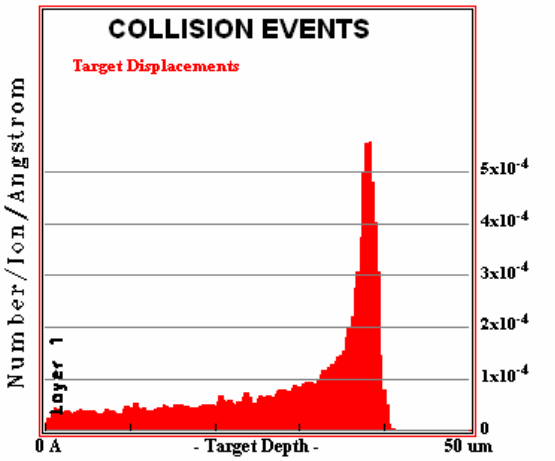

Figure 4.8. Collision events vs. depth for ZrC.

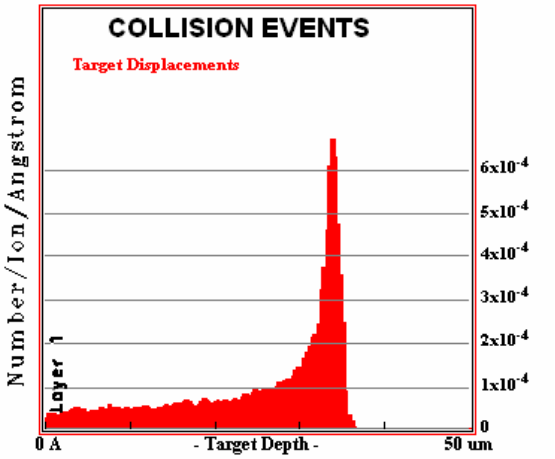

Figure 4.9. Collision events vs. depth for ZrN.

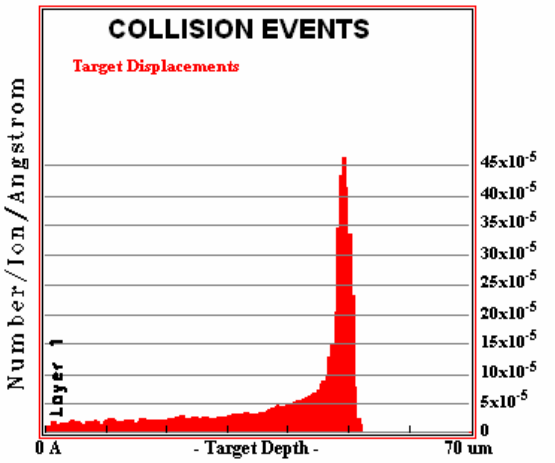

Figure 4.10. Collision events vs. depth for SiC.

Table 4.2. The range of depth in the region with "flat" damage values.

	Min depth of flat region	Max depth of flat region
TiC	0 μm	35 μm
TiN	0 μm	35 μm
ZrC	0 μm	35 μm
ZrN	0 μm	30 μm
SiC	0 μm	45 μm

4.3.2 DPA Rate Calculations

DPA rate was calculated using the ion beam parameters and damage values determined with SRIM. The governing equations are addressed as following. The flux is calculated using the equation:

$$\Phi = \frac{I}{q * Ar} \qquad \text{(Eq. 4.2)}$$

where Φ is the flux, I is the ion beam current, q is the electron charge, and Ar is the irradiated area of the sample. For our experiments, the flux will be constant for all the samples. The ion beam current was selected as 40 μA, an electron charge of 1.602×10^{-19} Columb, and the irradiated area was calculated according to the aperture size.

$$Ar = \frac{Ar_{aperture}}{Ar_{sample}} Ar_{sample} = Ar_{aperture} \qquad \text{(Eq. 4.3)}$$

where $Ar_{aperture}$ is the area of the aperture (16 mm x 10 mm) and Ar_{sample} is the area of the sample ($\pi*3^2$ mm^2). The number density of the sample was calculated:

$$N = \frac{\rho * A_v}{M} \qquad \text{(Eq. 4.4)}$$

where N is the number density, ρ is the density of the sample, A_v is Avogadro's number, and M is the molar mass of the sample. Each material will have individual values for these parameters, and they are listed in Table 4.3. The dpa rate can then be calculated with the equation:

$$dparate = \frac{D * \Phi}{N} \quad \text{(Eq. 4.5)}$$

where *dparat*e is the number of dpa per second and D is the damage value for the sample. The dpa rates were calculated and listed in Table 4.4.

Since the intent was to make hardness indentations on the irradiated samples, the radiated region must be at least ten times as thick as the indentation depth to eliminate the thickness effects. The depth of the indent is 1/7 the depth of the diagonal (ASTM 1327-03), and the minimum needed sample thickness, indent diagonal, indent depth, and depth of the flat damage region are listed in Table 4.5. These data indicate that hardness testing may be conducted on irradiated samples and only include the irradiated zone, with the exception of TiN. However, the TiN values were obtained for an extremely porous sample and not for new samples recently obtained. Therefore, further testing is needed before any determination can be made regarding TiN.

Table 4.3. Sample parameters for dpa rate calculations.

Sample	Atomic Mass (g)	Density (g/cm^3)	Damage (10^{-5} m^{-1})
TiC	60	4.93	4
TiN	62	5.4	4.375
ZrC	102	6.56	5
ZrN	104	7.32	5.2
SiC	40	3.18	2.5

Table 4.4. dpa rates for each sample.

Sample	TiC	TiN	ZrC	ZrN	SiC
dpa rate (10^{-4} dpa/s)	0.126	0.130	0.201	0.191	0.082

Table 4.5. Required sample thickness, indent depth, and irradiation depth for each sample.

Sample	Minimum sample thickness (μm)	Diagonal (μm)	Indent Depth (μm)	DPA depth (μm)
TiC	33	23	3.3	35
TiN	61	43	6.1	35
ZrC	31	22	3.1	35
ZrN	43	30	4.3	30
SiC	33	23	3.3	45

4.3.3 Proton Irradiation Conditions

During the course of an irradiation the current from the ion source is very rarely constant over a long period of time which has implications throughout the system. The most apparent effect of the current instability is the ultimate temperature at the stage. While another, more obscure effect is the energy of the beam as it travels through the accelerator. As charged particles travel through the accelerator due to the terminal potential the ions load the corresponding electronics. The bottom line is that as more current travels through the accelerator more power is needed to maintain a constant terminal potential otherwise the terminal potential and thus the beam energy will decrease. Changes in beam energy effect the positioning of the beam at the stage due to magnetic and electrostatic steering components between the accelerator and the experimental chamber. To cope with these variations in beam current and energy the operator must make frequent, minor adjustments to the ion source power and electrostatic steering components to make sure the intended stage temperature is maintained and the beam is centered.

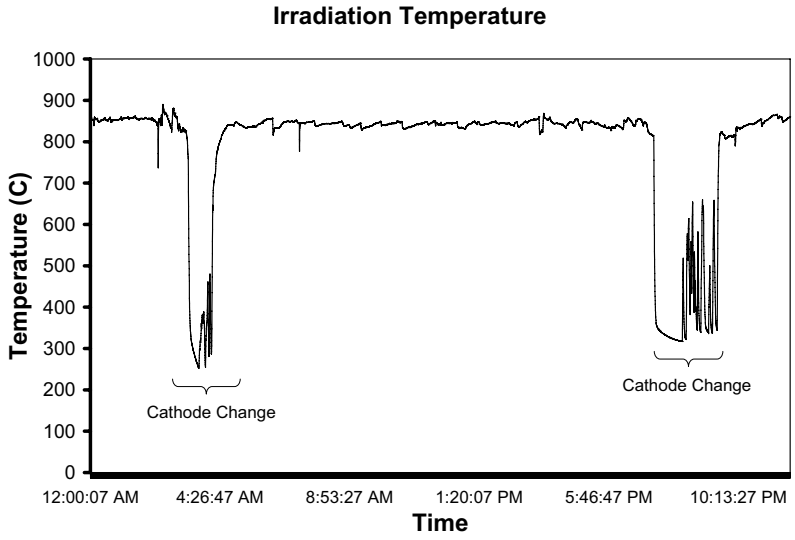

Figure 4.11. Temperature history during 3 dpa proton irradiation.

Another complexity associated with operational considerations is the need to change cathodes every 12 to 14 hours. Each cathode holds a limited amount of material to be sputtered to create the ion beam. When the source can no longer produce sufficient current, the source is powered down and a new cathode is installed. Figure 4.11 is a roughly 24 hour sample of data taken from an irradiation. Times during cathode changes are clearly distinguished by the pronounced drop in stage temperature, while the saw tooth look in the center of the graph is a result of adjustments to the source power needed to manage the stage temperature. The average temperature during this middle portion was 841°C with a standard deviation of 7°C.

4.3.4 Oxidation of Samples

Since the oxidation of the samples during irradiation could have significant impacts on the experiment results this issue was specifically addressed. Experiments were devised to measure oxidation rates of these samples in an environment that approximates that experienced during ion irradiation. The primary goal of these rough tests is to determine the thickness of oxide scale that can be expected during

the irradiation and aid in preparing TEM samples after irradiation. The experimental procedure and results are discussed below.

Oxidation experiments were conducted in a high temperature vacuum furnace at a pressure of approximately 10^{-5} Torr, and temperature 600, 800, 1000, and 1200ºC for 40 hours. The oxygen partial pressure (P_{O2}) in the furnace during the experiments is estimated assuming 20.9% oxygen in air and total pressure of 10^{-5} Torr. The partial pressure is then $3.2x10^{-4}$ accoring to Dalton's Law of Partial Pressures. Samples were polished to a 1 μm finish on both sides before testing. After testing, they were mounted in a carbon-based resin and polished as a cross-section to a 1 μm finish. Measurements of the oxide layer thickness were made from SEM micrographs. EDS was used to identify the main element (Ti, Zr, Si) in the ceramic and optical imaging was used to determine if the sample was carbide or a nitride. This is because the EDS cannot distinguish between C and N due to the low atomic number, and nitrides have a gold or orange color which can be seen using an optical microscope.

The average thickness of the oxidation layer was used to determine a parabolic rate constant for each sample at each temperature. The equation used to determine the parabolic rate constant is:

$$A = \frac{x^2}{2t} \qquad \text{(Eq. 4.6)}$$

where x is the average thickness of the oxidation layer and t is the time of the oxidation experiment, 40 hours for this set of experiments.

At least 20 measurements were taken on the oxidation layer for each sample at each side. Statistical analysis was conducted on each measurement set, including mean, standard error, median, standard deviation, sample variance, kurtosis, skewness, minimum, maximum, and the number of measurements. The average oxidation layers thicknesses for experiments conducted at 600, 1000, and 1200ºC are presented in Figure 4.12.

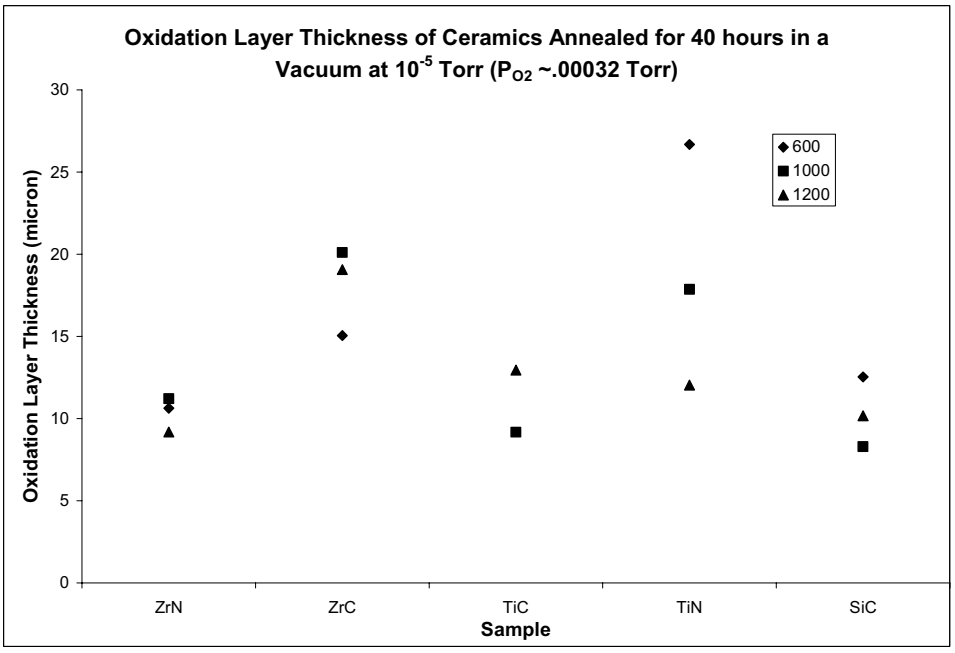

Figure 4.12. Average oxide layer thicknesses for ceramics oxidized in a vacuum of ~10^{-5} Torr.

4.4 References for Section 4

ASTM 1327-03, 2005, *Standard Test Method for Vickers Indentation Hardness of Advanced Ceramics*, ASTM International.

Bringas, F., M.T. Yamashita, I. D. Goldman, P.R. Pascholati, V. Sciani, 2005, "Measurement of Proton-Induced Reaction Cross Sections in Ti, Ni and Zr Near the Threshold," *AIP Conference Proceedings (2005), 769 (International Conference on Nuclear Data for Science and Technology, 2005, Part 2)*, pp. 1374-1377.

Davis, T., National Electrostatics Corporation, *Pelletron Accelerator Charging System*, http://www.pelletron.com/charging.htm, published 2001.

Hurley, George F. and James M. Bunch, 1980, "Swelling and Thermal Diffusivity Changes in Neutron-Irradiated Ceramics," *American Ceramic Society Bulletin*, Vol. 59, pp. 456-8.

Mansur, L.K., 1994, "Theory and Experimental Background on Dimensional Changes in Irradiated Alloys," *Journal of Nuclear Materials*, Vol. 216, pp. 97-123.

Ossi, Paolo M, 2001, "Structural Stability of Irradiated Ceramics," *Journal of Nuclear Materials*, Vol. 289, pp. 80-85.

University of Notre Dame, 2006, *SNICS II Sputter Ion Source*, http://www.nd.edu/~nsl/Research_Facilities/Snics/nsl_snics.html, published 2006.

Yano, Toyokiko, 1994, "Structural Properties and Neutron Irradiation Effects of Ceramics," *Materia*, Vol. 33, pp. 1369-79.

5. MECHANICAL PROPERTY MODELING

5.1 Introduction

One of the key issues related to the development of coated particle fuels is the thermomechanical interaction of the coating and buffer layer with the fuel kernel. In this section, we describe finite element analyses of such a fuel particle, taking into account differential expansion, gas pressure, creep, and swelling. The fuel is analyzed for cooling from room temperature, heating to operating temperature, long term operation, and shutdown. For this purpose, the fuel is assumed to be a spherical kernel, coated by a low density buffer layer, which is subsequently surrounded by a high density coating of the same material. The buffer is intended to help to absorb released fission gases, to accommodate differential expansion, and to absorb fission recoil atoms. The geometry of the "BISO"-type fuel form is shown schematically in Figure 5.1.

The buffer layer is porous in order to reduce its stiffness (and the resulting pressure on the coating) and to accommodate released fission gases. It is composed of the same material as the coating. By using the same material for the buffer as the coating, there is reduced expansion mismatch and less chance of chemical incompatibilities. These fuel particles would typically be employed by placing them in a ceramic matrix composed of the same material as the particle's outer ceramic coating. With this design, there is only one major interface between different materials: the kernel and the buffer.

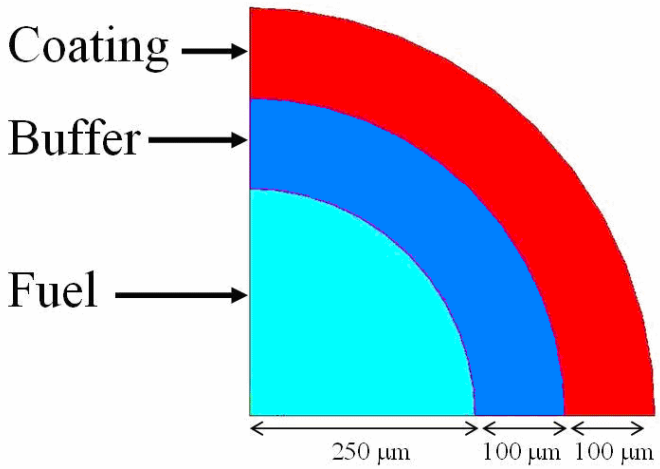

Figure 5.1. A quarter of the cross section showing the layers of a BISO micro fuel particle.

5.2 Modeling

The stress analysis is carried out using a commercial finite element code (ANSYS). The figure below is a picture of the model of the micro fuel particle. The micro fuel particle is a layered sphere, simulated with the 2-D shown in Figure 5.2.

By analyzing the model in a spherical coordinate system, only two dimensions need to be considered. This is because the symmetric nature of a sphere will produce the same values in both tangential directions. Therefore, in this model, only the stress in the radial direction and the tangential direction (which actually represents values for two dimensions) need to be found to analyze the entire sphere, as long as the geometry and loads are symmetric.

The material candidates investigated for the buffer and coating are SiC, TiC, ZrC, TiN, and ZrN. UC and UN are considered as fuel kernel materials. The baseline fuel form features a spherical fuel kernel with a 250 μm radius and buffer and coating thicknesses of 100 μm as seen in Figure 5.1. Buffer porosities of 50% and 75% are considered.

No significant temperature difference throughout the fuel particle is expected because these ceramics have high thermal conductivities and the small particle radius helps to maintain a low temperature gradient in the fuel.

The fuel particle coatings are assumed to be fabricated (by deposition from the vapor phase) at 1600ºC, at which point it is assumed there are no stresses on the particle at this initial temperature and time. The actual fabrication temperature will depend on the method employed, but this representative value is adequate for comparative purposes. Depending on the different steps and type of the fabrication of the fuel particle, this may not always be strictly true because this is a representative temperature of the fabrication process; however, it is assumed that the actual stresses at 1600ºC would be small compared to the stresses throughout the rest of its lifetime. The particle is then cooled to room temperature, heated to operating temperature in-reactor (assumed here to be 1100ºC), and then cooled again to room temperature after some period of operation. This temperature history is shown in Figure 5.3.

In all but the 3rd stress period (reactor operation) when the fuel particle stays at a constant temperature of 1100ºC, the differential thermal expansion of the layers is the predominant factor in the stress production. The stress from the thermal expansion in the fuel form occurs from the fuel shrinking more than the coating (and buffer) as the fuel particle cools. The coefficient of thermal expansion (CTE) dictates the amount of growth or shrinkage in the layers of the fuel particle due to changing temperatures. The CTE for the kernel and the coating materials are shown in Figure 5.4.

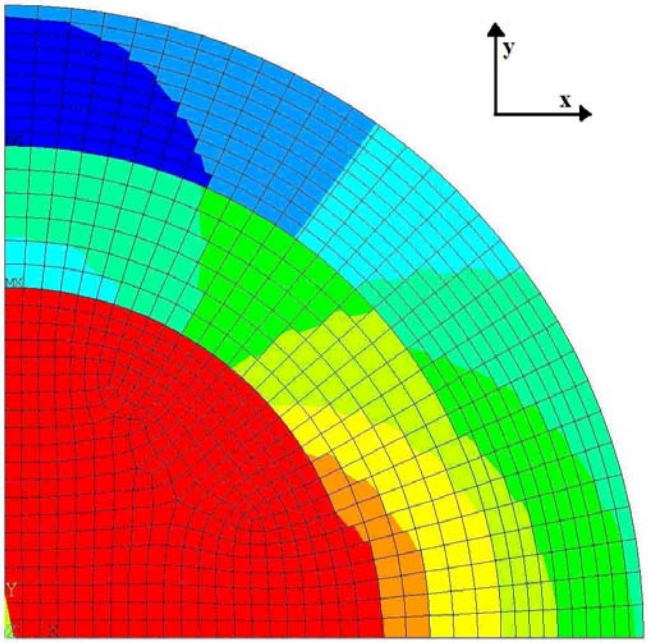

Figure 5.2. 2-D contour of the finite element model plotting x-component of stress in micro fuel particle. Dark blue represents compressive stress; red represents tensile stress.

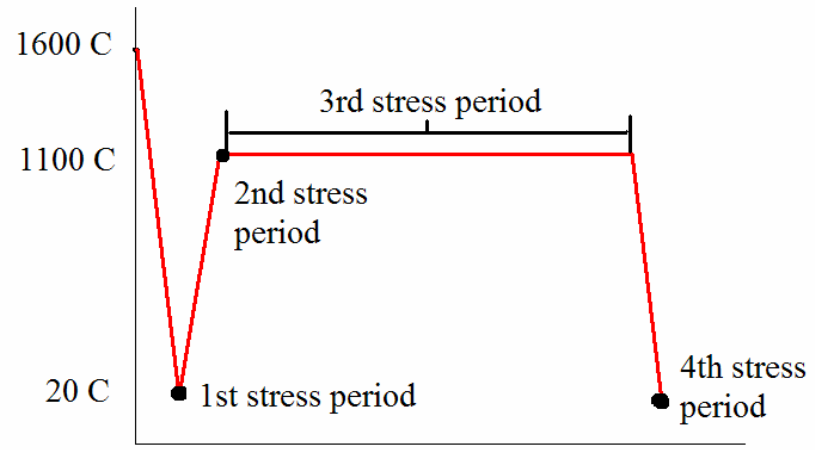

Figure 5.3. The temperature history of the life of the BISO fuel particle, as assumed in this analysis.

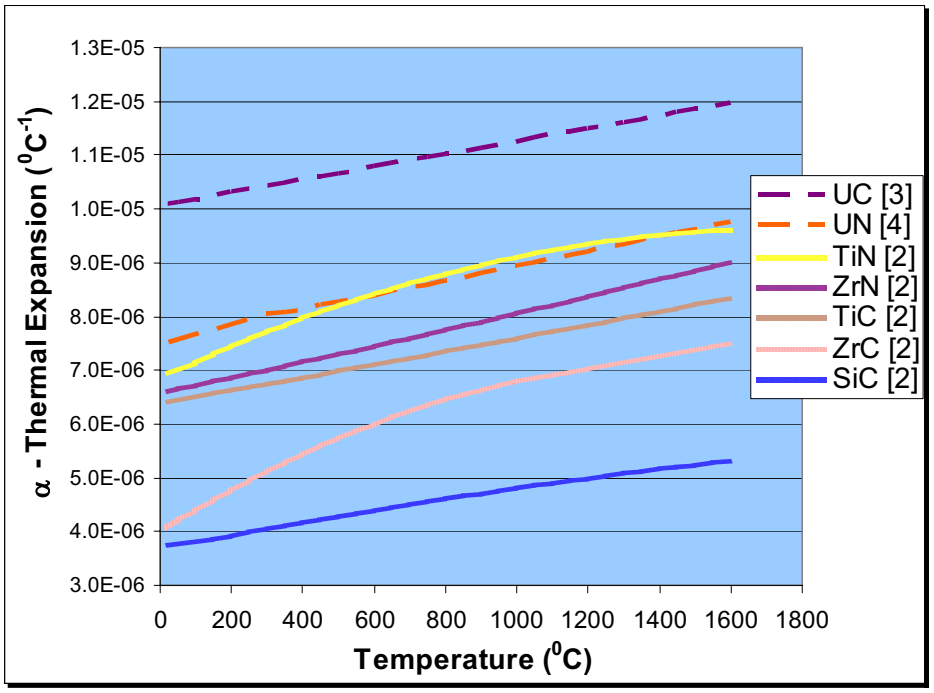

Figure 5.4. Average coefficients of thermal expansion for different fuels (dashed) and coatings (solid). All reference temperatures at 20ºC (Touloukian et al. 1977, Cahn et al. 1996).

The larger the difference in CTE between the fuel and the coating, the larger the magnitude of the stress will be in the particle because the difference in the rate at which the fuel and coating will shrink will be greater. From this, it is expected that UN and TiN have the most compatible thermal expansion of all the fuel and coating combinations.

In the 2nd period, the fuel temperature is increased to 1100ºC and the stress is decreased because this temperature is closer to the fabrication temperature.

In the 3rd period the reactor is assumed to be at full power, with commensurate production and release of fission gases, leading to pressure on the inside of the coating and swelling of the fuel. Using models presented previously (Petti 2004), the gas pressure is estimated to be approximately 4.8 MPa assuming 50% buffer porosity, 95% gas release, and one year of operation at a particle power of 63 mW (Table 5.1). The volumetric fuel swelling rate is assumed to be 9% per year for UC and 4.5% for UN. Thermal creep in the coatings is also included (see Table 5.2). No thermal creep is expected in the fuel kernel for this geometry, since the fuel is under a hydrostatic stress state. Coating (and buffer) swelling is assumed to be small compared to the fuel swelling, and no irradiation creep is included due to lack of available data.

The 4th and final stress period is after reactor shutdown when the temperature is reduced to room temperature (20ºC).

Table 5.1. Fuel particle parameters used in computations.

Fuel fission rate density	3.00×10^{13}	fissions/cm^3 s
Fuel kernel radius	250	μm
Buffer thickness	100	μm
Coating thickness	100	μm
Particle power	62.8	mW
Xe and Kr release fraction	95	%
gas pressure release	4.84	MPa/year
Kernel density (UC,UN)	(0.0143, 0.0113)	kg/cm^3
Annual Burn-up (UC,UN)	(31000, 24600)	MWd/mt per year
Annual Swelling (UC,UN)	(9, 4.5)	%

Table 5.2. Fuel kernel and coating materials properties used in computations.

Material	Elastic modulus (GPa)[a,b,c]	Poisson's ratio	Thermal Expansion	Creep[d,e]			
				$\dot{\varepsilon}$ [f] (s^{-1})	n	Q (kJ/mol)	T (^oC)
UN	265	0.27	Temperature dependent; see Figure 5.4	not considered - hydrostatic			
UC	225	0.28		not considered - hydrostatic			
TiC	470	0.19		5.55×10^{-6}	3	500	2300
SiC	410	0.14		1.39×10^{-5}	1	200	1600
ZrC	400	0.19		2.00×10^{-8}	3	600	1800
TiN	465	0.25		N/A			
ZrN	380	0.16		N/A			
Buffer	material and porosity dependent	0.33	(same as material)	(same as material)			

a. Cahn 1996
b. Bauccio 1994
c. Pierson 1996
d. Daniels 2002
e. Cannon 1983
f. $\dot{\varepsilon} = A\sigma^n \exp\left(\frac{-Q}{RT}\right)$

5.3 Results for Baseline Geometry

5.3.1 Cooling from Fabrication

Initially, the fuel particle will not have any internal stress when it is fabricated at 1600ºC. It is not until it begins to cool to a room temperature of 20ºC when the first stresses will occur. Thermomechanical stresses due to this cooling period are shown below. Figures 5.5 and 5.6 show the radial and tangential stresses, respectively, in the different candidate coatings, after cooling from fabrication. Cooling from fabrication causes the kernel to shrink more than any of the ceramic coatings, and stresses are dominated by tension in the radial direction and compression in the tangential for all material combinations analyzed. Note that in the following figures, positive stresses indicate tension and negative stresses indicate compression.

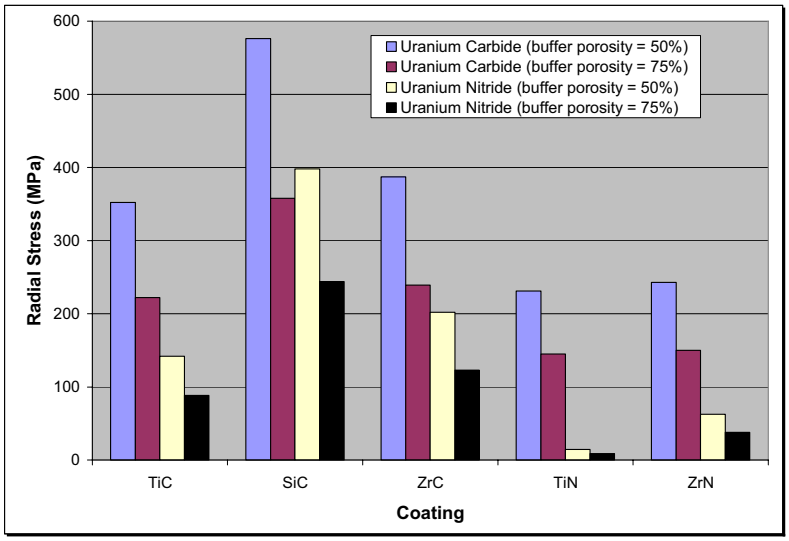

Figure 5.5. Maximum radial stress in the coating material after cooling from 1600ºC to room temperature.

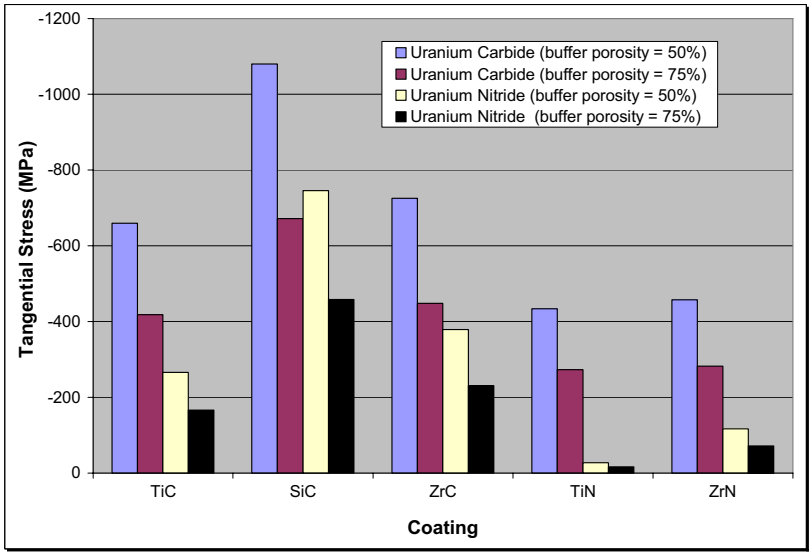

Figure 5.6. Maximum tangential stress in the coating material after cooling from 1600ºC to room temperature.

By comparing Figures 5.5 and 5.6, it can be seen that the absolute stresses in the radial and tangential directions are similar to each other for different kernels, coatings, and buffer porosities. Because the radius of the coating stays fairly constant, the tangential stress divided by the radial stress will also remain at a fairly constant ratio of approximately two. Therefore one can infer the stress in the radial direction from the values given for the tangential stress in this study. The maximum tangential and radial stress occurs on the inside of the coating. Because of the radius and thickness of the coating, the outside of the coating has a stress of about 75% of the maximum tangential stress. There is no radial stress on the outside of the coating because it is assumed the fuel particle is unconstrained (this is an area of future work).

5.3.2 Heating to Operational Temperatures

The stresses in the 2nd period react in very much the same manner as they did in the 1st stress period. Once again, the dominant effect is the thermal expansion. In fact, by comparing Figures 5.6 and 5.7, it can be seen that the different stresses in the 2nd period from the combinations of fuels and coatings have almost the exact same profile as the stresses from the 1st period.

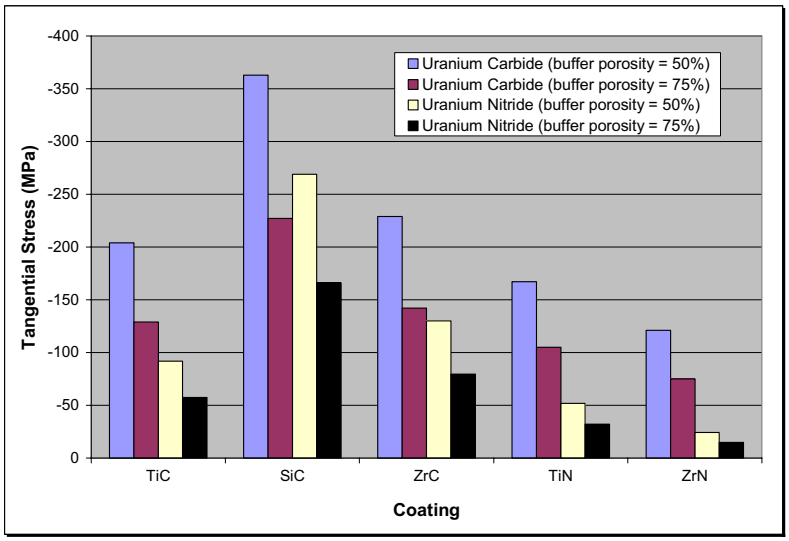

Figure 5.7. Maximum tangential stress in the coating material at 1100ºC.

5.3.3 Reactor Operation

The 3rd stress period is unique, because in this period, reactor conditions must be considered. As described before, these conditions include fuel swelling, coating and buffer creep, and fission gas pressure buildup. To better understand the fuel particle model, all of these conditions were tested individually with UC/TiC as a baseline.

5.3.3.1 Fission Gas Pressure. One of the operational processes is the pressure from fission gas release. This pressure will increase over time as gas is released from the kernel and accumulates in the porous buffer layer, which acts as a plenum. The values used for the thermomechanical models are calculated from the Redlich-Kwong equation of state (Petti 2004), with a conservative estimate of 95% fission gas release for both Xe and Kr. The fission gas pressure in the buffer was calculated to be 4.84 MPa per year in the first year, decreasing slightly to 4.69 MPa per year in the third year. When this is the only process within the fuel particle, this fission gas pressure pushes against the outer coating, and produces stresses as shown in Figure 5.8. As this figure shows, the gas pressure does not produce significant changes in the coating stress, only about 6 MPa on the coating. The actual coating stresses are likely to be even lower than predicted by this model because the fission gas release fraction from UN fuel may be well below the assumed 95% at these temperatures (El-Genk 2004).

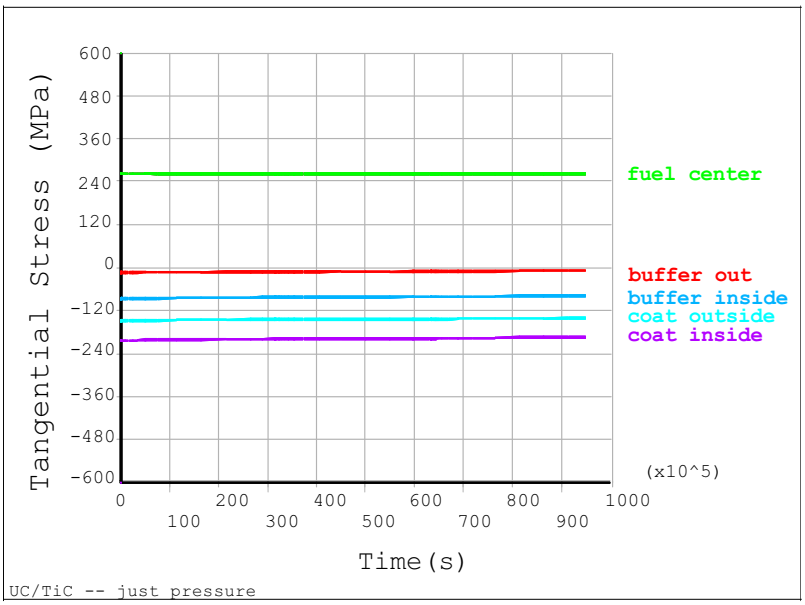

Figure 5.8. The tangential stress as the fission gas pressure increases in the BISO fuel over three years.

5.3.3.2 Swelling. Another of the operational processes is fuel swelling. Swelling is one of the largest concerns because of the type of fuels in consideration. Swelling in the fuel kernel for this analysis is considered to be isotropic and a function of the burn-up, temperature, and type of fuel.

For this analysis, the temperature during operation is constant at 1100ºC, the kernel is assumed to remain stoichiometric (despite fission), and the fuel fission rate density gives a burn-up of about 24,600 MWd/mt per year. A gas release of 95% is not assumed for the swelling as it is for fission gas pressure analysis. While 95% gas release is overly conservative for the stress from gas pressure, this would be an overestimate for swelling analysis considerations. Instead, experimental swelling results are used (based on the above criteria) instead of calculated predictions (based on gas release, among other things which are not well understood for UC). Matke shows that this criteria would result in about 9% swelling per year in UC (Matzke 1986), and this is what is used for the swelling analyses. However, this may be an underestimate because according to Ritzman (1970), these parameters could lead UC to swell 14% a year. Fuel swelling data is even less extensive for UN, but nitrides tend to show less swelling than carbides (Matzke 1986). UN appears to have a swelling rate half that of UC. Hence, a swelling rate of 4.5% per year is used for UN. The error associated with these numbers is expected to be large.

Swelling is first analyzed independently, once again using UC/TiC and a buffer porosity of 50%. The effect can be seen in Figure 5.9, which shows the dramatic increase in swelling stress with increasing burn-up (without creep relaxation).

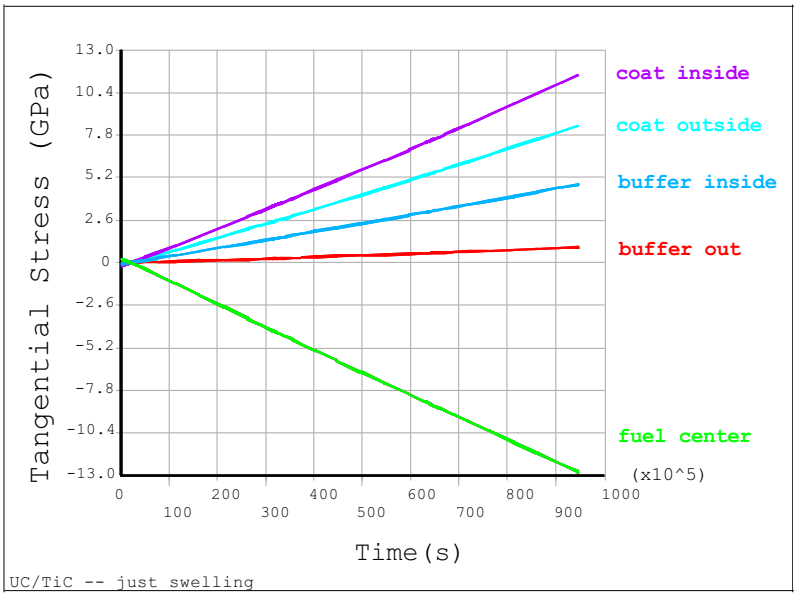

Figure 5.9. Tangential stress in the coating from the fuel swelling over the 3 years. No creep is included in this analysis, to demonstrate the potential of swelling to produce large stresses.

However, this analysis is simplified because it does not take into consideration that the elastic modulus in the kernel is dependent upon swelling and temperature. According to Cahn (Cahn et al. 1996), a temperature of 1100ºC will lower the elastic modulus by 10% in both UC and UN. He also reports the dependence of the elastic modulus of UC and UN as functions of fuel porosity. Increased porosity in the form of vacancies and gas bubbles is the major cause of swelling for these fuels. Assuming a swelling rate of 9% per year for UC, the kernel will have 27% porosity after three years. As reported by Cahn (Cahn 1996), the dependence of the UC modulus on porosity is:

$$E_p = 224.9(1 - 2.30 \times p). \qquad \text{(Eq. 5.1)}$$

Therefore the elastic modulus of UC will decrease by 49% after swelling for 3 years. These two changes in the elastic modulus will decrease the maximum tangential stress in the coating to 8.0 GPa. The ability of the coating stress to reach 8.0 GPa shows why swelling is the largest concern in this study as this result is many magnitudes beyond acceptable limits and it demonstrates the importance of creep in the process.

It is also important to recognize that swelling rate is dependent on the burn-up rate. However, the burn-up rate depends on particle power, which is assumed to be 63 mW for these results. If it is decided that more power is desired, this would proportionally increase the swelling rate as it would the gas pressure rate. This study recognizes at least 5 known possibilities which may help mitigate the stress from swelling: buffer porosity, kernel selection, coating swelling, particle parameters, and coating creep. The first two possibilities which could help mitigate this stress are increasing the buffer porosity and using a different choice for the fuel kernel. Both of these were individually tested, and can be seen below in Figures 5.10 and 5.11.

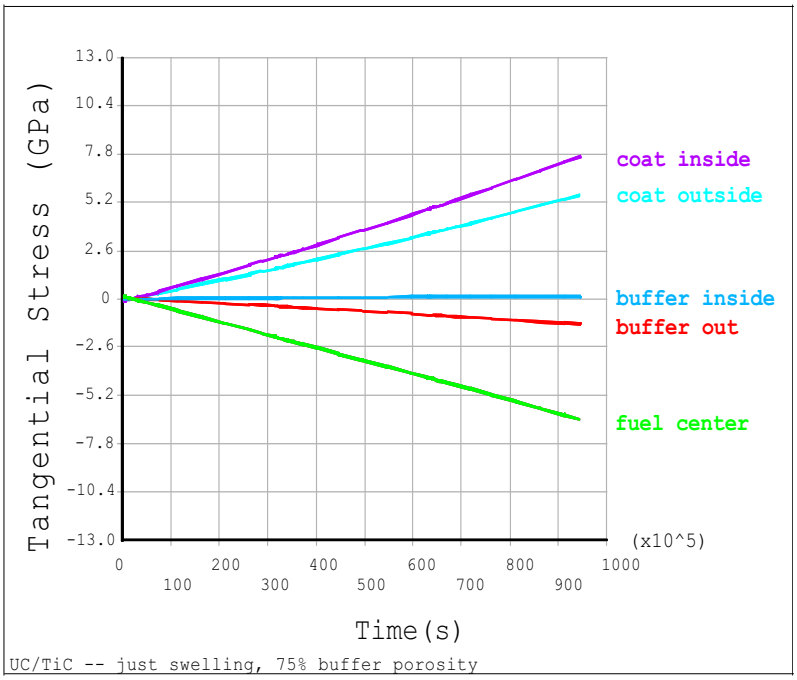

Figure 5.10. Tangential stress from swelling over 3 years in the BISO fuel particle with an increased buffer porosity of 75%.

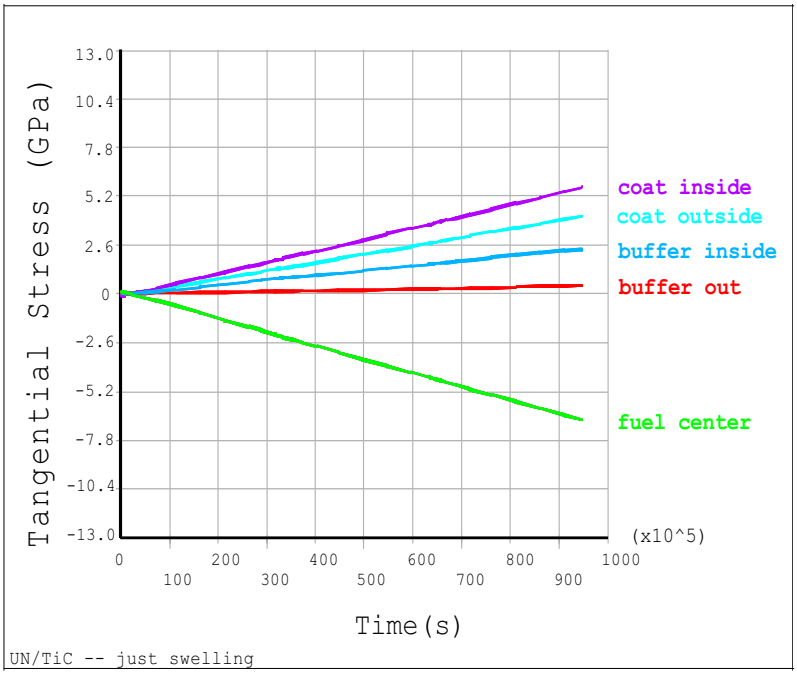

Figure 5.11. Tangential stress from swelling over 3 years in the BISO fuel particle with UN as the fuel.

It can be seen that increasing the porosity from 50% to 75% decreases the stress from swelling by about a third when swelling is the only inelastic strain considered. This creates an interesting relationship between swelling and fission gas release pressure. Increased porosity will lower the stress from swelling, but decreased porosity will help mitigate stress from gas release. However, because the gas release creates a small amount of stress on the coating compared to swelling for the same fission density, a higher porosity is preferable. The analysis shows the use of UN instead of UC cuts the amount of stress on the coating in half because it swells half as much. However, that analysis is again done without regard to the fact that the elastic modulus is dependent on porosity. The elastic modulus for UN is (Cahn 1996):

$$E_p = 260.4(1-p)^{3.002} \quad \text{(Eq. 5.2)}$$

The elastic modulus for UN is only expected to drop 32% from swelling over 3 years, because the swelling rate is not as great. Therefore, when considering the elastic modulus at high temperatures and increased porosity, the true maximum stress in the coating from just swelling of UN is 4.8 GPa. Therefore, the use of UN instead of UC reduces the tangential coating stress by 40% in this baseline analysis.

Another possibility to help reduce stress in the coating is the coating swelling itself. Just as in the case of the thermal expansions, if the fuel and the coating expand at the same rate, there will be no applied pressure between the layers. Swelling for these types of materials is largely unknown. However, contrary to previous studies, SiC has shown significant void swelling up to ~5% starting at 1000ºC (Zinkle 2000). Coating swelling would reduce stress between the kernel and the coating; however low coating swelling is also a requirement given for the GFR fuel matrix materials (Meyer 2003), and the matrix material which constrains the coating will then have an effect on the stress within the system.

5.3.3.3 Creep. The last process during reactor operation is creep. Thermal creep follows the relationship given in Eq. 5.3.

$$\dot{\varepsilon} = A\sigma^n \exp\left(\frac{-Q}{RT}\right) \quad \text{(Eq. 5.3)}$$

Where $\dot{\varepsilon}$ is the strain rate, σ is the stress, Q is the activation energy of the material, T is 1100ºC for this analysis, and A and n are material dependent constants given in Table 5.3.

As can be seen in Table 5.3, creep data for the nitride coatings is not available, so a proper analysis cannot be done for these materials. The amount of creep from irradiation is also unknown, but could have large effects on the fuel particle system, just as thermal creep does (as will be seen). Creep is considered in both the buffer and in the coating, but it is unnecessary to consider it in the kernel because the kernel is in a hydrostatic stress state. Creep is analyzed independent of the other processes with the same baseline—a UC/TiC combination and 50% buffer porosity—just as fuel swelling and fission gas pressure release are. This effect of creep can be seen in Figure 5.12.

Table 5.3. Thermal creep constants for advanced BISO coatings (Daniels 2002, Cannon 1983). The stress exponent (n) is indicative of the creep mechanism.

Materials	A	n	Q (kJ/mol)
TiC	229.3	3	500
SiC	3.01×10^{-5}	1	200
ZrC	6658767	3	600
TiN	N/A		
ZrN	N/A		

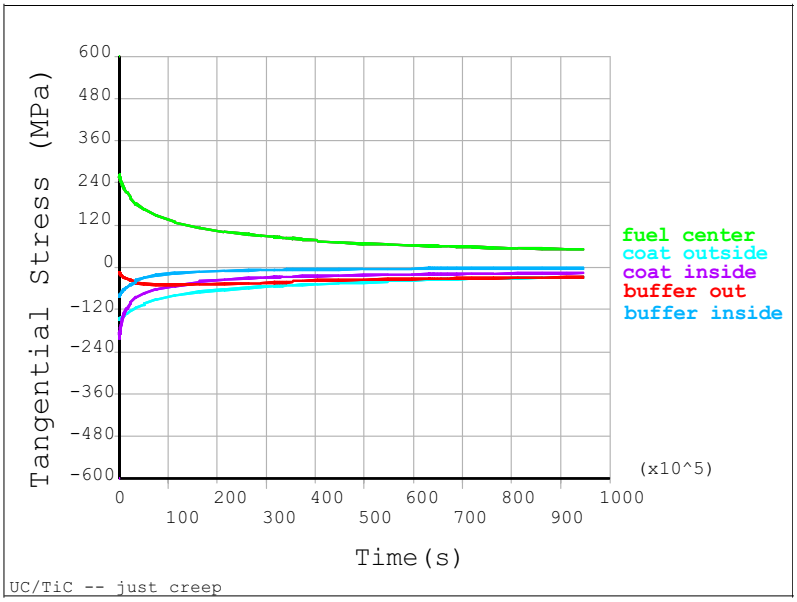

Figure 5.12. The influence of thermal creep on tangential stress for 3 years in the BISO fuel particle (without swelling).

It can be seen that the thermal creep will relax the stress incurred from the thermal expansion on time scales of the order of months and the thermal stress will converge towards zero. The creep will allow the coating to deform and the pressure between the layers of the fuel particle to come to equilibrium. The same is true for 75% buffer porosity, as can be seen in Figure 5.13.

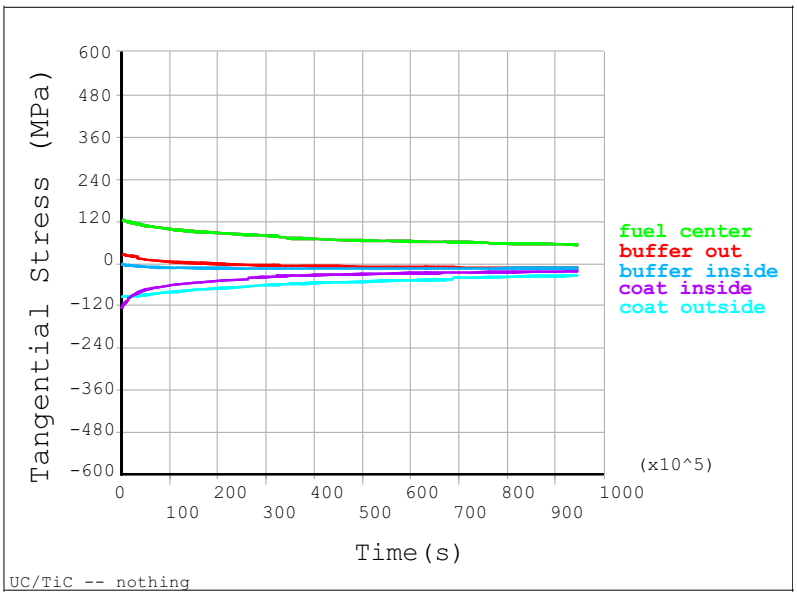

Figure 5.13. The influence of thermal creep on tangential stress for 3 years in the BISO fuel particle with an increased buffer porosity of 75% (without swelling).

5.3.3.4 Full Reactor Operation. When all of the reactor processes are considered together as we would expect during the reactor operation, it can be seen that the processes have an effect on each other, as seen in Figure 5.14.

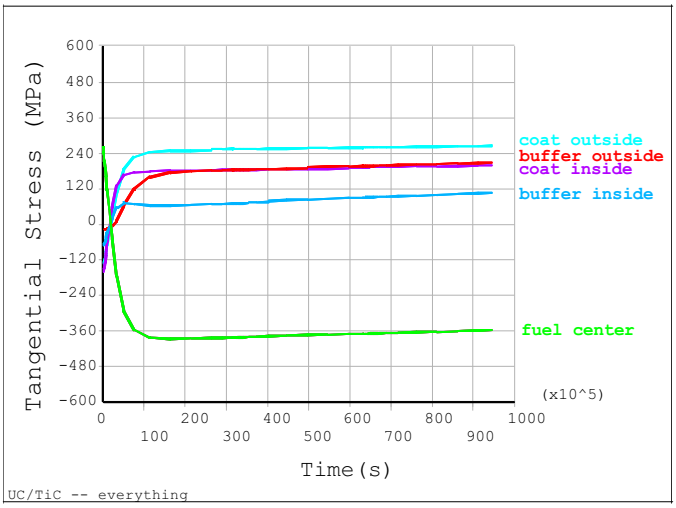

Figure 5.14. Tangential stress in the BISO fuel particle during 3 years of reactor operation.

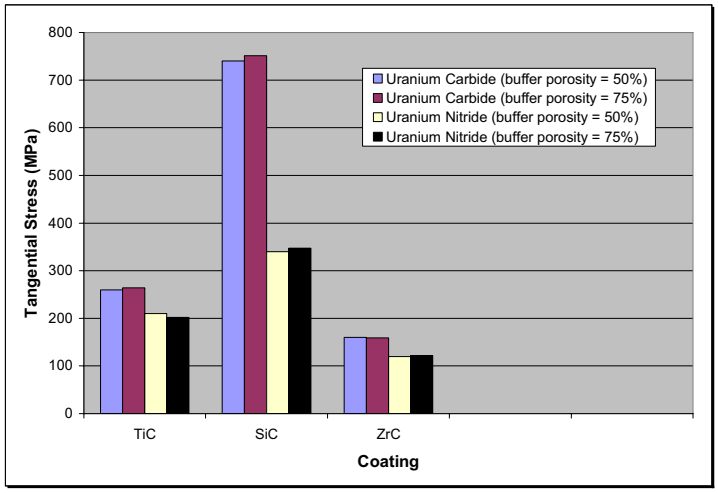

Figure 5.15. Maximum tangential stress in the coating materials during reactor operation. A proper analysis of the nitride coatings could not be completed because of their unknown thermal creep rates.

The stresses incurred from the individual reactor processes are not simply additive. In the previous sections, we saw that fission gas pressure was relatively insignificant, swelling created run-away stress, and creep would allow for slow relaxation until there was no more stress in the coating. Now it can be seen that there is a steady state stress, reached when the initial thermal stresses have relaxed and the swelling and creep strains balance each other. Creep maintains the stresses at a lower level, however too much creep can possibly lead to creep rupture. All of the fuel/coating combinations were analyzed, and the steady-state stress values (which are also the maximum) are reported in Figure 5.15. It is significant to note that the tangential stress is in tension, as opposed to previously when it was in compression in the first and second stress periods.

As can be seen, UC creates higher levels of stress than UN because of the higher swelling rate. Among the coatings, SiC has the greatest amount of stress because it has the lowest creep rate at this temperature and these stresses. Also, the swelling and creep rate dominate the results, making the thermal expansion mismatch and buffer porosity relatively unimportant for long term operation. As opposed to the earlier results, the maximum coating stresses in this case are tensile, due to gas pressure and interaction with the swelling fuel particle. The maximum stress moves to the outside surface of the coating.

5.3.4 Reactor Shutdown

After the fuel particles have operated for some time, they will be brought back to room temperature. Therefore, the differential thermal expansion in the fuel particle will once again change the stress in the coating. The maximum stress for the different fuel/coating combinations for this 4th stress period can be seen in Figure 5.16.

This figure may be confusing at first compared to the other stress periods because depending on the fuel and coating combination, some tangential stresses will return to compression while others will remain in tension. This however, becomes clear if one realizes that the stress in the coatings at room temperature would be exactly the same as they were before the reactor operation if there was no swelling, creep, and fission gas release. Because of these processes, 1600ºC is no longer an equilibrium point of no stress. However, the tangential stress increase from 20ºC (1st stress period) to 1100ºC (2nd stress period) is similar to the amount of stress that decreases from the end of reactor operation (3rd stress period) to 20ºC (4th stress period). This can be seen by comparing the stress difference of Figures 5.15 and 5.16 to the

difference of Figures 5.6 and 5.7. The placement of the maximum tangential stress is now dependent on the material combination. If the stress from the differential thermal expansion is great enough, it will return to being the dominant stress producer, and the maximum stress will once again occur on the inside of the coating. If however, the differential thermal expansion is not significant, the maximum tangential stress will remain on the outside of the coating. If the tangential stress in the coating from this stress period is low (<100 MPa), it is possible to have part of the tangential stress in the coating in tension and part in compression.

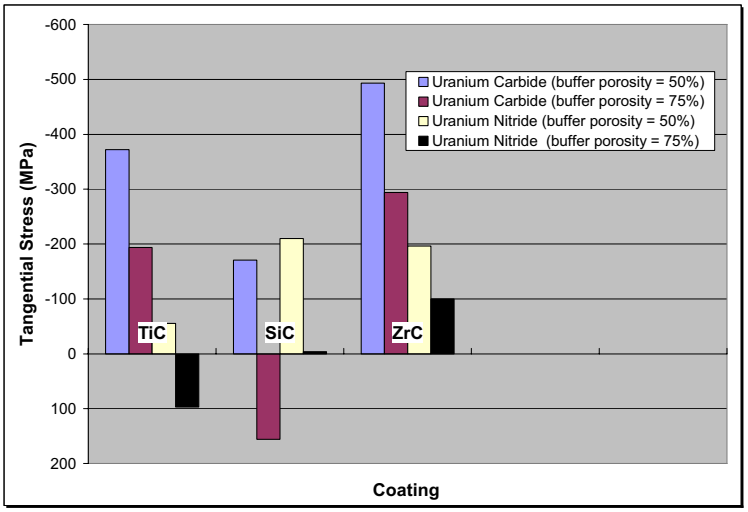

Figure 5.16. Maximum tangential stress in the coating materials after reactor operation. A proper analysis of the nitride coatings could not be complete because of their unknown thermal creep rates.

5.4 Fracture Model

A likely failure mode of coated fuel particles is fracture of the coating, leading to release of fission products. Such fracture is likely to be caused by tensile stresses such as the ones discussed in the previous sections. To address these issues, fracture mechanics models have been employed to study the effects of flaws within the coating.

The most critical flaw in a spherical shell coating will typically be an elliptical flaw either embedded within the coating or at the inner coating surface. No model is available for elliptical flaws in spherical shells, but simplified models are adequate for the current application.

There are existing fracture models for through-cracks in spherical shells (Folias 1965, Erdogan 1969) and, in comparing the results to those for through cracks in flat plates, one finds that sufficiently thin spherical shells behave identically to flat plates. This is shown in Figure 5.17, which shows the stress intensity as a function of crack size for both a thin spherical shell and a flat plate. As can be seen, for width or circumference of 880 microns and a thickness of 40 microns, the results are identical for crack sizes below about 20 microns. Hence, for small cracks, a flat plate model should be adequate for the preliminary assessment of the coatings considered in this work.

These results have been obtained using the following equations. The stress intensity K_I caused by a finite line crack of width 2*a* in a thin plate of width W and thickness *t* is given by:

$$K_I = \sigma \cdot (\pi \cdot a)^{\frac{1}{2}} \cdot \left[\frac{W}{\pi \cdot a} \cdot \tan\left(\frac{\pi \cdot a}{W} \right) \right]^{\frac{1}{2}} \quad \text{(Eq. 5.4)}$$

In a thin spherical shell of radius R and thickness t a finite line crack of the size $2a$ leads to a stress intensity of:

$$K_I = \sigma \cdot (\pi \cdot a)^{\frac{1}{2}} \cdot \left(1 + 1.41\lambda^2 + 0.04\lambda^3\right)^{\frac{1}{2}} \quad \text{(Eq. 5.5)}$$

where

$$\lambda = \frac{a}{(R \cdot t)^{\frac{1}{2}}}. \quad \text{(Eq. 5.6)}$$

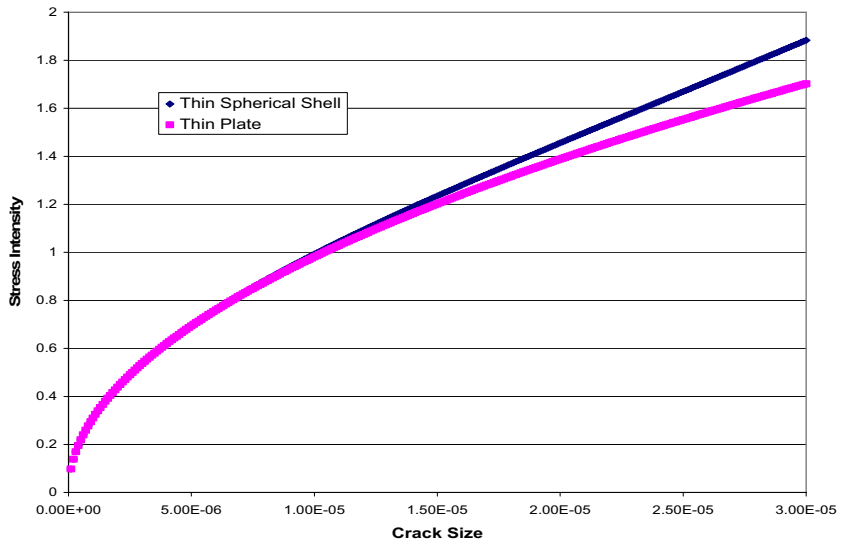

Figure 5.17. Stress Intensity Factor (MPa-m$^{1/2}$) for a thin plate and a spherical shell. Thicknesses are 40 µm; circumference and plate width are 880 µm.

Fracture models for elliptical cracks in flat plates are readily available. For such a crack with major radius b and minor radius a, the maximum stress intensity is given by:

$$K_I = \sigma \cdot (\pi \cdot a)^{\frac{1}{2}} \cdot \frac{1}{E(k)} \quad \text{(Eq. 5.7)}$$

where

$$E = \int_0^{2\pi} \left(1 - k^2 \cdot \sin^2 \varphi\right)^{\frac{1}{2}} d\varphi \quad \text{(Eq. 5.8)}$$

and

$$k = \left(1 - \frac{a^2}{b^2}\right)^{\frac{1}{2}} \qquad \text{(Eq. 5.9)}$$

This elliptical crack is assumed to be embedded within the coating. A modified version is the semi-elliptical surface crack, where the crack is located directly on the surface:

$$K_I = \sigma \cdot (\pi \cdot a)^{\frac{1}{2}} \cdot \frac{G}{E(k)} \qquad \text{(Eq. 5.10)}$$

with $G = 1.12$.

The results for the stress intensity factor from these two geometries is shown in Figure 5.18 for the case of b=2a. It is clear from this figure that for the same crack size the surface cracks are more likely to grow. Hence, only these cracks will be considered further.

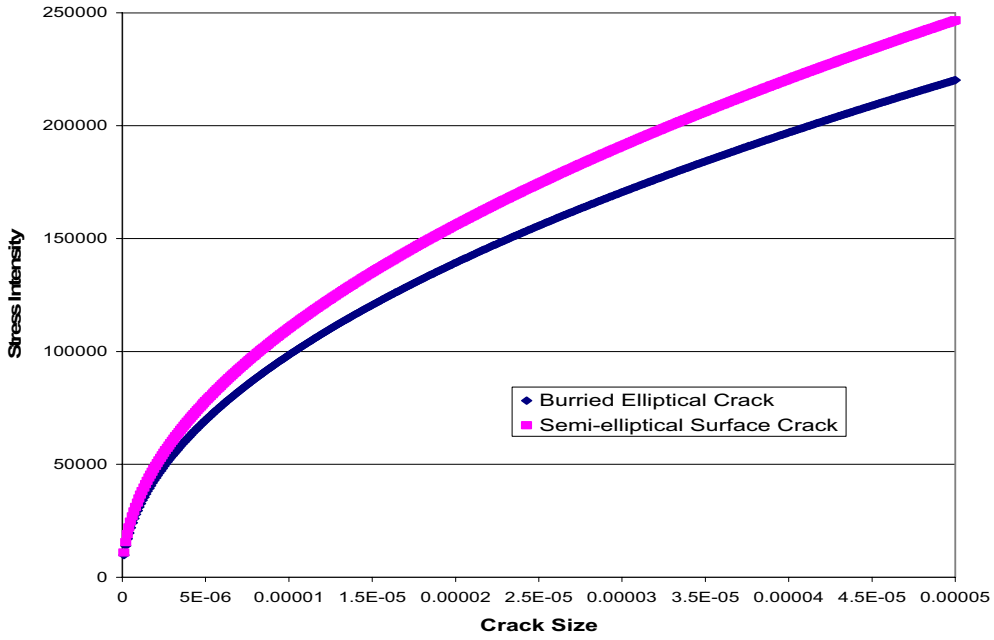

Figure 5.18. Stress intensities vs. crack size for embedded and surface elliptical cracks for b=2a.

In determining the failure loads for these coatings, one must compare the calculated stress intensity factor for a given load and geometry to the fracture toughness of the coating material. For polycrystalline silicon carbide (SiC), the fracture toughness is in the range $2.8MPa\sqrt{m} \le K_{I,c}^{SiC} \le 3.4MPa\sqrt{m}$ (Bellante 2005), but it exhibits a strong dependence on temperature and material processing. For single-crystal SiC one finds $K_{I,c}^{SiC} = 3.3MPa\sqrt{m}$ for temperatures below 500˚C, but approaching a value of $5.8MPa\sqrt{m}$ at 1500˚C (Henshall 1977). For sintered SiC slightly elevated values ($3.8MPa\sqrt{m} \le K_{I,c}^{SiC} \le 5.6MPa\sqrt{m}$, increasing with sintering temperature) are reported (Kim 2000). For hot pressed SiC the range $2.9MPa\sqrt{m} \le K_{I,c}^{SiC} \le 4.5MPa\sqrt{m}$ is reported (Shih 1979). It should be

noted that the hot pressed and sintered forms of SiC differ markedly in their temperature dependence. While $K_{I,c}^{SiC} = 3.1 MPa\sqrt{m}$ for sintered SiC, with a gradual increase with temperature above 1200˚C, the fracture toughness of the hot pressed version ($K_{I,c}^{SiC} = 3.7 MPa\sqrt{m}$) dramatically decreases with temperature above 1100˚C (to $K_{I,c}^{SiC} \le 2.6 MPa\sqrt{m}$ at 1400˚C).

For titanium carbide (TiC), the amount of available data is small, but it seems to exhibit a consistently higher toughness than SiC. A value of $K_{I,c}^{TiC} = 7.8 MPa\sqrt{m}$ is reported (Upadhyaya 1996, Chermant 1978) for room temperature. For single-crystal TiC a range of far lower values, $1.50 MPa\sqrt{m} \le K_{I,c}^{TiC} \le 3.58 MPa\sqrt{m}$ is reported (Maerky 1996) where the actual value is strongly dependent on direction. A lower range is given for hot pressed TiC ($3.53 MPa\sqrt{m} \le K_{I,c}^{TiC} \le 4.59 MPa\sqrt{m}$) (Song 2002). Although ZrC, TiN, and ZrN is not considered, future work is planned to look more in depth at these materials and their resistance to crack propagation.

Using the results for stress intensity factors for surface elliptical flaws in flat plates, one can compare the allowable pressures for fixed geometries and varying materials. The results are shown in Figure 5.19, which shows that the TiC coatings are more fracture resistant than SiC.

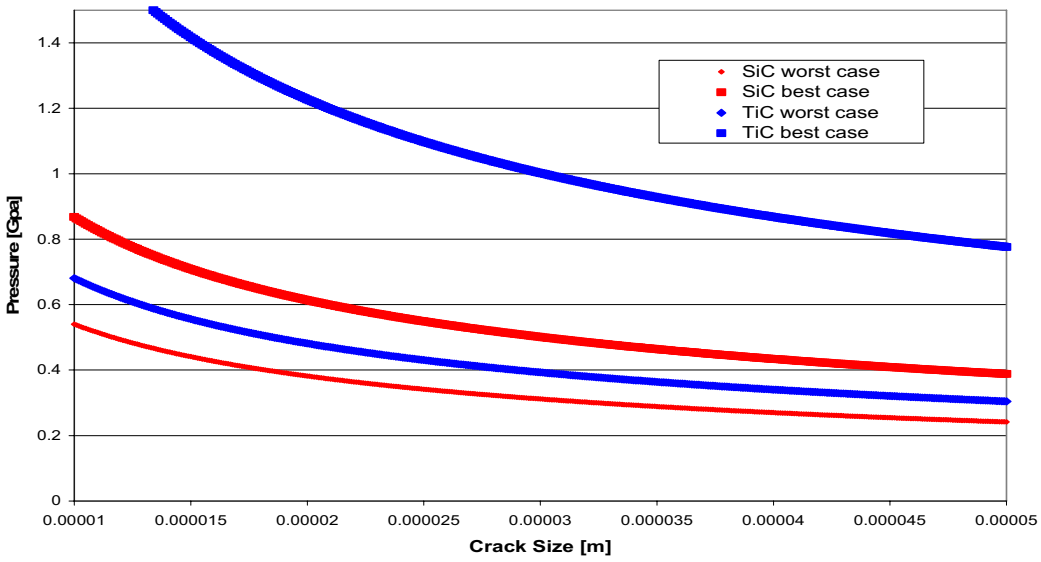

Figure 5.19. Allowable pressure for an elliptical surface flaw in a spherical shell for various materials.

5.5 References for Section 5

Bauccio, M.(Ed.), 1994, *ASM Engineered Materials Reference Book, Second Edition,* Materials Park, ASM International.

Bellante, J.J. and H. Kahn, 2005, "Fracture Toughness of Polycrystalline Silicon Carbide Thin Films," *Applied Physics Letters*, Vol. 86, No. 071920.

Cahn, R.W., et al., 1996, *Materials Science and Technology: Nuclear Materials, Vol. 10A*, John Wiley and Sons.

Cannon, W. R., and T. L. Langdon, 1983, "Creep of Ceramics. I. Mechanical Characteristics," *Journal of Materials Science*, Vol. 18, pp. 1-50.

Chermant, J.L. et al., 1978, *Engineering Fracture Mechanics of Ceramics; Volume 4*, 891, Binghampton: Plenum Publishing.

Daniels, C.A., 2002, *Ceramics: Structure and Properties, Mechanical Properties*, Washington: Abyss Books, pp. 123-124.

El-Genk, M., 1994, *A Critical Review of Space Nuclear Power and Propulsion 1984-1993*, New York: American Institute of Physics.

Erdogan, F. and J. J. Kibler, 1969, "Cylindrical and Spherical Shells with Cracks," *International Journal of Fracture Mechanics*, Vol. 5, pp. 229-237.

Folias, E. S., 1965, "A Finite Line Crack in a Pressurized Spherical Shell," *International Journal of Fracture Mechanics*, Vol. 1, pp. 20-46.

Henshall, J.L. et al., 1977, "Fracture Toughness of Single-Crystal Silicon Carbide," *Journal of the American Ceramics Society – Discussions and Notes*, Vol. 60, pp. 373-375.

Kim, Y.W., et al., 2000, "Pressureless Sintering of SiC-TiC Composites with Improved Fracture Toughness," *Journal of Materials Science*, Vol. 35, pp. 5569-5574.

Maerky, C. et al., 1996, "Indentation Hardness and Fracture Toughness in Single Crystal TiC," *Materials Science and Engineering A*, Vol. 209, pp. 329-336.

Matzke, H.J., *Science of Advanced LMFBR Fuels*, 1986, North-Holland.

Meyer, M.K. and N. Chauvin, 2003, "Overview of Gas Fast Reactor Inert Matrix Fuel Candidates," *Proceedings of GLOBAL 2003, New Orleans, Louisiana, November 16-20, 2003*.

Petti, D., 2004, *Development of Improved Models and Designs for Coated-Particle Gas Reactor Fuels, Final Report Under the International Nuclear Energy Research Initiative (I-NERI)*, INEEL/EXT-05-02615, December, 2004.

Pierson, H.O., 1996, *Handbook of Refractory Carbides and Nitrides*, Westwood: William Andrew Publishing/Noyes, 65.

Ritzman, R.L., et al., 1970, "Interpretations of Fission Gas Behavior in Refractory Fuels," *Nuclear Applied Technology*, Vol. 9, pp. 167-187.

Shih, T.T. and J. Opoku, 1979, "Application of Fracture Mechanics to Ceramic Materials; A State-of-the-Art Review," *Engineering Fracture Mechanics*, Vol. 12, pp. 479-498.

Song, G.-M. et al., 2002, "Mechanical Properties of Short Carbon Fiber-Reinforced TiC Composites Produced By Hot Pressing," *Materials Science and Engineering A*, Vol. 326, pp. 240-248

Touloukian, Y.S., et al., 1997, *Thermophysical Properties of Matter: Thermal Expansion of Nonmetallic Solids; Vol. 13*, NY-Washington: Purdue Research Foundation, IFI/Plenum.

Upadhyaya, G.S., 1996, *Nature and Properties of Refractory Carbides*, Commack: Nova Science Publishers.

Zinkle, S.J., and Ghoniem, N.M., 2000, "Operating Temperature Windows for Fusion Reactor Structural Materials," *Fusion Engineering and Design*, Vol. 51-52, pp. 55-71.